INVESTIGATION AND FABRICATION OF 2D PHOTONIC CRYSTALS STRUCTURES FOR LIGHT EMISSION AND OPTICAL MODES CONTROL AT 1.55 μm

Ko-Hsin Lee

▶ **To cite this version:**

Ko-Hsin Lee. INVESTIGATION AND FABRICATION OF 2D PHOTONIC CRYSTALS STRUCTURES FOR LIGHT EMISSION AND OPTICAL MODES CONTROL AT 1.55 μm. Physics [physics]. Université Paris Sud - Paris XI, 2008. English. NNT : . tel-00309092

HAL Id: tel-00309092

https://theses.hal.science/tel-00309092

Submitted on 5 Aug 2008

HAL is a multi-disciplinary open access archive for the deposit and dissemination of scientific research documents, whether they are published or not. The documents may come from teaching and research institutions in France or abroad, or from public or private research centers.

L'archive ouverte pluridisciplinaire **HAL**, est destinée au dépôt et à la diffusion de documents scientifiques de niveau recherche, publiés ou non, émanant des établissements d'enseignement et de recherche français ou étrangers, des laboratoires publics ou privés.

N^0 d'ordre : **9066**

UNIVERSITÉ PARIS XI
UFR SCIENTIFIQUE D'ORSAY

THÈSE

Présentée

Pour obtenir

Le GRADE de DOCTEUR en PHYSIQUE DE L'UNIVERSITÉ PARIS XI ORSAY

PAR

Ko-Hsin LEE

Investigation et fabrication de structures en cristaux photoniques bidimensionnels pour émission de lumière et contrôle de mode optique à 1,55μm

Soutenue le 30 juin 2008, devant la commission d'examen :

M. Jean-Pierre VILCOT	(Rapporteur)
M. Ahmed RHALLABI	(Rapporteur)
M. Daniel BOUCHIER	(Président du jury)
M. Jean-Louis LECLERCQ	(Examinateur)
M. Pascal CHABERT	(Examinateur)
M. Anatole LUPU	(Examinateur)
Mme Anne TALNEAU	(Directeur de thèse)

à mes parents

Résumé de la thèse

Ce travail de thèse porte sur des composants à cristaux photoniques (CP) bidimensionnels réalisés dans des matériaux à base d'InP pour un fonctionnement dans le domaine 1,55 μm. Au sein du CP, la périodicité de la constante diélectrique génère une bande interdite photonique, domaine de fréquence dans lequel la propagation des modes optiques est interdite. L'introduction de défauts dans le CP permet à certains modes optiques localisés d'exister. De telles structures peuvent alors être utilisées comme brique élémentaire d'un circuit intégré photonique. Nous avons étudié des adaptateurs de mode et des lasers monofréquences ainsi que des guides d'onde sur membrane InP.

Les CP sont ici un réseau de trous fabriqués à l'aide de la gravure ionique réactive associée à un plasma à couplage inductif. Dans un plasma Cl_2/Ar optimisé, nous avons obtenu une profondeur de gravure de 2,9 μm pour des trous de 250 nm diamètre. Nous avons montré que la présence de N_2 dans un plasma contenant du chlore renforce la gravure anisotrope et supprime la rugosité des surfaces gravées, et que l'addition de BCl_3 permet d'augmenter la verticalité des trous. Le plasma BCl_3/N_2 a permis d'obtenir les meilleurs profils et états de surface et une profondeur gravée de 1 μm.

Plusieurs géométries d'adaptateurs de mode à CP ont été étudiées et leurs spectres de transmission ainsi que la divergence du mode émergent ont été caractérisés et comparés avec les résultats de simulation. La meilleure géométrie conduit à une amélioration de l'efficacité de transmission d'un facteur 4. Les guides W1 sur membrane InP présentent des pertes de propagation de 25 dB/cm pour des fréquences situées sous la ligne de lumière.

Thesis abstract

This PhD work focuses on two-dimensional photonic crystals (PhC) devices based on InP materials for application around 1.55 μm wavelength. PhC is a periodic structure in dielectric constant and is characterized by photonic band gap, a frequency domain in which the light propagation is inhibited for certain directions. Introducing defects in the periodicity offers another manner for light guiding and photon localization, which may provide a platform for photonic integrated circuits. The investigated devices include PhC taper waveguides and multiple-constricted-waveguide lasers on InP substrate, and PhC channel defect waveguides on InP suspended membrane.

The perforated PhC structures are realized using reactive ion etching technique associated with inductive coupled plasma. A Cl_2/Ar plasma has been optimized and demonstrated an etch depth of 1.9~2.9 μm for 110~250 nm-diameter holes. We have demonstrated that the addition of N_2 into chlorine-containing plasmas can enhance the anisotropic etching and suppress the etched surfaces roughness. In addition, we have shown that adding BCl_3 augments the feature verticality. Extremely smooth etched sidewall surfaces are obtained when the etching is performed under the BCl_3/N_2 plasma; in which an etch depth of 1 μm can be achieved.

Several contour geometries of PhC tapers are studied and their transmission spectra and beam divergences are measured and compared with the simulation results. The transmission efficiency can be enhanced by a factor of 4 owing to the proper taper design. As for suspended membrane, a propagation loss of 25 dB/cm has been obtained for W1 PhC waveguide while operating below the air-light line.

Remerciements

Ce travail de thèse a été réalisé au Laboratoire de Photonique et de Nanostructures à Marcoussis ; je tiens à remercier Jean-Yves Marzin et Paul Voisin de m'y avoir accueillie. Je suis également redevable à Dominique Aymer de la Chevalerie et Sasha Ting, de l'Institut Français à Taipei, pour avoir supporter financièrement cette étude.

Je suis reconnaissante à Daniel Bouchier d'avoir présidé mon jury de thèse et je suis honorée que Jean-Pierre Vilcot et Ahmed Rhallabi aient accepté d'être rapporteurs. Leur lecture rigoureuse du manuscrit fut d'une grande aide. Après nous avoir assisté lors des caractérisations plasma, Pascal Chabert a bien voulu juger mon travail, je le remercie, ainsi que Jean-Louis Leclercq et Anatole Lupu qui en tant que membres du jury m'ont fait part de multiples et pertinentes suggestions concernant le manuscrit.

Je tiens à exprimer toute ma gratitude à Anne Talneau pour m'avoir proposé ce thème de recherche et avoir encadré mon travail de thèse. Je la remercie également pour toutes les discussions scientifiques que nous avons eues ensemble et le soutien qu'elle m'a apporté au cours de ces années passées au LPN.

Stéphane Guilet, avec qui j'ai collaboré intensivement, m'a révélé les moindres secrets des plasmas et de la gravure. Je n'oublierai pas nos jours de combat avec Sentech et nos nombreuses conversations sur la culture française. Je lui suis également reconnaissante pour les coups de main multiples et variés qui ont grandement simplifié mon séjour en France. Au travers de nombreuses et fructueuses discussions, Sophie Bouchoule m'a beaucoup apporté. Ses multiples suggestions et précieux conseils concernant le manuscrit me furent d'un grand secours. Son dynamisme et sa passion m'ont toujours permis de garder espoir.

Merci à Isabelle Sagnes dont la qualité des croissances MOVPE nous a permis d'entrer dans le monde des membranes. Je tiens également à exprimer ma gratitude à Gilles Partriarche pour ses mesures en TEM, dont la précision fit que l'on put mettre en évidence de nouveaux phénomènes. Les mesures de photoluminescence bénéficièrent de l'expertise de Karine Meunier, celle de champ lointain de l'aide de Kamel Merghem : sans eux, je n'aurais pu avoir certains des résultats présentés dans ce manuscrit.

Je remercie également Patric Strasser de l'ETH Zurich pour l'intéressante discussion que nous avons eue ensemble concernant la gravure ICP, Audrey Berrier et Srinivasan Anand de KTH Sweden pour les échantillons de puits quantiques qu'ils nous ont fourni.

Merci à tous les membres du LPN pour m'avoir aidé pendant ces années de travail. Plus particulièrement, je voudrais remercier Charlie Gosse pour ses conseils et son aide précieuse lors de la rédaction, des répétitions et finalement de l'écriture de la présente page. Je le remercie aussi pour sa considération et son aide, qui facilitèrent beaucoup ma vie en France. Je suis redevable à Ladislav Prkna, Timothy

Karle et Fabrice Raineri pour les discussions stimulantes sur la partie de modélisation, à Gautier Moreau, Guy Aubin, et Jean-Philippe Tourrenc pour m'avoir fait partager leurs connaissances en optique et finalement à Jérôme Danglot, Laurence Ferlazzo et Luc Le Gratiet pour m'avoir formé à diverses techniques expérimentales.

Je dois exprimer ma reconnaissance à toutes les personnes qui m'ont assistée au quotidien dans la salle blanche (Jean-Claude Esnault, Edmond Cambril, Xavier Lafosse, David Chouteau, Laetitia Leroy, Laurent Couraud, Christophe Dupuis, Christophe Roblin) et à l'atelier (Nicolas Allemandou, Gilbert Chanconie, Laurent Merzeau).

Un grand merci également à l'équipe du déjeuner: Aghiad Khadour, Hicham El Fatimi, Thomas Petitpré, Shéhérazade Azouigui, Hélène Goudket, Adel Boussek-sou, Mélanie LeDu, Hoang-Trung Nguyen, Yanko Todorov, Laura Thévenard, David Massoubre, Aiping Fang et Ding-Yi Cong. Mais ce ne fut pas seulement le partage du pain quotidien à la Sodexho, il y eut aussi d'inoubliables soirées, les balades à Paris, toutes les blagues échangées et les encouragements reçus. En particulier, je tiens à remercier Hicham pour la communication de ses techniques du ≪ Comment (sur)vivre en France quand on est étranger? ≫.

Olivier Oria, Nicolas Trenado et Eric Eusebe m'ont enseigné la beauté et la joie de la salsa. Christiane Colinot, mon professeur de français, m'a aidé à m'exprimer de telle façon que les gens puissent me comprendre. Damien Lucot et Christophe Gosset m'ont fait découvrir la vie nocturne parisienne et m'ont, à cette occasion, offert quelques cours de français supplémentaires. Damien se distingua particulièrement par ses nombreux encouragements. Je tiens ici à tous les remercier.

Merci aussi à tous ceux que j'ai rencontré pendant cette période: Abderrahim Ramdane, Anthony Martinez, Christophe Péroz, Ming-Cheng Cheng, Lina Gatilova, Elizaveta Semenova, Olga Boyko, Abdelkarim Ouerghi, Rémy Braive, Nguyen-Quang Tuong, Nadia Belabas-Plougonven, Rama Raj, Emile Grémion, Joseph Dufouleur, Giancarlo Faini, Katarzyna Kowalik, Arkadiusz Kudelski, Marta Gryglas, Jan Suffczynski, Roland You, Eric Lecompte, Romain Giraud, Marjorie Thomas, Christian Ulysse, Dominique Mailly, Gabriele Vecchi, Jean-Marc Jancu, Lorenzo Bernardi, Sébastien Gleyzes, Ying-Xin Liang, Jing Chen, Ling-Sheng Ling, Jian Shi, Guilhem Velve-Casquillas. Je me souviendrai longtemps des moments passés ensemble dans le bureau, dans le bus ou dans le couloir.

Il y a quatre ans, un copain m'avait conseillé de choisir le chemin le plus dur à suivre. Aujourd'hui, je ne sais pas si ce choix est le plus pertinent à faire... Mais, bon... Je suis quand même contente car on ne fait jamais la route totalement seule. Merci à Shih-En Tseng, Etienne Lesage et Julien Ridoux pour m'avoir aidé à effectuer mes premiers pas en France. Merci à Alain et Annie Lesage, Valérie et Ronan Guilet pour m'avoir chaleureusement invité et fait déguster la meilleure cuisine française, celle que l'on mange en famille.

Une pensée également pour les amis qui m'ont soutenu durant toutes ces années. Merci à Ru-Yu et Zoé pour n'avoir jamais refusé mes coups de téléphone à minuit.

Merci à Matthias pour les paroles qui m'ont rendu plus clame. Merci à Ru-Mei pour ses encouragements à base de raviolis chinois frais apportés par avion. Merci à Chris pour toutes ses blagues. Merci finalement pour le soutien provenant des ≪ outsiders ≫: Bee, Ya-Ying, Liang, Ching-Ting, Ya-Tse, Amy. Grâce à eux je n'ai pas encore oublié mon mandarin, je suis juste victime d'un petit changement d'accent.

Enfin je voudrais exprimer toute ma gratitude à mes parents pour la confiance qu'ils m'ont accordée durant toutes ces années, mes soeurs et mon frère pour leur support indéfectible. J'aurais aussi une pensée pour Nini qui malheureusement n'a pas eu l'occasion de partager la fin de ce voyage avec moi.

Contents

1 Introduction **21**

1.1 Research evolution on photonic crystals 21

1.2 Thesis scope 23

1.3 Thesis contribution 25

2 Properties of 2D photonic crystals **27**

2.1 The Maxwell's equations and scalability of master equation . . 27

2.2 Computation methods 29

2.2.1 Plane wave expansion method 29

2.2.2 Finite difference time domain method 30

2.3 Band structures and band map 30

2.4 Structure designs 33

2.4.1 PhC channel defect waveguide on substrate 34

2.4.2 PhC coupled cavity waveguide 37

2.4.3 PhC suspended membrane waveguide 38

3 Photonic crystals fabrication **41**

3.1 Introduction 41

3.2 Vertical stacking 45

3.2.1 Laser 46

3.2.2 Taper waveguide 46

3.2.3 Membrane 47

3.3 Electron beam lithography 48

3.4 Reactive ion etching 50

3.4.1 Mechanisms of reactive ion etching 50

3.4.2 Capactively coupled plasma reactive ion etching 52

3.4.3 Inductively coupled plasma reactive ion etching 53
3.5 ICP Cl_2/Ar plasma for PhC holes structure deep etching . . . 54
3.5.1 Etching conditions investigation 55
3.5.2 Optimized etching conditions and RIE lag for ICP Cl_2/Ar plasma 63
3.5.3 Comparison of ICP and CAIBE for PhC holes deep etching 65
3.5.4 Etched PhC devices performances: free-carrier lifetime and optical propagation losses measurements 66
3.6 ICP $Cl_2/BCl_3/N_2$ and BCl_3/N_2 plasma for smooth sidewall surfaces 69
3.6.1 Evolutions of N_2 and BCl_3 in PhC holes structures etching 70
3.6.2 ICP $Cl_2/BCl_3/N_2$ plasma characterization: positive ion current density measurement 75
3.6.3 ICP BCl_3/N_2 plasma: elimination of undercut 77
3.6.4 Etched surface characterization: TEM-EDX analysis . 79
3.6.5 Discussion 83
3.6.6 Etched PhC devices performance: free-carrier lifetime measurement 85
3.7 Conclusion 86

4 Photonic crystals tapers 87
4.1 Introduction 87
4.2 Theory of coupling 89
4.2.1 Gaussian beam 89
4.2.2 Coupling from diode laser/planar waveguide to optical fiber 91
4.2.3 Coupling losses 91
4.3 PhC taper waveguide designs 93
4.3.1 Taper designs based on Bragg effect domination 93
4.3.2 Taper designs based on refractive index contrast domination 95
4.4 PhC tapers simulation 97
4.4.1 Simulation results of PhC stair and variant stair tapers 97
4.4.2 Simulation results of PhC stair and variant stair tapers 100

4.5 PhC tapers fabrication . . . 101
4.6 Optical characterization: light transmission and light divergence . . . 102
4.6.1 Measurement setup . . . 102
4.6.2 Light transmission . . . 103
4.6.3 Beam divergence . . . 104
4.6.4 Coupling losses estimation . . . 109
4.7 Conclusion . . . 112

5 Photonic crystals laser 113
5.1 Introduction . . . 113
5.2 Laser designs based on coupled-cavity . . . 115
5.3 PhC laser designs based on multiple constricted waveguides . . . 118
5.4 Simulation of constricted waveguides . . . 119
5.4.1 Simulation results of W5/W3 constricted waveguides . . . 120
5.4.2 Simulation results of W5/W1 constricted waveguides . . . 121
5.4.3 Discussion: MCW design rules . . . 123
5.5 PhC multiple-constricted-waveguides laser fabrication . . . 124
5.6 Discussion . . . 125

6 Photonic crystals membrane waveguides 127
6.1 Introduction . . . 127
6.2 Selective wet etching calibration . . . 128
6.3 PhC suspended membrane waveguide . . . 130
6.3.1 Fabrication . . . 130
6.3.2 Propagation losses measurement . . . 131
6.4 Discussion . . . 133

7 Conclusion 135

Bibliography 137

Résumé (en français) 151

List of Figures

1.1 The schematic views of (a) 1D Bragg mirror, (b) 2D and (c) 3D photonic crystals. 22

1.2 The schematic figures of 2D PhC with light confinement through index guiding in the vertical direction by (a) a planar heterostructure waveguide (n_2>n_1 and n_2>n_3) or (b) a suspended membrane in air. 23

2.1 Schematic of (a) a 2D triangular lattice of air columns (a: lattice constant, d: hole diameter) and (b) its corresponding first Brillouin zone. The blue tetragon refers to the supercell used for the 2D PWE calculation. 31

2.2 The band structures for a 2D PhC triangular lattice of air columns (a = 400 nm, f = 35%, n_{eff} = 3.25, n_{air} = 1) calculated by the 2D PWE method for (a) the TE and (b) the TM polarizations. 31

2.3 The band map with variations of filling factors in the TE and TM polarizations for a 2D PhC triangular lattice of air columns (a = 400 nm, n_{eff} = 3.25, n_{air} = 1). 32

2.4 The dispersion diagram along ΓK direction in TE polarization for a 2D PhC triangular lattice of air columns (a = 400 nm, f = 35%, n_{eff} = 3.25, n_{air} = 1); in which, the air light line (solid line) and the InP substrate line (dashed line) are indicated. 33

2.5 (a) The schematic of $W3$ waveguide along the ΓK direction ($W3^{[\Gamma K]}$). The blue rectangular refers to the supercell used for 2D PWE calculation. (b) The dispersion diagram for $W3^{[\Gamma K]}$ (a = 400 nm, d = 250 nm, n_{eff} = 3.25, n_{air} = 1) in the TE polarization within band gap (u = 0.223 $\sim$ 0.314 along the ΓK direction). Locations of MSB (with 5th order mode) and crossing point of fundamental even mode in a $W3^{[\Gamma K]}$ are pointed out. The air light line is marked as gray. (c) The transmission spectrum of $W3^{[\Gamma K]}$ simulated by 2D FDTD method. 35

2.6 (a) The schematic of $W3$ waveguide along the ΓM direction ($W3^{[\Gamma M]}$). The blue rectangular refers to the supercell used for 2D PWE calculation. (b) The dispersion diagram for $W3^{[\Gamma M]}$ ($a = 400$ nm, $d = 250$ nm, $n_{eff} = 3.25$, $n_{air} = 1$) in the TE polarization within band gap ($u = 0.198 \sim 0.297$ along the ΓM direction). The intervals of MSB (pink regions) for a fundamental even mode propagation and the air light line (gray) are pointed out. (c) The transmission spectrum of $W3^{[\Gamma M]}$ simulated by 2D FDTD method. 36

2.7 (a) The schematic of a PhC constricted waveguide along the ΓK direction from $W5$ constricted to $W1$ with a period of $3 \times a$. (b) The dispersion diagram of the constricted waveguide shown in (a) ($a = 400$ nm, $d = 250$ nm, $n_{eff} = 3.25$, $n_{air} = 1$) in the TE polarization within the PBG. The mini-gaps (pink regions) for the fundamental even mode (red line) propagation is concerned. (c) The fundamental even mode profiles within four repeated supercells when $u = 0.2259$ (point A) and $u = 0.2662$ (point B). 38

2.8 (a) The schematic of the supercell in the vertical direction for the suspended membrane calculation by the 3D PWE method. (b) The simulation of dispersion diagram for a $W1$ PhC suspended membrane waveguide (280 nm-thick membrane, $n = 3.17$, $a = 400$ nm, and $d = 250$ nm). (c) The group velocities versus the wave vectors for the fundamental even mode guiding in the $W1$ PhC suspended membrane waveguide. The group velocity is derivated approximately from the $\omega - \mathbf{k}_x$ relation. . . . 39

3.1 The vertical stacking of a single-confinement heterostructure laser with InGaAs/InGaAsP multiple quantum-wells as the active region. 46

3.2 The vertical stacking of a InP/InGaAsP heterostructure planar waveguide. 47

3.3 The vertical stacking of an InP membrane waveguide with InGaAs as the sacrificial layer. 47

3.4 The schematic figure of an electron beam pattern generator system. . . . 49

3.5 The SEM top views of PhC holes with shifted positions (away from the standard PhC matrix) and diminished sizes defined by EBL. (a) A single electron-beam dose is used for exposure, and so that holes are merged due to the proximity effect. (b)The compensation of proximity effect by reducing the exposure electron-beam doses for diminished size holes with small intervals. 50

3.6 The schematic of four processes taking place during reactive ion etching, including (a) the sputtering, (b) the chemical etching, (c)the ion enhanced etching, and (d) the inhibitor ion enhanced etching. 51

3.7 (a) The schematic of a CCP-RIE system. (b) An etched SiO_2 dielectric mask using a CHF_3-based plasma in CCP-RIE system. 53

3.8 The schematic of an ICP-RIE system with a planar triple spiral antenna. 54

3.9 SEM cross-section views of PhC holes (d = 180 nm) and trenches etched by Cl_2/Ar plasmas with various ICP powers: (a) 0 W, (b) 100 W, and (c) 200 W. 56

3.10 The etch rate (square) and selectivity (star) for 180 nm-diameter PhC holes etched by Cl_2/Ar plasmas with various ICP powers. 56

3.11 The etch rate (square) and selectivity (star) for 180 nm-diameter PhC holes etched by Cl_2/Ar plasmas with various bias voltages. 58

3.12 SEM cross-section views of PhC holes (d = 180 nm) etched by Cl_2/Ar plasmas with the various bias voltages: $|V_{bias}|$ = (a) 50 V, (b) 100 V, and (c) 150 V. 58

3.13 The schematic of scattered ions resulted from (a) normal and (b) inclined incident ions impinging on sloped mask (80^0, 65^0). 59

3.14 SEM cross-sections of PhC holes (d = 180 nm) etched by Cl_2/Ar plasmas with the various gas pressures: (a) 0.5 mTorr, (b) 1 mTorr, (c) 2 mTorr, and (d) 5 mTorr. 60

3.15 The etch rate (square) and selectivity (star) for (a) 180 nm-diameter PhC holes and (b) 3 μm-wide trenches etched by Cl_2/Ar plasmas with various gas pressures. 60

3.16 The InP etch rate for 180 nm-diameter PhC holes etched by Cl_2/Ar plasmas with various electrode temperatures. 62

3.17 SEM cross-section views of (a) a triangular matrix of PhC holes (a = 300 nm, d = 130 nm) after the Cl_2/Ar (4/16 sccm) plasma etching in an ICP-RIE system. (b) Magnified view on the hole sidewalls. 64

3.18 The etch depths with evolution of PhC holes diameters etched by an ICP Cl_2/Ar plasma with 4 sccm-Cl_2, 16 sccm-Ar, p = 0.5 mTorr, P_{ICP} = 150 W, $|V_{bias}|$ = 130 V, T = 180^0C. (Etch time = 9 mins) 65

3.19 Time-resolved photoluminescence for InP/InGaAsP multiple quantum-wells structures with PhC holes etched by an ICP Cl_2/Ar plasma. The non-etched stack result is indicated for comparison (black line). 67

3.20 SEM side view of W3 PhC and the access ridge. 68

3.21 SEM cross-section views of 3 μm-wide trenches etched by (a) an ICP Cl_2/BCl_3 (33/16 sccm) plasma at 0 V-bias voltage and (b) an ICP $Cl_2/BCl_3/N_2$ plasma with 67%-N_2 at -200 V-bias voltage. 71

3.22 SEM cross-section views of PhC holes etched by ICP $Cl_2/BCl_3/N_2$ plasmas with various N_2 ratios: (a) 14%, (b) 62%, and (c) 67%. The Cl_2 and BCl_3 mass flow rates were fixed at 33 and 16 sccm, respectively. 72

3.23 The InP etch rates for 3 μm-wide trenches (square) and 240 nm-diameter PhC holes (triangle) etched by $Cl_2/BCl_3/N_2$ plasmas with various N_2 ratios. 72

3.24 SEM cross-section views of PhC holes etched by ICP $Cl_2/BCl_3/N_2$ plasmas with various BCl_3 ratios: (a) 0%, (b) 11%, and (c) 15%. The Cl_2 and N_2 mass flow rates were fixed at 33 and 99 sccm, respectively. (d) The InP etch rates for 3 μm-wide trenches (square) and 240 nm-diameter PhC holes (triangle) with various BCl_3 ratios. 74

3.25 The InP etch rates for 3 μm-wide trenches (square) and 240 nm-diameter PhC holes (triangle) etched by $Cl_2/BCl_3/N_2$ plasmas with various BCl_3 ratios. 74

3.26 The evolutions of positive ion current density with (a) the ICP power (triangle; p = 5 mTorr) and the total gas pressure (square; P_{ICP} =1 000 W) in a $Cl_2/BCl_3/N_2$ (33/16/99 sccm) plasma, (b) the Cl_2 ratio (black square; F_{BCl3} = 16 sccm and F_{N2} = 99 sccm), the BCl_3 ratio (red empty square; F_{Cl2} = 33 sccm and F_{N2} = 99 sccm) and the N_2 ratio (blue circle; F_{Cl2} = 33 sccm and F_{BCl3} = 16 sccm) in a $Cl_2/B_{Cl3}/N_2$ plasma with p = 5 mTorr and P_{ICP} = 1000 W. 76

3.27 SEM cross-section views of PhC holes etched by (a) a Cl_2/N_2 (33/99 sccm) plasma with p = 5 mTorr, P_{ICP} = 1000 W, $|V_{bias}|$ = 200 V, (b) a BCl_3/N_2 (24/99 sccm) plasma with p = 5 mTorr, P_{ICP} = 1000 W, $|V_{bias}|$ = 350 V. The SiO_2 mask was removed in both cases. 78

3.28 TEM images of etched PhC holes in InP/InGaAs heterostruture by an ICP BCl_3/N_2 plasma: (a) enlarged view of the PhC holes, (b) magnification on the sidewalls and the InP/InGaAs interface, and (c) magnification on the InP sidewall surface. 81

3.29 TEM images of etched PhC holes in InP/InGaAs heterostruture by an ICP Cl_2/N_2 plasma: (a) enlarged view of the PhC holes, (b) magnification on the InP/InGaAs interface, (c) magnification on the InP sidewall surface, and (d) magnification on the InGaAs sidewall surface. 82

3.30 Schematic of several possible representative etching reactions on InP surface under a BCl_3/N_2 plasma. 84

3.31 Time-resolved photoluminescence for InP/InGaAsP multiple quantum-wells structures with PhC holes etched by an ICP $Cl_2/BCl_3/N_2$ plasma. The non-etched stack result is indicated for comparison (black line). . . 85

4.1 The schematic of mode sizes comparison between a PhC waveguide elliptic mode and a single-mode fiber circular mode. 89

4.2 The schematic of near-field and far-field of a Gaussian beam. 90

4.3 The coupling losses with variation of mode sizes (w_{0x}, w_{0y}) from a diode laser/planar waveguide to a single-mode optical fiber with a mode size of 10 μm-wide ($\eta = 0.96$). The coupling losses were calculated based on equation (4.6). 92

4.4 The SEM top views of the fabricated (a) PhC stair (8-periods) taper and (b) PhC variant-stair (8-periods) and the gradual diminished diameters of 4 holes in the transition region. 94

4.5 The schematic of PhC tapers with the contours of gaussian curve, double-parabola, and semi-ellipse. 95

4.6 The SEM top views of (a) the PhC curved taper with contour of gaussian curve and the input/output access ridges. (b) Magnification of varied hole sizes and positions together with the standard PhC triangular matrix. . . 102

4.7 The schematic of system setup for (a) the light transmission measurement and (b) the far-field measurement. 103

4.8 The spectrally resolved transmission diagrams for (a) the gaussian curve taper, (b) the W3 guide, and (c) the semi-ellipse taper. 104

4.9 The notations of propagation losses within a conventional plain ridge, a W3 guide, and a PhC taper. The light is injected by a micro-lensed fiber and is collected either by another micro-lensed fiber or by a cleaved-facet fiber. 110

5.1 The schematic illustration longitudinal modes, gain profile, loss profile, and the resulting lasing modes for (a) a single-cavity semiconductor laser and (b) a coupled-cavity semiconductor laser. 116

5.2 The notations used for effective mirror reflectivity theory of coupled-cavity laser. 117

5.3 The schematic figure of PhC multiple-constricted-waveguides. The cavity length and the narrowing section length are defined as in the figure. . . . 119

5.4 The schematic figures of simulated PhC constricted waveguide for (a) W5 constricted to W3 and for (b) W5 constricted to W1. The length of narrowing section is designated as $N \times a$ (N is an integral number). T and R signify the transmission and reflection through constriction section. 119

5.5 The simulation results of (a) transmission and (b) reflection efficiencies for the fundamental mode with variation of narrowing section lengths in W5/W3 constricted waveguides. 120

5.6 The simulation results of (a) transmission and (b) reflection efficiencies for the fundamental mode with variation of narrowing section lengths in W5/W1 constricted waveguides. 121

5.7 The simulated coupling constants with variation of narrowing section lengths for W5/W1 constricted waveguides at several different wavelengths. 122

5.8 (a) SEM top view of etched PhC multiple W5/W1 constricted waveguide laser. (b) Magnification on the constrictions and coupled cavities. 124

5.9 The simulation results of H^+ ion distributions in vertical and lateral directions in (a) InP and (b) photo-resist SPR 200-7 materials. 125

6.1 The schematic of selective wet etching process on a InP membrane with PhC holes structure. (a) PhC holes after dry etching and removal of mask. The etch depth is extended to the sacrificial layer. (b) The solution enters through the PhC holes and etches selectively the sacrificial InGaAs layer. 128

6.2 The SEM top views of (a) a InP suspended membrane with PhC holes structure. The selective wet etching of InGaAs layer was realized using a H_2SO_4:H_2O_2:H_2O = 1:1:10 solution (4 minutes). (b) Magnified view on PhC holes. 129

6.3 The SEM cross-section views of (a) a InP suspended membrane with PhC holes structure. The selective wet etching of InGaAs layer was realized using a H_3PO_4:H_2O_2:H_2O = 1:1:5 solution (3 minutes). (b) Magnified view on hole sidewalls. 129

6.4 The SEM cross-section views of (a) a InP suspended membrane with PhC holes structure. The selective wet etching of InGaAs layer was realized using a solution based on Fe_3^+ ions (1.75 minutes). (b) Magnified view on hole sidewalls. 130

6.5 The SEM cross-section views of (a) a InP W1 PhC suspended membrane waveguide after InGaAs wet etching and supercritical drying in CO_2. (b) Magnification on the InP membrane with PhC holes. The PhC etching was performed using an ICP BCl_3/N_2 (24/99 sccm) plasma with 5 mTorr-gas pressure, 1000 W-ICP power, and -270 V-bias voltage. 131

6.6 (a) Dispersion curve of InP W1 PhC suspended membrane waveguide for 280 nm-thick membrane (resized from figure 2.8(b)). (b) Spectrally resolved transmission spectrum of a fabricated 774 μm-long W1 guide. . 132

List of Tables

3.1 The enthalpies of vaporization (Δ_{vap}H) for indium chloride, phosphorus chloride, gallium chloride, arsenic chloride, indium iodide, and phosphorus iodide. 43

3.2 The summary of developed etching methods and plasmas for PhC holes structure etching in InP materials. 44

3.3 The investigated ICP power range and other etching conditions in Cl_2/Ar plasmas. 55

3.4 The investigated bias voltage range and other etching conditions in Cl_2/Ar plasmas. 57

3.5 The investigated gas pressure range and other etching conditions in Cl_2/Ar plasmas. 59

3.6 The investigated Cl_2 : Ar mass flow rates and other etching conditions in Cl_2/Ar plasmas. 61

3.7 The investigated electrode temperature range and other etching conditions in Cl_2/Ar plasmas. 62

3.8 The optimized Cl_2/Ar plasma etching conditions for PhC holes structure. 64

3.9 The investigated N_2 ratio range and other etching conditions for Cl_2/BCl_3/N_2 plasmas. 71

3.10 The investigated BCl_3 ratio range and other etching conditions for Cl_2/BCl_3/N_2 plasmas. 73

3.11 The etching conditions of BCl_3/N_2 plasma adopted to eliminate the undercut. 78

4.1 The schematic of PhC tapers with geometries of stair (8-periods), variant stair (8-periods), stair (4-periods), and variant stair (4-periods); and their simulated transmission (black line)/reflection (gray line) flux and modal distribution efficiency for the fundamental even mode (black line), the second even mode (red line), the third even mode (gray dashed line) with the function of wavelength. 99

4.2 The schematic of PhC tapers with contours of gaussian curve, double-parabola, and semi-ellipse; and their simulated transmission (black line)/reflection (gray line) flux and modal distribution efficiency for the fundamental even mode (black line), the second even mode (red line), the third even mode (gray dashed line) with the function of wavelength. 100

4.3 The measured far-field divergence diagrams for PhC tapers with geometries of stair (8-periods), variant stair (8-periods), stair (4-periods), and variant stair (4-periods) at 1.45 μm and 1.6 μm wavelength. 106

4.4 The measured far-field divergence diagrams for the PhC tapers with contours of gaussian curve, double-parabola, and semi-ellipse at 1.45 μm and 1.6 μm wavelength. The divergence diagram for a cleaved-facet single-mode fiber at 1.55 μm is shown for reference. 107

4.5 The summary of measured coupling efficiency enhancement and estimated modal conversion rates and divergence angles for designed PhC tapers. 108

4.6 The estimated coupling losses to a cleaved-facet single-mode fiber for the W3 guide without taper, the variant-stair taper (8-periods), the semi-ellipse taper, and the gaussian curve taper. The physical length of the PhC taper section is 34.4 μm.) 111

Chapter 1

Introduction

1.1 Research evolution on photonic crystals

The photonics is being developed rapidly in the recent years and had been applied in diverse domains. Moreover, with the demands of enormous information transportation and processing in communication networks, the manner through electrical signals is reaching the limitations. An alternative through the optical signals which benefits from high speed transmission and reduced cross-talks between channels is believed to achieve this objective. The optical signals transmission has been realized by optical fibers and optical components like waveguides and resonators have also been demonstrated. As for the optical signals processing, photonic integrated circuits (PICs) in which the photonic devices are compact and monolithically integrated are preferable. With the developments on nanofabrication, the PICs can be scaled down in dimension and can be fabricated in conventional semiconductor materials like silicon, GaAs, and InP. Hence, not only lights can be confined and guided tightly due to the high refractive index contrast, but more complex functions with electronic components are also feasible.

Photonic crystal (PhC) is one of the choices for miniaturization and integration of photonic devices. It was first proposed in 1987 simultaneously by E. Yablonovitch and S. John for spontaneous light emission inhibition [Yablonovitch1987] and photon localization [John1987]. By a more strict definition [Yablonovitch2007], PhC is designated to a structure with periodic variation of dielectric constant in two or three dimensions. The index contrast should be high (≥ 2) and the periodicity is at the order of light wavelength in material. Figure 1.1(b) and (c) show the schematic views of two-dimensional (2D) and three-dimensional (3D) PhC structures. In 2D PhC, the dielectric constant variation is periodic along two axes and homogeneous in the third direction. Similarly, it is periodic along all three axes for 3D PhC. The one-dimensional (1D) multilayer structure named as Bragg mirror is shown schematically in figure 1.1(a).

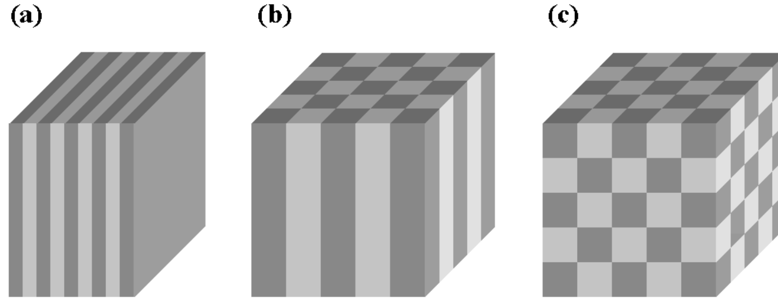

Figure 1.1: The schematic views of (a) 1D Bragg mirror, (b) 2D and (c) 3D photonic crystals.

The principle characteristic of PhC is the presence of photonic band-gap (PBG), which inhibits the light propagation in certain directions with specified frequencies. The photonic band-gap is analogous to the electronic band-gap in semiconductor crystals. A complete photonic band-gap, in which the light of any polarization incident at any angle is reflected by PhC, can only exist in a 3D system. As for 2D PhC, the PBG involves the light propagation in the plane of periodicity. Even though the 3D PhC can offer a complete PBG for a manipulation of light in all three dimensions in space, the fabrication is extremely challenging [Yablonovitch1991, Cheng1995, Cheng1996]. As a result, 2D PhC combined with the index guiding in the third direction, or called quasi-3D, is more applicable [Krauss1996, Villeneuve1998]. In this case, the light confinement in the third direction is insured by the refractive index contrast realized either in a planar waveguide composed of heterostructures or in a membrane suspended in air as presented in figure 1.2. This method is expected greatly to carry out the PICs and several photonic components including PhC waveguides and PhC cavities based on this conception have already been demonstrated. Nevertheless, the out-of-plane radiation losses into air or substrate may somehow degrade and limit the optical performances.

The applications of PhC structures can be further extended when the defects are introduced. Defects are referred to the violation of translation symmetry in PhC structures through, for instance, omitting a lattice site or perturbing the site positions and sizes. By creating defects inside PhC structures, the localized modes can be obtained within the PBG. With proper defects designs, it then is possible to localize light, to alter the optical density of states, and to control the light propagation at desired wavelengths [Joannopoulos1995]. The linear defects in 2D PhC structures can be served as waveguides to guide lights for wavelengths within the PBG; while the point defects can form cavities with small volumes. Numbers of photonic devices including the guiding bends [Mekis1996, Baba1999, Talneau2002], splitters [Sugimoto2002, Boscolo2002, Lin2002], add-drop filters [Fan1998, Olivier2003a], and waveguide crossings [Johnson1998, Lan2002]

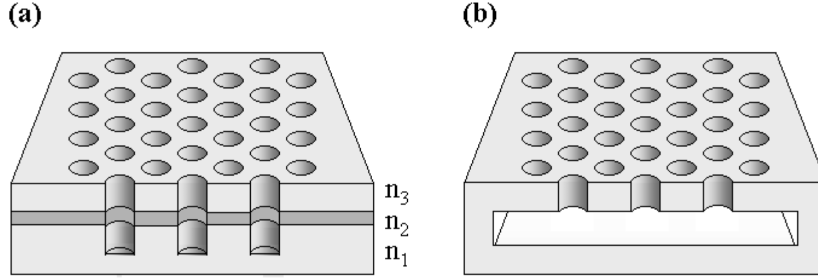

Figure 1.2: The schematic figures of 2D PhC with light confinement through index guiding in the vertical direction by (a) a planar heterostructure waveguide ($n_2>n_1$ and $n_2>n_3$) or (b) a suspended membrane in air.

have been fabricated with PhC line defects. In addition, the high quality factor has been presented in 2D PhC with point defects [Akahane2003], which can be used to realize low-threshold cavity lasers [Painter1999, Vuckovic2002, Loncar2002, Seo2007]. The dispersion curves of defect modes at the band-edge can be relatively flat; and it implies reduced group velocities. The lasing is thus anticipative at the band-edge due to an enhanced light-matter interaction [Sugitatsu2003].

Other unique phenomena of PhC like the superprism and the negative refraction are also exploited for the applications of wavelength division multiplexing [Kosaka1998, Kosaka1999] and near-field imaging [Foteinopoulou2003, Cubukcu2003]. Moreover, PhC fibers [Russell2006] are well investigated and supplied commercially.

1.2 Thesis scope

This thesis concerns mainly the 2D PhC devices with InP-based materials operating at wavelength around 1.55 μm. The III-V compound semiconductors (ex: GaAs and InP) are known to have direct band-gaps, which permit to realize simultaneously the active and passive functions on the same substrate. The emitted light wavelength covers a wide range (0.7$\sim$1.7 μm), in which, 1.3 μm and 1.55 μm are favorable for the telecommunication applications due to the reduced dispersion and attenuation.

The PhC devices investigated within this dissertation include the PhC tapers, the PhC constricted waveguide lasers, and the PhC suspended membrane waveguide. The essential PhC building block of air holes on InP-based materials (refractive index $\sim$ 3.17) operating at 1.55 μm wavelength has a periodicity in the order of 400 nm. The linear defects introduced into plain PhC can provide the light guiding and can be extended to be cavities. The efficient coupling to a single mode fiber and the wavelength selection/tuning are the objectives of PhC tapers and PhC constricted waveguide lasers designs, respectively. As for PhC suspended membrane waveguides, they may allow low-loss propagation and reduced group

velocities, which can enhance the light-matter interaction. The realization of compact 2D PhC devices with the scale of sub-micrometers requires delicate fabrication techniques like electron beam lithography and plasma dry etching. A lot of efforts are thus focused on the development of inductively coupled plasma reactive ion etching (ICP-RIE) for PhC holes structure. Following is a brief outline of involved thesis research scopes.

Chapter 2 first reviews the electromagnetic theory in a periodic medium of dielectric constant and gives the corresponding propagation equation. The band structure of our PhC building block is demonstrated in order to indicate the PBG range. Moreover, the dispersion curves of investigated InP PhC devices including the channel defect waveguide, the coupled-cavity waveguide on substrate, and the suspended membrane waveguide are also calculated to identify the guiding modes.

Chapter 3 lists in detail the composition parameters of investigated PhC devices, mask preparation, and the developments on inductively coupled plasma reactive ion etching (ICP-RIE). The Cl_2/Ar plasma is optimized for deeper PhC holes etching (> 2 μm). Furthermore, the chlorine-containing plasma with the addition of N_2 is developed and investigated with the expectation to suppress etched surface damages. The positive ion fluxes in plasmas are measured to estimate the ionic sputtering during the etching process. The optical propagation and the etched surfaces characterizations are reported as well in order to acquire the performances of etched PhC profiles.

Chapter 4 demonstrates the simulation, fabrication, and performances of designed PhC taper waveguides. The tapers are served to couple efficiently a diode laser or a planar waveguide to a cleaved-facet single-mode fiber. With PhC environments, short tapers are achievable and the footprint can be reduced largely in PICs. Here, the taper designs based on Bragg effect and refractive index contrast are studied and simulated by 2D finite-difference-time-domain (FDTD). The transmission efficiency and beam divergence of fabricated PhC tapers are presented.

Chapter 5 intends to simulate the effective transmission/reflection coefficients and the phase change while traversing a PhC constricted waveguide section. In a conventional cleaved-coupled-cavity laser, the wavelength selection can be achieved by adjusting the lengths of gap and the second cavity at given facet reflectivity values. Similarly, this gap section can be imitated in a PhC waveguide by constricting partly the width of linear defect. The coupling constant variations can be extracted from the simulation results, which may assist to conceive PhC constricted waveguide lasers.

Chapter 6 presents the calibrations of selective wet etching for InP PhC suspended membrane waveguide fabrication. The results of optical propagation measurement would also be presented to obtain the propagation losses value.

1.3 Thesis contribution

The main thesis contribution concerns the development of ICP BCl_3/N_2 plasma for InP PhC holes etching. The reactive ion etching for InP-based materials has been known to be strenuous compared to silicon and GaAs. With the BCl_3/N_2 plasma, the etched surfaces are very smooth by introducing N_2 gas while the chemical etching and the feature verticality are sustained by BCl_3. Even though the etch depth is less than 1 μm for 250 nm-diameter holes, it can still be applied for PhC membrane fabrication and lead to lower scattering losses coming from rough surfaces. The etched surfaces are examined as well by transmission electron microscopy equipped with energy dispersive X-ray analysis (TEM-EDX) to clarify the passivation composition.

In literatures, PhC tapers with different geometries expanding the mode size of 1∼2 μm to 8∼10 μm in planar orientation have been calculated numerically. However, an experimental demonstration of PhC tapers coupling to a cleaved-facet single-mode fiber is realized here for the first time (chapter 4). The transmission and far-field patterns are characterized for the fabricated tapers and compared to the simulation results. The coupling efficiency can be enhanced by a factor of 4 once the PhC taper is added and only 20% of modal conversion to higher modes is found after traversing the taper section.

Additionally, the fabrication processes are optimized within this dissertation for InP PhC suspended membrane waveguide with smooth etched surfaces. A quantitative propagation losses value (25 dB/cm) of this device is also given (chapter 6). It may provide a platform for the study of small group velocity and the application of delay lines and non-linear devices [Vecchi2007a, Vecchi2007b].

Chapter 2

Properties of 2D photonic crystals

2.1 The Maxwell's equations and scalability of master equation

In all macroscopic media, including periodic structures like photonic crystals, the light propagation is governed by Maxwell's equations. In cgs units, Maxwell's equations can be expressed as the following:

$$\nabla \cdot \mathbf{B} = 0 \tag{2.1}$$

$$\nabla \times \mathbf{E} + \frac{1}{c}\frac{\partial \mathbf{B}}{\partial t} = 0 \tag{2.2}$$

$$\nabla \cdot \mathbf{D} = 4\pi\rho \tag{2.3}$$

$$\nabla \times \mathbf{H} - \frac{1}{c}\frac{\partial \mathbf{D}}{\partial t} = \frac{4\pi}{c}\mathbf{J} \tag{2.4}$$

where the $\mathbf{H}(\mathbf{r})$ and $\mathbf{E}(\mathbf{r})$ are the magnetic field and the electric field, respectively. $\mathbf{D}$ and $\mathbf{B}$ are the displacement and magnetic induction fields, and ρ and $\mathbf{J}$ are the free charges and current.

The media studied here are restricted to be homogenous dielectric materials with no free charges or currents. In most dielectric materials, the magnetic permeability is close to unity and it thus gives $\mathbf{B} = \mathbf{H}$. Further, it is assumed that the displacement field is related to the electric field in a linear regime and the material is isotropic and lossless, which implies that the dielectric constant is a scalar and real. It then can relate the displacement and electric fields as $\mathbf{D}(\mathbf{r}) = \varepsilon(\mathbf{r})\mathbf{E}(\mathbf{r})$, where ε is the dielectric constant. With all these assumptions, Maxwell's equations are then simplified as:

$$\nabla \cdot \mathbf{H}(\mathbf{r},t) = 0 \tag{2.5}$$
$$\nabla \times \mathbf{E}(\mathbf{r},t) + \frac{1}{c}\frac{\partial \mathbf{H}(\mathbf{r},t)}{\partial t} = \vec{0} \tag{2.6}$$
$$\nabla \cdot \varepsilon(\mathbf{r})\mathbf{E}(\mathbf{r},t) = 0 \tag{2.7}$$
$$\nabla \times \mathbf{H}(\mathbf{r},t) - \frac{\varepsilon(\mathbf{r})}{c}\frac{\partial \mathbf{E}(\mathbf{r},t)}{\partial t} = \vec{0} \tag{2.8}$$

Since Maxwell's equations are linear, the time dependency can be separated out by expanding the fields into a set of harmonic modes: $\mathbf{H}(\mathbf{r},t) = \mathbf{H}(\mathbf{r})e^{i\omega t}$ and $\mathbf{E}(\mathbf{r},t) = \mathbf{E}(\mathbf{r})e^{i\omega t}$. Therefore, we only need to tackle the following equations:

$$\nabla \cdot \mathbf{H}(\mathbf{r}) = 0 \tag{2.9}$$
$$\nabla \cdot \mathbf{D}(\mathbf{r}) = 0 \tag{2.10}$$
$$\nabla \times \mathbf{E}(\mathbf{r}) + \frac{i\omega}{c}\mathbf{H}(\mathbf{r}) = \vec{0} \tag{2.11}$$
$$\nabla \times \mathbf{H}(\mathbf{r}) - \frac{i\omega}{c}\varepsilon(\mathbf{r})\mathbf{E}(\mathbf{r}) = \vec{0} \tag{2.12}$$

By eliminating $\mathbf{E}(\mathbf{r})$ in equation (2.9) and (2.10), the *master equation* can be expressed as:

$$\nabla \times \left[\frac{1}{\varepsilon(\mathbf{r})}\nabla \times \mathbf{H}(\mathbf{r})\right] = \left[\frac{\omega}{c}\right]^2 \mathbf{H}(\mathbf{r}) \tag{2.13}$$

For a given $\varepsilon(\mathbf{r})$, $\mathbf{H}(\mathbf{r})$ can then be determined through equation (2.9) and (2.13). The electric field can be found using:

$$\mathbf{E}(\mathbf{r}) = \left[\frac{-ic}{\omega\varepsilon(\mathbf{r})}\right] \nabla \times \mathbf{H}(\mathbf{r}) \tag{2.14}$$

An important property of electromagnetism is that there is no fundamental length scale in a macroscopic dielectric medium system; therefore the master equation is independent of length scale. For two photonic crystals with the physical dimensions differed only by a factor, the optical modes in one photonic crystal can be deduced from another one by simply rescaling the wavelength and frequency. For example, consider a scale parameter s which compresses or expands the dielectric constant $\varepsilon(\mathbf{r}) : \varepsilon'(\mathbf{r}) = \varepsilon(\mathbf{r}/s)$. We perform the change of variables in the master equation using $\mathbf{r}' = s\mathbf{r}$ and $\nabla' = \nabla/s$.

$$s\nabla' \times \left[\frac{1}{\varepsilon(\mathbf{r}'/s)}s\nabla' \times \mathbf{H}(\mathbf{r}'/s)\right] = \left[\frac{\omega}{c}\right]^2 \mathbf{H}(\mathbf{r}'/s) \tag{2.15}$$

Replace $\varepsilon(\mathbf{r}'/s)$ by $\varepsilon'(\mathbf{r}')$ and divide s on the two sides. It gives:

$$\nabla' \times \left[\frac{1}{\varepsilon'(\mathbf{r}')}\nabla' \times \mathbf{H}(\mathbf{r}'/s)\right] = \left[\frac{\omega}{cs}\right]^2 \mathbf{H}(\mathbf{r}'/s) \tag{2.16}$$

Equation (2.16) is still a master equation with a solution: $\mathbf{H}'(\mathbf{r}') = \mathbf{H}(\mathbf{r}'/s)$, for a frequency of $\omega' = \omega/s$.

2.2 Computation methods

Several approaches have been proposed to calculate numerically the propagation of electromagnetic waves in photonic crystals. The Plane wave expansion [Ho1990, Plihal1991] and the finite-difference-time-domain [Taflove1995] are the two methods used more frequently and are described briefly as following.

2.2.1 Plane wave expansion method

The plane wave expansion (PWE) method can be used to calculate the dispersion relation and the field distribution in the case of infinite 2D or 3D photonic crystals structures. Its principle is to solve Maxwell's equations in the reciprocal space and in the frequency domain. Since the dielectric constant ε is a periodic function of space in PhC structures, the Bloch theorem can be applied and the field vector $\mathbf{H}$ can then be expressed as a plane wave modulated by a periodic function:

$$\mathbf{H}_{\mathbf{k}} = e^{i\mathbf{k}\cdot\mathbf{r}}\mathbf{u}_{\mathbf{k}}(\mathbf{r})$$

where the $\mathbf{u}_{\mathbf{k}}$ is a periodic function on the lattice, $\mathbf{u}_{\mathbf{k}}(\mathbf{r}) = \mathbf{u}_{\mathbf{k}}(\mathbf{r}+\mathbf{R})$ for all lattice vectors $\mathbf{R}$, and $\mathbf{k}$ is a wave vector within the first Brillouin zone of the reciprocal lattice. By choosing a finite number of plane waves, eigenvalues can be calculated for each wavevector within the first Brillouin zone.

The PWE method is only used for infinitely periodic structures and not for the cases when the Bloch theorem is not applicable, ex: non-periodic structures, dominant finite size, and boundary conditions. Nevertheless, cavities or straight waveguides can be simulated by the implementation of supercell method [Meade1991].

In this thesis work, the dispersion diagrams of 2D PhC channel waveguides, 2D PhC constricted waveguides, and 3D PhC suspended membrane waveguides are all calculated using the PWE method. Considering the convenience and the limitation, the 2D and 3D PWE calculations are realized by the helps of CrystalWave [PhotonDesign] and MIT photonic-bands [Johnson2001] programs, respectively.

2.2.2 Finite difference time domain method

The finite-difference-time-domain (FDTD) method is extensively used in the electromagnetism calculation since it can be applied to deal with almost all kinds of geometries. In the FDTD method, the space and the time are divided into a mesh of nodes, or known as the finite-element calculation. The Maxwell's equations are re-formulated by those finite difference equations that relate the fields at each grid point to the ones at neighboring points. They are then solved under the constraints of boundary conditions, and the time evolutions of electromagnetic fields are updated and stored at each grid point. By the Fourier transformation, the spectral behavior can be deduced from the time evolutions.

The calculation time required for FDTD method is proportional to the number of the discretisation points in the computational domain. When the grid points are dense enough, the solutions of Maxwell's equations are more exact. Moreover, we can introduce the absorbing boundary conditions, such as the perfectly matched layers (PML) [Berenger1994] during the calculations. The absorption rates in PML increase gradually towards the edges in order to eliminate the back reflections at the boundaries.

The light confinement in vertical direction in a 2D planar PhC device is generally provided by the refractive index contrast in the heterostructure. A 3D simulation is very time- and memory-consuming; therefore, a 2D approximation with the concept of the effective index is developed and the results in a good agreement with the 3D simulation have been reported [Qiu2002].

Within this dissertation, the propagation simulations on PhC laser and PhC taper waveguide structures are calculated by 2D FDTD method with the effective index approximation.

2.3 Band structures and band map

The PhC structures considered within this thesis are composed of triangular lattices of air columns in the semiconductor materials. Figure 2.1 illustrates the schematic top view of a 2D PhC triangular lattice of air columns and its corresponding Brillouin zone in the reciprocal space. A PhC structure can be characterized by the lattice constant (a) and the filling factor (f). The filling factor represents the ratio of the air volume to the total volume of PhC. For a triangular lattice of air columns with a hole diameter (d), the filling factor is expressed as: $f = \pi d^2/2\sqrt{3}a^2$

In figure 2.2, the band structure of a PhC triangular lattice of air columns in a material with $n_{eff} = 3.25$, $a = 400$ nm, and $f = 35\%$ (hole diameter $d = 250$ nm) calculated by PWE method is presented at the edge of irreducible Brillouin zone ($\Gamma MK\Gamma$) for the transverse electric (TE) and transverse magnetic (TM) polarizations. The TE and TM polarizations are defined as the magnetic and the electric fields being in parallel with the air columns, respectively. A photonic band

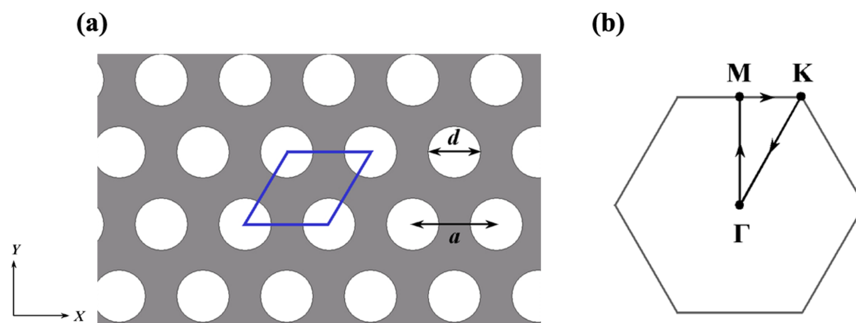

Figure 2.1: Schematic of (a) a 2D triangular lattice of air columns (a: lattice constant, d: hole diameter) and (b) its corresponding first Brillouin zone. The blue tetragon refers to the supercell used for the 2D PWE calculation.

gap (PBG) for the TE polarization is obtained at normalized frequency ($u = a/\lambda$) ranging 0.223∼0.297 (figure 2.2(a)), corresponding to the wavelength interval at 1346∼1793 nm for a = 400 nm. More precisely, the electromagnetic modes with the frequencies locating within the PBG are not allowed to propagate in the photonic crystal. It should be noted that the PBG is applied only to the in-plane (x-y plane) light propagation in a 2D PhC system and there are no band gaps for out-of-plane propagation (z-direction). Customarily, the band *below* and *above* the band gap are named as *dielectric band* and *air band*, respectively. In a dielectric band (lower band), the electromagnetic fields are localized mostly in the dielectric materials. On the contrary, in an air band (upper band), electromagnetic fields are localized more in the air regions. In general, the span of PBG increases

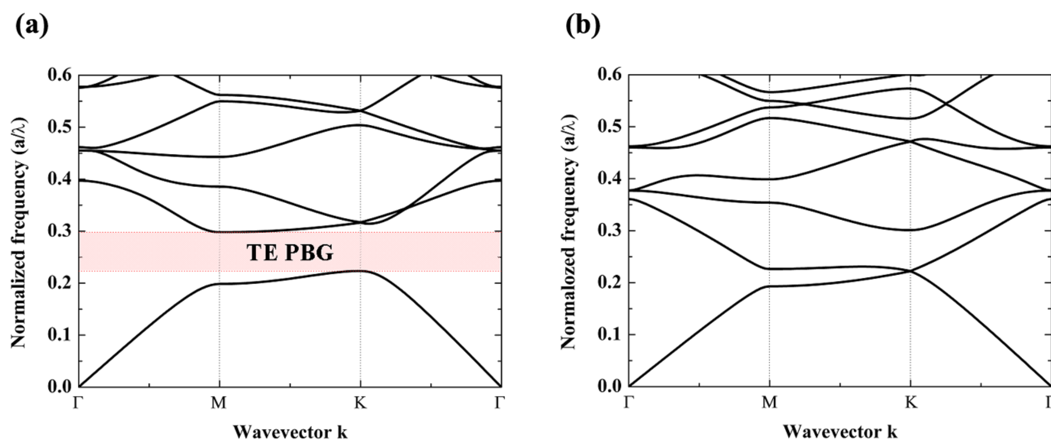

Figure 2.2: The band structures for a 2D PhC triangular lattice of air columns (a = 400 nm, f = 35%, n_{eff} = 3.25, n_{air} = 1) calculated by the 2D PWE method for (a) the TE and (b) the TM polarizations.

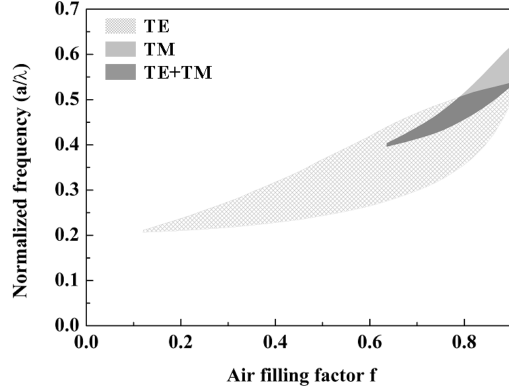

Figure 2.3: The band map with variations of filling factors in the TE and TM polarizations for a 2D PhC triangular lattice of air columns ($a = 400$ nm, $n_{eff} = 3.25$, $n_{air} = 1$).

monotonically as the refractive index contrast increases for a PhC.

However, for the TM polarization (figure 2.2(b)), only a narrow stop band in the ΓM wavevector direction is presented. A photonic band gap in the TM polarization does not exit in the case of $f = 35\%$ when $n_{eff}/n_{air} = 3.25/1$.

The relation of the lowest band gap with variations of the filling factor is demonstrated in figure 2.3. The band gap in the TE polarization appears once the filling factor is superior to 12%. It is visible that, with increasing the filling factor, the mid-gap normalized frequency and the band gap width tends to increase as well till $f \sim 70\%$. Further, the band gap in both TE and TM polarizations is not obtained until the filling factor is more than 64%. Nevertheless, a high filling factor is not favored from the view point of fabrication since large air holes are difficult to be realized in a dense periodicity. For optical applications at 1.55 μm, our interest is therefore restricted in the TE polarization with a moderate filling factor within the range of 30∼45%. Hence, the 2D PhC triangular lattice with parameters ($a = 400$ nm, $d = 250$ nm) are treated as an essential composition block for the PhC devices studied in this dissertation.

The light propagation discussed above is in the plane of periodicity ($\mathbf{k}_z = 0$). As mentioned in chapter 1, we investigate 2D PhC structures with vertical confinement through refractive index contrast in a InP-based heterostructure or in a InP suspended membrane. Figure 2.4 presents the dispersion diagram along ΓK direction in TE polarization calculated based on the same PhC parameters as in figure 2.2. The light lines for air cladding and for InP substrate are also indicated. The mode is leaky to the air while it lies above the air light line. Between the air light line and substrate line, modes are radiated only into the substrate. For a 2D PhC structure etched into InP-based heterostructure, the leaky modes coupled to substrate are inevitable since the PBG ranges always above the substrate line.

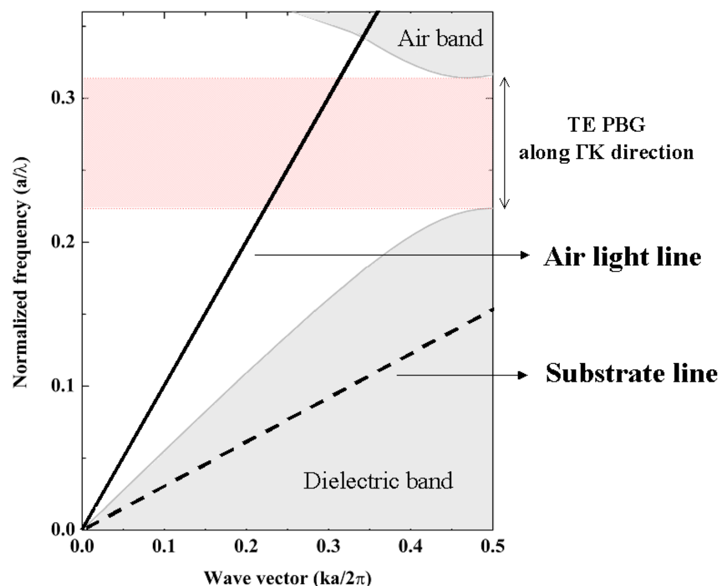

Figure 2.4: The dispersion diagram along ΓK direction in TE polarization for a 2D PhC triangular lattice of air columns ($a = 400$ nm, $f = 35\%$, $n_{eff} = 3.25$, $n_{air} = 1$); in which, the air light line (solid line) and the InP substrate line (dashed line) are indicated.

2.4 Structure designs

In section 2.3, the conception of photonic band gap in a 2D PhC plain structure is presented. This unique behavior may differ once the defect is included into the PhC plain structures. The term of defect is employed for the distinction purpose and it signifies that the translation symmetry is broken. Defects in a PhC structure can be classified as the *point* defect, the *linear* defect, and the *planar* defect. For instance, in a 2D matrix of air columns, the point defect refers to the removal/addition of air columns or the increase/diminish of air column diameters. As for linear defect, it involves the removal of air column rows. The planar defect is formed by modifying the thickness of one layer in a multilayer film system. Within the PBG, it is possible that certain modes can be sustained due to the presence of defects in the PhC structures. This phenomenon allows one to trap, localize or guide the light.

In the following, the dispersion curves ($\omega - \mathbf{k}_x$ relations) of the channel waveguide, the constricted waveguide, and the suspended membrane waveguide based on PhC structures with defects are presented with the help of plane wave expansion calculation method.

2.4.1 PhC channel defect waveguide on substrate

The PhC channel defect waveguides are obtained by introducing the line defects, in which one or several rows of air columns are removed away from a plain PhC matrix. For convenient purpose, terminological term, *Wn*, is used to indicate the removal of n rows of air columns. The direction of line defect can be along either the ΓK or the ΓM wave vector direction.

Modes are orthogonal in the dispersion diagrams of PhC channel defect waveguides. The dispersion curve of one mode can intersect with other modes through the types of crossing and anti-crossing. Theoretically, in a crossing point, the mode coupling does not occur and the profile of individual mode is then not affected. On the contrary, the mode coupling takes place around the anti-crossing point and results in a narrow mini-gap in the guided transmission spectrum. This phenomenon is named as the mini-stop band (MSB) and has been confirmed experimentally [Olivier2002, Olivier2003b].

In figure 2.5(b), the dispersion diagram of a $W3$ PhC channel defect waveguide ($a = 400$ nm, $d = 250$ nm, $n_{eff}/n_{air} = 3.25/1$) along the ΓK direction ($W3^{[\Gamma K]}$) is simulated in the TE polarization by the PWE method in a designated supercell (figure 2.5(a)). Within the band gap ($u = 0.223 \sim 0.314$ at ΓK direction), several guided modes are observed; thus it is concluded that $W3^{[\Gamma K]}$ is a multimode waveguide. The fundamental even mode sustained by the $W3^{[\Gamma K]}$ waveguide within the band gap is marked as the red line and it operates mainly above the air light line.

In a PhC waveguide with the symmetric boundary, e.g. $W1$ and $W3$, the mode coupling occurs only between modes with the identical parity. Mode parity is defined according to the field profile with respect to the central axis of the waveguide. For even modes, the field profiles are symmetric and the mode orders are odd numbers. On the contrary, field profiles are asymmetric and the mode orders are even numbers for odd modes. Hence, the MSB can occur at the edge of the Brillouin zone between modes of the same order and as well as within the Brillouin zone between different mode orders with the identical parity. Considering the fundamental even mode of the $W3^{[\Gamma K]}$, shown in figure 2.5(b), the MSB and crossing are pointed out at the interactions of dispersion curves of the 1st and the 5th mode order and the 1st and the 4th mode order, respectively. For the anti-symmetric boundary (e.g. $W2$ and $W4$), yet the mode coupling happens when the modes are with opposite parities.

While the light with the frequency and the propagation constant corresponding to the MSB of one PhC defect waveguide, the light intensity decreases along the propagation direction due to the mode coupling. In figure 2.5(c), the transmission spectrum of the $W3^{[\Gamma K]}$ is calculated by the 2D FDTD method in the TE polarization. The fundamental even mode excited on a ridge waveguide is injected into one side of the $W3^{[\Gamma K]}$ and the transmitted power is collected on another ridge waveguide at the exit side. Within the band gap range, one dip in the transmission spectrum is found at $u = 0.263$, which corresponds to the MSB position in the

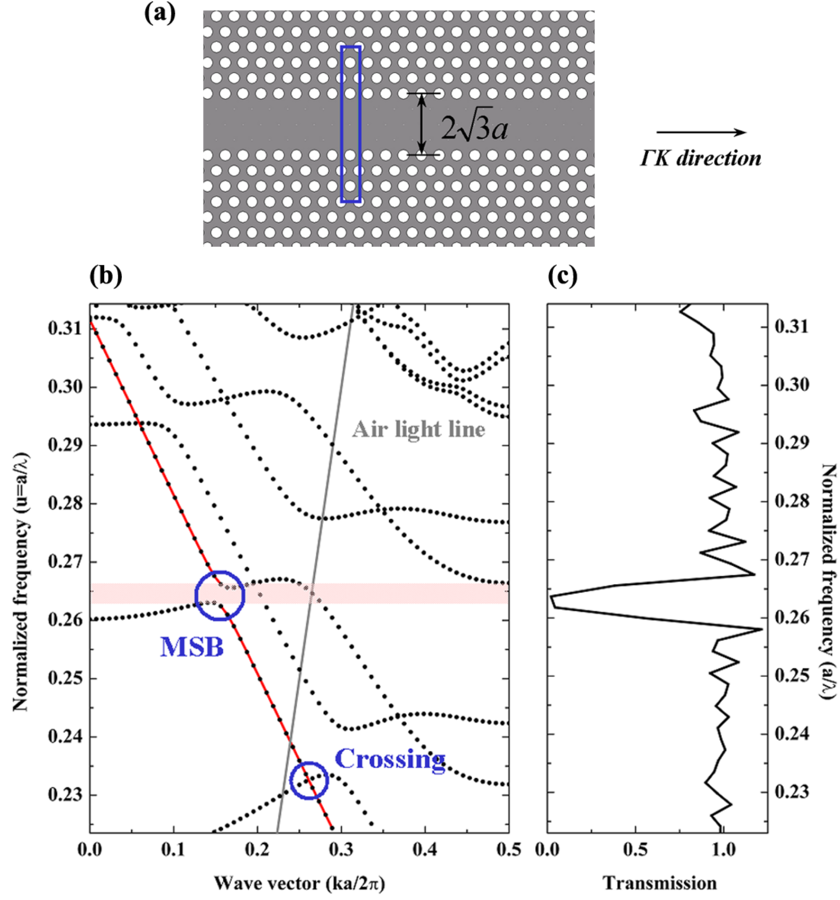

Figure 2.5: (a) The schematic of $W3$ waveguide along the ΓK direction ($W3^{[\Gamma K]}$). The blue rectangular refers to the supercell used for 2D PWE calculation. (b) The dispersion diagram for $W3^{[\Gamma K]}$ (a = 400 nm, d = 250 nm, n_{eff} = 3.25, n_{air} = 1) in the TE polarization within band gap ($u = 0.223 \sim 0.314$ along the ΓK direction). Locations of MSB (with 5th order mode) and crossing point of fundamental even mode in a $W3^{[\Gamma K]}$ are pointed out. The air light line is marked as gray. (c) The transmission spectrum of $W3^{[\Gamma K]}$ simulated by 2D FDTD method.

dispersion curve (figure 2.5(b)) and is the coupling between the fundamental even mode and the 5th order mode.

For comparison, the dispersion diagram for the $W3$ channel defect waveguide along the ΓM direction $W3^{[\Gamma M]}$ illustrated in figure 2.6(a) is calculated and presented in figure 2.6(b). Within the band gap ($u = 0.198 \sim 0.297$ at ΓM direction), the phenomena of MSB is observed as well and its occupation is considerable. It has been reported that, since the amplitude of corrugation is larger, the spanning range of MSB is more extensive for the ΓM type channel defect waveguide on sub-

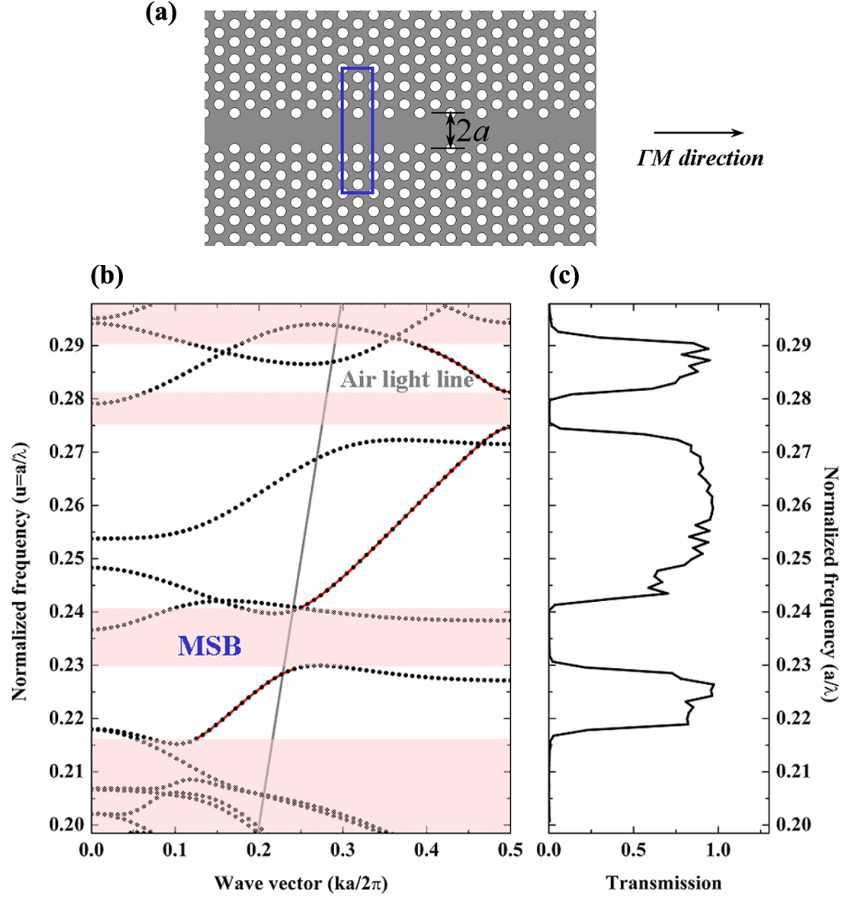

Figure 2.6: (a) The schematic of $W3$ waveguide along the ΓM direction ($W3^{[\Gamma M]}$). The blue rectangular refers to the supercell used for 2D PWE calculation. (b) The dispersion diagram for $W3^{[\Gamma M]}$ (a = 400 nm, d = 250 nm, n_{eff} = 3.25, n_{air} = 1) in the TE polarization within band gap ($u = 0.198 \sim 0.297$ along the ΓM direction). The intervals of MSB (pink regions) for a fundamental even mode propagation and the air light line (gray) are pointed out. (c) The transmission spectrum of $W3^{[\Gamma M]}$ simulated by 2D FDTD method.

strates than for the ΓK type [Olivier2002]. Once the fundamental even mode is injected into a $W3^{[\Gamma M]}$, the coupling to higher modes is more frequent in ΓM type and it results in a higher in-plane propagation loss compared to the $W3^{[\Gamma K]}$. As shown in figure 2.6(c), the average transmission ratio for the $W3^{[\Gamma M]}$ within the band gap range is much smaller than the $W3^{[\Gamma K]}$. Hence, the choice of the ΓK or ΓM direction solely depends on what kinds of optical functionalities that the designs intend to present. Within this dissertation, the line defect is mainly chosen along the ΓK direction in order to minimize the influences of MSB.

In a narrower PhC channel defect waveguide such as $W1$, it exhibits a simpler propagation regime involving only one even mode and one odd mode. Compared to $W3$, the fundamental even mode is less confined within the $W1$ and it leads to a higher propagation loss both in the in-plane and the out-of plane directions. Considering the potential applications in photonic integrated circuits, the wide PhC waveguides (ex: $W3$ and $W5$) are still attractive even with the multimode propagation regimes and the appearance of MSB.

2.4.2 PhC coupled cavity waveguide

Beside the channel defect waveguide based on PhC structures, another design, the coupled-resonator optical waveguide (CROW), proposed by A. Yariv [Yariv1999] has become attractive for more complex optical functions. CROW is a periodic array of resonators in which the light propagates due to the weak coupling between the nearest resonators. A key property of CROW is that the light can propagate at a significantly reduced group velocity. Therefore, people attempt to introduce the CROW design into PhC laser structures [Happ2003] since a lower group velocity results in a longer photon lifetime and it leads to an enhanced lasing gain for a specific wavelength.

The 2D PhC constricted waveguide, one example of the coupled cavity waveguides (CCW) has been reported by de Rossi [deRossi2005] and is presented here. The structure is a $W5$-based waveguide along the ΓK direction with constrictions to $W1$, as illustrated in figure 2.7(a). The interval distance between two constrictions is $3 \times a$ (a is the periodic constant of the PhC structure) and the supercell used for 2D PWE calculation is indicated by the blue rectangular. In the design of Happ, the cavities are well closed and separated by the PhC structures; but the one of de Rossi is not. The coupling is in a stronger regime for the designs of de Rossi since a $W1$-like waveguide transverses the whole CCW section and connects all the cavity-like units. The dispersion diagram of the constricted waveguide simulated by 2D PWE with the supercell method is presented in figure 2.7(b). We consider only the dispersion curve of the fundamental even mode (red line) in the TE polarization within the band gap. It is observed that the light propagation is strictly forbidden at certain frequency ranges, which are referred as the mini-gaps and have been verified experimentally [Bayindir2000, Olivier2001]. At the band edges, ex: point A and B, the slopes of dispersion curve are flatter; in which, the group velocity is reduced and is suitable for the laser operation. In an InP/InGaAsP multiple quantum-wells (MQW) structure with lasing emission around 1.55 μm, the corresponding lattice constants can be 350 nm and 412 nm while operating at point A and B, respectively. The mode profiles at point A and B are shown in figure 2.7(c) where the fundamental even mode is sustained along the ΓK direction.

The study devoted to the constriction reflectivity will be presented in chapter 5. It is expected that, by knowing the reflectivity and the phase change at each

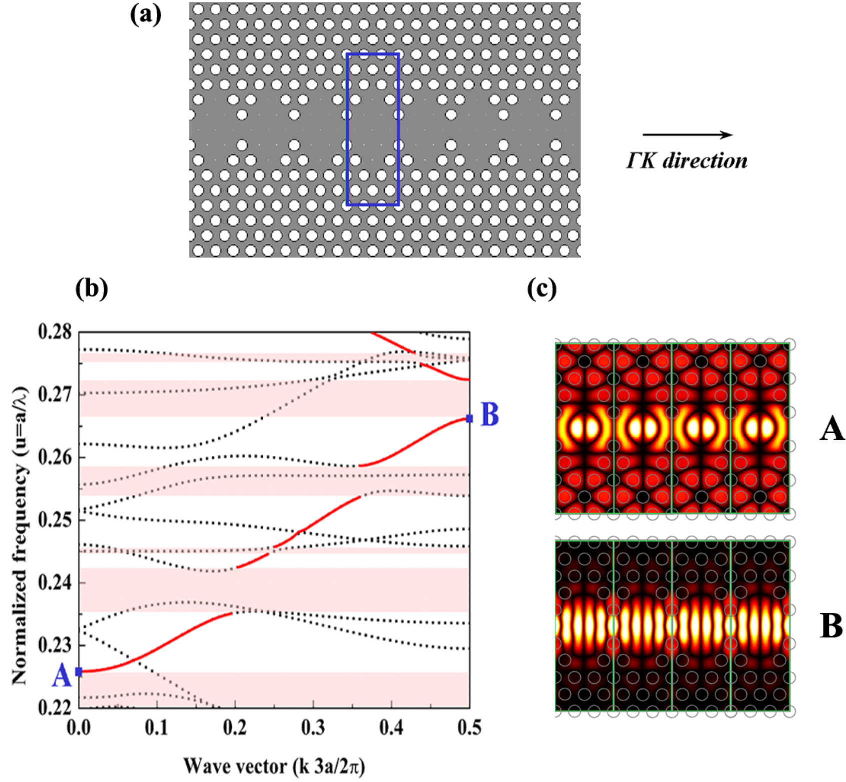

Figure 2.7: (a) The schematic of a PhC constricted waveguide along the ΓK direction from $W5$ constricted to $W1$ with a period of $3 \times a$. (b) The dispersion diagram of the constricted waveguide shown in (a) (a = 400 nm, d = 250 nm, n_{eff} = 3.25, n_{air} = 1) in the TE polarization within the PBG. The mini-gaps (pink regions) for the fundamental even mode (red line) propagation is concerned. (c) The fundamental even mode profiles within four repeated supercells when $u = 0.2259$ (point A) and $u = 0.2662$ (point B).

internal constriction, we are able to conceive the optimized PhC CCW layout to enhance the intensity of the resonance frequency.

2.4.3 PhC suspended membrane waveguide

For a PhC membrane device without the continuous translation symmetry in the third direction, the 2D calculation is still preferred since much less time-consuming is required compared to the 3D calculation. As a result, the term of effective index corresponding to the specific environment of guiding membrane and cladding should be introduced into the 2D calculation. However, in such a high-index-contrast structure, ex: air/InP/air suspended membrane, the approximation of effective index along the vertical direction can only be valid within a narrow fre-

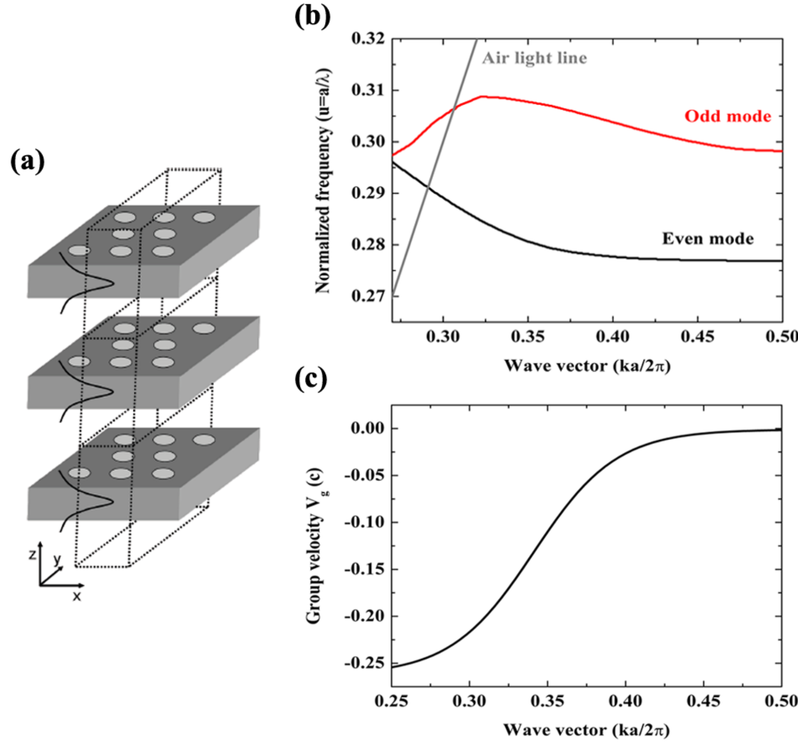

Figure 2.8: (a) The schematic of the supercell in the vertical direction for the suspended membrane calculation by the 3D PWE method. (b) The simulation of dispersion diagram for a $W1$ PhC suspended membrane waveguide (280 nm-thick membrane, $n = 3.17$, $a = 400$ nm, and $d = 250$ nm). (c) The group velocities versus the wave vectors for the fundamental even mode guiding in the $W1$ PhC suspended membrane waveguide. The group velocity is derivated approximately from the $\omega - \mathbf{k}_x$ relation.

quency range and cannot present the general property of the suspended membrane structure. In this case, the 3D calculation is a more suitable choice while tackling the high-index-contrast membrane structure even with disadvantages of long calculation time and enormous computing memory. For a 3D PWE calculation, the choice of supercell should include as well the third dimension in the vertical direction. As shown in figure 2.8(a), the interval of two adjacent supercells in the vertical direction should be large enough to avoid the modes coupling.

In figure 2.8(b), the dispersion diagram of a $W1$ PhC symmetric suspended membrane waveguide along the ΓK direction is calculated by the 3D PWE method. The thickness of guiding layer is 280 nm with the refractive index of 3.17 (InP material) and the PhC triangular matrix has a periodicity of 400 nm with a 250 nm hole diameter. Within the band gap, one even and one odd modes are sustained by $W1$. The propagation is theoretically lossless in the out-of-plane direction for guiding through the fundamental even mode operating below the air light line. It is

observed that, for the fundamental even mode, there are two propagation regimes of the rapid and the slow group velocities. The rapid regime situates just below the air light line with a group velocity ($\mathbf{V}_g^{[\Gamma K]} \equiv \partial\omega/\partial\mathbf{k}_x$) along ΓK direction in the order of $c/4.5$ (c is light velocity in vacuum). When $\mathbf{k}_x$ ranges at $0.4 \sim 0.5[\times 2\pi/a]$, the dispersion curve is flatter. $\mathbf{V}_g^{[\Gamma K]}$ is less than $c/40$ at $\mathbf{k}_x = 0.4[\times 2\pi/a]$ and can even be as slow as $c/400$ at $\mathbf{k}_x = 0.48[\times 2\pi/a]$. Ideally, the group velocity may reduce to 0 at $\mathbf{k}_x = 0.5[\times 2\pi/a]$ when $u = 0.276$. Figure 2.8(c) presents the approximated group velocities versus the wave vectors for the fundamental even mode guiding in a 280 nm-think InP PhC suspended membrane waveguide. It should be noted that the group velocity is a vector term; therefore the reduction in group velocity presented here only concerns the ΓK direction. The more detailed introduction concerning the PhC suspended membranes will be presented in chapter 6.

Chapter 3

Photonic crystals fabrication

3.1 Introduction

The realizations of photonic crystals operating at the telecommunication wavelengths in semiconductor materials are challengeable since all the dimensions, like the hole diameters and the intervals of holes, are in order of sub-micrometer. Relying on a versatile assistance of electron beam lithography, yet it is possible to manufacture such small dimension features with a high resolution and an accurate overlap.

The fabrication of InP/InGaAsP photonic crystal devices presented in this dissertation is realized initially by the epitaxy of InP and InGaAsP materials on InP substrates via metal-organic vapor phase epitaxy (MOVPE). The double-mask process is adopted here for the PhC patterns transfer. The bottom mask is often the dielectric material and is deposited on the semiconductor samples by plasma enhanced chemical vapor deposition (PECVD). The top mask is an electron sensitive resist, in which the PhC patterns are defined through electron beam lithography (EBL). The defined patterns are transferred into the dielectric mask by capactively coupled plasma reactive ion etching (CCP-RIE) with a CHF_3-based plasma and then into the InP-based materials by inductively coupled plasma reactive ion etching (ICP-RIE) using a chlorine-containing plasma. In the following sections, the fabrication conditions and parameters would be presented (section 3.2~3.4). In particular, the PhC holes etching using ICP chlorine-containing plasma would be discussed. The studies are dedicated to the process optimization in LPN for InP PhC holes etching using an ICP Cl_2/Ar plasma (section 3.5) and the surface roughness suppression using the $Cl_2/BCl_3/N_2$ and BCl_3/N_2 plasmas (section 3.6).

The fabrication of photonic devices requires an etching method which allows one to transfer desired patterns with a high reliability. Especially, with the reduction of feature dimensions, the anisotropy is no doubt the key point for the high aspect ratio etching. *Aspect ratio* is defined as the etch depth with respect

to the feature width; and for 2D PhC, an aspect ratio higher than 10:1 is favored for applications. To meet this criterion, the plasma assisted dry etching equipped with the anisotropic property is a better candidate than the wet etching.

The evolution of plasma etching originates from the ion beam etching (IBE) with inert (ex: Ar) plasmas. However, the etching of InP-based materials by this approach of ion sputtering always leads to rough surfaces. It has been proposed that, due to the preferential sputtering of phosphor (P) [Pearton1990], the surface is enriched with indium (In) [MacLaren1992]. As a result, the indium islands are formed and act as the seeding points for cone, which are interpreted as the surface roughness.

To balance the sputtering rate difference between indium and phosphor, the gas chemistries which are reactive with InP materials to form volatile etch products should be introduced during the plasma etching. The hydrocarbon chemistries (ex: CH_4, C_2H_6) can be used for InP-based materials etching. The mechanism of hydrocarbon chemistries is to provide the CH_3 radicals which can react with indium to form the volatile $In(CH_3)_x$ etch products. The CH_4/H_2 plasma has been proposed for InP large-area etching in capacitively coupled plasma reactive ion etching (CCP-RIE) and in electron cyclotron resonance (ECR) ion source [Pearton1994]. However, it is with the drawbacks of low etch rate and polymer formation. The hydrocarbon chemistries tend to form the polymers along the surface sidewalls, which may enhance the anisotropy; but, those excessive polymers are deposited as well on reactor walls and cause the contamination citePearton1996.

Another option, the chlorine-containing plasmas are therefore employed to enhance the etching and eliminate the issue of polymer formation. The concept of chlorine-containing chemistries is that the generated Cl radicals react with InP to form $InCl_x$ and PCl_x products. However, the $InCl_x$ products at room temperature are low-volatile compared to the PCl_x. In table 3.1, the enthalpies of vaporization (Δ_{vap}H) for the indium chloride (InCl, $InCl_2$, $InCl_3$) and the phosphorus chloride (PCl_3) are listed. The values of Δ_{vap}H for $InCl_x$ products are three to five times larger than the one of PCl_3. Those $InCl_x$ products not only slow down the etch rate, but also nucleate to form the $InCl_x$ islands which lead to the surface roughness [Vernon1992]. To settle this drawback, the substrate heating ($> 150^0C$) [McNevin1986] and/or the ion bombardment are required to promote the desorption of $InCl_x$ products.

For comparison, the enthalpies of vaporization for the gallium chloride and the arsenic chloride are listed as well in table 3.1. Unlike the thermodynamical property difference between $InCl_3$ and PCl_3, the Δ_{vap}H values of $GaCl_3$ and $AsCl_3$ products are quite similar. Further, the atomic masses of Ga and As are close to each other and it then does not show the preferential etching under the ion sputtering. Hence, compared wit the InP material, the etching rates for Ga and As are more assembling under the reactive ion etching with chlorine-containing plasma and the surfaces are expected to less rough.

Etch product	Δ_{vap}H (KJ/mol)
InCl	117.6 $^{a)}$
$InCl_2$	97.7 or 176.2 $^{a)\dagger}$
$InCl_3$	158 $^{a)}$
PCl_3	30.5 $^{b)}$
$GaCl_3$	23.9 $^{b)}$
$AsCl_3$	35.01 $^{b)}$
InI	90.8 $^{b)}$
PI_3	43.9 $^{b)}$

$^{a)}$ Ref. McNevin1986; $^{b)}$ Ref. Handbook of chemistry and physics;
† Depending on the experimental condition divergences

Table 3.1: The enthalpies of vaporization (Δ_{vap}H) for indium chloride, phosphorus chloride, gallium chloride, arsenic chloride, indium iodide, and phosphorus iodide.

Within the reported chlorine-containing plasmas in ECR systems for InP-based materials large-area etching, the Cl_2/N_2 plasma has presented the smooth etched surfaces with an etch rate more than 100 nm/min at a substrate temperature of 200^0C [Miyakuni1995]. The etching could be realized at a temperature less than 100^0C using a Cl_2/Ar plasma [Thomas1995, Lee1996a, Lee1996b]. In this context, the sputtering by Ar^+ ions promotes the desorption of $InCl_x$ etch products and thus an etch rate higher than 1 μm/min was obtained even at a lower temperature. In addition, the BCl_3/Ar and the BCl_3/N_2 plasmas were also studied and presented comparable results [Ren1995, Ren1996a].

Except the ECR sources, inductively coupled plasma (ICP) sources are developed and applied more widely to etch the III-V materials. The ICP sources can be scaled up easier than the ECR sources and a wide range of gas pressure operation is possible. The ICP chlorine-containing plasmas including the $SiCl_4$, Cl_2/Ar, Cl_2/N_2, and BCl_3/N_2 gas mixtures, have been proposed to etch InP-based materials [Shul1997, Etrillard1997]. An etch rate higher than 2 μm/min was obtained using an ICP $SiCl_4$ plasma with a substrate temperature of 80^0C. An ICP $Cl_2/Ar/H_2$ ICP plasma presented a highly anisotropic ridge profile due to the addition of H_2 [Rommel2002].

The above statements are for the large-area etching. It should be noted that in the closed, dense, and small features, such as a trench array (1-D PhC) or a hole matrix (2-D PhC), the etching mechanisms may differ from the ones in large-areas. In another word, an optimized plasma etching process for ridge features may not be applicable for PhC hole features with success. The plasma etching

Etching	Plasma	Results	Reference
CAIBE	Ar plasma $+Cl_2$ gas	• 5μm etch depth for d=250nm	Kotlyar2004a Mulot2004a
ECR-RIE	Cl_2/Ar	• 3.1μm etch depth for d=250nm	Happ2001a
ICP-RIE	$Cl_2/CH_4/H_2$	• Low aspect ratio (3:1)	Heijden2003 Strasser2004
	$SiCl_4$	• 4.5μm etch depth for d=270nm	Pommereau2004
	Cl_2	• 2.3μm etch depth for d=200nm • Undercut	Carlstrom2005
	Cl_2/O_2	• 1.9μm etch depth for d=240nm • Undercut reduction	Heijden2005 Carlstrom2006
	$Cl_2/Ar/N_2$	• 3.5μm etch depth for d=250nm	Strasser2005 Strasser2007
	HI/Xe	• 2.3μm etch depth for d=180nm • Lower etching temperature (70^0C)	Ide2006

Table 3.2: The summary of developed etching methods and plasmas for PhC holes structure etching in InP materials.

for InP PhC holes was first developed in the ECR sources using a Cl_2/Ar plasma [Happ2001a] and an etch depth of 3.1 μm for 250 nm-diameter holes was obtained. The etching realized using the $SiCl_4$ plasma in an ICP-RIE presented successfully an etch depth of 4.5 μm for 270 nm-diameter holes [Pommereau2004]. Apart from the ICP-RIE system, the deep etched holes could be realized alternatively in chemically assisted ion beam etching (CAIBE) systems with chlorine as the reactive gas [Mulot2004a, Kotlyar2004a]. An etch depth more than 5 μm was obtained for 250 nm-diameter holes [Kotlyar2004a] by this method.

Even though it demonstrates a very good result for the InP PhC holes deep etching by CAIBE, it seems that the surface homogeneity is not secured completely. On the contrary, in an ICP-RIE system, the etching is generally less dependent of locations in the chuck and it is thus more suitable for the fabrication of photonic integrated devices. An ICP $Cl_2/CH_4/H_2$ plasma was first proposed to etch the InP PhC holes [Heijden2003, Strasser2004], but it presented an aspect ratio not more than 3:1. A pure Cl_2 plasma was later reported and an etch depth of 2.3 μm was obtained for 200 nm-diameter holes [Carlstrom2005]. Nevertheless, it suffered from the isotropic etching; therefore the undercut was found and the hole profiles were not quite vertical. People attempted hereafter to add other gases (ex: Ar, H_2, N_2, O_2) into the Cl_2 plasma to diminish the lateral etching through the

formation of sidewall passivation or the supply of ion sputtering. A Cl_2/O_2 plasma has been demonstrated to reduce the undercut through the sidewall passivation [Heijden2005, Carlstrom2006]. Apart from it, the $Cl_2/Ar/N_2$ plasma has also been investigated and an etched depth of 3.5 μm was obtained for 250 nm-diameter holes with a nearly vertical profile [Strasser2005, Strasser2007].

A main disadvantage encountered while etching the InP-based materials using chlorine-containing plasma is that an elevated substrate temperature is often necessary to enhance the desorption of $InCl_x$ etch products. The HI gas was then introduced to etch the InP-based materials at a lower temperature [Matsutani2003, Loncar2004, Fujita2004], since the InI_x etch products have a lower enthalpy of vaporization than $InCl_x$, as listed in table 3.1. A HI/Xe plasma has been demonstrated at a substrate temperature of 70^0C and an etch depth of 2.3 μm for 180 nm-diameter holes was obtained [Ide2006]. In this gas mixture, the e-beam resist could still be served as the etching mask, which simplified the fabrication processes. The etching results for PhC holes structure are summarized in table 3.2.

3.2 Vertical stacking

A critical step of photonic device fabrication is the preparation of epitaxial layers. It is often carried out by the metalorganic vapor-phase epitaxy (MOVPE) growth technique. MOVPE is widely used in the industries for the fabrication of commercial optoelectronic devices due to the relative rapid growth rate and the high wafer throughput. Compared to molecular beam epitaxy (MBE), MOVPE has the advantage of somewhat greater flexibility in materials composition, especially for alloys containing phosphorus. The precursor materials used in MOVPE include the metalorganic and the hydride gases. Following the cracking of precursors at the heated substrate surface, the epitaxial layers are formed through the reaction of constituent chemicals.

In this dissertation, studies are dedicated to the InP-based materials photonic devices including the heterostructure lasers, the guiding waveguides, and the guiding membranes. The growth of InP, InGaAsP, and InGaAs epitaxial layers were realized by MOVPE on n-type (doped with sulfur, density $\sim 5 \times 10^{18}$ cm^{-3}) InP substrates. The sources of gallium and indium were provided by the trimethylgallium (TMGa) and the trimethylindium (TMIn) metalorganic compounds, respectively. The hydride sources, arsine (AsH_3) and phosphine (PH_3) were used as the sources of arsenic and phosphorus [McCrary1991]. The samples with epitaxial layers were fabricated by Isabelle Sagnes et al. in LPN.

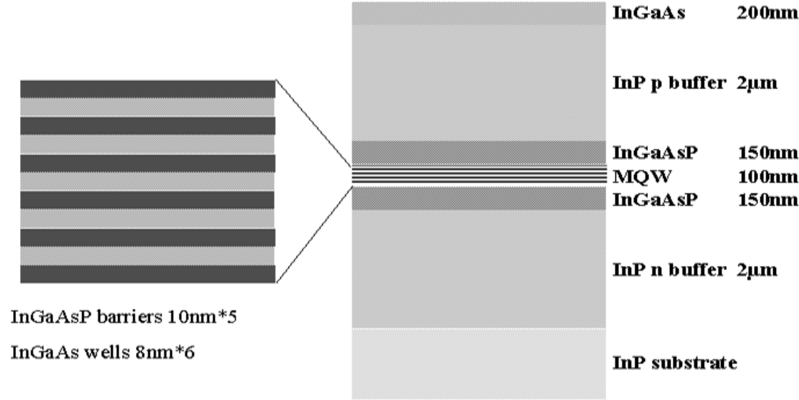

Figure 3.1: The vertical stacking of a single-confinement heterostructure laser with InGaAs/InGaAsP multiple quantum-wells as the active region.

3.2.1 Laser

The laser structure studied in this dissertation, as shown schematically in figure 3.1, is a typical separate-confinement heterostructure (SCH) structure with the multiple quantum-wells (MQW) as the active region. The active region was composed of six $In_{0.53}Ga_{0.47}As$ quantum-wells compressively strained for the TE gain enhancement separated by five $In_{0.79}Ga_{0.21}As_{0.46}P_{0.54}$ barriers. Due to the compressive strain, the electric fields of photons are polarized mainly in the transverse plane. This is desirable since the PhC defect modes that have been mentioned in chapter 2 are predominantly in TE polarization. The thickness of each quantum-well and barrier were 8 nm and 10 nm, respectively. The active region was buried between two 150 nm-thick $In_{0.79}Ga_{0.21}As_{0.46}P_{0.54}$ layers and the optical confinement was mainly provided by the refractive index contrast between the $In_{0.79}Ga_{0.21}As_{0.46}P_{0.54}$ layers and the p-type (doped with Zn, density $\sim 5 \times 10^{17}$ cm^{-3}) and n-type (doped with Si, density $\sim 1 \times 10^{18}$ cm^{-3}) InP buffer layers. A $In_{0.53}Ga_{0.47}As$ layer highly doped (with Zn, density $\sim 5 \times 10^{18}$ cm^{-3}) was grown on the top as the ohmic contact layer.

To present the unique properties of PhC in this laser structure, it is straightforward that the PhC holes should penetrate the active region and extend as deep as possible in order to minimize the out-of-plane losses at the bottoms of holes through the light diffraction [Ferrini2003]. Hence, an etch depth more than 4 μm hole features is expected to be reached.

3.2.2 Taper waveguide

The vertical stacking of the taper waveguide, as illustrated in figure 3.2, consisted of a 2 μm-thick InP buffer layer (refractive index, $n = 3.17$), a 500 nm-thick InGaAsP

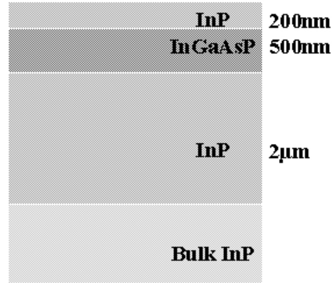

Figure 3.2: The vertical stacking of a InP/InGaAsP heterostructure planar waveguide.

(photoluminescence at 1.18 μm, $n = 3.38$) as the guiding layer, and a 200 nm InP layer capped on the top. The thickness of the guiding layer and the cladding layers were chosen appropriately to attain a fundamental mode light propagation and were also compromised by the limited etch depth of PhC holes using the present etching method developed in LPN [Lee2006]. The maximum field intensity was located in the InGaAsP guiding layer with a confinement factor of 86% and the corresponding effective index (n_{eff}) for the fundamental even mode was 3.28 for this vertical stacking. This value of effective index can be adopted for the 2D FDTD simulations to reduce the calculation time.

3.2.3 Membrane

Another waveguiding structure is the suspended membrane in air, which presents a largest refractive index contrast. As mentioned in the section 2.4.3, the light propagation within the PhC suspended membrane waveguide is theoretically lossless while operating below the air-light line. The vertical stacking of membrane waveguide was composed of a 1.5 μm-thick $In_{0.53}Ga_{0.47}As$ sacrificial layer grown on a n-type InP substrate by MOVPE, followed by a 260 nm-thick InP guiding layer, as illustrated in figure 3.3. The InGaAs layer was removed away by a selective wet etching and it thus leaded to a suspended InP membrane in air. As calculated, the confinement factor was 98% in this air/InP/air symmetric waveguide.

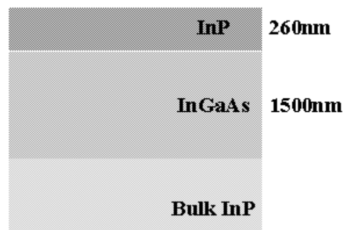

Figure 3.3: The vertical stacking of an InP membrane waveguide with InGaAs as the sacrificial layer.

From the dispersion diagrams of the InP PhC suspended membrane waveguide calculated by the 3D PWE method, the mode coupling to the odd mode may occur when the membrane thickness is more than 280 nm; but a thin membrane is too fragile for the fabrication processes. Based on these two reasons, a InP thickness of 260 nm was chosen. Further, to avoid the light scattering to the InP substrate during the measurements, a thick InGaAs sacrificial layer was preferred, which allowed an air space of 1.5 μm below the membrane after the selective wet etching.

3.3 Electron beam lithography

Electron beam lithography (EBL) is a specialized technique for creating the extremely fine patterns. In contrast to the resolution limited by the light wavelength used for exposure in optical lithography, the wavelength of electron beam is so small that the diffraction cannot define the lithographic resolution; instead, it is limited by the resist resolution.

The principle of EBL is to utilize a focused electron beam typically with energies of several keV to hundreds of keV for exposing features on the electron sensitive resist. The electron beam lithography system is composed of an electron gun, the electromagnetic lens, the beam deflectors, and a movable stage. A schematic figure illustrating the electron beam exposure system is shown in figure 3.4. The energetic electrons are generated from a field-effect electron gun and accelerated through a high voltage. Several electromagnetic lenses are used for the focalization and the deflection of electron beam. An aperture is employed to adjust the electron beam size in order to improve the focus. The beam deflectors can deflect the focused electron beam within a typical range of 500 μm. During the exposure, the electron beam scans on the resist surface by means of the beam deflectors within one writing field. For larger displacements, the movable stage is involved with a precision of 0.6 nm controlled by the laser interferometers.

The designed PhC patterns studied within this dissertation were fabricated in by a LEICA EBPG 5000+ e-beam pattern generator system in LPN. A double-mask strategy was adopted including a 250 nm-thick SiO_2 dielectric mask deposited by PECVD and a polymethylmethacrylate (PMMA) electron beam resist solution spanned on the surface by spin coating. It was then baked at 180^0C for 30 minutes to evaporate the solvent, and a 300 nm-thick resist layer was left. The patterns including PhC holes and trenches were defined in the PMMA layer using EBL and the exposure was performed with a maximum electron energy of 100 keV. The required electron doses for holes and trenches were in the range of 1000-2000 μC/cm^2 for a writing step of 2.5 nm. After the exposure, the PMMA resist was developed in Methyl-isobutyl-Ketone/Isopropanl (MIBK/IPA) and served as the mask for the etching of underlying SiO_2 layer.

Generally, feature sizes may differ from the designed ones due to the electron

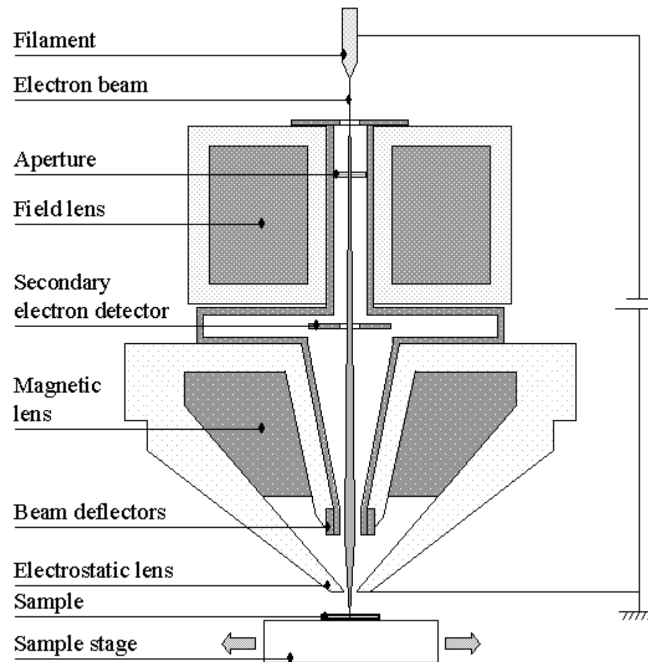

Figure 3.4: The schematic figure of an electron beam pattern generator system.

scattering in materials, called the *proximity effect*. As the focused beam travels through the resist, some electrons experience small angle forward scattering and some are bounced back by the substrate with large angles leading to the backward scattering. Therefore, the parasitic exposure is formed outside the area that was directly exposed by the electron beam. It has been reported that the electron beam energy can have influences on the proximity effect: higher the beam energy is, more electrons are scattered backward far from the center. For 100 keV electron energy, the backward scattering causes a background dose with a range of 15 μm approximately; but, the range is about 2 μm for 30 keV electron energy. The exposed materials can decide as well the extent of the proximity effect. Electrons are less scattered in the silicon compared to the III-V semiconductor materials (ex: GaAs and InP) since the atomic numbers of In and Ga are much larger than Si. It is possible to compensate the proximity effect by either adjusting the pattern distributions, modifying the hole sizes, or reducing the dose amounts.

In 2D PhC devices, to present some specific optical functions, hole positions may be shifted away from the standard PhC meshes and certain hole sizes may be adjusted as well. The proximity effect should thus be considered and the electron beam doses should be modified in order to obtain correct patterns. For instance, the PhC tapers presented in chapter 4 consist of the input/output ridge waveguides, the PhC standard matrix, and the varied holes in positions and sizes for the purpose of smooth transition. For this specific exposure, the electron beam dose

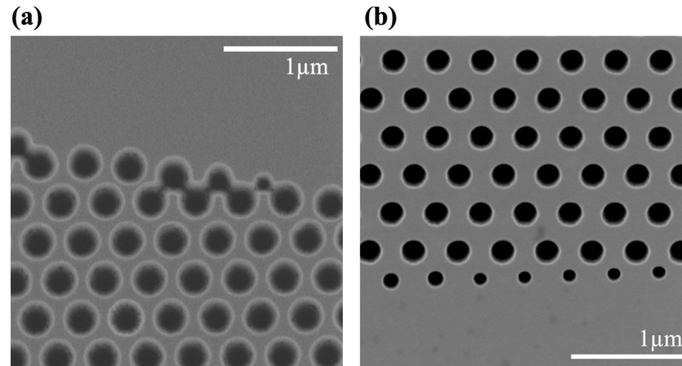

Figure 3.5: The SEM top views of PhC holes with shifted positions (away from the standard PhC matrix) and diminished sizes defined by EBL. (a) A single electron-beam dose is used for exposure, and so that holes are merged due to the proximity effect. (b)The compensation of proximity effect by reducing the exposure electron-beam doses for diminished size holes with small intervals.

for the ridges exposure was smaller than the one for PhC holes exposure. As shown in figure 3.5(a), the PhC standard matrix and the varied holes were exposed at a single electron-beam dose. After the etching process and removing the mask, the PhC standard matrix was found to be well transferred. But, certain varied holes in positions were merged with the matrix due to the proximity effect. To compensate this error, a smaller electron beam dose was reserved for the varied holes exposure. As presented in figure 3.5(b), after calibrations, patterns can be exposed successfully using proper and gradual electron-beam doses. Besides, a program of proximity effect correction (PEC) which can enhance the exposure yields is now being under investigation in LPN.

3.4 Reactive ion etching

3.4.1 Mechanisms of reactive ion etching

The etching process is used for patterns transfer and is generally categorized as wet and dry etching. For the wet etching in a solution, the etch rates are similar in all the directions; as a result, it leads to the isotropic etched profiles and the undercut. When the film thickness is small relative to the pattern size, the undercut is insignificant; but, it is not allowed in small and dense features (ex: PhC hole structures). The issues of isotropic etching and undercut can be settled by utilizing the dry etching method.

Reactive ion etching (RIE) is one common used dry etching method. It is performed using a plasma discharge in a reactive gas to create radical species and positive ions. Radical species react with the sample surface and form the volatile

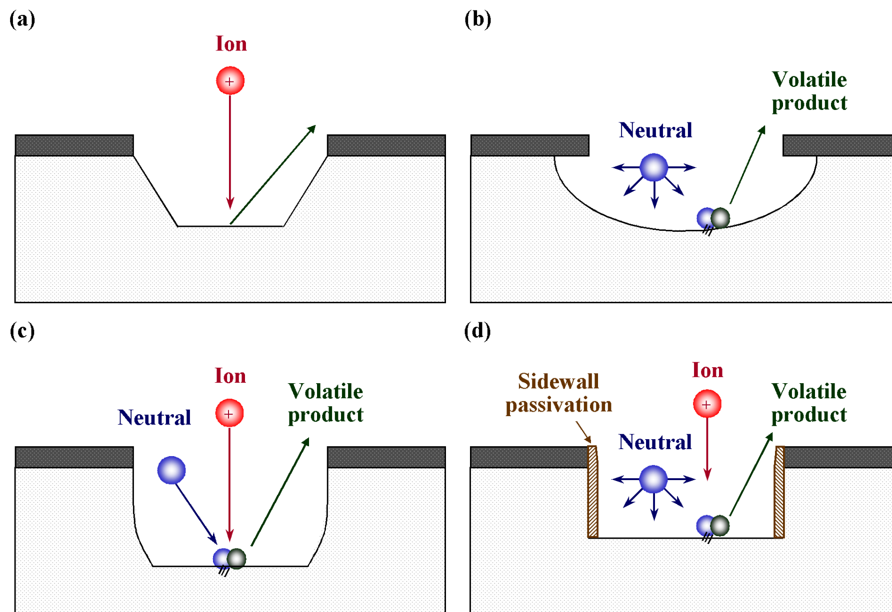

Figure 3.6: The schematic of four processes taking place during reactive ion etching, including (a) the sputtering, (b) the chemical etching, (c)the ion enhanced etching, and (d) the inhibitor ion enhanced etching.

compounds, which evaporate subsequently from the surface. Positive ions, under the electrical field acceleration, can cause the energetic ion bombardment on the sample surface. With the RIE, the loosened mask adhesion occurring often in wet etching is prevented and the profiles of etched features can be controlled by varying the plasma chemistry and other parameters.

During the RIE etching, four main processes may take place, as illustrated in figure 3.6, including:

1. Sputtering: a purely physical process caused by the surface bombardment with energetic ions. It contributes mainly to the anisotropic etching, but may result in high surface damage, low etch rates, and low selectivity. (figure 3.6(a))

2. Chemical volatilization: or called the chemical etching. It is related to the chemical reactions between the etched layer and the neutral species generated in the plasma to form volatile compounds. The chemical etching is often isotropic and is characterized by low surface damage, high etch rate, and high selectivity. (figure 3.6(b))

3. Ion enhanced chemistry: a combination of physical and chemical processes. The chemical reactions occurring on the sample surface are enhanced by the ion bombardment. It is considered that the energy supplied to the sample

surface by the collisions induced by ion bombardment increases the mobility of molecules. The formation and the desorption of volatile compounds can therefore be enhanced. (figure 3.6(c))

4. Inhibitor ion enhanced chemistry: an ion enhanced etching and an inhibitor that passivates the surfaces is also involved. The sidewall passivation is a result of formation along the sidewall of the etched feature, which can slow down or inhibit completely the lateral etching. The passivation is prevented by the ion bombardment at the bottom of the feature and the anisotropic etching is thus obtained. (figure 3.6(d))

In the RIE etching, the generated plasma is characterized as *cold plasma*, which means that the plasma is in a low-pressure operation and in a non-equilibrium thermodynamic state. In a cold plasma, the electron temperature can reach to $10^4 - 10^5$ K, while the temperatures of ions and neutrals can stay as low as room temperature. The sources used extensively to generate the plasma for processing are through the radio-frequency (rf) and can be classified into capactive, inductive, and wave sources. The plasma density in a capactively couple plasma (CCP) is in the order of $10^9 - 10^{10}$ cm^{-3}. The inductively coupled plasma (ICP) , also referred as high-density source, have a plasma density typically ranging at $10^{10} - 10^{11}$ cm^{-3}. Within this dissertation, the CCP and ICP are used for the etch mask fabrication and the PhC structures etching, respectively, and are illustrated in the following sections.

3.4.2 Capactively coupled plasma reactive ion etching

The dry etching method for InP compound materials often involves two important requirements: a chlorine-containing plasma and a high temperature ($> 150^0$C) environment. In this case, the PMMA resist is not a good candidate for InP etching since its etch rate is elevated in the chlorine-containing plasma and a high temperature often leads to degradation and deformation. Therefore, the dielectric mask (ex: SiO_2 and SiN_x) is employed widely for InP etching and another fabrication step of pattern transfer from the PMMA to the dielectric mask is required and is often realized by capactively coupled plasma reactive ion etching (CCP-RIE).

In a CCP-RIE system, it consists of a cylindrical vacuum chamber and two parallel electrodes, as shown in figure 3.7(a). The plasma is generated by the application of rf voltage, for which, a rf generator with frequency of 13.56 MHz is capactively coupled to the bottom electrode plate. The oscillating electric field in the chamber ionizes and dissociates the reactive gas. Due to larger mobility of electrons compared to massive ions, electrons accumulate on the bottom electrode and a self-induced negative bias builds up when the plasma is ignited. This dc bias voltage accelerates the positive ions towards the bottom electrode and contributes to the ion bombardment.

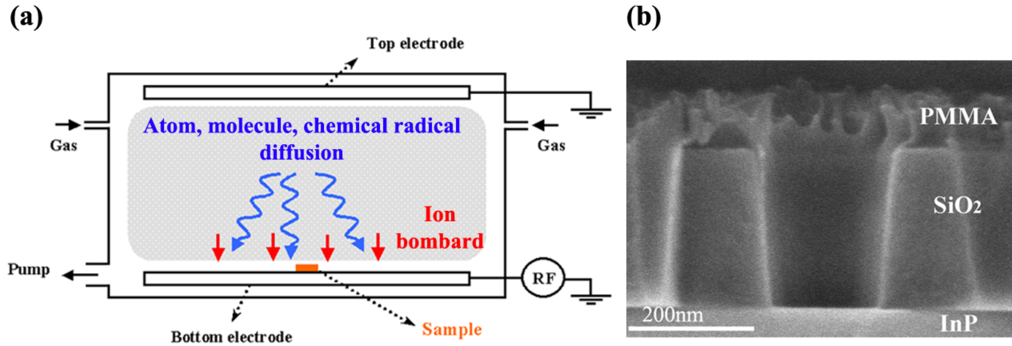

Figure 3.7: (a) The schematic of a CCP-RIE system. (b) An etched SiO_2 dielectric mask using a CHF_3-based plasma in CCP-RIE system.

The PhC patterns transfer was performed in a Nextral NE100 parallel plates reactor system using a CHF_3-based plasma. The chamber pressure was maintained at 4 mTorr and the rf power was kept at 20 W during the etching. Under these conditions, the large-area etch rates were about 10.5 nm/min and 6.8 nm/min for SiO_2 and PMMA layers, respectively. Considering the aspect ratio dependent etching (ARDE) [Gottscho1992], or commonly called as the RIE lag, the etch rates can be influenced strongly by the feature dimensions; hence, the required time to fully open the densely packed features is needed to be prolonged. In a PhC structure with a 110 nm-hole diameter, the required time to etch away the 250 nm-thick SiO_2 layer was increased with a factor of 1.35 compared to the one in large-area. Figure 3.7(b) shows the SEM cross-section view of an etched SiO_2 mask in a PhC matrix with PMMA resist left on the top. The sidewall of SiO_2 was smooth and nearly vertical with a small inclination angle of 3^0, which may minimize the pattern deformation coming from SiO_2 mask. The PMMA resist was removed subsequently using an O_2 plasma in CCP-RIE system.

3.4.3 Inductively coupled plasma reactive ion etching

The InP-based PhC etching was realized using inductively coupled plasma reactive ion etching (ICP-RIE) performed in a Sentech SI-500 system with a planar triple spiral antenna. As shown schematically in figure 3.8, the reactor is equipped with two rf generators, operating at 13.56 MHz frequency, which allows the liberties of controlling separately the plasma densities and ion energies. The ICP source is coupled to the plasma through a Al_2O_3 ceramic window. The diameter of the plasma reactor is 36 cm and the distance from the ceramic window to the sample holder is about 8.5 cm. Samples are glued on a 4-inches silicon carrier, which is mechanically clamped above the rf-biased electrode. The sample carrier is thermally coupled to the electrode through He backside cooling and the electrode temperature is regulated by resistive heating and water cooling. In this system, the high

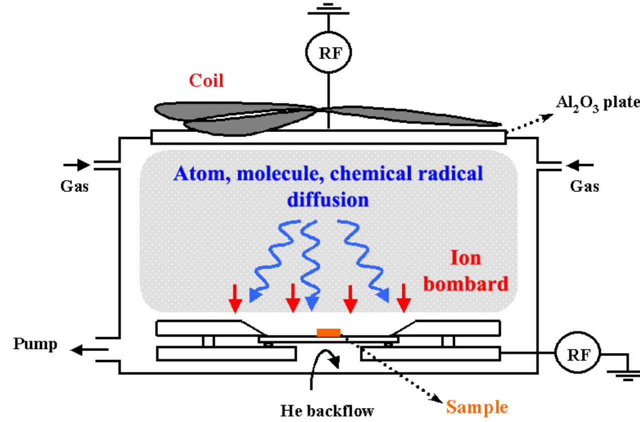

Figure 3.8: The schematic of an ICP-RIE system with a planar triple spiral antenna.

density inductive mode is operated when the rf power injected into the inductively coupled plasma source is more than 150 W.

3.5 ICP Cl_2/Ar plasma for PhC holes structure deep etching

From the empirical etch results in the CAIBE [Kotlyar2004a, Mulot2004a] and ICP [Strasser2005, Strasser2007] systems, the Cl_2/Ar plasma is chosen for InP PhC holes deep etching realization executed in LPN. In order to optimize the etching conditions, a series of experiments was performed with the variations of the electrode temperature (T), the rf power injected into the inductively coupled plasma source (ICP power, P_{ICP}), the self-induced dc bias voltage ($|V_{bias}|$), the total gas pressure (p), and the total gas flow (F). The etch mask was a 250 nm-thick SiO_2 layer and the patterns of test samples included a 3 μm-wide single trench and PhC matrices with the lattice constant ranging from 150 nm to 450 nm, in which the hole diameters varied correspondingly between 100 nm and 250 nm to sustain more or less a constant air filling factor of 33%. The scanning electron microscopy (SEM) was used to examine the etched profiles and etch depth after cleaving through the etched PhC holes. Since the cleavage line might not pass through the center of holes completely, the estimated etch depth would have an uncertainty of $\pm$10%.

Subsequently, the PhC devices were fabricated using the ICP Cl_2/Ar plasma with the optimized etching conditions in order to demonstrate the light emission and light guiding functions.

3.5.1 Etching conditions investigation

A. Cl_2/Ar ratio dependence

The Cl_2 and Ar gas ratios have direct impacts on the etched profiles. Generally speaking, for trench features etching, a higher Cl_2 ratio can lead to a higher etch rate and a higher selectivity due to the fact that Cl_2 is very active chemically to InP materials, but little to the SiO_2 mask. It is well known that the etching is isotropic-dominated under a Cl_2 plasma and the addition of Ar may further enhance the Cl_2 dissociation rate; hence, a large number of chlorine radicals is created and it leads to the lateral etching. At small features, this lateral etching is more significant and should be avoided. However, with the additional of Ar, the removal of etch products and InP materials can be accelerated in the vertical direction by the ion bombardment and the anisotropy can thus be improved.

Based on these arguments, a relative low Cl_2 ratio ranging between 15∼25% in a Cl_2/Ar plasma was therefore investigated. A gas ratio higher than 25% may often result in severe isotropic profiles and a too low Cl_2 ratio would turn the etching to a physical regime and degrade the selectivity.

B. ICP power dependence

The rf power injected to the inductively coupled plasma source (ICP power, P_{ICP}) has a direct impact on the electron density in the plasma, as well as the ion and neutral radical densities. The etched holes and trenches profiles were studied with the variations of the ICP power (0∼200 W) with other parameters fixed as in table 3.3. Note that in the case of 0 W, the plasma was still generated by another rf power injected to the electrode (RIE power). The induced bias voltage was maintained at a fixed value by the simultaneous regulation of RIE power.

Examining the etched trenches profiles with the variations of P_{ICP} in figure 3.9, the undercut found at 0 W-P_{ICP} implied an excess chemical etching. As the P_{ICP} increased, the undercut was eased and a trench with nearly vertical sidewall was obtained when P_{ICP} was 100 W. In a higher value, i.e. 200W, the sidewall became rougher and it indicated a physical etching domination. The InP etch rate in trench features increased from 220 to 320 nm/min with the increase of P_{ICP} from 0 to 200 W, but the selectivity (InP : SiO_2) decreased from 33 to about 18

ICP power (W)	**0 ∼ 200**
Bias voltage (V)	-100
Gas pressure (mTorr)	1
Cl_2 : Ar mass flow (sccm)	2 : 6
Electrode temperature (^{0}C)	180

Table 3.3: The investigated ICP power range and other etching conditions in Cl_2/Ar plasmas.

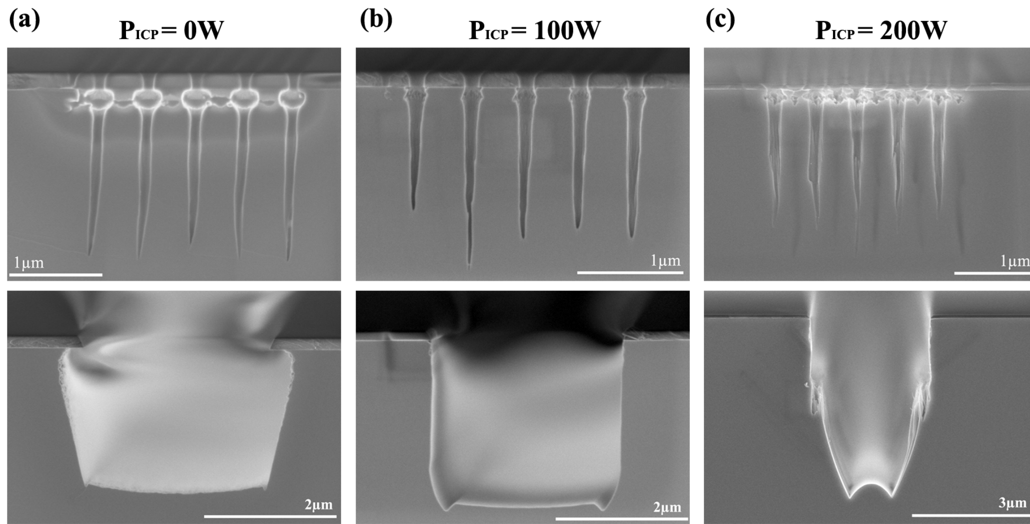

Figure 3.9: SEM cross-section views of PhC holes (d = 180 nm) and trenches etched by Cl_2/Ar plasmas with various ICP powers: (a) 0 W, (b) 100 W, and (c) 200 W.

(figure not shown). It is believed that, with the increase of P_{ICP}, the positive ion density increased in the plasma and so did the radical density, and then a higher etch rate was caused due to the ion enhanced etching. Nevertheless, the SiO_2 mask could be degraded severely by the ion bombardment and a lower selectivity was found at a higher P_{ICP} value.

In the holes profiles, similar undercut and rough sidewalls as in the case of trenches were also observed with the increase of P_{ICP} (figure 3.9). At 100 W-P_{ICP}, a compromise presenting the smoother surfaces and only a slight undercut was obtained. Hence, in the following investigation of Cl_2/Ar plasma optimized etching conditions, the P_{ICP} was often operated around 100 W. The etch rates

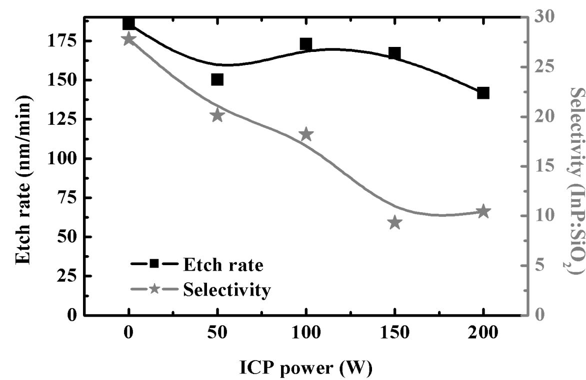

Figure 3.10: The etch rate (square) and selectivity (star) for 180 nm-diameter PhC holes etched by Cl_2/Ar plasmas with various ICP powers.

were at the range of 140~180 nm/min and did not show a strong dependence on the ICP power, as shown in figure 3.10. On the contrary, the selectivity decreased monotonically (from 28 to 10) with the P_{ICP} since the SiO_2 mask etch rate is related directly to the ion density.

C. Bias voltage dependence

The increase of absolute self bias dc voltage ($|V_{bias}|$) often indicates a higher ion energy and the etch rate augments straightforwardly due to the ion enhanced etching. The features were etched with different bias voltages (-50~-150 V) with other parameters fixed as in table 3.4. In the trench features, the typical trend of increasing etch rate with $|V_{bias}|$ was observed (figure not shown); but the sputtering degraded SiO_2 mask and the selectivity (InP : SiO_2) thus decreased with the $|V_{bias}|$.

However, in hole features, the etch rate did not show a linear increasing comportment with $|V_{bias}|$ (figure 3.11). Apart the volatilization, the removal of etch products can be realized by the ion sputtering with the proper energies. In a lower $|V_{bias}|$, i.e. 50 V, the etch products might not be removed away instantaneously due to the insufficient sputtering rate and the reaction of radicals with the underneath InP was probably impeded. Instead of reaching the bottom of holes, radicals were consumed mostly on the top of holes. As a result, the etching was not extended in the vertical direction (figure 3.12(a)) and the etch rate was the smallest. As $|V_{bias}|$ was 100 V (figure 3.12(b)), the sputtering facilitated the removal of etch products and the bottom of holes could be exposed to the radicals for the subsequent chemical reactions. We then observed that the etch rate increased as well as the selectivity when $|V_{bias}|$ increased to about 100 V.

When further increasing the $|V_{bias}|$, the undercut appeared once more on the top of holes (figure 3.12(c)). The similar undercut while etching submicron-wide trenches patterns in Si materials was reported by S. Ohki et. al. [Ohki1987]. They observed that the amount and location of undercut were strongly related to the slope angle and the thickness of mask. An explanation considering the ion enhanced etching on the upper sidewalls due to the energetic ions scattered from the opposite sloped mask was proposed and was verified by the simulation. In our case, the mask was at first with a slope angle of 80^0. The scattered ions due to the sloped mask hence ranged at 375~500 nm below the mask (figure 3.13(a)). With the etch time

ICP power (W)	100
Bias voltage (V)	**-50 ~ -150**
Gas pressure (mTorr)	1
Cl_2 : Ar mass flow (sccm)	2 : 6
Electrode temperature (^{0}C)	180

Table 3.4: The investigated bias voltage range and other etching conditions in Cl_2/Ar plasmas.

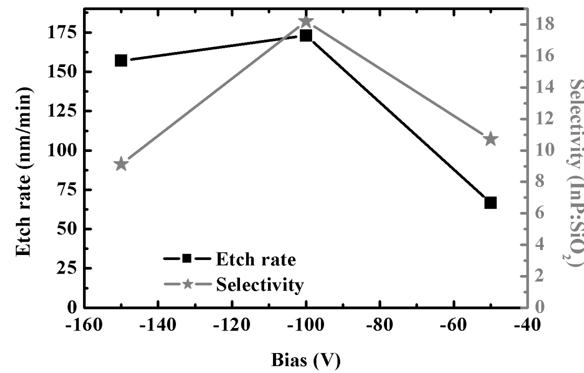

Figure 3.11: The etch rate (square) and selectivity (star) for 180 nm-diameter PhC holes etched by Cl_2/Ar plasmas with various bias voltages.

increased, the mask was degraded and became less steep. Assumed that the mask was with a slope angle of 65^0 approaching the end of etching cycle, the ions could thus be scattered greatly and located at 50∼150 nm which corresponded roughly to the position of undercut.

In addition to the sloped mask, the inclined incident ions might contribute partly to the undercut formation. In a Cl_2/Ar ICP-RIE plasma, it has been reported by J. R. Woodworth that the ion angular distribution in half-width ranged from 4.5^0 and 8.5^0 with the distributions broadening with increase in pressure in the 2.5∼20 mTorr range [Woodworth1997]. Thoses ions equipped with transverse ion energies might enhance the ion-ehanced-etching in the lateral direction especially on the top of holes where the chlorine radicals are abundant. Figure 3.13(b) shows the deflected ions arising from inclined incident ions (5^0) scattered on the surface of sloped mask. The locations of scattered ions therefore ranged at 200∼375 nm for 80^0 sloped mask and ranged at 25∼125 nm for 65^0 sloped mask. Those ranges seemed to be closer to the location of undercut observed experimentally (figure 3.12(c))

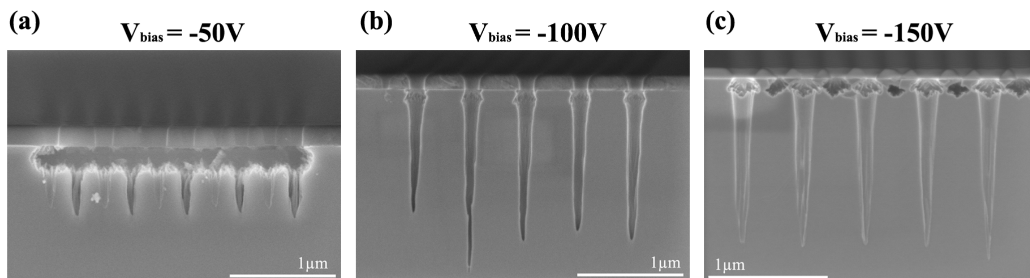

Figure 3.12: SEM cross-section views of PhC holes (d = 180 nm) etched by Cl_2/Ar plasmas with the various bias voltages: $|V_{bias}|$ = (a) 50 V, (b) 100 V, and (c) 150 V.

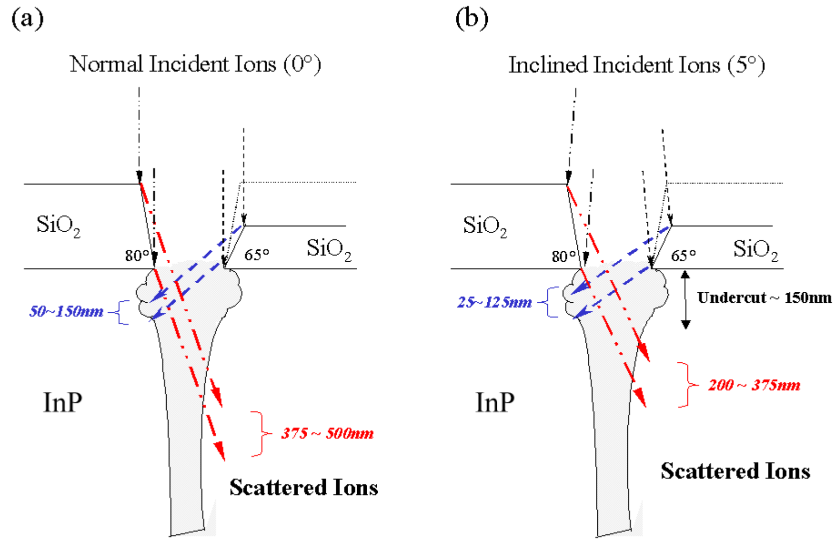

Figure 3.13: The schematic of scattered ions resulted from (a) normal and (b) inclined incident ions impinging on sloped mask (80^0, 65^0).

D. Gas pressure dependence

The role of Cl_2/Ar total gas pressure on the etched holes profiles were studied (figure 3.14(a)-(d)) with other parameters fixed as in table 3.5. From the SEM cross-section views, it can be concluded that a Cl_2/Ar plasma operating at an extreme low gas pressure, i.e. 0.5 mTorr, was preferred for the PhC hole etching since the under-etching was not visible compared to the ones etched at higher gas pressures.

At a higher gas pressure when other etching conditions were invariant and shown in table 3.5, the neutral radical densities should be increased. The abundant chlorine radicals thus leaded mostly to the isotropic etching, as shown in figure 3.14(b)-(d), the extent of lateral etching was proportional to the gas pressure. At p = 1 mTorr, the undercut was eased largely and it was finally prevented at p = 0.5 mTorr. The etch rate at p = 1 mTorr was the highest and the one at p = 0.5 mTorr was just slightly lower (figure 3.15(a)); but, the selectivity at 0.5 mTorr gas

ICP power (W)	100
Bias voltage (V)	-100
Gas pressure (mTorr)	**0.5 ∼ 5**
Cl_2 : Ar mass flow (sccm)	2 : 6
Electrode temperature (^{0}C)	180

Table 3.5: The investigated gas pressure range and other etching conditions in Cl_2/Ar plasmas.

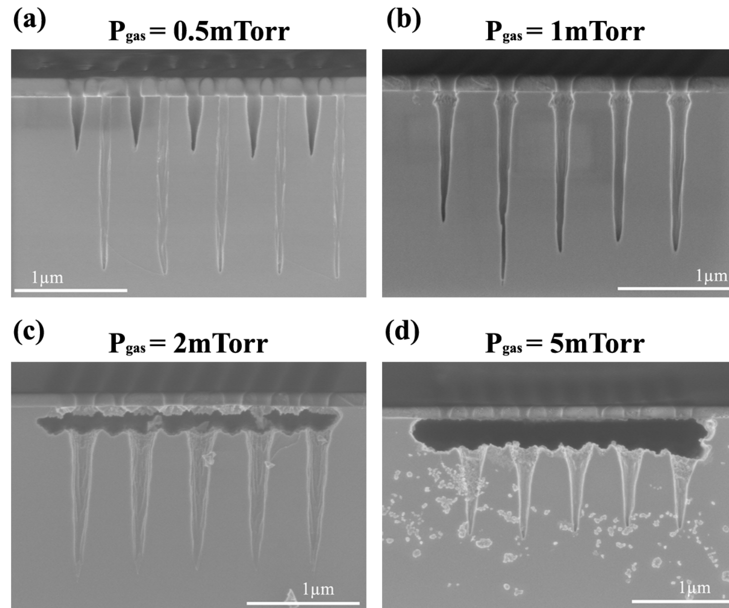

Figure 3.14: SEM cross-sections of PhC holes (d = 180 nm) etched by Cl_2/Ar plasmas with the various gas pressures: (a) 0.5 mTorr, (b) 1 mTorr, (c) 2 mTorr, and (d) 5 mTorr.

pressure showed a highest value within the investigation range. This observation was similar to the experimental results of P. Strasser et. al. [Strasser2005]. They introduced He inert gas for the purpose of dilution in order to further decrease the partial gas pressure of Cl_2 and Ar under the pumping limitation.

Intuitively, the plasma etching is supposed to be more efficient in a high gas pressure circumstance, as the radical source is abundant so that the radical consummation due to etching would not be limited. It should be noted that this trend can only be valid for large-area features. As presented in figure 3.15(b), for

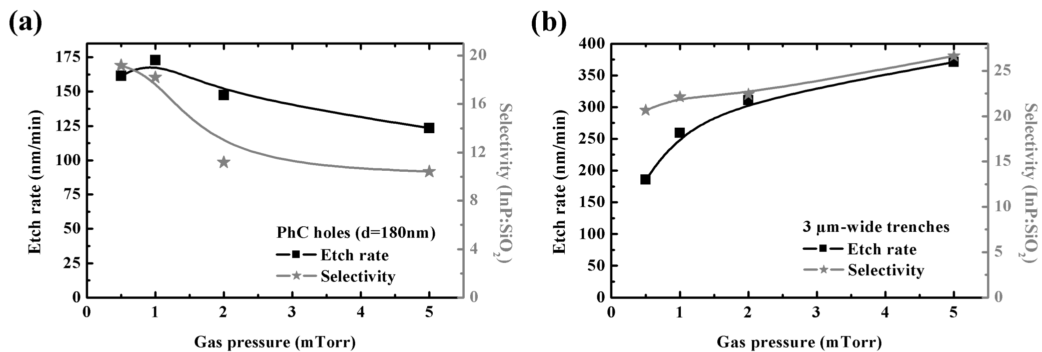

Figure 3.15: The etch rate (square) and selectivity (star) for (a) 180 nm-diameter PhC holes and (b) 3 μm-wide trenches etched by Cl_2/Ar plasmas with various gas pressures.

3-μm wide trenches, both the InP etch rate and the selectivity increased with the gas pressures. But, the behaviors were totally inverse to the ones for PhC holes (3.15(a)). While tackling the etching in small opening features, the evacuation issue has to be always considered. In PhC holes, an elevated gas pressure might obstruct the evacuation of etched products, and it then raised the possibility of reactant re-deposition and resulted in a limited etch depth in the vertical direction. Moreover, in a high gas pressure, the ions suffered more from the scattering while traveling through the trajectory between the plasma sheath and sample surface. The scattered ions were no more unidirectional, but with an angular distribution. In addition, due to the chlorine radicals centered mostly on the top of holes, the undercuts were therefore observed. In an extreme case, holes were merged together and a SiO_2 suspended mask was formed. Another merit of low gas pressure operation was that the etch rates of trenches and holes were comparable, ~170 nm/min, which was important for the simultaneous etching of photonic devices including different feature sizes.

E. Total gas flow (species residence time) dependence

At a fixed gas pressure value, the variation of total gas flow indicates the change of species residence time. Since the chemical reaction is involved in a plasma-assisted etching method, the species content, the species density, the species residence time, etc, may have influences on the etching results. In this subsection, the variation of total gas flow was studied with other optimized parameters chosen from the prior investigations (table 3.6). The P_{ICP} and $|V_{bias}|$ were fixed at 150 W and 130 V, respectively. The Cl_2/Ar ratio was maintained as 1/4 and an extremely low gas pressure was chosen at 0.5 mTorr in order to minimize the undercut in PhC hole features. With increasing the total gas flow from 15 to 20 sccm, the etch rate and the selectivity in PhC holes augmented with a ratio of 25% (from 170 to 210 nm/min) and 15%, respectively. In the trench features, these increases were even more visible and could reach 40%.

The residence time can be determined from parameters including reactor volume, reactor gas pressure, and mass flow rate. In a high density C_4F_8/Ar plasma with a 10 mTorr working pressure, Y. Chinzei et al. have measured a general decrease in CF_x radicals concentrations when the residence time was increased within

ICP power (W)	150
Bias voltage (V)	-130
Gas pressure (mTorr)	0.5
Cl_2 : Ar mass flow (sccm)	**3 : 12 and 4 : 16**
Electrode temperature (^{0}C)	180

Table 3.6: The investigated Cl_2 : Ar mass flow rates and other etching conditions in Cl_2/Ar plasmas.

ICP power (W)	150
Bias voltage (V)	-170
Gas pressure (mTorr)	0.5
Cl_2 : Ar mass flow (sccm)	4 : 16
Electrode temperature (^{0}C)	**180 ~ 195**

Table 3.7: The investigated electrode temperature range and other etching conditions in Cl_2/Ar plasmas.

the 10~100 ms range. They considered taht the observed decreased radical density with increasing the residence time was attributed to the collisions in the reactor, especially with the chamber wall [Chinzei1998a, Chinzei1998b]. A similar effect could occur for the Cl radicals in our case.

A detailed study of dependences of the ion density, the radical density and the InP PhC holes etch rate on the residence time in a Cl_2/Ar plasma has not been realized yet. But, with the deduction mentioned above, it was presumed that the chlorine radical amount might increase as well at a shorter residence time. In the case of 20 sccm total gas flow rate, i.e. 40 ms-residence time, the chlorine radical density was supposed to be slightly larger than in the case of 15 sccm (52 ms-residence time). Those raised chlorine radicals contributed to the InP etching and leaded to a higher etch rate and a higher selectivity.

F. Temperature dependence

It has been reported already in the literature that the InP etch rate under a Cl_2-based plasma can be influenced by the heating temperature [McNevin1986]. Here, a small range of electrode temperature within 180^0C~195^0C was investigated to look for an etching temperature under machine constraint. Other parameters were fixed during the etching (F_{Cl2} = 4 sccm, F_{Ar} = 16 sccm, p = 0.5 mTorr,

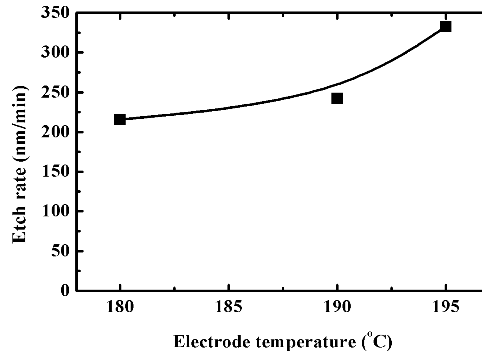

Figure 3.16: The InP etch rate for 180 nm-diameter PhC holes etched by Cl_2/Ar plasmas with various electrode temperatures.

P_{ICP} = 150 W, $|V_{bias}|$ = 170 V), as shown in table 3.7. The sample was glued on a silicon carrier using the vacuum paste, but a temperature gradient may still present between the electrode and the sample surface.

In figure 3.16, the InP etch rate increased with the electrode temperature when it was more than 180^0C. From this behavior, it might also suggest that, under these gas conditions (Cl_2/Ar = 4/16, P = 0.5 mTorr), the etching was not limited by the supply of chlorine radicals. For a deep etching, a higher electrode temperature is no doubtfully preferred since the SiO_2 mask etch rate is insensitive to the temperature and it then results in a higher selectivity. However, due to the machine limitation, a compromise should be established in order not to endanger its functionality. An electrode temperature ranging at 180^0C$\sim$$190^0$C was therefore chosen for the experiments and the etch rates was intended to be raised by other contributions (ex: the ion bombardment, the plasma density).

To obtain vertical PhC hole profiles without undercut by an ICP Cl_2/Ar plasma etching, the following criterions should be concerned:

1. The Cl_2 ratio should not exceed 25% to prevent a severe undercut; a Cl_2 ratio less than 15% is not preferred since both the etch rate and the selectivity (InP : mask) reduce.

2. An extreme low gas pressure is critical for small and dense features etching.

3. A complete high density inductive mode (P_{ICP} > 150 W) may not be quite suitable for PhC holes etching. A moderate value ranging at 100$\sim$150 W can minimize the undercut and the rough sidewall surfaces.

4. A low species residence time (large total gas flow) might be preferred for the chlorine radical generation, but the maximum gas flow value can often be limited by the pumping efficiency. However, an excess chlorine radical density might probably lead to the isotropic etching.

5. A high temperature operating between 180^0C and 195^0C shows no obvious change on the PhC holes profiles, but the etch rate increases slightly with the temperature.

3.5.2 Optimized etching conditions and RIE lag for ICP Cl_2/Ar plasma

From the investigations on the Cl_2/Ar plasmas presented in section 3.5.1 A-F, the etching conditions have been optimized (table 3.8) for the InP PhC sub-micrometer

ICP power (W)	150
Bias voltage (V)	-130
Gas pressure (mTorr)	0.5
Cl_2 : Ar mass flow (sccm)	4 : 16
Electrode temperature (^{0}C)	**190**

Table 3.8: The optimized Cl_2/Ar plasma etching conditions for PhC holes structure.

hole features under the constraint of 250 nm-thick SiO_2 dielectric mask. The ICP source power was set as 150 W and the bias voltage was maintained at -130 V during the whole etching process in order to reduce the mask etching rate. A low Cl_2 ratio is preferred since the isotropic etching is notable especially for small feature sizes. The optimized gas pressure was set as 0.5 mTorr with a Cl_2 mass flow rate of 4 sccm and an Ar mass flow rate of 16 sccm. The ion current density under these conditions was at the range of 0.28 mA/cm^2. The etching was realized at 180^{0}C$\sim$190^{0}C electrode temperature to facilitate the volatilization of the chemical reactant $InCl_x$.

Figure 3.17(a) shows the SEM cross-section view of 130 nm-diameter holes in a triangular matrix with a periodicity of 300 nm. The etch depth reached 2 μm with a selectivity of $\sim$12. The hole shape was nearly vertical, but with visible rough sidewall surfaces, as presented in figure 3.17(b). The sidewall roughness was suspected coming from the physical bombardment of energetic Ar ions and/or from the unequal chemical etch rates between In and P.

Figure 3.18 presents the etch depths with various PhC holes diameters under the same etching conditions. A typical lag effect of etch depth on absolute feature size was observed, with a depth of 1.9 μm for 110 nm-diameter holes and a depth of 2.9 μm for 240 nm-diameter holes. This dependency of etch depth on the feature size is

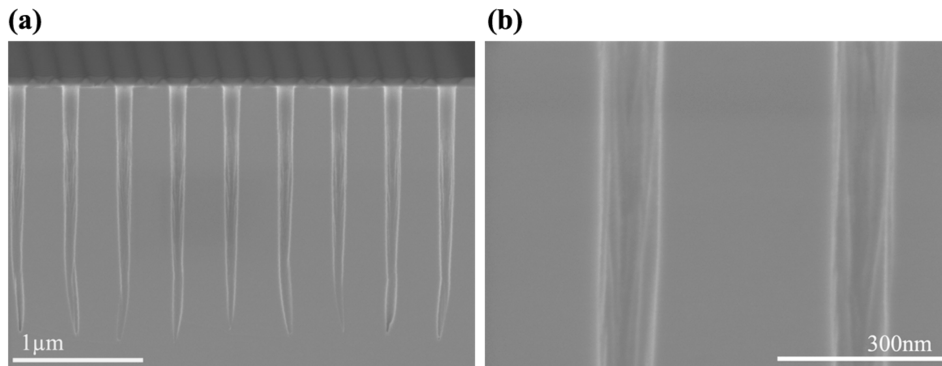

Figure 3.17: SEM cross-section views of (a) a triangular matrix of PhC holes (a = 300 nm, d = 130 nm) after the Cl_2/Ar (4/16 sccm) plasma etching in an ICP-RIE system. (b) Magnified view on the hole sidewalls.

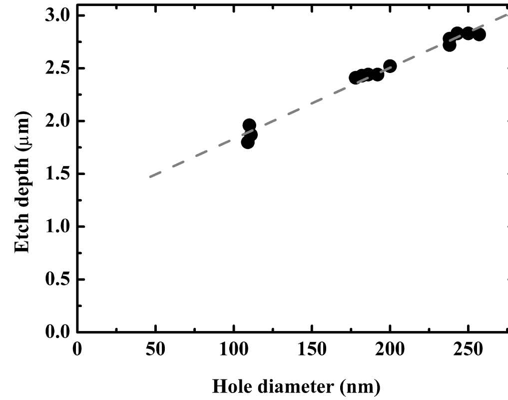

Figure 3.18: The etch depths with evolution of PhC holes diameters etched by an ICP Cl_2/Ar plasma with 4 sccm-Cl_2, 16 sccm-Ar, p = 0.5 mTorr, P_{ICP} = 150 W, $|V_{bias}|$ = 130 V, T = 180^0C. (Etch time = 9 mins)

often addressed as *RIE lag*, or known more accurately as the *aspect ratio dependent etching (ARDE)*. It is generally considered that the ions/radicals transports till the feature bottom and the evacuation/re-adsorption of etch products are related to the feature geometries and sizes [Gottscho1992].

With these Cl_2/Ar plasma etching conditions, we are able to etch the PhC holes of variable diameters simultaneously, as small as 110 nm, with a minimum etch depth of 2 μm. The diminished holes are expected to be applied in other PhC device designs.

3.5.3 Comparison of ICP and CAIBE for PhC holes deep etching

Comparing the etched results of InP PhC holes by two different plasma sources in an ICP and in a CAIBE system, we observe an apparent difference on the selectivity. As reported by M. Mulot [Mulot2004a] and M. V. Kotlyar [Kotlyar2004a], the selectivity (InP : mask) could reach more than 25:1 for about 250 nm-diameter holes etched by Ar/Cl_2 CAIBE. But, the selectivity was in the order of 18:1 for holes with similar diameters etched using an ICP Cl_2/Ar plasma. Considering the ion current density, the value of the optimized ICP Cl_2/Ar plasma presented in this dissertation was 0.28 mA/cm^2 measured using a rf planar electrostatic probe [Braithwaite1996]. On the contrary, it was only about 0.04 mA/cm^2 in the CAIBE system [Berrier2007], which was seven times smaller. In an ICP system, the elevated amount of ions composed of Ar^+, Cl_2^+ and Cl^+ degraded the dielectric mask in a higher rate than in a CAIBE system. As a result, a lower selectivity in the ICP system was observed and leaded to a limited etch depth.

To settle the drawback of lower selectivity in an ICP-RIE system using a Cl_2/Ar plasma, the hard masks including a 600 nm-thick SiO_2 mask or a titanium/SiN_x hybrid mask have been proposed by R. Wüest [Wüest2005]. With the hard mask design, a maximum etch depth of 3.5 μm was obtained for 200 nm-diameter holes using an ICP Cl_2/Ar/N_2 plasma. Nevertheless, due to the requirement of certain PhC devices (ex: PhC tapers), the dimensions and positions of PhC holes may vary and the hole diameter can be diminished to 100 nm. The realization of hard mask (~600 nm) for the varied-size and small holes could not be achieved with success based on the current technology. Therefore, the development of thick mask was not being pursued in LPN within the dissertation scope.

With the optimized InP Cl_2/Ar plasma etching conditions (F_{Cl2} = 4 sccm, F_{Ar} = 16 sccm, p = 0.5 mTorr, P_{ICP} = 150 W, $|V_{bias}|$ = 130 V, T = 180^0C~190^0C), a maximum etch depth of 2.9 μm for 240 nm-diameter holes can be achieved under the constraint of a 250nm-thick SiO_2 mask. At a smaller feature size, 110 nm-diameter, an etch depth of 1.9 μm can be obtained as well successfully.

The selectivity (18 : 1, for d = 240 nm-holes) under these etching conditions might be hard to be further improved due to a relatively higher positive ion current density. But, the development on thick masks for certain PhC devices would allow to obtain deeper etch depths.

3.5.4 Etched PhC devices performances: free-carrier lifetime and optical propagation losses measurements

From the SEM cross-section views presented in figure 3.17, it is difficult to quantitatively evaluate and estimate the performances of PhC devices etched using the optimized ICP Cl_2/Ar plasma. Hence, the free-carrier lifetime and the light propagation losses measurements were performed on a PhC device with multiple quantum-wells and on a PhC channel defect waveguide, respectively.

A. Carrier lifetime

The carrier generation and recombination dynamics can be examined by time-resolved photoluminescence measurement. The defects formed on the etched sidewalls in PhC increase the surface recombination states, and thus decrease the free-carrier lifetime. Hence, the free-carrier lifetime is a good indication on the qualities of etched sidewalls in PhC lattices.

The sample used for the carrier lifetime characterization consisted of two Ga_x-$In_{1-x}As_yP_{1-y}$ quantum wells emitting at 1.55 μm wavelength embedded in 1.18

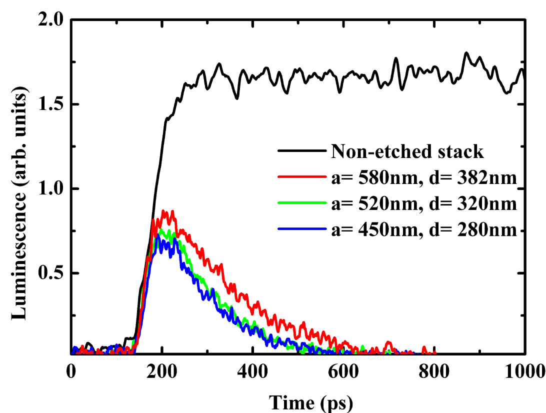

Figure 3.19: Time-resolved photoluminescence for InP/InGaAsP multiple quantum-wells structures with PhC holes etched by an ICP Cl_2/Ar plasma. The non-etched stack result is indicated for comparison (black line).

μm barriers grown on an InP substrate [Carlstrom1999]. The PhC structures studied here were triangular lattices with periodicities ranging between 450∼580 nm and hole diameters varying between 280∼380 nm. The etching was realized using an ICP Cl_2/Ar plasma with optimized conditions described in section 3.5.2. After etching, the photoluminescence measurement was performed using a pulsed tunable Ti:sapphire laser with a spot size of 40 μm-diameter focused on the sample surface and the emitted light was later spectrally dispersed and detected by an avalanche photodiode. The measured time-resolved photoluminescence intensities of samples with and without PhC structures are presented in figure 3.19. The highest intensity for samples with PhC structures was about two times smaller than the non-etched stack (regions without PhC structures). The free-carrier lifetime could be derived from the slope of light intensity with the function of time and it was in the order of 3∼6 ns for the non-etched stack. On regions with PhC structures, it then decreased to 100∼150 ps depending on the PhC lattice parameters. Since the number of surface states increased along the etched PhC hole sidewalls, the electron-hole recombination was enhanced and it leaded to a reduced carrier lifetime. It is believed that a larger carrier lifetime would be obtained in the case of PhC structures with smooth sidewall surfaces.

A similar carrier lifetime value in the order of 100∼270 ps has been measured by the time-resolved reflectivity on PhC structures etched using a Cl_2/Ar plasma in a different ICP-RIE system [Holzman2005].

B. Propagation losses

To evaluate the optical performances of an etched PhC device, a W3 PhC waveguide was fabricated and the transmission spectrum was measured to derive the light propagation losses. The optical waveguide was a InP/InGaAsP/InP het-

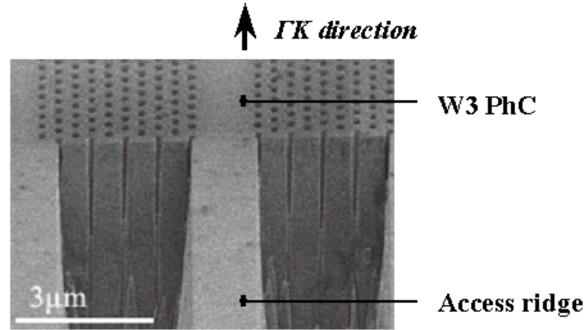

Figure 3.20: SEM side view of W3 PhC and the access ridge.

erostructure consisting of a 500 nm-thick InGaAsP guiding layer and a 200 nm-thick InP top cladding layer. The two dimensional PhC matrix was a triangular array of holes with a period of 400 nm and a hole diameter of 240 nm, corresponding to an air filling factor of 33%. Three rows of holes were removed along the ΓK direction to serve as a W3 line defect. Four PhC section lengths, ranging from 60 to 240 rows were designed. The W3 PhC waveguide was inserted between two access ridge guides, whose width was 1.45 μm. The ridges and the PhC holes were etched during the same run using an ICP Cl_2/Ar plasma with the optimized conditions reported in section 3.5.2. Figure 3.20 shows the transition region between access ridge and W3 PhC waveguide. The etched depth was 4 μm in the access ridge region and 2.8 μm for the PhC holes.

The light propagation losses measurement within the PC waveguide was realized using an external tunable light source and the Fabry-Perot resonance technique [Talneau2001]. This approach is fully independent of the coupling efficiency between the fiber and the access ridge guide. The access ridge demonstrated a propagation losses value of 15 dB/cm, a correct one for the deeply etched ridges, which revealed the smooth sidewalls in the etched profiles. The propagation losses in the W3 PhC waveguide exhibited a value of 80 dB/cm. From the calculation, it has been reported that a low optical losses value could be obtained when the PhC holes are etched through an InP/InGaAsP/InP planar waveguide with a etch depth more than 2 μm [Ferrini2003], and with vertical and smooth sidewalls. For PhC holes etched using an ICP Cl_2/Ar plasma presented in this dissertation, the etch depth could reach 2.8 μm for 240 nm-diameter holes with nearly vertical sidewalls. Therefore, the propagation losses were considered to be mainly attributed to the residual sidewall roughness [Bae2003], as can be testified in figure 3.17(b).

Up to date, the propagation losses for W3 PhC InP/InGaAsAsP/InP planar waveguides etched by other plasma sources have also been reported. A value of 100 dB/cm was obtained by M. Mulot while using a CAIBE Ar/Cl_2 etching process [Mulot2003]. A smaller propagation losses value can be obtained when the InGaAsP core layer is thicker. Values of 18 dB/cm by a CAIBE Ar/Cl_2 process

[Kotlyar2004b] and 15 dB/cm by ECR-RIE Cl_2/Ar process [Zimmermann2004] were found for 1600 nm- and 900 nm-thick guiding layers, respectively. However, higher order modes transmissions may be sustained as well in the case of thick guiding layer.

The free-carrier lifetime for InP/InGaAsP multiple quantum-wells with PhC holes structures etched using the ICP Cl_2/Ar plasma is in the order of 100∼150 ps, relative to 3∼6 ns for regions without PhC structures. The lifetime value can be prolonged by reducing the formation of defects along the etched hole sidewalls.

The light propagation losses exhibits a value of 80 dB/cm for a W3 PhC InP/InGaAsP/InP channel defect waveguide. This value is expected to be reduced by suppressing the surface roughness due to the ICP Cl_2/Ar plasma etching.

3.6 ICP $Cl_2/BCl_3/N_2$ and BCl_3/N_2 plasma for smooth sidewall surfaces

The ICP Cl_2/Ar plasma has been reported in the section 3.5 for the intention of deep etching in small-hole features. The addition of Ar can ignite plasma more easily abd provide positive ions for the efficient sputtering. The results present a good selectivity between InP and SiO_2 mask (∼18:1), which favors the fabrication of 2D PhC planar devices. Nevertheless, the residual sidewall roughness could not be suppressed completely by optimizing the etching conditions, as shown in figure 3.17(b). It is known that not only the limited etch depth, but the surface roughness also contributes partly to the optical propagation losses in 2-D PhC channel defect waveguides. Therefore, the suppression of surface roughness or the minimization of etch-induced damages are required to be investigated.

The concept of sidewall passivation was at first introduced to enhance the etched feature anisotropy. By passivating the sidewall surfaces, the lateral etching can be prevented; but, the etching persists in the vertical direction since the bottom surface is exposed to the ion bombardment. Inheriting this idea, the passivation along the PhC etched sidewalls is expected to suppress the surface roughness by balancing the etch rates for In and P under the chlorine-containing plasmas. Several approaches have been studied and proposed to passivate the sidewall surfaces during PhC structures etching. One was to introduce N_2 into a Cl_2/Ar plasma [Strasser2007]; others were to employ other plasma chemistry mixtures (e.g. Cl_2/O_2 [Carlstrom2006] and Cl_2/N_2 [Combrie2005].

The addition of N_2 gas is considered to improve the anisotropic etching and to suppress the sidewall roughness [Miyakuni1995, Carlstrom1999, Frost1998] by the

help of passivation through the formation of In-N, N-P, and In-N-P bonds. Moreover, with this passivation layer, the P deficiency issue [Pearton1990] which occurs frequently in the chlorine-containing plasmas might be minimized. S. Miyakuni has demonstrated that vertical InP ridge profiles with smooth surface can be obtained using an ECP Cl_2/N_2 plasma. P. Strasser also noticed that the addition of N_2 into a ICP Cl_2/Ar plasma might prevent the undercut occurring on the top of PhC holes [Strasser2007], even though the surface roughness seemed not to be reduced remarkably. In the reactive ion beam etching (RIBE), the utilization of nitrogen ion beam has been reported to result in smooth and less-damaged surfaces on InP [Katzschner1986, Gortz1995, Iber1997, Dinges1991, Frost1998].

In addition to Cl_2, BCl_3 is another gas source of providing the chlorine radicals and is under consideration within this dissertation for the PhC holes etching. The Cl_2/BCl_3 plasma discharge was used at first for III-V materials ridge structures etching and it yielded a higher etch rate compared to a pure Cl_2 plasma. Further, the anisotropy was improved as well largely [Franz1998, Franz2001]. The addition of BCl_3 into a Cl_2 plasma might generate both the reactive species and the heavy ions. Under the electric field acceleration, those oriented heavy ions can lead to energetic ion bombardment and improve the anisotropy.

Based on the statements mentioned above, the ICP $Cl_2/BCl_3/N_2$ and BCl_3/N_2 plasmas were adopted within this dissertation for the InP PhC holes etching to reach our expectations of roughness suppression and features verticality enhancement. In the following series of experiments, the etching conditions of $Cl_2/BCl_3/N_2$ and BCl_3/N_2 plasmas would be investigated with the variations of N_2 and BCl_3 ratios. The existence of passivation in our specific plasma and feature conditions would also be verified. By measuring the positive ion flux in the plasma, we might be able to estimate the ion sputtering during the etching. Finally, the free-carriers lifetime is measured for a multiple quantum-wells structure with PhC holes fabricated by an optimized BCl_3/N_2 plasma and compared to the one fabricated by a Cl_2/Ar plasma.

3.6.1 Evolutions of N_2 and BCl_3 in PhC holes structures etching

To investigate the roles of N_2 and BCl_3 on the etched PhC hole profiles, a series of etching experiments with variations of N_2 and BCl_3 ratios were realized on n-doped InP substrates with a 250 nm-thick SiO_2 layer as the mask. The rf power injected into the inductively coupled plasma source (ICP power, P_{ICP}), the self-induced dc bias voltage ($|V_{bias}|$), and the total gas pressure (p) were maintained at 1000 W, -200 V, and 5 mTorr, respectively. The electrode temperature was set as 190^0C during the whole etching process in order to facilitate the volatilization of the chemical reactant $InCl_x$ [McNevin1986]. For convenience, the Cl_2, BCl_3, and N_2 mass flow rates respect to the total gas flow are designated as $\%Cl_2$, $\%BCl_3$, and

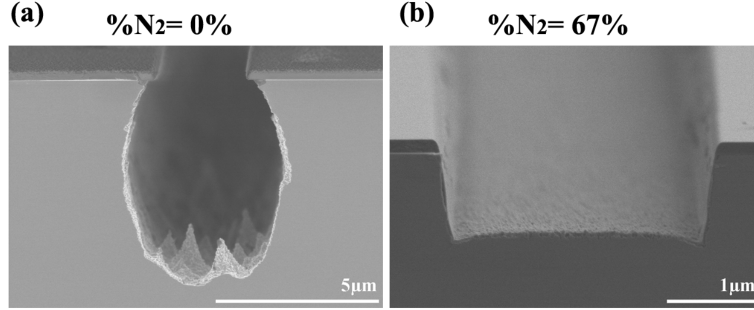

Figure 3.21: SEM cross-section views of 3 μm-wide trenches etched by (a) an ICP Cl_2/BCl_3 (33/16 sccm) plasma at 0 V-bias voltage and (b) an ICP $Cl_2/BCl_3/N_2$ plasma with 67%-N_2 at -200 V-bias voltage.

%N_2. In $Cl_2/BCl_3/N_2$ and BCl_3/N_2 plasmas, since the maximum etch depth was not pursued for applications of suspended membranes, the etch time was limited on purpose to be less than two minutes in order to minimize the profile deformations due to the mask erosion.

A. N_2 ratio in $Cl_2/BCl_3/N_2$ plasma vs. etched PhC hole profiles

The etched profiles with the evolution of N_2 ratios (%N_2, N_2 mass flow rate/total gas flow) in a $Cl_2/BCl_3/N_2$ plasma were studied when the mass flow rates of Cl_2 and BCl_3 were fixed at 33 sccm and 16 sccm, respectively. The N_2 mass flow rate then varied between 0 and 99 sccm, corresponding to 0% $\sim$ 67%-N_2. A remarkable improvement on the feature anisotropy due to the N_2 is presented in figure 3.21 on a trench pattern. In figure 3.21(a), a 3 μm-wide trench was etched using a Cl_2/BCl_3 plasma (i.e. 0%-N_2) with $|V_{bias}| = 0$. A high selectivity (InP: SiO_2) more than 600:1 was obtained, which once verified the advantage of etching InP materials using a chlorine-based plasma. Under these conditions, the chemical etching played an important role; the etched profile thus presented a bowing shape and the etched surfaces were extremely rough. The grass situating especially on the bottom was considered to be composed of the In or $InCl_x$ droplets which have been reported

ICP power (W)	1000
Bias voltage (V)	-200
Gas pressure (mTorr)	5
Cl_2 : BCl_3 mass flow (sccm)	33 : 16
N_2 mass flow (sccm)	**0~99 (0%~67%)**
Electrode temperature (^{0}C)	190

Table 3.9: The investigated N_2 ratio range and other etching conditions for $Cl_2/BCl_3/N_2$ plasmas.

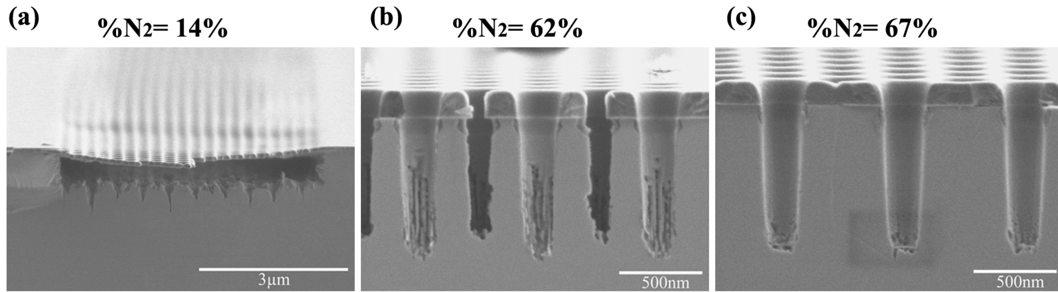

Figure 3.22: SEM cross-section views of PhC holes etched by ICP $Cl_2/BCl_3/N_2$ plasmas with various N_2 ratios: (a) 14%, (b) 62%, and (c) 67%. The Cl_2 and BCl_3 mass flow rates were fixed at 33 and 16 sccm, respectively.

in the literatures. With the addition of N_2, the anisotropic etching can be largely improved. As shown in figure 3.21(b) where the $\%N_2$ was 67% and the $|V_{bias}|$ was 200 V, the trench pattern was well transferred from SiO_2 mask to InP substrate. The etched surfaces were also much smoother in a high $\%N_2$ environment; however, the selectivity diminished to less than 9.

In PhC hole structures, the similar trend with $\%N_2$ was observed as well with other fixed etching conditions shown in table 3.9. When the $\%N_2$ was inferior to 30%, the isotropic etching was dominant, as shown in figure 3.22(a). It should be noted that, in PhC holes, only one hundred nanometers of lateral etching is hazardous and would merge all the holes. As a result, a suspended SiO_2 mask was left on the top. With the increase on $\%N_2$, the anisotropy was improved noticeably, as in figure 3.22(b) where the $\%N_2$ was 62%. The PhC patterns were well transferred from mask to InP substrate, but the sidewall surfaces still stayed rough on the bottom of holes. The smooth sidewall was finally obtained in the case of 67%-N_2, as shown in figure 3.22(c), with an etch depth of ~880 nm for 240

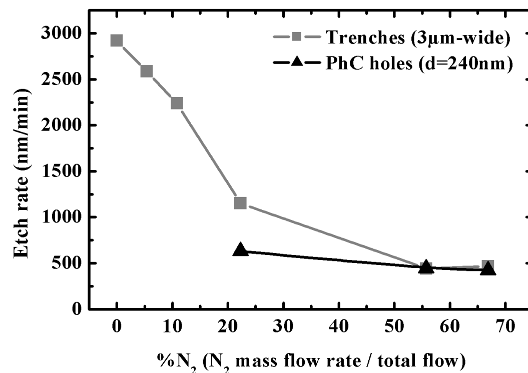

Figure 3.23: The InP etch rates for 3 μm-wide trenches (square) and 240 nm-diameter PhC holes (triangle) etched by $Cl_2/BCl_3/N_2$ plasmas with various N_2 ratios.

nm-diameter holes. The slight roughness situating at the bottom of PhC holes was due to the ion bombardment.

The InP etch rate in trenches and PhC holes with variation of $\%N_2$ is plotted in figure 3.23. Since the etch depths in the merged PhC hole patterns could not be determined when $\%N_2$ was less than 30%, only the etch depths of trenches were recorded. In general, the etch rate decreased with the increase of $\%N_2$ in a $Cl_2/BCl_3/N_2$ plasma. There was no visible etch rate difference between the trench and the PhC hole features when $\%N_2$ was more than 55%. With the decrease of $\%N_2$, the aspect-ratio dependent etching (ARDE) effect appeared.

B. BCl_3 ratio in $Cl_2/BCl_3/N_2$ plasma vs. etched PhC hole profiles

Some samples were also etched with variation of BCl_3 ratio ($\%BCl_3$, BCl_3 mass flow rate/total gas flow) when the Cl_2 and N_2 mass flow rates were maintained at 33 sccm and 99 sccm, respectively. With other fixed parameters mentioned in table 3.10, the BCl_3 mass flow rate varied between 0 and 24 sccm, i.e. 0% ∼ 15%-BCl_3. Figure 3.24(a) shows the etched PhC holes while $\%BCl_3$ was 0%. The sidewall surfaces were very smooth under the SEM examination; though the etching rate was low (∼325 nm/min) and the profile was conical with a $\sim6^0$ inclination angle from the plumb line. Compared to the PhC hole structures etched by a pure Cl_2 plasma which presented an isotropic profile similar to figure 3.22(a), the diminished lateral etching owing to the addition of N_2 was once verified.

On the contrary, when $\%BCl_3$ was increased to ∼11%, a pronounced improvement on profile verticality was obtained, as shown in figure 3.24(b), with a $\sim3^0$ inclination angle. In this case, the etch rate was 420 nm/min for 240 nm-diameter holes and the InP : SiO_2 selectivity was more than 8. But, the bottom of the profile appeared lumpy to some extent. With further increasing BCl_3 ratio to 15%, the etch rate increased to 450 nm/min and the verticality was improved to have only a $\sim1^0$ inclination angle, as shown in figure 3.24(c). Unfortunately, the sidewall surface on PhC structures became rougher. This trend of roughness was similar to figure 3.22(b), where the $\%N_2$ was slightly less than the optimized ratio. In figure 3.25, it is found that the InP etch rate increases almost linearly with BCl_3 ratios in $Cl_2/BCl_3/N_2$ plasmas for both trenches and PhC holes features.

ICP power (W)	1000
Bias voltage (V)	-200
Gas pressure (mTorr)	5
Cl_2 : N_2 mass flow (sccm)	33 : 99
BCl_3 mass flow (sccm)	**0∼24 (0%∼15%)**
Electrode temperature (^{0}C)	190

Table 3.10: The investigated BCl_3 ratio range and other etching conditions for $Cl_2/BCl_3/N_2$ plasmas.

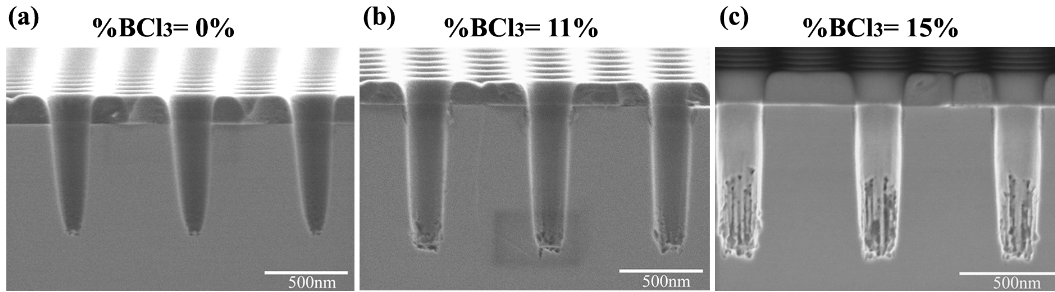

Figure 3.24: SEM cross-section views of PhC holes etched by ICP $Cl_2/BCl_3/N_2$ plasmas with various BCl_3 ratios: (a) 0%, (b) 11%, and (c) 15%. The Cl_2 and N_2 mass flow rates were fixed at 33 and 99 sccm, respectively. (d) The InP etch rates for 3 μm-wide trenches (square) and 240 nm-diameter PhC holes (triangle) with various BCl_3 ratios.

The sidewall roughness is often coming from the unequal etch rates, through the sputtering and the chemical etching by the chlorine radicals, between In and P. In a Cl_2/N_2 plasma, as shown in figure 3.24(a), a certain balance might be achieved and leaded to smooth sidewall surface. However, the sputtering might be deficient slightly, it then would cause a lower etch rate and a conical profile. In a BCl_3-containing plasma, except the chlorine radicals, Cl_2^+ and Cl^+ ions, the BCl_3^+, BCl_2^+, BCl^+ may also exist in the plasma. When BCl_3 was added into the Cl_2/N_2 plasma, the minority species, like BCl_3^+, BCl_2^+, BCl^+, can assist the removal of InP materials and chemical reactants through the sputtering. As in figure figure 3.24(b), with 11%-BCl_3, the profiles were found to be more vertical than in 0%-BCl_3, while the smooth sidewall surfaces could still be sustained. At a higher %BCl_3, ~15%, the elevated amount of positive ions and chlorine radicals brought damages on the surfaces.

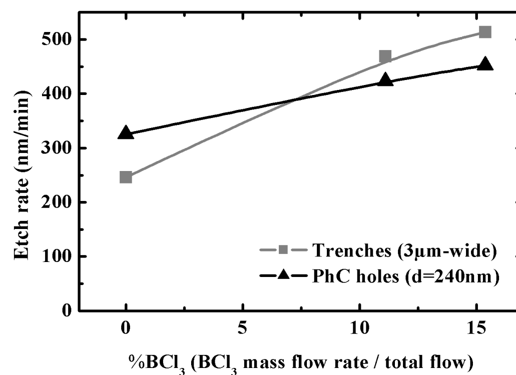

Figure 3.25: The InP etch rates for 3 μm-wide trenches (square) and 240 nm-diameter PhC holes (triangle) etched by $Cl_2/BCl_3/N_2$ plasmas with various BCl_3 ratios.

For the InP PhC holes etching using a $Cl_2/BCl_3/N_2$ plasma:

– N_2 is demonstrated to inhibit largely the lateral etching and lead to smooth sidewall surfaces when the N_2 ratio is more than 65%.

– BCl_3 is shown to improve the feature verticality and to increase the etch rate. With BCl_3 ratio variation from 0% to 15%, the sidewall inclination angle diminishes from 6^0 to 1^0 and the etch rate increases 38%. A higher BCl_3 ratio may cause as well the surface damages.

3.6.2 ICP $Cl_2/BCl_3/N_2$ plasma characterization: positive ion current density measurement

By knowing the positive ion fluxes in the plasma, we are able to estimate the ionic sputtering during the etching process. The positive ion fluxes in $Cl_2/BCl_3/N_2$ plasmas with variation of parameters including the ICP power, the total gas pressure, and the gas contents were measured using a rf planar electrostatic probe [Braithwaite1996] provided by P. Chabert from LPTP (Laboratoire de Physique et Technologie des Plasmas). The probe was located on the chamber wall, about 15 cm away from the sample in the same horizontal plane. The reference setting was chosen as the $Cl_2/BCl_3/N_2$ plasma with gas flow rates of 33/16/99 sccm (i.e. 22%-Cl_2, 11%-BCl_3, 67%-N_2) and p = 5 mTorr, P_{ICP} = 1000 W. The evolution of positive ion current density with each parameter was recorded while keeping other parameters constant and identical to the reference setting.

Figure 3.26(a) shows the evolutions of positive ion current density with the ICP power and the total gas pressure. The measured ion flux was found to increase linearly with ICP power while operating in the high density inductive mode. With the increase of ICP power from 200 W to 1000 W (400% increase rate), the accompanying change in the positive ion current density was from 0.241 to 1.41 mA/cm^2, corresponding to 485% increase rate. With an opposite behavior, the positive ion current density decreased with the increase of total gas pressure. When the total gas pressure increases, the probability of collision and recombination between particles also increases due to the reduced average mean free path. Therefore, positive ions would be neutralized more quickly in a higher gas pressure.

Figure 3.26(b) presents the evolutions of positive ion current density with Cl_2, BCl_3, and N_2 gas ratios. The ratio of one gas varied when the mass flow rates of two other gases were fixed as mentioned above. The positive ion current density was found to increase monotoncially with Cl_2 and BCl_3 ratios; but, a saturation was found when the BCl_3 ratio was about 35%. While introducing N_2 into the Cl_2/BCl_3 plasma, the positive ion current density increased rapidly from 1.45 mA/cm^2 to the maximum value of 1.87 mA/cm^2 at 19%-N_2. Later, it decreased when %N_2 was more than 20%.

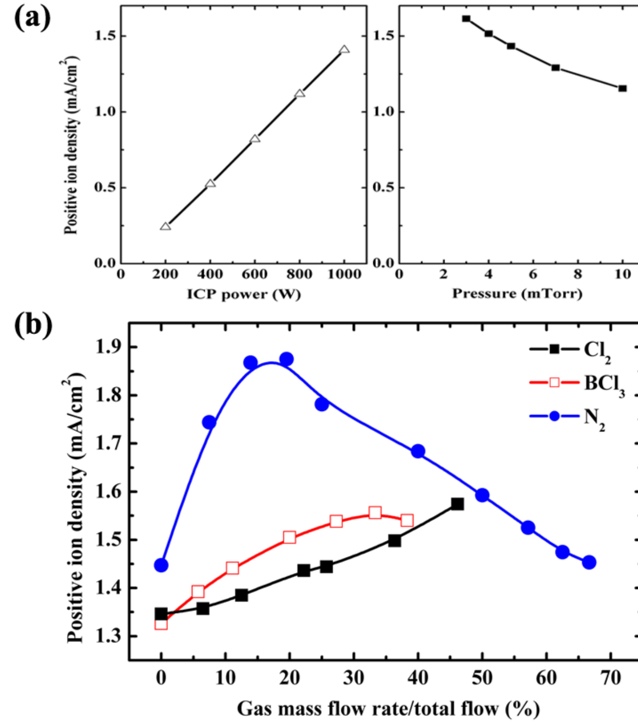

Figure 3.26: The evolutions of positive ion current density with (a) the ICP power (triangle; p = 5 mTorr) and the total gas pressure (square; P_{ICP} =1 000 W) in a $Cl_2/BCl_3/N_2$ (33/16/99 sccm) plasma, (b) the Cl_2 ratio (black square; F_{BCl3} = 16 sccm and F_{N2} = 99 sccm), the BCl_3 ratio (red empty square; F_{Cl2} = 33 sccm and F_{N2} = 99 sccm) and the N_2 ratio (blue circle; F_{Cl2} = 33 sccm and F_{BCl3} = 16 sccm) in a $Cl_2/B_{Cl3}/N_2$ plasma with p = 5 mTorr and P_{ICP} = 1000 W.

From the literatures, it has been reported that N_2 can enhance the dissociation rate of BCl_3 [Constantine1995, Ren1996a]. The excess nitrogen radicals may react with boron to form boron-nitrogen (BN), which liberates the chlorine radicals that could in turn form positive ions. The increases in the intensities of Cl^+ and Cl_2^+ emission had been observed in an ECR BCl_3/N_2 plasma using optical emission spectroscopy (OES) by F. Ren [Ren1996b]. H. S. Kim et al. have identified the positive ions in an ICP Cl_2/BCl_3 plasma using quadrupole mass spectrometer (QMS) [Kim1999]. And it was found that, in a Cl_2-rich gas mixture, the Cl_2^+ was the main ion species and BCl_2^+ was the second most one. Besides these two positive ion species, Cl^+, BCl_3^+, and BCl^+ were observed as well, but in a smaller amount. With the increase of BCl_3 ratio in a Cl_2/BCl_3 plasma, the total ion amount had only a slight decrease and the BCl_2^+ ion became the main species in the plasma.

On another side, it has also been demonstrated that the addition of N_2 to a Cl_2 plasma could increase the electron temperature (T_e) and leaded to an decrease in

the electron density and the total positive ions density [Kim2005]. Our measurement of positive ion current density in the $Cl_2/BCl_3/N_2$ plasma with N_2 ratio is consistent with this trend when $\%N_2$ is more than 20%. As for the abrupt increase on the positive ion current density from 0% to 20%-N_2, it might be attributed to the enhancement of BCl_3 dissociation rate by N_2, as observed by F. Ren.

Within the $Cl_2/BCl_3/N_2$ plasma, except the Cl^+ and Cl_2^+ ions, BCl_3^+, BCl_2^+, and BCl^+ are also the possible positive ions existing in the plasma. Compared to Cl^+ and Cl_2^+, even though the amount of BCl_3^+, BCl_2^+ might be relatively small, their molecule mass are large and can contribute to ionic sputtering and enhance the desorption of $InCl_x$ products significantly. When BCl_3 is added in a Cl_2/N_2 plasma, not only the amount of heavy positive ions increases, but the amount of total positive ions might also augment partly due to the N_2-enhanced BCl_3 dissociation rate. Moreover, BCl_3 can provide as well the chlorine radicals. Based on these reasons, the InP etch rate was observed to increase with BCl_3 ratio, as discussed in section 3.6.1-B.

In $Cl_2/BCl_3/N_2$ plasmas, the positive ion current density is found to

– increase linearly with the ICP power since the dissociation and ionization rates are influenced directly by the applied power.

– decrease with the total gas pressure since the probability of collision and recombination between particles increases due to the reduced average mean free path; and the positive ions are thus neutralized more easily.

– increase with the Cl_2 ratio due to the abundant supply of Cl_2^+ and Cl^+ ions.

– increase with the BCl_3 ratio due to the supply of positive ions. The N_2-enhanced BCl_3 dissociation might also provide the positive ions. But, a saturation is reached when BCl_3 ratio is about 35%.

– increase with the N_2 ratio till 20%. It is probably attributed to the N_2-enhanced BCl_3 dissociation.

– decrease with the N_2 ratio while more than 20%.

3.6.3 ICP BCl_3/N_2 plasma: elimination of undercut

For the $Cl_2/BCl_3/N_2$ plasmas, the formation of undercut was observed at times. A representative undercut situating on the top of holes is presented in figure 3.27(a). The etching was realized using an ICP Cl_2/N_2 (33/99 sccm) plasma with p = 5 mTorr, P_{ICP} = 1000 W, and $|V_{bias}|$ = 200 V. This lateral etching is probably attributed to the combined effects of the ions with divergent angles [Ying1997],

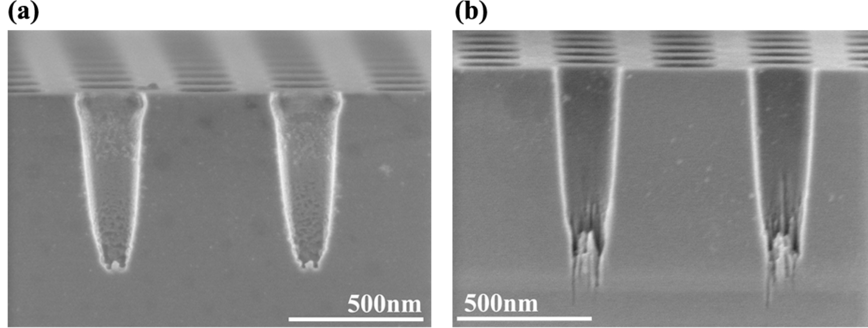

Figure 3.27: SEM cross-section views of PhC holes etched by (a) a Cl_2/N_2 (33/99 sccm) plasma with p = 5 mTorr, P_{ICP} = 1000 W, $|V_{bias}|$ = 200 V, (b) a BCl_3/N_2 (24/99 sccm) plasma with p = 5 mTorr, P_{ICP} = 1000 W, $|V_{bias}|$ = 350 V. The SiO_2 mask was removed in both cases.

the sloped mask [Ohki1987] and the chemical reaction favored by chlorine radicals [Kotlyar2004a]. It is known that positive ions and radical densities rise in high ICP power state. Instead of a single direction perpendicular to the surface, the ions might impinge on the sample surface with a certain direction distribution. Morever, in a slightly elevated working gas pressure, ex: 5 mTorr in our case, the direction distribution of positive ions might be further extended. In addition, the ions may be scattered by the sloped mask and then impinge on the upper part of PhC holes. The ion sputtering can speed out the removal of chemical reactants along the surface and so that the InP is exposed to the chlorine radicals for the subsequent chemical reactions. Further, owing to the specific isolated hole structures, the local chlorine radical density is considered to be higher on the top of holes which provides source for the chemical reactions.

Based on these arguments, the undercuts were found under our etching conditions. Hence, we modified the plasma chemistry compositions and other parameters in order to eliminate the undercut which can degrade the PhC device performances. The Cl_2 was taken away and therefore BCl_3 turned to be the only source to provide the chlorine radicals for chemical etching. In general, the dissociation rate of BCl_3 is lower than that of Cl_2 under the same plasma conditions. But, in our case, the

ICP power (W)	1000
Bias voltage (V)	-350
Gas pressure (mTorr)	5
BCl_3 : N_2 mass flow (sccm)	24 : 99
Electrode temperature (^{0}C)	190

Table 3.11: The etching conditions of BCl_3/N_2 plasma adopted to eliminate the undercut.

concentration of neutral chlorine in a BCl_3/N_2 plasma was hard to be evaluated and compared to Cl_2/N_2 and $Cl_2/BCl_3/N_2$ plasmas without further measurements since the addition of N_2 has been reported to increase the dissociation rate of BCl_3 and generate chlorine radicals. However, it is believed that the heavy BCl_2^+ and BCl_3^+ ions concentrations in a BCl_3/N_2 plasma should be higher than the other two gas mixtures. These heavy ions can be served for the efficient sputtering and may improve the feature verticality.

A BCl_3/N_2 plasma process was then studied with the mass flow ratios of 24 sccm-BCl_3 and 99 sccm-N_2 to attain anisotropic profiles. The P_{ICP} was kept as 1000 W as before, but the rf power was further increased to maintain $|V_{bias}|$ as 350 V because an elevated ion energy is preferential for vertical profile etching. Under these conditions (table 3.11), the positive ion current density was measured to be 1.45 mA/cm^2. The etched PhC hole profiles are presented in figure 3.27(b), in which the etch rate was 530 nm/min and the selectivity was 8 for 250 nm-diameter holes. The smooth sidewall surfaces were found till 350 nm-deep from the top surface without undercut. In this process, a high ion energy was chosen without introducing the surface damages on the sidewalls. The roughness on the bottom surface was due to the severe ion sputtering with an elevated ion energy. For applications of InP PhC membrane waveguide that will be introduced in chapter 6, this roughness situating on the bottom has no impact on the device performances after all the fabrication steps.

The undercut occurred at times while using $Cl_2/BCl_3/N_2$ and Cl_2/N_2 plasmas can be eliminated through replacing Cl_2 completely by BCl_3 and increasing the ion energy. The presence of BCl_3 mainly provides the chlorine radicals and the heavy positive ions (ex: BCl_2^+ and BCl_3^+), which may enhance the feature verticality. The BCl_3/N_2 proportion is delicate since a higher BCl_3 ratio would cause the surface damages; and a lower etch rate and a less-vertical feature profile would be expected when BCl_3 amount is insufficient.

3.6.4 Etched surface characterization: TEM-EDX analysis

In order to clarify the existence of passivation layer during the etching and further identify its composition, the sidewall surfaces of PhC holes in InP/InGaAs heterostructure etched by ICP N_2-based (BCl_3/N_2 and Cl_2/N_2) plasmas were analyzed by transmission electron microscopy equipped with energy dispersive X-ray analysis (TEM-EDX). The sample consisted of a 775 nm-thick InGaAs layer grown on a n-doped InP substrate by MOVPE, followed by a 340 nm-thick InP layer. After the ICP etching, the sample was cleaved through PhC holes, mounted on the

holder by the glue, polished mechanically, and thinned using ion beam milling for the TEM observation.

A. PhC holes structure etched by ICP BCl_3/N_2 plasma

The TEM cross-section views of PhC holes passing through the InP and InGaAs layers are shown in figure 3.28(a)-(c) with SiO_2 mask left on the top. The etching was performed using an ICP BCl_3/N_2 plasma with conditions (24 sccm-BCl_3, 99 sccm-Cl_2, p = 5 mTorr, P_{ICP} = 1000 W, and $|V_{bias}|$ = 270 V). Since the holes were filled completely with the mounting epoxy glue, which was a material with a brighter contrast compared to the SiO_2 mask and the semiconductor materials, the confusion of the material identification would not occur. From figure 3.28(b), we observed that the PhC hole sidewall was inclined with an angle of 4.7^0 from the plumb line and that there was no visible etching divergence in lateral direction between InP and InGaAs layers, which indicated that these etching conditions were advantageous for the InP-based heterostructure etching. As shown in figure 3.28(c), the magnification of sidewall surface on InP layer, the surfaces were perfectly smooth and no roughness was observed till the order of few nanometers.

Along the InP and InGaAs sidewalls, we observed a very thin amorphous layer with a thickness inferior to 2 nm, as indicated by arrows in figure 3.28(c). Through the EDX analysis, this layer consisted of silicon and oxygen; but, no nitrogen was found. The re-deposition of silicon might either come from the dielectric mask (SiO_2) or from the sample carrier (Si wafer) during the ICP-RIE etching. The presence of oxygen might be due to the surface oxidation once the sample was exposed under the atmosphere. Since this amorphous layer was very thin and situated closely to the InP and InGaAs layers, it was not possible to identify the existences of In, P, Ga, or As. It should be emphasized that, from our EDX analysis, the nitrogen element was found neither within this thin amorphous layer nor on the mask surface.

It has been reported in the literatures that the nitridation is likely to occur on the InP surfaces under the N_2-containing plasmas. The nitridation products may take place through the formation of $InPN_x$ [Soukiassian1992], InN [Pan1996], or In-N, In-N-P, P-N bonding [Suzuki2000] relying on the conditions of nitrogen ion beams. S. Miyakuni has observed as well the reactants of InN and P_3N_5 using X-ray photoelectron spectroscopy (XPS) on InP large-area surfaces after the Cl_2/N_2 ECR plasma etching. However, from our TEM-EDX analysis, no nitrogen was identified along the hole sidewalls; and it then suggests that, under our specific plasma conditions, the nitridation may not be anticipated on InP surfaces during the etching.

B. PhC hole structures etched by ICP Cl_2/N_2 plasma

For comparison, another InP/InGaAs heterostructure sample with PhC holes patterns was etched using an ICP Cl_2/N_2 plasma with 33 sccm-Cl_2, 99 sccm-N_2,

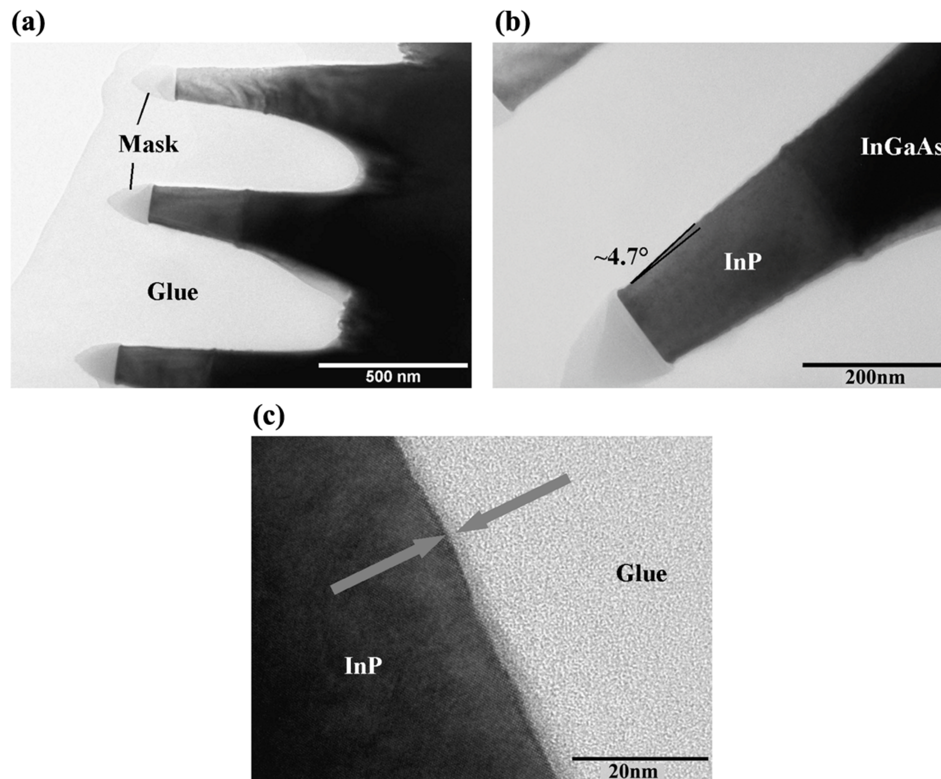

Figure 3.28: TEM images of etched PhC holes in InP/InGaAs heterostruture by an ICP BCl_3/N_2 plasma: (a) enlarged view of the PhC holes, (b) magnification on the sidewalls and the InP/InGaAs interface, and (c) magnification on the InP sidewall surface.

p = 5 mTorr, P_{ICP} = 1000 W, and $|V_{bias}|$ = 200 V. As presented in figure 3.29(a) and (b), the PhC hole sidewall had an inclination angle of $\sim 11^0$ in InP layer after etching; furthermore, the unequal etch rates between InP and InGaAs layers were observed in the lateral direction. From the undercut situating on the top of InGaAs layer, it signified that the etching realized using this Cl_2/N_2 plasma was more isotropy-dominated than using the BCl_3/N_2 plasma (section 3.6.4-A).

Between the semiconductor materials and the glue, an amorphous layer was observed and indicated by the arrows in figure 3.29(c) and (d). It situated mainly along the surfaces of the SiO_2 mask and the InP layer, and it was found as well on the InGaAs layer sidewalls and on the interface of SiO_2 mask and InP layer, but not at the bottom of PhC holes. Its thickness was in the order of 25 nm along the InP section (figure 3.29(c)) and diminished to 3 nm on the InGaAs section (figure 3.29(d)). The quantitative composition analysis through EDX presented a major concentration of 74%-phosphor (P) in this amorphous layer. In addition, it contained oxygen (O), indium (In), and chlorine (Cl) elements with an atomic percentage of 19%, 4%, and 3%, respectively. Examining the SiO_2 mask, InP

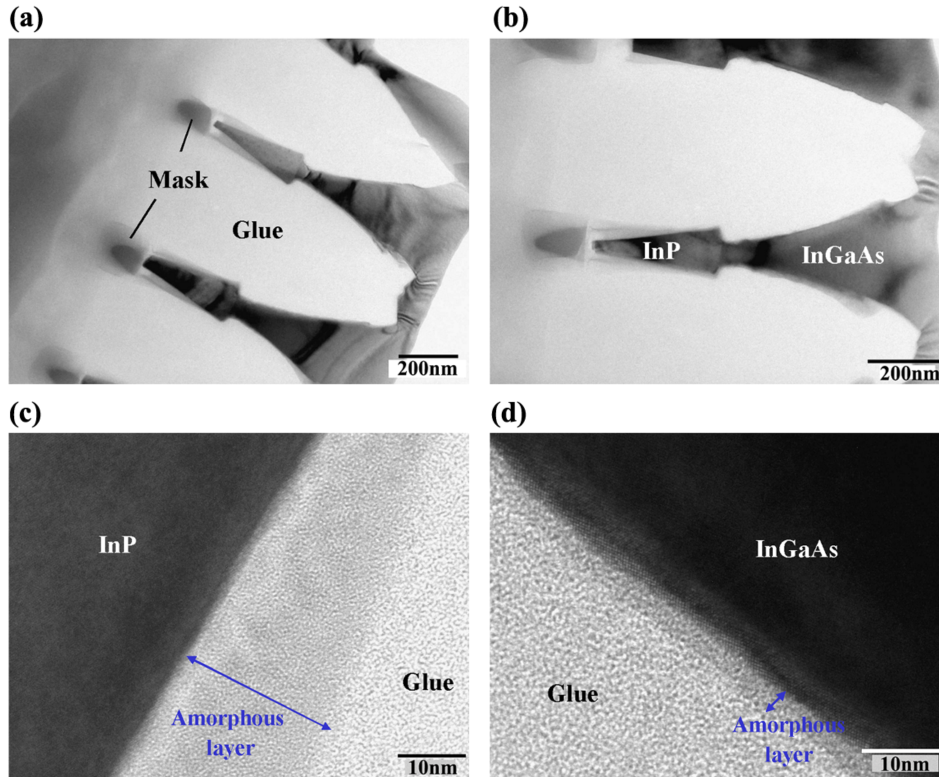

Figure 3.29: TEM images of etched PhC holes in InP/InGaAs heterostruture by an ICP Cl_2/N_2 plasma: (a) enlarged view of the PhC holes, (b) magnification on the InP/InGaAs interface, (c) magnification on the InP sidewall surface, and (d) magnification on the InGaAs sidewall surface.

and InGaAs sidewall surfaces, the nitrogen element was not identified from EDX analysis and it thus suggested that the nitridation was not occurring either under these ICP Cl_2/N_2 plasma conditions. Our result is similar to another one realized on InP-based isolated patterns including ridges and micro-pillars etched using an ICP $Cl_2/H_2/N_2$ plasma [Bouchoule2008]. In which, the passivation layer was observed along the InP-based materials and was consisted mainly of Si, O, and P, but nitrogen was never found.

With the observation of P within the amorphous layer along the InGaAs layer and the SiO_2 mask surfaces, it was then believed that the phosphor etched in InP layer was transported and deposited on InGaAs and mask surfaces during the etching. However, from figure 3.29(b), this P-enriched amorphous layer with a thickness of 15 nm was found below the mask. Usually, this region was in contact with the mask and was not exposed directly to the plasma. Hence, we suspect that In might diffuse during etching, which leaded to this P-enriched amorphous layer.

It should be noted that this P-enriched amorphous layer was not observed under

the ICP BCl_3/N_2 plasma (section 3.6.4-A), a similar gas mixture as Cl_2/N_2. Till now, the formation mechanism of P-enriched amorphous layer is not known yet and it requires further investigations to clarify the causes of the indium diffusion and the preferential phosphor re-deposition under the ICP Cl_2/N_2 plasma.

The sidewall surfaces etched using the ICP BCl_3/N_2 plasma present a perfectly smooth state and no passivation layer is formed during the etching. On the contrary, a P-enriched amorphous layer is found along the sidewall surfaces and on the mask while the etching is realized under the ICP Cl_2/N_2 plasma.

3.6.5 Discussion

From the TEM-EDX analysis, the surfaces passivation during the etching is proved not to be through the nitridation within our specific plasma conditions. Therefore, the lateral etching reduction and roughness suppression within the PhC holes due to the presence of N_2 in Cl_2/BCl_3 and BCl_3 plasmas are then more probably attributed to the dilution of chlorine radicals. In a lower chlorine radical concentration, the global InP etch rate diminished; but, the chemical etch rate difference between In and P might not be so evident due to a limited chlorine radical supply and the etched surfaces are thus smoother.

For the experiments investigating the evolution of N_2 ratio, the total gas flow is not kept constant and the species thus have a longer residence time in the plasma when N_2 ratio decreases. Due to a longer residence time, plus an abundant chlorine radical supply, the isotropic etching dominates in the low N_2 ratio environment, as shown already in figure 3.22(a). With the increase on N_2 ratio, the isotropic etching is eased and thus the anisotropic profiles can be obtained. The diminution of InP etch rate in high N_2 ratio (figure 3.23) is then mainly due to the dilution and the shorter residence time of chlorine radicals, as well as a reduced positive ion current density (figure 3.26(b)).

Following the same concept, the achievement of smooth sidewall surfaces in PhC holes under the BCl_3/N_2 plasma is also due to the dilution of chlorine neutral radicals in the plasma. The improved feature verticality is attributed to the presence of heavy positive ions including BCl_3^+ and BCl_2^+, which might probably enhance as well the desorption of $InCl_X$ and the sputtering rate of In.

From the TEM-EDX analysis, it is found that the passivation through nitridation does not occur during the ICP N_2-based plasma etching. The fact of lateral etching reduction and roughness suppression within the PhC holes due to the presence of N_2 in a chlorine-containing plasma is more probably attributed to the dilution of chlorine radicals.

Based on the litteratures, our etching experiments, and etched surface characterization, we consider several possible representative etching reactions which may occur during the etching of InP materials under an ICP BCl_3/N_2 plasma, as shown schematically in figure 3.30. In a BCl_3/N_2 plasma, the neutral species may include Cl, Cl_2, and N_2; and the positive ions may contain Cl^+, Cl_2^+, BCl_3^+, BCl_2^+, BCl^+ and N_2^+. The possible reactions are as follows:

1. Formation and vaporization of $InCl_x$ and PCl_x etch products.
2. Sputtering of In and P by Cl_2^+, Cl^+, and N_2^+ ions.
3. Ion-assisted chemical desorption of $InCl_x$, PCl_x, In, and P by Cl_2^+, Cl^+, and N_2^+ ions.
4. Sputtering of In and P by BCl_3^+, BCl_2^+, and BCl^+ ions.
5. Ion-assisted chemical desorption of $InCl_x$, PCl_x, In, and P by BCl_3^+, BCl_2^+, and BCl^+ ions.

A main difference between a Cl_2/N_2 plasma and a BCl_3/N_2 plasma is that the item 4 and 5 would not take place under a Cl_2/N_2 plasma. But, we believe that a higher etch rate and a more vertical profile are obtained probably by the helps of BCl_3^+ and BCl_2^+ heavy ions. In addition, these heavy ions might assist the desorption of $InCl_x$. Since the required energy and the occurring rate for each reaction are not totally understood yet, it still requires other quantitative plasma measurements (ex: OES and QMS) and extensive modeling to build up the exact mechanism. The composition identification by OES in an ICP Cl_2/H_2 plasma

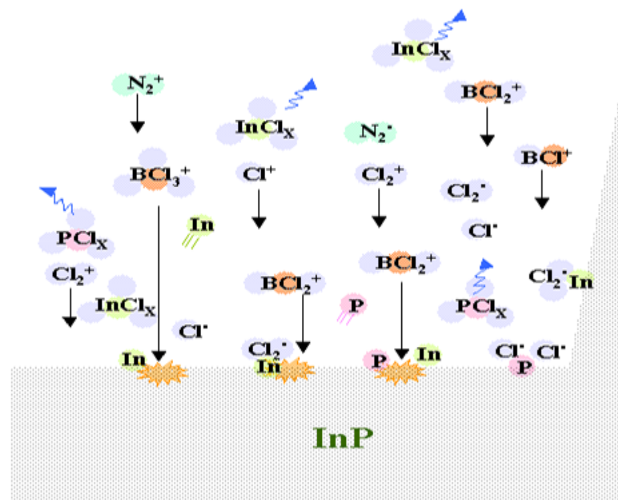

Figure 3.30: Schematic of several possible representative etching reactions on InP surface under a BCl_3/N_2 plasma.

is being executed presently in LPN [Gatilova2008] and the BCl_3/N_2 and Cl_2/N_2 plasmas will be investigated in the near future.

3.6.6 Etched PhC devices performance: free-carrier lifetime measurement

With the same conception as in section 3.5.4-A, the increased surface recombination states due to the appearance of sidewall surface defects under a N_2-based ICP plasma were measured by time-resolved photoluminescence measurement. The PhC holes in an InP/InGaAsP multiple quantum-wells structure for carrier lifetime characterization was etched using an ICP $Cl_2/BCl_3/N_2$ (33/16/99 sccm) plasma with p = 5 mTorr, P_{ICP} = 1000 W, and $|V_{bias}|$ = 200 V.

The relative luminescence intensities for the non-etched stack and regions with PhC structures are presented in figure 3.31. The highest emitting photoluminescence intensity on regions with PhC structures was 15%∼30% higher than the non-etched stack. But, it then decayed more quickly and gave a free-carrier lifetime value of 1415 ps and 1400 ps for PhC lattices with a = 580 nm and 520 nm, respectively, relative to 6 ns for the non-etched stack. Compared to the results reported in section 3.5.4-A, the free-carrier lifetime of sample etched using the $Cl_2/BCl_3/N_2$ plasma has a larger value than the one etched using the Cl_2/Ar plasma (100-150 ps). This comparison suggests that the sidewall surface presents a smoother state while etching under the $Cl_2/N_2/BCl_3$ plasma than under the Cl_2/Ar plasma, which can be verified as well by examining the sidewall morphologies (figure 3.17(b) and figure 3.24(b)). An elevated carrier lifetime value indicates that the surface states are not formed massively after the etching, and which is

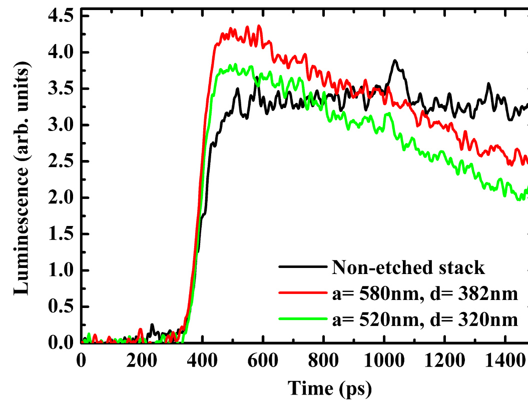

Figure 3.31: Time-resolved photoluminescence for InP/InGaAsP multiple quantum-wells structures with PhC holes etched by an ICP $Cl_2/BCl_3/N_2$ plasma. The non-etched stack result is indicated for comparison (black line).

beneficial to the fabrication of PhC emitters.

The free-carrier lifetime for InP/InGaAsP multiple quantum-wells with PhC holes structures etched using the ICP $Cl_2/N_2/BCl_3$ plasma is in the order of 1400~1415 ps, relative to 3~6 ns for regions without PhC structures. This elevated value indicates that surface defects are not formed massively after the etching compared to the ICP Cl_2/Ar plasma.

3.7 Conclusion

Within this dissertation, the ICP-RIE etching processes with Cl_2/Ar, Cl_2/ BCl_3/N_2, and BCl_3/N_2 plasmas are studied and presented. In a Cl_2/Ar plasma, an etch depth of ~3 μm is obtained and can be applied for the fabrication of InP PhC planar waveguides. Another application on laser structures requiring an etch depth more than 4 μm is expected to be realized successfully by increasing the mask thickness. However, due to the anticipated fabrication complexity of thick mask on PhC taper waveguides with indispensable small features, the development of thick mask was not proceeding within this thesis scope. Hence, the CAIBE method with Cl_2 as the reactive gas is adopted for the laser structure etching.

The sidewall roughness is often coming either from the sputtering by the energetic positive ions and/or from the unequal chemical etch rates between In and P under a chlorine-containing plasma. In a Cl_2/N_2 plasma, nitrogen is introduced to retard the isotropic etching and reduce the surface roughness. It is concluded from the above experiments that a smooth sidewall surfaces in PhC structures can be obtained when N_2 ratio reaches ~67% in the plasma. But, it leads to a lower etch rate and a conical profile with the undercut. Therefore, BCl_3 is added into plasma and is shown to enhance the feature verticality and to augment the etch rate. A smooth and vertical hole profile without undercut is obtained when BCl_3 ratio is about 19% (81%-N_2). With this BCl_3/N_2 plasma, even though the etch depth is limited to about 800 nm, it can still be applied for the fabrication of InP PhC membrane devices.

The reason of lateral etching and surface roughness reductions due to the introduction of N_2 is more likely due to the dilution of chlorine radicals; but, the surface nitridation may not be involved. To comprehend the mechanisms with presence of N_2 during the etching, more rigorous studies with helps of OES and QMS should be performed to identify the etched products and the species (ions, neutrals) within the plasma.

Chapter 4

Photonic crystals tapers

4.1 Introduction

In the photonic integrated circuits (PIC), the lights are confined tightly in the optical waveguides that maintain a small and elliptical mode profile. However, there are moments that the lights are required to transmit into the free space or into the optical fibers. A typical case is to assemble the light from a semiconductor diode laser to a single-mode optical fiber which has a relatively larger mode size (8∼10 μm) and a circular mode profile. It has been known that smaller the mode profile is emitting from a diode laser, more the light beam would diverge. In this case, the alignment between a diode laser and an optical fiber becomes more difficult and the transmission efficiency is thus poor. Hence, an intermediate region, which can present an optimized coupling efficiency between PIC and the free space/optical fiber and meantime can control the mode profile and the mode size, is demanded. A device exhibiting this specific optical function is designated as a spot-size converter or a mode adapter. The term, taper, is employed since its layout often involves the variation in structural dimensions. Except for expanding the mode sizes, the tapers can also be served differently as collimators in a wavelength division multiplexing (WDM) system.

For conventional planar waveguides, several taper geometries have been proposed to convert the guided mode size in the lateral plane. The strategy involves either the multiple diffractions in periodical segmented guide [Weissman1995] or the gradual variation of effective index and dimension [Bendelli1991, Wei1997, Mitomi1994, Park2001, Almeida2003]. In a periodically segmented waveguide, the beam is periodically focused and diffracted. The average index difference over a period reduces towards the fiber end and it thus leads to mode size mismatch diminution. However, in this design, the reflection at each interface may degrade the transmission efficiency. Another type of taper waveguides based on converting both the refractive index and the cross-sectional dimension is employed more

widely. The contours of taper waveguides often include linear, convex-like and concave-like forms. In this type of tapers, the lengths are often in the order of several hundred micrometers. A nano-taper as short as 40 μm has been demonstrated successfully, which can used to couple a fiber and a sub-micrometer waveguide [Almeida2003].

The developments based on PhC waveguides (PhCW), like a PhC sharp bend [Mekis1996], are expected to reduce greatly the footprint in PIC. For the applications at infrared or visible wavelengths, the dimension of PhC units is in the order of sub-micro or nano-meters. For such small features, the difficulties of PhC devices arise not only from the fabrication processes, but also from the experimental measurement techniques. To be able to transmit the light between PhC components (ex: PhC waveguides) and other photonic components without degrading the device functionalities, the taper designs based on PhC structures are then being investigated.

Inherited from the conventional taper designs, people have implemented the periodic segmented waveguides into PhC waveguides [Johnson2002] [Bienstman2003]. As through the index contrast variation, it has been reported either by modifying the structural shapes [Happ2001c, Mekis2001, Pottier2003, Dossou2006, Khoo2005] or by varying the sizes of certain lattice units to provide the mode conversion [Lalanne2002, Talneau2004b]. Most of investigations concern the coupling between a narrow PhCW and a ridge waveguide with similar width (< 2 μm). E. H. Khoo has considered the case of coupling from a wide ($\sim$10 μm) ridge waveguide to W1 guide through PhC tapers [Khoo2005]. This study was devoted to numerical simulations; however, the experimental performances were not known.

In this dissertation, the efforts are devoted to develop the taper structures in PhC environments which can provide a low-loss, efficient coupling from a PhCW component to a cleaved-facet single-mode fiber (SMF). For PhCW, the optical mode is often elliptic, with a with a size of 1$\sim$2 μm in the lateral plane. In contrast, SMF holds a 8$\sim$10 μm-wide circular optical mode. The visible difference of mode sizes between PhCW and SMF is shown schematically in figure 4.1. The current coupling scheme generally uses a micro-lensed fiber, which is not beneficial for the optical integration and with a low alignment tolerance. If one is able to enlarge the mode size at the exit of PhCW, a direct coupling to a cleaved-facet SMF would be preferred. Here, we investigate mainly the modal size transformation in the lateral plane; and the developed taper designs can be applied in PICs.

In the following PhC taper designs, the modal size in vertical direction is not converted since the vertical stacking layer is not modified. In addition, we do not consider the case when tapers are operated by reducing the guiding layer to a very small tip and it then transfers the mode into a thick underlying layer. Therefore, the taper efficiency cannot be compared to the performances reported in the literatures, in which modes are transformed in both orientations. Here, the

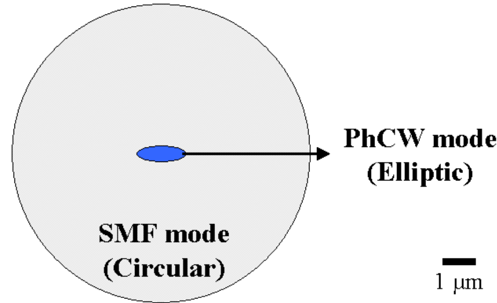

Figure 4.1: The schematic of mode sizes comparison between a PhC waveguide elliptic mode and a single-mode fiber circular mode.

modal behavior when traversing the taper is concerned. We pay attention mainly to the fundamental mode optical power at the input and output waveguides. For designed tapers, we expect to minimize the unwanted modal conversion to higher-order modes or radiation modes, as well as the reflection efficiency.

4.2 Theory of coupling

In this section, the coupling theory between a semi-conductor planar waveguide (or a laser) and an optical fiber would be reviewed. The fundamental notations are first introduced in order to express numerically the coupling coefficient and the coupling losses; and then the coupling losses due to the lateral, angular misalignments and the focalization are addressed briefly.

4.2.1 Gaussian beam

The field profile of fundamental mode coming from a diode laser/planar dielectric waveguide posses a perfect plane wave front on the exit facet. This profile traveling latter in a free space can be generally expressed as a Gaussian curve and its electric field $\phi(r)$ in TE polarization can be approximated as [Kamoun1997]

$$\phi(r) = \sqrt{\frac{2}{\pi}} \frac{\phi_0}{w(z)} exp\left[-\frac{r^2}{w^2(z)} - \frac{ik_0 r^2}{2R(z)}\right] \tag{4.1}$$

where the $w(z)$, $R(z)$, and r are the radius of mode on $1/e^2$ intensity, the curvature radius, and the radial coordinate, respectively.

Since the dimensions of guiding layers in diode lasers/planar waveguides are comparable to the light wavelength of interest, the light diffraction should be therefore considered on the exit side. From the exit facet, the light beam diverges and obeys the following rules:

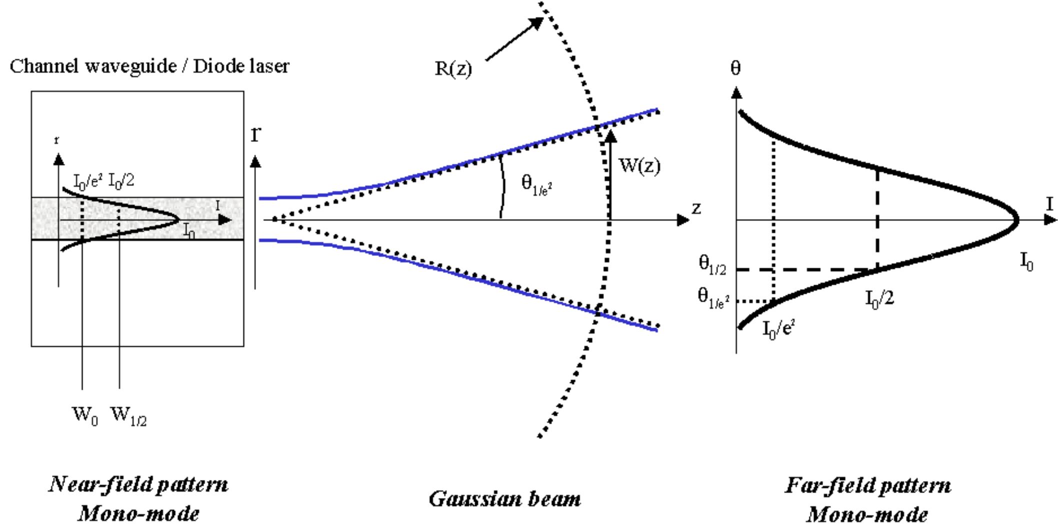

Figure 4.2: The schematic of near-field and far-field of a Gaussian beam.

$$w(z) = w_0\sqrt{1+\left(\frac{z}{z_R}\right)^2} \quad \text{and} \quad R(z) = z\left[1+\left(\frac{z_R}{z}\right)^2\right]$$

where $Z_R = \pi w_0^2/\lambda$ is the Rayleigh distance.

The field distribution close to the exit facet (i.e. *near-field*) is then expressed as

$$\phi(r) = \sqrt{\frac{2}{\pi}}\frac{\phi_0}{w_0}exp\left[-\frac{r^2}{w_0^2}\right] \tag{4.2}$$

where w_0 is the radius of mode on $1/e^2$ intensity at z = 0, or is also called as the *beam waist.*

While being far from the facet, in another word: $z >> z_R$ and $R(z) \approx z$, the field distribution, referring as the *far-field*, is the Fourier transform of the near-field and becomes a spherical wave centered at z = 0. The schematic of near-field and far-field is presented in figure 4.2. The radius of mode on $1/e^2$ intensity is expressed as $w(z) \approx w_0 z/z_R$, with the half divergence angle on $1/e^2$ intensity given by $\theta_{1/e^2} \equiv w(z)/R(z) = w_0/z_R = \lambda/\pi w_0$.

Customarily, another formalism of half-width on half intensity is also often employed, where the field diameter on half-intensity ($w_{1/2}(z)$) is given by

$$w_{1/2}(z) = \sqrt{2log2}w(z) \approx 1.177w(z) \tag{4.3}$$

and at z = 0, $w_{1/2} = \sqrt{2log2}w(0)$. The total divergence angle ($\theta_{1/2}$) on half-

intensity is then expressed as

$$\theta_{1/2} = \frac{w_{1/2}(z)}{2R(z)} = log2\frac{\lambda}{\pi w_{1/2}} \approx \frac{0.69\lambda}{\pi w_{1/2}} \tag{4.4}$$

Consequently, the laser beam is less divergent when the mode size emitted from the diode is larger. It also explains intuitively that the diffraction phenomenon is less important when the mode diameter is larger at a given wavelength.

4.2.2 Coupling from diode laser/planar waveguide to optical fiber

To express the coupling efficiency between two mono-modes structures, the *coupling coefficient* (C) is often used. In the case of coupling from a diode laser/planar waveguide to an optical fiber, it represents the ratio of excited power in an optical fiber to the total power brought by the incident light beam. The coupling coefficient is determined by the overlap integration of two fields calculated in the plane perpendicular to the propagation direction and is expressed as follows:

$$C = \eta \frac{\left| \int\int \phi_1 \phi_2^* dxdy \right|^2}{\int\int |\phi_1|^2 dxdy \int\int |\phi_2|^2 dxdy} \tag{4.5}$$

where ϕ_1 is the field of incident light beam and ϕ_2 is the eigenmode of single-mode optical fiber with cleaved-facet. η is the transmission coefficient of a normal incident wave at the interface of air/fiber and is given by $\eta = 4n/(1+n)^2$, where n is the effective index of the optical fiber.

4.2.3 Coupling losses

To express quantitatively the losses due to the coupling at the interface of diode laser/planar waveguide and optical fiber, the coupling losses are defied as $P = 10log_{10}C$ and the sources of coupling losses are usually categorized as follows:

1. Refractive index mismatch:

The refractive index of optical fiber core is 1.5. In an ideal case when the fields overlap completely, the maximum coupling coefficient therefore equals to the transmission coefficient and it gives an inevitable coupling losses value of -0.18 dB.

2. Intrinsic losses:

Those are the losses coming from the mismatch of mode sizes between a diode laser/planar waveguide and an optical fiber under the optimal alignment condition. Assumed that the mode profiles are gaussian beam-like and the eigenmode of optical fiber is always circular, the coupling coefficient can then be approximated as

$$C_{max} = \eta \frac{2w_{0x}w_{0f}}{(w_{0x}^2 + w_{0f}^2)} \frac{2w_{0y}w_{0f}}{(w_{0y}^2 + w_{0f}^2)} \tag{4.6}$$

where w_{0x} and w_{0y} are the lateral and vertical radius of mode in a diode laser/planar waveguide, respectively; and w_{0f} is the mode radius of the single-mode fiber. The variation of coupling losses with the function of w_{0y} is shown in figure 4.3 for several different w_{0x} values. In general, the coupling efficiency is higher when the mode sizes (w_{0x}, w_{0y}) are comparable to the one of optical fiber. In the case of 10 μm-wide optical fiber mode, the absolute coupling losses value reaches a minimum when $2w_{0x} = 2w_{0y} = 2w_{0f} = 10$ μm.

In an actual case, the mode size at the exit of PhCW and PhC laser is less than 2 μm ($2w_{0x}$ = 1~2 μm, $2w_{0y}$ = 1 μm); then, the coupling losses are in the range of -10 dB. In order to diminish the coupling losses due to the mode size mismatch, two methods are thus employed widely, including the reduction of mode size at the fiber side using a micro-lens and the augmentation of mode size at the laser/waveguide side using a taper structure.

3. Extrinsic losses:

Those are the coupling losses due to the geometric misalignment which involves three orientations in the lateral, longitudinal planes, and in angular direction. Generally speaking, the misalignment in the lateral plane has a more significant contribution on the coupling losses than the other two.

When we use a micro-lensed fiber to collect the light coming from a diode laser/planar waveguide, the alignment tolerance (-1 dB in coupling losses with respect to the maximum coupling efficiency) in the lateral plane is often inferior to 1 μm. This value can be improved to $\pm$ 1.5 μm if a cleaved-facet fiber is adopted

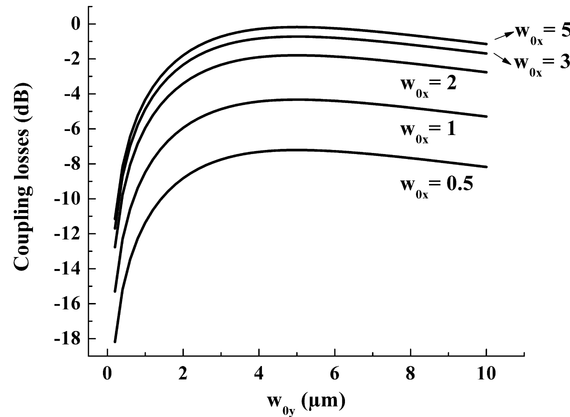

Figure 4.3: The coupling losses with variation of mode sizes (w_{0x}, w_{0y}) from a diode laser/planar waveguide to a single-mode optical fiber with a mode size of 10 μm-wide (η = 0.96). The coupling losses were calculated based on equation (4.6).

and can even reach ± 2.4 μm in an ideal case, i.e. $w_{0x} = w_{0y} = w_{0f} = 5$ μm, when a taper is used at the device edge [Kamoun1997]. Hence, the micro-lensed fiber is generally not preferred from the viewpoint of optical integration due to the low alignment tolerance compared to a cleaved-facet fiber. The augmentation of mode size using a taper is thus chosen for enlarging the mode size at the laser/waveguide side to increase the mode overlap with the optical fiber.

In the longitudinal and angular orientations, the alignment tolerances are usually in the range of 30∼40 μm and $\pm 3^0 \sim \pm 12^0$, respectively, while using a cleaved-facet fiber [Kamoun1997].

The coupling efficiency between laser/waveguide and optical fiber can be enhanced, as well as the alignment tolerances, by using a taper design to increase the mode overlap.

4.3 PhC taper waveguide designs

For PhC channel defect wavguides operating within the photonic band gap, the light confinement in the planar orientation can be attained by the index contrast simultaneously with the PhC effect. We then consider here two types of tapers. One relates to the periodic environment, in which the Bragg effect contributes greatly to the modal propagations. The PhC channel waveguide with gradual variations in defect width can lead to a mode size transformation. Another type is mainly based on the refractive index contrast. This concept has been studied widely in conventional heterostructure tapers [Bendelli1991, Wei1997, Mitomi1994, Park2001] and can be extended in PhC tapers. Here, the PhC holes structures provide not only the index contrast, but also can form accurately the desired index variation geometries. In both cases, the length of tapers can be limited to be less than 40 μm when PhC structures are implemented. In a large width PhC defect waveguide, the guiding through Bragg effect is often reduced while it relies mainly on the index contrast.

It should be noted that our PhC tapers are composed of high-index-contrast materials. In another word, the mode size of W23 guide should be smaller than the optical fiber eigenmode for an identical given physical width. It would result in degradation in coupling efficiency; nevertheless, we concern mainly the modal occupation and modal conversion while traversing the designed PhC tapers.

4.3.1 Taper designs based on Bragg effect domination

It has been reported that the W1 PhCW possess a single fundamental even mode propagation. However, its small confined structure causes poor coupling efficiency

with other conventional ridge waveguides. A taper section situating between a W1 guide and a deep ridge waveguide with a gradual variation of air hole sizes has been proposed [Lalanne2002] and a higher transmission efficiency has been obtained experimentally [Talneau2004b].

Based on the above conception, our PhC stair/variant-stair tapers composed of several channel defect waveguide sections varied in width and hole size are then conceived. For the systematic study purpose, our PhC tapers always start with a W3 guide and end with a W23 guide, whose width corresponds to the physical width of the optical fiber core. The *stair* taper is designed when the taper width $W(2i+1)$ varies from W3 to W23 (i = 1-11) with 8-rows-long at each section (see figure 4.4(a) for a stair taper after the fabrication processes). In another case, the *variant-stair* taper, the diameters of 4 holes at the end of each section reduces gradually, as shown in figure 4.4(b). This design is expected to reduce the reflection by smoothing out the abrupt interface. For these two tapers, the guiding mechanism is sustained mainly by the PhC channel defect waveguides; in another word, the PhC properties would be more explicit than the curved tapers mentioned in 4.3.2.

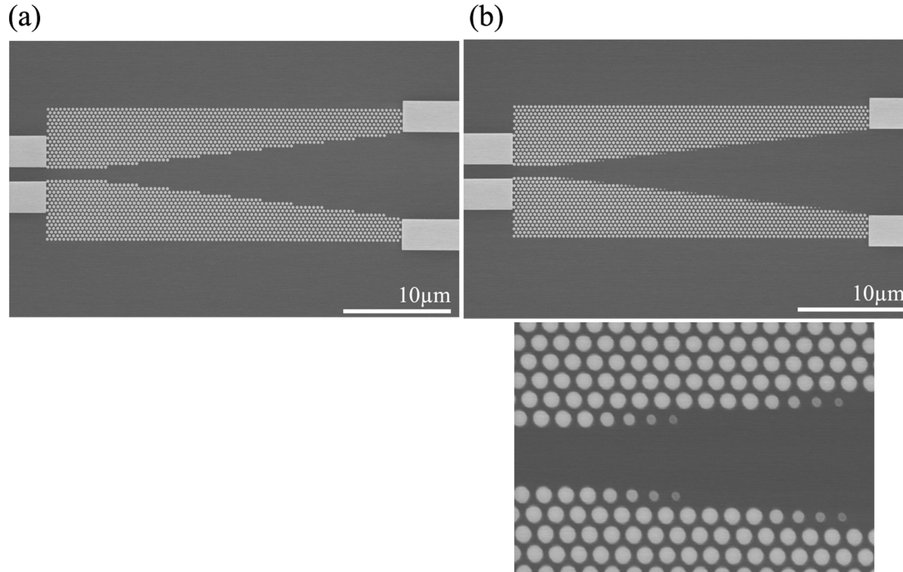

Figure 4.4: The SEM top views of the fabricated (a) PhC stair (8-periods) taper and (b) PhC variant-stair (8-periods) and the gradual diminished diameters of 4 holes in the transition region.

4.3.2 Taper designs based on refractive index contrast domination

In conventional planar waveguides, the taper designs based on the mechanism of effective index contrast through structure shape variation have been already widely used. The tapers with linear, convex, and concave contours have been proposed to convert the mode size from 1 μm-wide to 8 μm-wide. However, a main drawback is that the required taper length is often in the order of hundred micrometers. With the development on PhC, the taper length is expected to be reduced largely once the PhC structures are implemented.

The perforated PhC structures in a semiconductor can be treated as an artificial material holding a different effective refractive index than the origin bulk without PhC. Therefore, the contour variation of this artificial material can be mimicked simply by altering the PhC distributions. Especially, by the help of electron beam lithography, the PhC distributions can be controlled accurately.

Following the proposed geometries in conventional planar waveguides, a series of PhC curved tapers is designed. By introducing the PhC structures, the taper length can be thus reduced from several hundreds micrometers in conventional implementations to $\sim$34 μm. Similar to the section 4.3.1, the PhC curved taper starts as well with a section of W3 guide ($\sim 4\times a$-long) and ends up with a W23 guide. Three contours of curved tapers are studied here, including the *gaussian curve*, the *double-parabola*, and the *semi-ellipse*, which are shown schematically in figure 4.5. In order to well fit the proposed index contrast contours, the positions and diameters of certain holes are then slightly shifted and decreased.

The semi-ellipse geometry design has been proposed based on the ray model

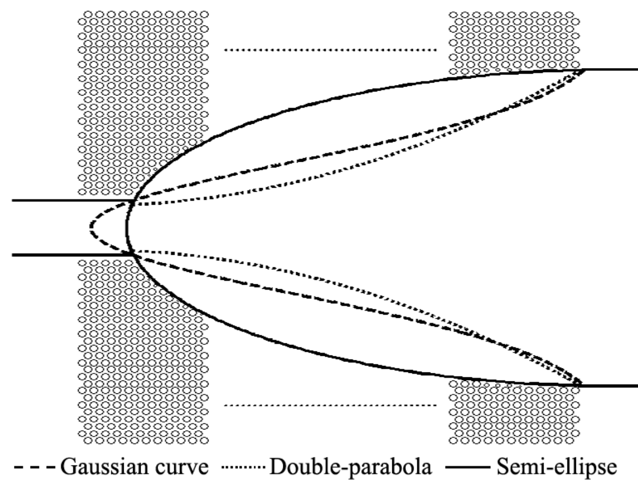

Figure 4.5: The schematic of PhC tapers with the contours of gaussian curve, double-parabola, and semi-ellipse.

calculation at index contrast interfaces [Wei1997] for the purpose to focus beams at a certain distance away from the exit side. In this design, the diverged beams can be reflected on two branches of ellipse and are then all focused on a focal point. In contrast, the collimated beams hold the original trajectories. We investigate this geometry to demonstrate its specific modal behaviour because the required distance for converging beams might be too long and is thus not favoured for compactness consideration.

Here, the contours of gaussian curve and double-parabola are studied following the PhC curved tapers proposed by Khoo et al. [Khoo2005]. They calculated, by using the step transition method, the transmission efficiencies through concave and convex tapers and compared to the linear tapers. In which, the convex contour demonstrated the best modal conversion in TM polarization from a wide (∼10 μm) ridge waveguide to W1 guide on a large wavelength span, for a square matrix of rods. Consequently, we investigate the contours of gaussian curve (similar to convex) and double-parabola (similar to concave) in a triangular matrix of air holes in TE polarization from a W3 guide to a wide ridge waveguide.

Our designed PhC tapers with a section length of 86-periods for expanding the mode size from a W3 guide (1∼2 μm-wide) to a W23 guide (8 μm-wide) are based on the following conceptions:

1. The lights confined are realized by the PhC channel defect waveguides. By varying gradually the width of defect waveguides, the mode profiles can be extended. We propose taper geometries of stair and variant-stair, in which the width of PhC defect waveguides varies from W3 to W23 with a fixed section length of 8-periods. In the variant-stair taper, the diameters of 4 last holes in each section are diminished in order to reduce the scattering at the transitions.

2. If treating the perforated PhC structures as another material holding a smaller effective index than the bulk material, the lights confinement can then be realized due to the refractive index contrast. Based on the taper studies in conventional planar waveguides, we propose the PhC curved tapers with contours of gaussian curve, double-parabola, and semi-ellipse. The positions and diameters of certain PhC holes are varied and diminished to well fit the proposed contour, and it can be controlled with a precision with the help of electron-beam lithography.

4.4 PhC tapers simulation

The simulations of PhC tapers were performed using the 2-D FDTD method [PhotonDesign]. The advantage of FDTD method is that it can calculate the input/output intensities for a finite device. The transmission efficiency and the modal distributions of the transmitted power on the exit guide were both addressed. The essential PhC unit for tapers consisted of a triangular air hole array in a high refractive index slab (n_{eff} = 3.25). The lattice period was 400 nm and the filling factor was about 35% corresponding to 250 nm hole diameter. Under these conditions, the photonic band gap (PBG) in transverse-electric (TE) polarization in normalized frequency ($u = a/\lambda$) ranged within 0.22∼0.29 (see chapter 2). In the variant stair taper, the diminished holes sizes had air-filling factors as 25%, 16%, 10%, 5%.

All PhC tapers were inserted within two sections of conventional access ridges with widths of 1.38 μm and 8.3 μm matching to a W3 guide at the entrance and a W23 guide at the exit side, respectively. The insertion of access ridges is mandatory, since the commercial software can calculate the modal distribution of optical field only in the case of index contrast waveguide. Hence, the modes in PhC waveguide are projected into a ridge waveguide. The total length of PhC taper was fixed as 86-periods, i.e. ∼34.4 μm. The TE fundamental even mode was launched with a 20 fs pulsed width centered at 1.55 μm in the input access ridge. Two detectors were placed in the input and output access ridges to acquire the reflection and transmission intensities, respectively. A third sensor was placed immediately after the light source to serve as the reference. The simulations were performed in the case that the material losses were not under consideration.

4.4.1 Simulation results of PhC stair and variant stair tapers

Table 4.1 summaries the simulated total transmission/reflection flux normalized to the reference sensor and the modal occupations at the output ridge with respect to the injected fundamental mode for PhC stair and variant stair tapers. In the ideal case without material losses, the average transmission efficiency integrated for all the modes was found to be ∼95% for all the designs except at 1.52 μm wavelength. As for the simulated reflection efficiency, it presented an average value less than 0.5%, but not around 1.52 μm, where the intensity ratio was about 0.5. The visible dip around 1.52 μm in the transmission efficiency diagram was attributed to the mini-stop band (MSB) of a W3 guide [Olivier2002] that was adopted as the beginning of our tapers. The presence of this MSB is unavoidable while working with the PhC channel defect waveguides, therefore the lattice constant should be chosen properly to exclude this MSB from the working wavelength range of interest.

The analysis of modal occupations of transmitted power showed that the 1st

odd mode occupation was with an extremely low value less than 2% for all the tapers (not shown). The stair and variant-stair tapers both presented a fundamental even mode dominate status. In the wavelength range out of MSB region, the average fundamental even mode occupation was about 67% and 69.5% for the stair (8-periods) taper and the variant-stair (8-periods) taper, respectively. As for the 2nd even mode, its average occupation was in the range of 16∼19%. For the variant-stair taper, the ratio of fundamental even mode is slightly higher than the one in abrupt form. The gradually diminished diameters holes showed somehow a reduction of the scattering at the transitions, but only with a minor improvement.

To demonstrate the performances in a shorter taper length, we designed a stair and a variant-stair taper with a transition section of 4-periods-long. The two last holes of each section had diminished diameters for the stair-variant (4-periods) taper. In order to keep an equivalent overall length, a 48-periods-long W23 guide was added, as shown in table 4.1. In general, the average transmission efficiency was comparable to other tapers; but, the influence of W3 MSB was less severe in short tapers. Analyzing the modal occupations, the 2nd even mode had an average ratio of 36.5% for both cases; and the fundamental even mode ratio was 32% and 37% for the stair (4-periods) taper and the variant-stair (4-periods) taper, respectively. It should be noted that the ratio of 3rd even mode ratio had a value of 15∼16%, which could not be neglected. It has been reported that, by 3D FDTD simulation, the radiation losses due to the mode-profiles mismatch can be reduced by tuning the position and the diameter of certain holes in PhC micro-cavities [Sauvan2005]. In our calculation, the varied diameters might depart from the optimal values and it then leaded to an excitation of higher-order modes. From these simulation results, we may conclude that a shorter design is less tolerant to the fabrication errors.

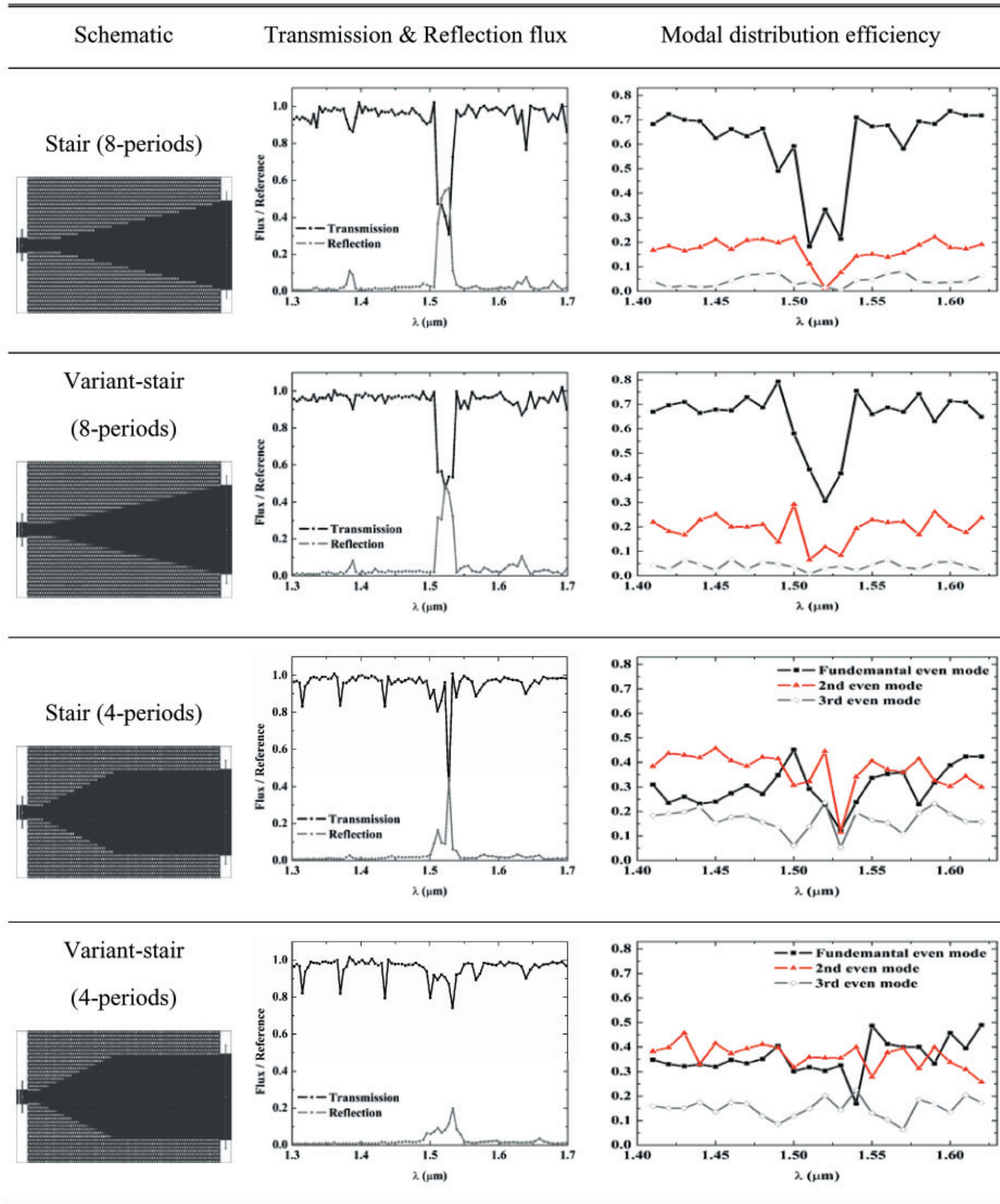

Table 4.1: The schematic of PhC tapers with geometries of stair (8-periods), variant stair (8-periods), stair (4-periods), and variant stair (4-periods); and their simulated transmission (black line)/reflection (gray line) flux and modal distribution efficiency for the fundamental even mode (black line), the second even mode (red line), the third even mode (gray dashed line) with the function of wavelength.

4.4.2 Simulation results of PhC stair and variant stair tapers

Table 4.2 summaries the simulated transmission/reflection efficiency and the modal occupations for PhC curved tapers. In the transmission efficiency diagrams, an average ratio of 95% was obtained for this category of tapers and the W3 MSB was observed as well. For the double-parabola taper, the section with a width close to W3 guide was longer than other tapers; as a result, the transmission intensity at the MSB wavelength was expected to be the lowest.

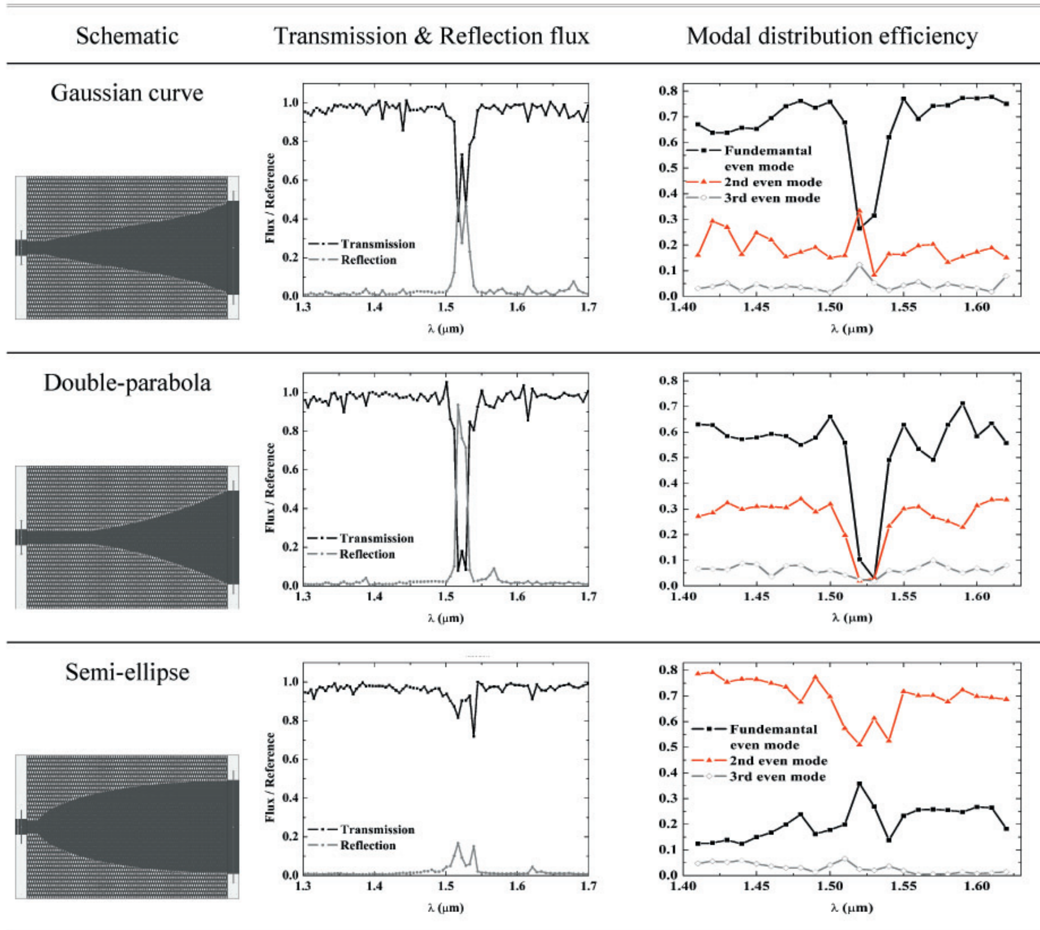

Table 4.2: The schematic of PhC tapers with contours of gaussian curve, double-parabola, and semi-ellipse; and their simulated transmission (black line)/reflection (gray line) flux and modal distribution efficiency for the fundamental even mode (black line), the second even mode (red line), the third even mode (gray dashed line) with the function of wavelength.

From the results of modal occupations, the 1st odd mode and the 3rd even mode occupations were with an extremely low value of $< 2\%$ and $< 5\%$, respectively, for all the PhC curved tapers. The average ratio of fundamental even mode out of MSB range was found to be highest for the gaussian curve taper, $\sim$73%; and it was about 60% for the double-parabola taper. Unlike these two tapers, the semi-ellipse taper had a 2nd even mode dominate status, in which, about 70% of the incident fundamental mode was coupled to the 2nd even mode.

The simulations of transmission efficiency and the modal distributions for our designed PhC tapers (34 μm-long) are realized using the 2D-FDTD calculation.

1. In the transmission diagrams, the mini-stop band appears for all the PhC tapers. The mini-stop band is a unique property of PhC defect waveguides, in which the transmitted powers are reduced for certain specific frequency ranges.

2. In the modal distributions, all the tapers, except the semi-ellipse taper, show a fundamental even mode dominant status. The average ratio of fundamental even mode out of MSB range is about 73% for the gaussian curve taper. In a semi-ellipse taper, about 70% of injected fundamental even mode is coupled to the 2nd even mode.

In a shorter PhC taper section, while the holes positions and diameters are not optimized, the fields mismatch would lead to the coupling to higher-orders modes. Hence, the short PhC tapers are more sensitive to the fabrication errors.

4.5 PhC tapers fabrication

The simulated PhC tapers were subsequently fabricated on a semi-conductor heterostructure waveguide consisting of a 200 nm-thick InP cap layer and a 500 nm-thick InGaAsP guiding layer grown on the InP substrate (see section 3.2.2). The patterns of PhC tapers and input/output access ridges were defined by electron beam lithography. We adjusted the electron beam doses after calibrations in order to minimize the proximity effect. After patterns definition, samples were etched in an ICP-RIE system using a Cl_2/Ar plasma [Lee2006]. An etched depth of 2.8 μm with a nearly vertical profile was obtained for 250 nm-diameter holes and the air-filling factor after fabrication was about 30%. The samples were thinned mechanically to a thickness of 120$\sim$140 μm to facilitate the realization of cleavage. The top views of the fabricated PhC curved taper with contour of gaussian curve are presented in figure 4.6, where the access ridges are visible on the borders.

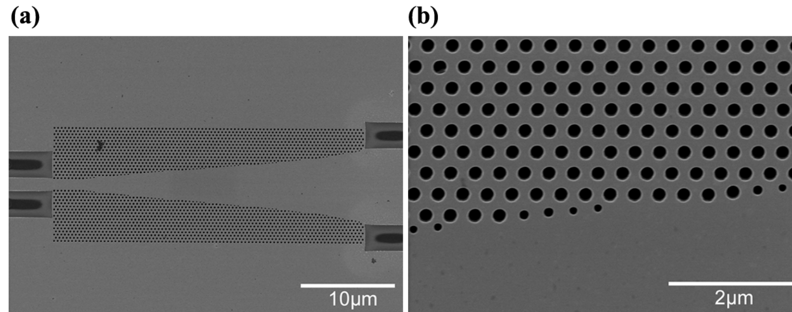

Figure 4.6: The SEM top views of (a) the PhC curved taper with contour of gaussian curve and the input/output access ridges. (b) Magnification of varied hole sizes and positions together with the standard PhC triangular matrix.

Our designed PhC tapers are fabricated on a InP/InGaAsP/InP planar heterostructure waveguide. The patterns are realized using electron-beam lithography with electron beam doses modifications in order to minimize the proximity effect. They are latter etched using an ICP Cl_2/Ar plasma and an etch depth of 2.8 μm is obtained for 250 nm-diameter holes.

4.6 Optical characterization: light transmission and light divergence

To demonstrate the performances of designed PhC tapers, the optical characterizations including the light transmission and the light divergence measurements were performed.

4.6.1 Measurement setup

The measurements of light transmission and beam divergence were both performed in TE polarization within the wavelength range of 1.5-1.62 μm generated by two tunable diode laser sources. The light was injected into the access ridge (1.38 μm-wide) via a micro-lensed fiber. An infrared CDD camera was placed temporarily at the exit side for the fiber-ridge alignment. The movements of injected and collected fibers were controlled by the piezo-electrical motors in order to fine-tuning the positions.

The transmission spectra were collected by a cleaved-facet single-mode fiber and read out by a power meter. Figure 4.7(a) shows the system setup for the PhC tapers transmission measurement. The transmission spectrum collected by a

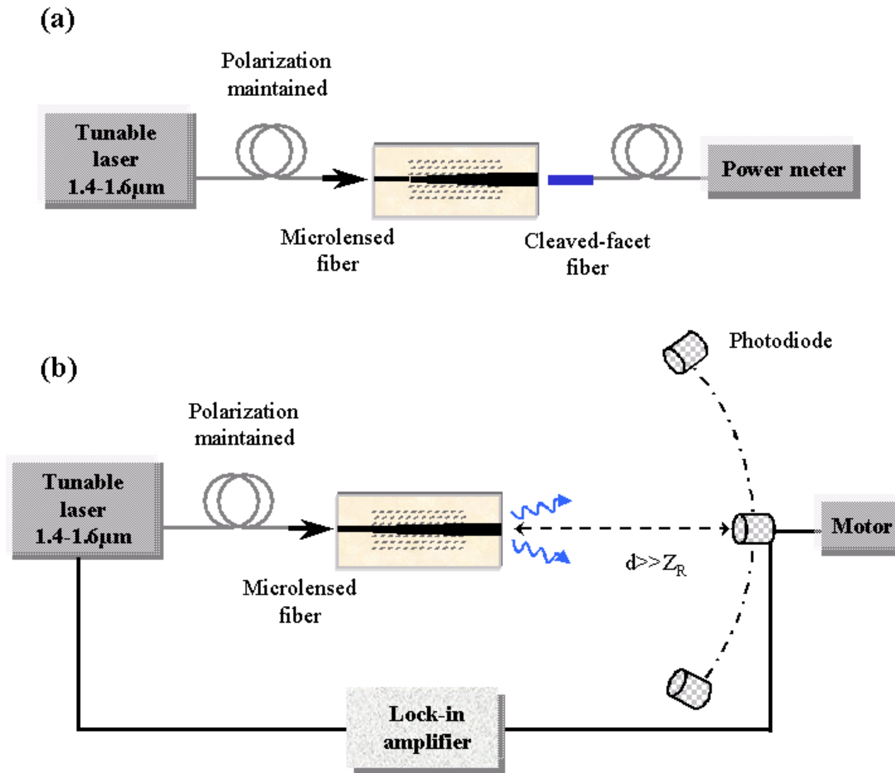

Figure 4.7: The schematic of system setup for (a) the light transmission measurement and (b) the far-field measurement.

micro-lensed fiber for a plain 1.38 μm-wide ridge waveguide was also performed for comparison.

As for the beam divergence, it was realized by the far-field measurement using a scanning photodiode, as shown schematically in figure 4.7(b). The light injection and the alignment were executed through a micro-lensed and a camera, as mentioned above. Situating about 5 cm away from the exit side of PhC tapers, the photodiode can detect the light signals while scanning within -45 and 45 degree in the horizontal plane because only the modal transformation in the lateral plane was investigated. A lock-in amplifier synchronized to the laser impulse frequency was used to enhance the signal intensities.

4.6.2 Light transmission

Figure 4.8 shows the measured transmission spectra for the PhC gaussian curve taper, the W3 guide, and the PhC semi-ellipse taper with an input laser power value of 2 mW. The dip around 1.54 μm gaussian curve taper was attributed to the mini-stop band (MSB, referring to section 2.4.1), which appeared as well in

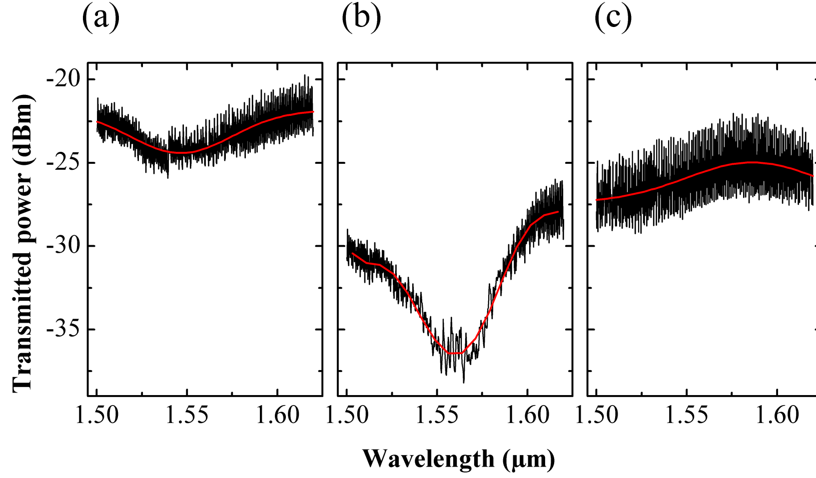

Figure 4.8: The spectrally resolved transmission diagrams for (a) the gaussian curve taper, (b) the W3 guide, and (c) the semi-ellipse taper.

the spectrum of W3 guide with the same total length (figure 4.8(b)). This MSB was not visible on the transmission spectrum of semi-ellipse taper (figure 4.8(c)) because the light propagation was mainly supported by the 2nd even mode, as calculated and presented in table 4.2. Owing to a higher-order modes transmission regime, the coupled optical power was found to be lower in the semi-ellipse taper compared to the gaussian curve taper.

To estimate the coupling efficiency enhancement, the optical powers collected by a cleaved-facet SMF from a 1.38 μm-wide ridge and from a 8.3 μm-wide ridge were compared. The light propagated through a W3 guide section in the former case and through a PhC taper section in the latter one. Comparing the transmitted powers shown in figure 4.8(a) and (b), the highest enhancement by a factor of 4 in the wavelength range of 1.61-1.62 μm was obtained in the case of the gaussian curve taper. But, it should be noted that this enhancement was for certain wavelength ranges limited by the MSB. This result is in agreement with simulation results (table 4.2), which shows a higher transmission ratio on the fundamental even mode for the gaussian curve taper than others.

4.6.3 Beam divergence

The modal conversion efficiency for designed PhC tapers can be evaluated as well from their light divergence diagrams. Table 4.3 and 4.4 present the far-field patterns measured for the PhC stair and curved tapers, respectively, at 1.45 μm and 1.6 μm wavelength, whose intensities are already normalized to the maximum measured values. Within far-field patterns, it is difficult to distinguish completely the fundamental even mode and the 2nd even mode since their mode profiles are partly

overlapped. Nevertheless, we still classify coarsely the patterns as the fundamental even mode, 2nd even mode, and even higher-orders modes.

The fundamental even mode was found to be dominant in both the stair (8-periods) taper and the variant-stair (8-periods) taper. On the lateral wings of far-field pattern for the variant-stair taper, the ratio of 2nd even mode intensity was estimated to be about 0.2 with respect to the fundamental even mode. The ratio was higher and reached 0.34 for the stair taper, in which, the divergence angle (on $1/e^2$ intensity) of fundamental even mode was about 19^0 at 1.6 μm wavelength, corresponding roughly to a mode size of 6.1 μm-diameter. In a shorter wavelength, the ratios of higher-order modes seemed to be further reduced.

The far-field patterns for short tapers showed a high-order modes propagation regime which was similar to the simulation results presented in table 4.1, except that the modal distributions did not match completely. In a short stair taper (4-periods) taper, the three lowest even modes were all observed at 1.45 μm wavelength, but not totally at 1.6 μm wavelength. For the short variant-stair (4-periods) taper, the similar trend was observed as well; however, the measured intensities of higher-order modes were reduced obviously compared to the simulation result and the ones of stair taper. We think that certain disagreements between the simulation and measurement are probably attributed to the hole sizes variation after fabrication.

For the curved tapers, the far-field patterns presented a fundamental even mode dominant status for designs with contours of gaussian curve and double-parabola, accompanying with small amounts of higher order modes on the lateral wings. For the gaussian curve taper, the ratio of 2nd even mode intensity was 0.22 with respect to the fundamental even mode at 1.6 μm wavelength. In both PhC tapers, the high-order modes intensities were reduced at 1.45 μm wavelength, but the divergence angles further increased.

The performance of double-parabola taper was in general similar to the one of gaussian curve taper, but its high-order modes showed a larger occupation. In contrast, by analyzing the far-field patterns of semi-ellipse taper, the 2nd even mode was relative principal with an intensity ratio of 1.21 times with respect to fundamental mode at 1.6 μm wavelength. These results have a similar trend to the simulation results.

For the gaussian curve taper, the divergence angle was about 23^0 for the fundamental even mode at 1.6 μm wavelength, which corresponded roughly to a mode size of 5.1 μm-diameter. However, the measured divergence angle for a cleaved-facet SMF was in the order of 16.4^0 on $1/e^2$ intensity. A coupling loss may thus be imposed between the fiber and the PhC taper.

The measured couping efficiency enhancements and divergence angles together with the estimated modal conversion for several fabricated PhC tapers are listed in table 4.5.

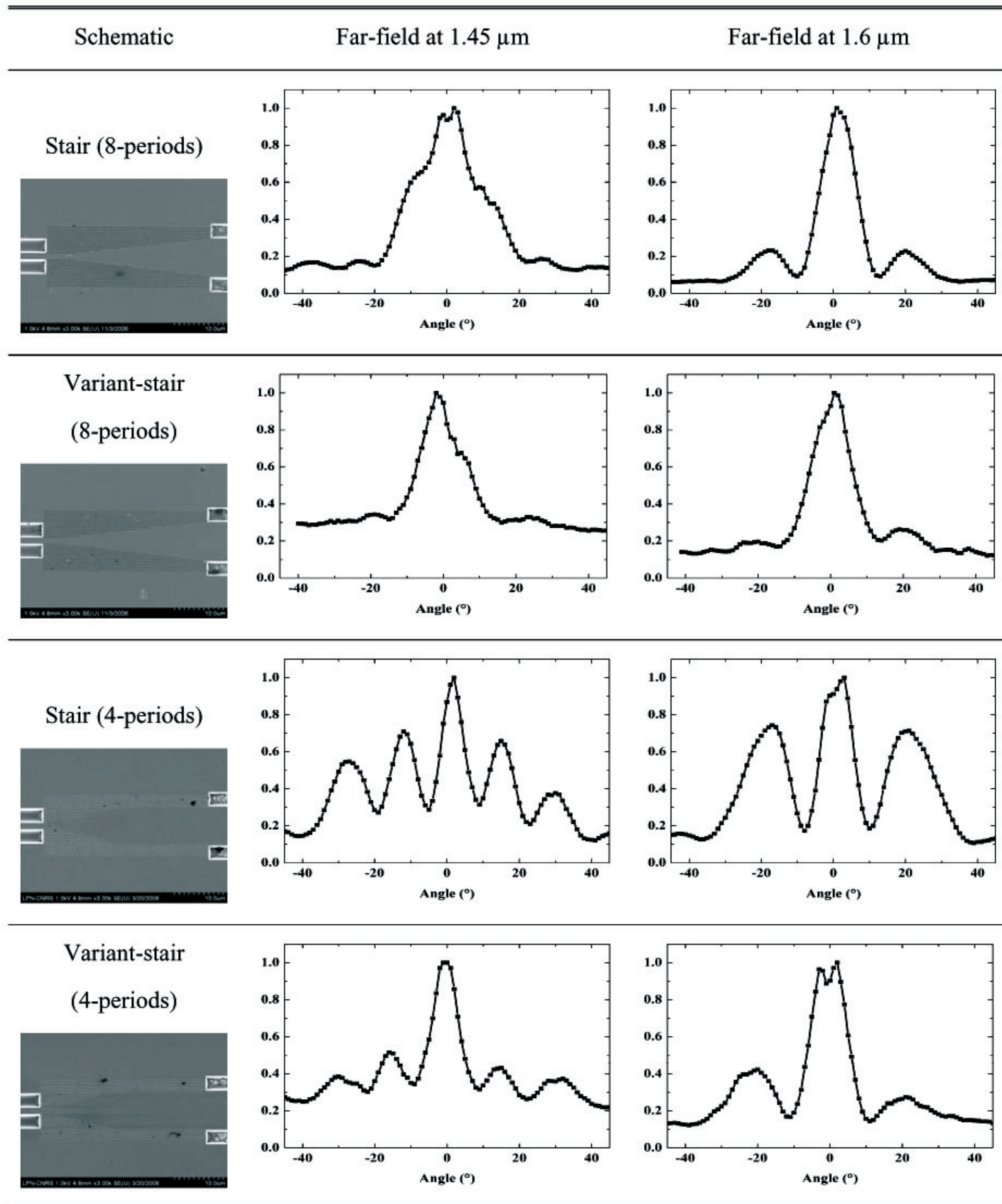

Table 4.3: The measured far-field divergence diagrams for PhC tapers with geometries of stair (8-periods), variant stair (8-periods), stair (4-periods), and variant stair (4-periods) at 1.45 μm and 1.6 μm wavelength.

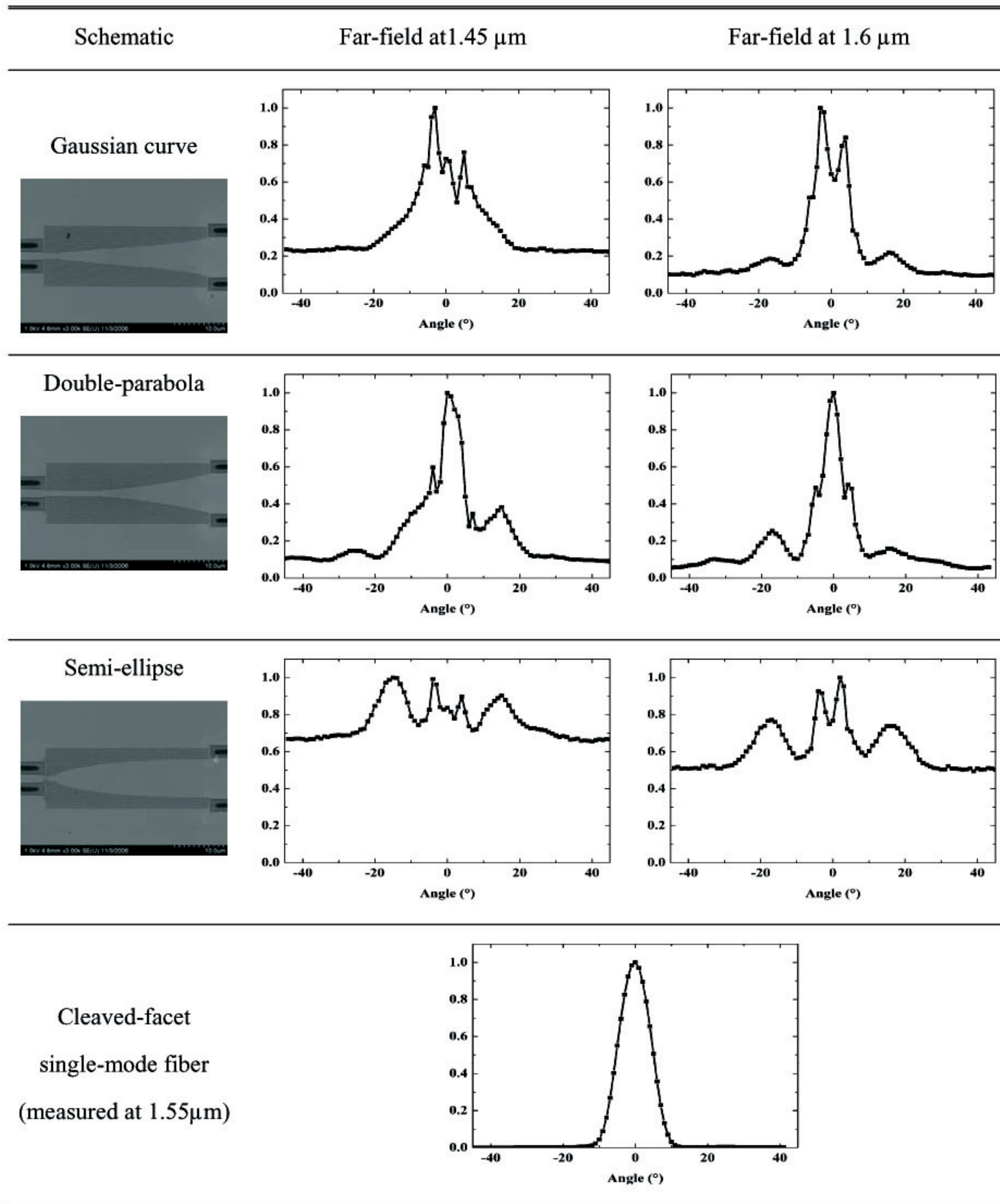

Table 4.4: The measured far-field divergence diagrams for the PhC tapers with contours of gaussian curve, double-parabola, and semi-ellipse at 1.45 μm and 1.6 μm wavelength. The divergence diagram for a cleaved-facet single-mode fiber at 1.55 μm is shown for reference.

PhC taper geometry	Coupling efficiency enhancement a)	Estimated modal conversion b) ($2^{nd}/1^{st}$ even mode, 1.6μm)	Divergence c) (1st even mode, 1.6μm)
Stair (8-periods)	–	0.34	19°
Variant-stair (8-periods)	–	**0.2**	25°
Stair (4-periods)	–	> 2	–
Variant-stair (4-periods)	–	0.65	–
Gaussian curve	**3.9**	**0.22**	23°
Double-parabola	–	0.48	20°
Semi-ellipse	1.8	1.21	–
Cleaved-facet SMF			16.4° (at1.55μm wavelength)

$^{a)}$: Coupling efficiency enhancement is derived from the comparison of transmission spectrums at 1.61-1.62 μm wavelength for PhC tapers and PhC W3 guide. Their overall (ridge + PhC section) lengths are identical.

$^{b)}$: The modal conversion values are estimated from the measured intensity of 2nd even mode with respect to the one of fundamental even mode.

$^{c)}$: From the far-field patterns, the divergence angle values are decided on $1/e^2$ intensity at 1.6 μm wavelength.

Table 4.5: The summary of measured coupling efficiency enhancement and estimated modal conversion rates and divergence angles for designed PhC tapers.

Optical characterizations including the transmission spectra collected by a cleaved-facet fiber and the far-field measurement are performed for our designed PhC tapers.

1. In the transmission spectra, the reduced transmitted power around 1.54 μm wavelength is observed for a W3 guide due to the mini-stop band of fundamental even mode propagation. In taper designs, this reduction is found to be more eased since the width comparable to a W3 guide is much shorter.

2. From the transmitted power diagrams, an enhancement by a factor of 4 is obtained with the presence of gaussian curve taper compared to a W3 guide.

3. For the far-field patterns, a similar trend to the simulation results is observed for all the designed PhC tapers. The light divergence angles are about 19^0 and 23^0 corresponding to mode sizes of 6.1 μm and 5.1 μm in the lateral plane for the stair taper and the gaussian curve taper. The 2nd even mode intensity ratio is found to be lowest, in the range of 0.2∼0.22 with respect to the fundamental even mode, for the variant-stair and gaussian curve tapers.

4.6.4 Coupling losses estimation

As introduced in section 4.1.3, the coupling losses of fabricated PhC tapers to a cleaved-facet single-mode fiber are being estimated in this section by analyzing the transmitted powers in the conventional plain ridge, W3 guide, and PhC tapers within the wavelength range of 1.61∼1.62 μm which is out of MSB range.

In our devices, the reduced transmitted powers may arise from the propagation losses in ridges and PhC section, the coupling losses at the ridge-PhC waveguide intersection, the coupling losses between fibers and input/output access ridges. The lengths of input/output access ridges and the PhC section are designated as L_{R1}, L_{R2}, and L_{pc}, respectively. α_R and α'_R account for the propagation losses coefficients for the 1.38 μm and 8.3 μm-wide ridges; and α_{W3} and α_T refer to the propagation losses in a W3 guide and an arbitrary PhC taper section. $C_{\mu R}$ represents the coupling losses from a micro-lensed fiber to the 1.38 μm-wide ridge and $C_{R\mu}$ denotes the coupling losses in an inverse transmission direction. C_{W3} and C_T are those coupling losses from the output access ridge to a cleaved-facet fiber in the cases of possible modal distribution modification by a W3 guide and any PhC taper. An additional coupling loss at the ridge-PhCW intersection (A) should also be included. The notations of losses are presented schematically in figure 4.9. Further, a plain ridge (without PhC section) is designed and measured as well for retrieving the coupling losses (1.38 μm-wide ridge to micro-lensed fiber) value. The alignment using piezo-electrical motors is reproducible and gives a small error in the order of 0.5 dB between each measurement. Then, we suppose that the alignments between fibers and waveguides are invariant.

For a plain ridge, the transmitted power collected by a micro-lensed fiber ($L_{total\mu1}$) was measured and the total losses can be expressed as

$$L_{total\mu1} = C_{\mu R} + \alpha_R \cdot L_R + C_{R\mu} = -21.6dB \qquad (4.7)$$

L_R is a known value (= 369 μm) by measuring directly the plain ridge length and α_R is estimated to be about -15 dB/cm from the previous calculation [Talneau2001]. Assumed that within the plain ridge, the mode profile is conserved during the propagation; in another word, the fields overlap integration between fibers and ridges is identical at the input and output sides. Hence, the coupling losses $C_{\mu R}$ and $C_{R\mu}$

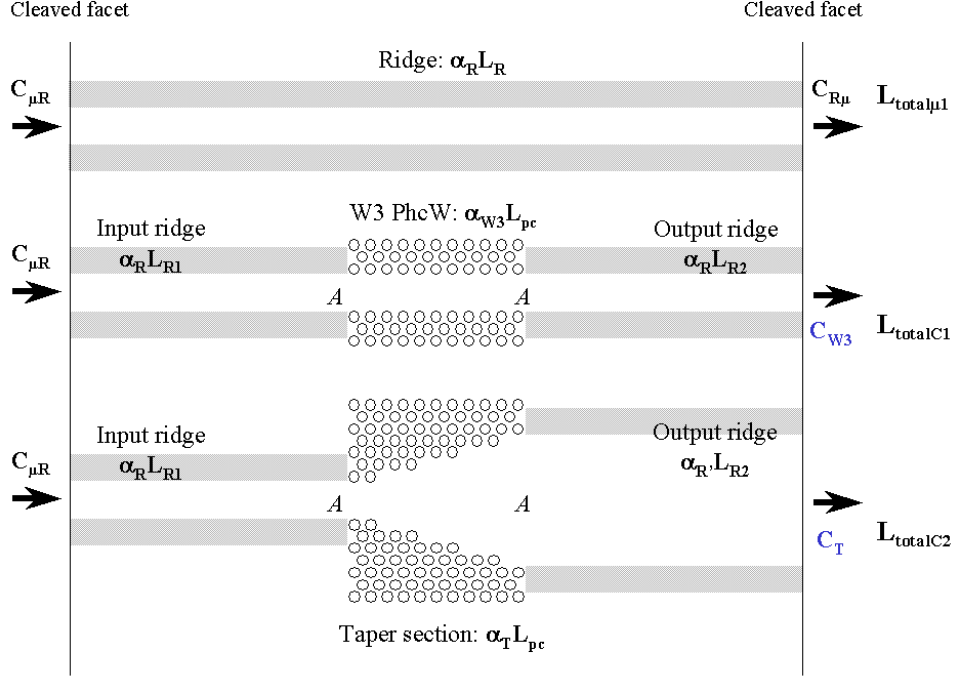

Figure 4.9: The notations of propagation losses within a conventional plain ridge, a W3 guide, and a PhC taper. The light is injected by a micro-lensed fiber and is collected either by another micro-lensed fiber or by a cleaved-facet fiber.

are differed by the value of transmission coefficient η. As shown in section 4.2.2, the transmission coefficient is calculated approximately to be 0.96 and 0.705 for coupling into a planar waveguide (n = 3.38) and into a fiber (n = 1.5), respectively. By designating the field overlap as M, the coupling losses at the input and output sides can be reformulated as $C_{\mu R} = 10log_{10}(0.705M)$ and $C_{R\mu} = 10log_{10}(0.96M)$. The, equation 4.7 can be solved and it gives $C_{\mu R}$ = -11.2 dB.

In a W3 guide, the total losses value retrieved from a cleaved-facet fiber can be expressed as

$$L_{totalC1} = C_{\mu R} + \alpha_R \cdot L_{R1} + \alpha_{W3} \cdot L_{pc} + \alpha_R \cdot L_{R1} + 2 \times A + C_{W3} = -30.9dB \quad (4.8)$$

In which, $C_{\mu R}$ is known from the above calculation and L_{pc} is designed as ∼34 μm. The overall length of access ridges ($L_{R1} + L_{R2}$) thus equals to $L_R - L_{pc}$. From section 3.5.4-B, the propagation losses value is reported to be -80 dB/cm in a W3 guide etched using an ICP Cl_2/Ar plasma. Moreover, the coupling efficiency at the intersection of ridge-W3 is often evaluated as 95%, which corresponds to -0.223 dB coupling losses. With these values, the C_{W3} is then estimated to be -18.5 dB from equation 4.8.

	Estimated coupling losses (dB) (to a cleaved-facet fiber)
W3 PhCW (without taper)	-18.5
PhC variant-stair taper (8-periods)	-12.7
PhC semi-ellipse taper	-16.2
PhC gaussian curve taper	-12.7

Table 4.6: The estimated coupling losses to a cleaved-facet single-mode fiber for the W3 guide without taper, the variant-stair taper (8-periods), the semi-ellipse taper, and the gaussian curve taper. The physical length of the PhC taper section is 34.4 μm.)

In an arbitrary PhC taper, the similar total losses can also be expressed and the measured result for the guassian curve taper is shown as

$$L_{totalC2} = C_{\mu R} + \alpha_R \cdot L_{R1} + \alpha_T \cdot L_{pc} + \alpha_R \cdot L_{R2} + 2 \times A + C_T = -25.1dB \quad (4.9)$$

The propagation losses coefficients of narrow PhCW and ridge waveguides are usually larger than the wide ones. But, the lengths of PhC taper section and access ridges are shorter than 150 μm in our samples; the losses differences between narrow and wide waveguides are small. Here, to simplify the calculation, we then assume that the propagation losses in a PhC taper section is equivalent to the one in a W3 section (i.e. $\alpha_T = \alpha_{W3}$). The propagation losses coefficient of the output ridge is also assumed to be identical to the one of the input ridge, which means $\alpha_R^{'} = \alpha_R$ = 15 dB/cm. Hence, based on these values, the coupling loss to a cleaved-facet fiber for the gaussian curve taper is estimated to be -12.7 dB.

Table 4.6 lists the coupling losses values for several PhC tapers with geometries of variant-stair (8-periods), semi-ellipse, and gaussian curve estimated by the same concept mentioned above. The absolute coupling losses value for a W3 guide is found to be reduced once the PhC taper is implemented. From the results, the variant-stair and gaussian curve tapers both show the best mode conversion efficiency and the coupling losses is estimated to be in the order of -12.7 dB.

The coupling losses from our designed PhC taper devices to a cleaved-facet single-mode fiber can be obtained by comparing the difference of measured total losses and those losses at other sections/interfaces. The coupling losses transmission intensity for a plain ridge injected and collected by a micro-lensed fiber is measured to derive the coupling losses from a micro-lensed fiber to a ridge.

Within proposed PhC tapers, the coupling efficiency is estimated to be highest for the variant-stair and the gaussuan curve geometries with a coupling losses in the order of -12.7 dB.

4.7 Conclusion

In this chapter, the simulation, fabrication and optical characterizations are investigated for PhC tapers which can be served as one building block in the future photonic integrated circuit. The tapers are fabricated on a planar heterostructure waveguide composed of PhC hole structures, in which the optical modes in lateral plane are confined by both the PhC band gap effect and the variation of the effective index (n_{eff}). The stair/variant-stair and curved tapers with a length of 34.4 μm are proposed to converse the optical modes from a 1.38 μm-wide ridge to a 8.3 μm-wide ridge, which corresponds to the physical core width of a cleaved-facet single-mode fiber. The 2-D FDTD simulations are performed to analyze the modal distributions at the exit side. The optical characterizations including the transmission spectra and the far-field patterns within 1.45$\sim$1.62 μm wavelength range show a similar trend to the simulation results.

Within proposed taper geometries, the variant-stair taper, where diameters of certain holes are diminished in order to reduce the scattering, and the gaussian curve taper show a fundamental even mode dominancy and a minimum coupling losses value. By the help of PhC taper, the coupling losses to a cleaved can be improved from -18.5 dB for a W3 guide to -12.7 dB. The transmitted power is also found to be enhanced by a factor of 4 for the gaussian curve taper.

The performances of our proposed PhC taper designs are believed to be further improved from the expectations of MSB prevention and the coupling losses reduction. The appearance of mini-stop band (MSB) would diminish the transmitted power for certain wavelength range. Even though it can not be avoided in a PhC channel defect waveguide, it is still possible to exclude the influence of MSB on the wavelength range of interest by choosing an appropriate PhC lattice periodicity. As for the coupling losses, it is expected to be reduced by further increasing the width at the exit side of PhC taper. Since the refractive index contrast in a InP-based ridge waveguide is much larger than the one in optical fiber, the mode size of waveguide is smaller than the fiber eigenmode size under the same physical width criterion. Moreover, with the introduction of the vertical taper, a circular mode profile at the exit side of waveguide is feasible. With these perspectives, the fields overlap between a cleaved-facet single-mode fiber and a photonic device can be increased and the coupling efficiency can thus be improved.

Chapter 5

Photonic crystals laser

5.1 Introduction

As mentioned already, PhC is considered as a good candidate for the integrated photonic circuits realization, in which the active functions including light emission and amplification with high performances are important research subjects. Generally, the light source devices are expected to provide proper power levels, to be operated in a low threshold current, and to be integrated monolithically with other components (ex: PhC waveguides and ridge waveguides). Several approaches of PhC based lasers have been proposed such as the defect cavity lasers [Seo2007], the large-area lasers using 2D PhC as mirrors [O'Brien1996], and the coupled-cavity lasers [Happ2003].

The defect cavity lasers could have a high quality factor and a very small modal volume. At first, the lasing in a PhC cavity was reported to be generated through the optical pumping [Painter1999]. Then, with the improvements on fabrications and designs, the electrically driven cavity laser has been demonstrated on membranes [Park2004]. Till now, the single-mode lasing has been achieved with a threshold current as low as $\sim$100 μA pulsed current [Seo2007]. However, in suspended membranes, the disadvantages of poor heat dissipation and difficult electrical implementation would still limit the applications.

In conventional laser structures, the selectivity on emitted mode generally can be improved by the helps of two mechanisms known as the distributed feedback and the coupled-cavity. By making the feedback frequency dependent to the cavity losses, the side modes are suppressed both due to lower gain values and larger losses, and it then leads to a sing-mode emission. Similarly, these two mechanisms can be applied in PhC-based laser structures.

2D PhC matrix can be alternatively incorporated as the resonator mirrors in large-area ridge lasers. This concept is basically inherited from the deeply etched one-dimensional distributed Bragg reflectors (1D DBR mirrors) [Baba1996,

Smith1996]. Generally, the facet cleavages and facet coatings are not quiet suitable for the fabrication of photonic integrated circuits. Nevertheless, for the PhC mirrors, the reflectivity is estimated to be nearly unity in the ideal case for certain wavelength range and the threshold current can thus be lowered. A short cavity length down to 100 μm with two PhC mirrors has been fabricated with a low threshold current of 7.6 mA under continuous wave (cw) operation [Happ2001a]. Moreover, with a design of coupled-cavity, in which the PhC acted as the rear mirror and the intra-cavity mirror, the longitudinal wavelength selection could be provided with a side-mode suppression ratio (SMSR) more than 35 dB [Happ2001b].

From another viewpoint, the corrugations inside a PhC channel defect waveguide can be viewed as distributed-feedback-like gratings. A SMSR exceeding 40 dB has been reported for optically pumped PhC waveguide lasers along ΓK and ΓM directions [Checoury2004]. Through the electrically driven, a SMSR more than 25 dB for the fundamental mode existing within the photonic gap was also obtained when an additional periodicity of air holes was included [Talneau2004a].

While employing the PhC, its unique dispersion relation may allow the mode selection through another mechanism. It has been shown that the lasing could occur at the edge of the defect waveguide mode in a 2D PhC membrane [Sugitatsu2003]. In the dispersion curve of PhC line-defect membrane waveguide, the group velocity tends to be zero at the edge of Brillouin zone. In another word, the lasing oscillation is preferential at these edges since the optical densities of state are higher than other frequencies. Therefore, with an appropriate choice of PhC periodicity, the emitted wavelength selection can be achieved.

Since the proposal of coupled-resonator optical waveguide (CROW) [Yariv1999], its unique small group velocities property may enable the applications on optical delay lines, buffers, and lasers. The CROW is composed of a periodic array of resonators with weak inter-resonator coupling. The light guiding is realized more likely by hopping along this series of coupled resonators. A CROW laser has been simulated numerically and the lasing threshold was shown to be lowered due to the reduced group velocity [Mookherjea2004]. In a PhC environment, the concept of CROW was equally introduced. An electrical driven PhC laser was fabricated based on coupled hexagonal defect micro-cavities and the mini stop bands were thus created within the photonic band gap due to the individual cavity modes coupling [Happ2003]. In this structure, a single-mode lasing with a SMSR more than 40 dB was obtained and the emitted power could be up to 2.6 mW under the cw operation.

For the structure mentioned above [Happ2003], the relatively high threshold current (∼15 mA) in PhC coupled cavity waveguide laser would probably origin from the limited overlap between confined light mode and injected current distribution, especially with etched holes situating along the cavity axis. Therefore, a constricted PhC waveguide was proposed to incorporate with the laser structure to form a two-coupled cavity [deRossi2005]. In this structure, no holes were

drilled along the cavity axis, which might lead to a higher external efficiency. The constricted section acted as an internal reflector and the transmission/reflection coefficients could be adjusted by varying the section length, the hole sizes, and the constricted levels.

Here, our research interests focus on the electrical driven edge emitting lasers with PhC structures for mode selection and tuning. The designs are conceived and chosen under the considerations of mono-mode operation, wavelength selection, low threshold current, and high external efficiency. In a coupled-cavity laser design, all these considerations can be achieved. Within this dissertation, we investigate the multiple-constricted-waveguides (MCW) lasers which behave like a CROW while the cavities are strongly coupled. Therefore, the calculation of coupling coefficients developed by A. Yariv [Yariv1999] can not be applied in the case of MCW. In the following, we calculate the modal transmission and reflection ratios for one single constriction using the 2D FDTD calculation method. By knowing these values as well as the phase changes, the geometry of unit cavity can then be determined.

5.2 Laser designs based on coupled-cavity

The coupled-cavity laser has been known to provide the mode selectivity as well as the wavelength tunability. Its geometry consists of two cavities and the cavity to be coupled to can be external or integrated monolithically with the semiconductor laser. The mechanism of mode selectivity in coupled-cavity laser is to modulate one facet reflectivity to be wavelength-dependent. In another word, by choosing the refractive index, cavity length and other parameters of the second cavity, the effective facet reflectivity can be controlled artificially. The cavity loss thus varies with respect to different longitudinal modes of the laser cavity. As shown schematically in figure 5.1(b), the loss profile is generally periodic in the coupled-cavity laser. In this case, the mode is selected when the cavity loss is lowest and simultaneously the gain profile reaches closely to the maximum. Other longitudinal modes with lowest loss profile can be discriminated from the main peak due to a larger gain reduction. With a proper design, the side-mode suppression ratio is in the order of 20$\sim$30 dB. On the contrary, if the loss profile is independent of wavelength (figure 5.1(a)), the modes can distinguished only by the gain profile which is often equipped with a wide bandwidth.

The coupled-cavity laser can be categorized as active-passive and active-active schemes, relying on whether the second cavity is biased electrically to provide gain. In the active-passive one, the wavelength is tuned by changing the cavity length or the temperature. But, in the active-active one, both cavities are driven by the injection current and can be controlled independently. The refractive index varies with the carrier density and it then also leads to the wavelength tuning.

Here, the theory and notation of coupled-cavity are briefly reviewed for a gen-

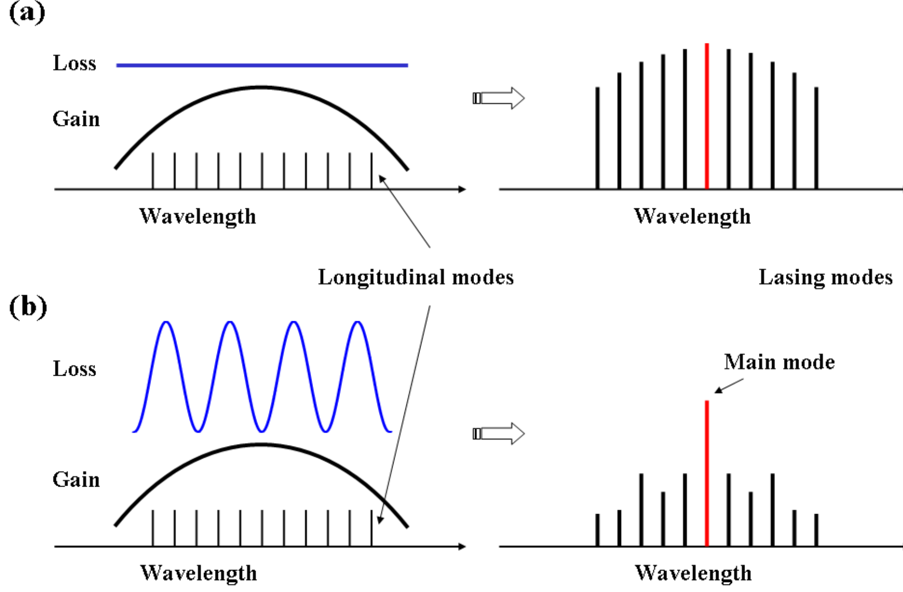

Figure 5.1: The schematic illustration longitudinal modes, gain profile, loss profile, and the resulting lasing modes for (a) a single-cavity semiconductor laser and (b) a coupled-cavity semiconductor laser.

eral case that the laser gain is provided by the two cavities, instead of the gap region. To simplify the analysis, it is assumed that the field distribution of fundamental mode within the waveguide is unaffected by the inter-cavity coupling and that only the axial propagation in each cavity is considered.

As presented in figure 5.2, the incident field E_1 to one facet next to the gap is partly reflected back to cavity 1 and partly transmitted to cavity 2 and vice versa for the incident field E_2. The reflected field $E_1^{'}$ is composed of the reflection from E_1 and the transmission from E_2. The fields within two cavities can then be related through the scattering-matrix approach as

$$\begin{pmatrix} E_1^{'} \\ E_2^{'} \end{pmatrix} = \begin{pmatrix} S_{11} & S_{12} \\ S_{21} & S_{22} \end{pmatrix} \begin{pmatrix} E_1 \\ E_2 \end{pmatrix} \tag{5.1}$$

S_{11} and S_{22} represent the effective reflection coefficients at the facets of gap, while S_{12} and S_{21} refer to the effective transmission coefficients from cavity 1 to cavity 2 and vice versa. These coefficients can be related to the gap facet reflectivity (r_1 and r_2), gap length (L_{gap}) and the complex propagation constant (β_{gap}) accounting for the phase shift and loss as the optical field traversing the gap. The expressions are as follows:

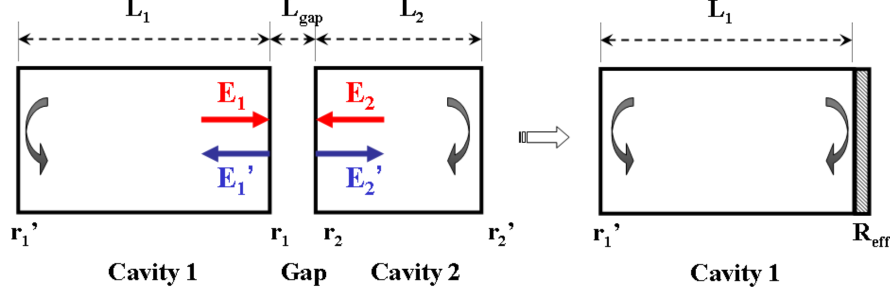

Figure 5.2: The notations used for effective mirror reflectivity theory of coupled-cavity laser.

$$S_{11} = r_1 - \frac{r_2(1-r_1^2)exp(2i\beta_{gap}L_{gap})}{1-r_1r_2exp(2i\beta_{gap}L_{gap})} \tag{5.2}$$

$$S_{22} = r_2 - \frac{r_1(1-r_2^2)exp(2i\beta_{gap}L_{gap})}{1-r_1r_2exp(2i\beta_{gap}L_{gap})} \tag{5.3}$$

$$S_{12} = S_{21} = \frac{[exp(2i\beta_{gap}L_{gap})(1-r_1^2)(1-r_2^2)]^{1/2}}{1-r_1r_2exp(2i\beta_{gap}L_{gap})} \tag{5.4}$$

where $\beta_{gap} = n_{gap}k_0 + i\alpha_{gap}/2$, k_0 and α_{gap} are the wave number and loss in gap, respectively. For convenience, the term of complex coupling parameter can be therefore defined as

$$\tilde{C} = C \cdot exp(i\theta) = (\frac{S_{12}S_{21}}{S_{11}S_{22}})^{1/2} \tag{5.5}$$

in which, C is the strength of mutual coupling and θ is the coupling phase. For given facet reflectivity values, C oscillates with the gap length and the light wavelength.

Now, we consider the reflected field traveling inside one cavity. After one round trip, the incident field can be written as

$$E_1 = r_1^{'}exp(2i\beta_1L_1)E_1^{'} \tag{5.6}$$

$$E_2 = r_2^{'}exp(2i\beta_2L_2)E_2^{'} \tag{5.7}$$

where the complex propagation constant is $\beta_m = n_mk_0 + i\alpha_m/2$ (m = 1,2), and α is the mode gain. Introduce equation (5.6) and (5.7) into (5.1), and the nontrivial solutions are obtained only when

$$[1 - r_1^{'}S_{11}exp(2i\beta_1L_1)][1 - r_2^{'}S_{22}exp(2i\beta_2L_2)] = r_1^{'}r_2^{'}S_{12}S_{21}exp(2i\beta_1L_1)exp(2i\beta_2L_2) \tag{5.8}$$

equation (5.8) is also known as the eigenvalue equation for the coupled-cavity system.

With another view point, the cavity 2 can be treated as a laser facet equipped with an effective reflectivity which is wavelength-dependent, as illustrated in figure 5.2 (right). Then, the eigenvalue equation can be reformed as $(1-r_1^{'}R_{eff}exp(2i\beta_1 L_1)) = 0$, in which the effective reflectivity is expressed as follows:

$$R_{eff} = S_{11} + \frac{r_2^{'} S_{12} S_{21} exp(2i\beta_2 L_2)}{1 - r_2^{'} S_{22} exp(2i\beta_2 L_2)} = S_{11}\left(1 + \frac{\tilde{C}^2 f_2}{1 - f_2}\right) \tag{5.9}$$

and $f_2 = r_2^{'} S_{22} exp(2i\beta_2 L_2)$ represents the fraction of amplitude coupled back into the laser cavity after a round trip in cavity 2.

With the concept of effective-mirror reflectivity, the coupled-cavity laser is then equivalent to the single-cavity laser with facet reflectivity coefficients $r_1^{'}$ and R_{eff} and the corresponding mirror loss of cavity 1 can be written as

$$\alpha_{mirror} = \frac{1}{L_1} \ln \frac{1}{r_1^{'} R_{eff}} \tag{5.10}$$

5.3 PhC laser designs based on multiple constricted waveguides

To increase the external efficiency of PhC CROW laser [Happ2003], the design is modified by introducing the constrictions. The presence of constriction leads to two different cavities which are not completely isolated. A multiple-constricted-waveguides (MCW), as shown in figure 5.3, can be somehow treated as a variety of CROW; but the extent of coupling is stronger in MCW than in CROW. Therefore, the developed theory and notations in CROW [Yariv1999] might be applied similarly in MCW with modifications.

A MCW system can be characterized by knowing the cavity length and the complex coupling parameter between cavities. The cavity length is defined as the distance between two consecutive constrictions (figure 5.3); and the narrowing section length that would be used for simulation is also indicated. The coupling parameter often relates the narrowing section length and the effective transmission/reflection coefficients. In the following section, we intend to obtain the transmission and reflection efficiencies and the phase changes while the light traversing a single PhC constriction section by 2D FDTD calculation.

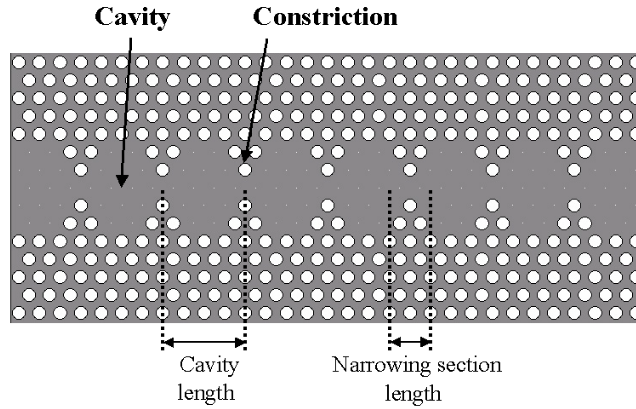

Figure 5.3: The schematic figure of PhC multiple-constricted-waveguides. The cavity length and the narrowing section length are defined as in the figure.

5.4 Simulation of constricted waveguides

Considering a single constriction section, as shown schematically in figure 5.4, it is analogy to the gap region with a coupled-cavity system. As a result, the concept of effective-mirror reflectivity mentioned in section 5.2 can also be applicable in the PhC constricted waveguides. To obtain successfully the reflectivity of effective mirror, parameters including the facets reflectivity, coupling constant, phase shift in constriction, the mode gain in the constriction section and the second cavity are required to be known. Within this dissertation, we attempted to simulate the effective transmission and reflection coefficient of a PhC constricted waveguide with varied constriction section lengths using 2D FDTD method [PhotonDesign].

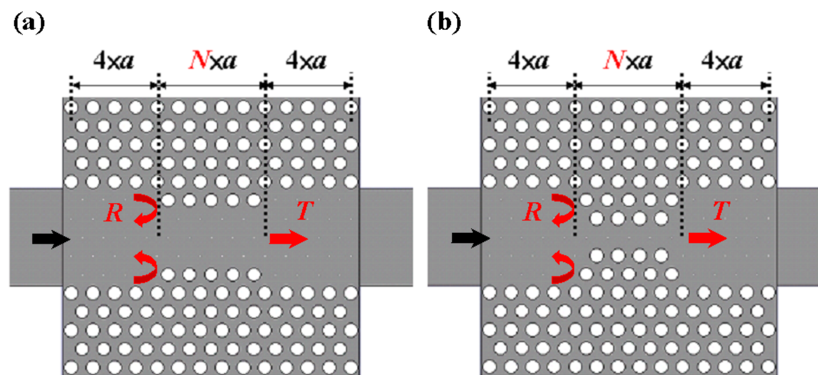

Figure 5.4: The schematic figures of simulated PhC constricted waveguide for (a) W5 constricted to W3 and for (b) W5 constricted to W1. The length of narrowing section is designated as $N \times a$ (N is an integral number). T and R signify the transmission and reflection through constriction section.

The simulated constricted waveguide consisted of a W5-based PhC channel defect waveguide along ΓK direction, constricted either from W5 to W3 (W5/W3, figure 5.4(a)) or from W5 to W1 (W5/W1 figure 5.4(b)). The essential PhC is a triangular array of air holes (a = 400 nm, d = 250 nm) drilled into a material with an effective index of 3.25. The W5 section length was chosen as $8 \times a$ and the narrowing section was inserted between. The narrowing section length is designated as $N \times a$ with N investigated from 1 to 7 and 2 to 7 for W5/W3 and W5/W1, respectively. Therefore, the total PhC constricted waveguide length was known to be $(8 + N) \times a$. It was then inserted within two 1.8 μm-wide conventional access ridges, which couple well to W5 sections. The access ridges are required imperatively since the source generation and the acquisition of modal transmission and reflection intensities can only be achieved by this way. The TE fundamental even mode was with a 20 fs pulsed width centered at 1.55 μm in the left input access ridge. Three detectors were placed in the input and output access ridges to serve as the reference and to acquire the reflected as well as the transmitted powers. The simulations were performed in the case that the material losses were not under consideration.

5.4.1 Simulation results of W5/W3 constricted waveguides

The simulated transmitted power and reflected power corresponded to notations of E_2' and E_1', respectively, as noted in figure 5.2. Since the simulation was executed when only the field (E_1) was incident into the constricted waveguide, the transmission and reflection intensities normalized to the incident intensity thus

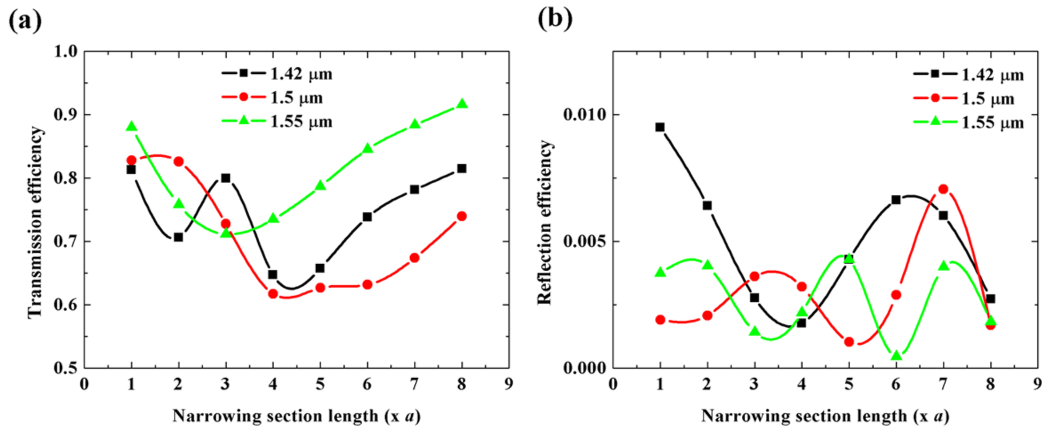

Figure 5.5: The simulation results of (a) transmission and (b) reflection efficiencies for the fundamental mode with variation of narrowing section lengths in W5/W3 constricted waveguides.

implied the effective transmission coefficient S_{21} $(= E_2'/E_1)$ and the effective reflection coefficient S_{11} $(= E_1'/E_1)$. Figure 5.5 presents the simulation results of transmission/reflection efficiencies for the fundamental even mode with varied narrowing section lengths for three different wavelengths including 1.42, 1.5 and 1.55 μm. Compared to other modes, the fundamental even mode is more involved in the lasing, because the overlap of active region and optical mode is largest. Hence, only the evolution of the fundamental even mode is concerned here.

The reflection efficiency is smaller than 0.01 (figure 5.5(b)), which suggests a strong coupling regime between two cavities in W5/W3 constricted waveguide. As for the transmission efficiency, the occupation of fundamental mode ranges generally between 0.6 and 0.9 depending on the selected wavelengths and the narrowing section lengths. It should be pointed that both S_{21} and S_{11} vary with the gap width for a given wavelength (equation (5.4) and (5.2)) and the propagation constants differs due to different wavelengths. Therefore, as shown in figure 5.5(a), we observe a significant variation of transmission efficiencies with narrowing section lengths as well as wavelengths. Higher-orders even modes can be excited as well when the incident light traversing the constriction section. The maximum efficiency might reach 0.25 for the 2nd even mode (not shown).

5.4.2 Simulation results of W5/W1 constricted waveguides

The same method to simulate the transmission/reflection efficiencies for the fundamental mode was performed in W5/W1 constricted waveguide and the results are presented in figure 5.6. Since the liner defect width is reduced in W5/W1

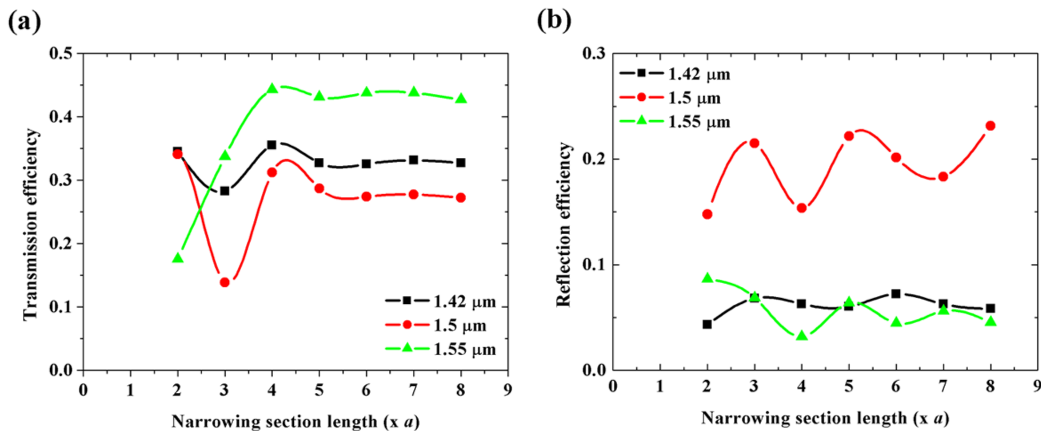

Figure 5.6: The simulation results of (a) transmission and (b) reflection efficiencies for the fundamental mode with variation of narrowing section lengths in W5/W1 constricted waveguides.

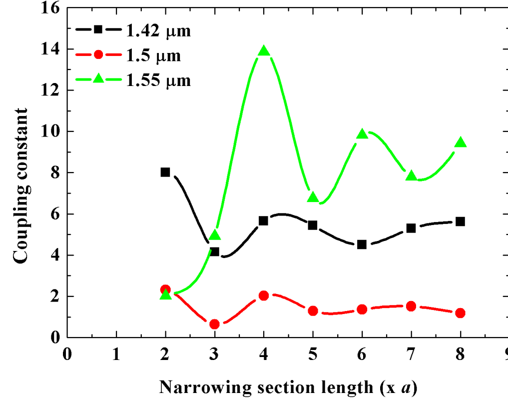

Figure 5.7: The simulated coupling constants with variation of narrowing section lengths for W5/W1 constricted waveguides at several different wavelengths.

constriction, the transmission is expected to be lower and it thus leads to higher reflection efficiency than the W5/W3 constriction. The fundamental mode transmission efficiency varies both with narrowing section lengths and wavelengths in the range between 0.15 and 0.45 (figure 5.6(a)). While for a longer constricted section, $> 5\times a$, the values change less obviously with respect to the section length. As for the fundamental reflection efficiency, it is 0.05 averagely for 1.42 and 1.55 μm-wavelength, and increases to 0.2 for 1.5 μm wavelength (figure 5.6(b)). The occupations of higher-orders modes (i.e. the 2nd even and the 3rd even modes) in transmission and reflection intensities are relatively larger in W5/W1 constriction than in W5/W3 constriction.

In W5/W1 constricted waveguide, the overall calculated powers can be less than 0.8 for certain wavelength ranges. In which, the coupling efficiency to the access ridge guide for the transmitted/reflected fundamental modes is believed to be slightly worse than in W5/W3 constricted waveguide. Therefore, the reduced fundamental mode occupations (calculated at the access ridges) are attributed not only to the fact of coupling to higher-orders modes, but also to a poorer mode matching between access ridges and W5 PhC section containing constrictions.

As mentioned in equation (5.5), the coupling constant (C) relates the effective transmission coefficients (S_{12} and S_{21}) and effective reflection coefficients (S_{11} and S_{22}). The simulations presented above are reversible; in another word, $S_{12} = S_{21}$ and $S_{11} = S_{22}$. Therefore, the coupling constant can be simplified to be $C = S_{21}/S_{11}$. Dividing the transmission efficiency by the reflection efficiency, we can obtain the coupling constant variation shown in figure 5-7. The coupling constant is known to depend both on the gap length and wavelength. Hence, the oscillation with the narrowing section length is observed and its wavelength dependence is found and contained through propagation constant (β) values.

5.4.3 Discussion: MCW design rules

The above simulation results have several uncertainties. For modal occupations calculation, the conventional access ridges are required in simulations. In this case, the modal occupations are calculated when the measured powers are projected into the modes sustained in access ridges. The actual modal distributions of PhC waveguide modes cannot be obtained by the Photo Design simulation tool.

Besides the constraints due to the presence of access ridges, the coupling phase θ cannot be obtained either through this simulation program. For one sensor, the phase difference with respect to the reference sensor is calculated while taking into account the light propagation in both directions. In another word, the phase variations of transmission beam and reflection beam are not distinguished. We are not able to evaluate the coupling phase variation with the narrowing section length. Both the data of reflection amplitude and reflection phase change at one constriction are required to calculate the cavity length for the condition of constructive interference. But, it was not progressed successfully since we were not able to retrieve the phase of reflection at the constriction using the Photon Design simulation tool.

From the previous work [deRossi2005] and the above results, we chose the case W5 waveguide constricted to W1 along the ΓK. From figure 5.5(b), the reflection efficiency in W5/W3 constriction is very small. With this constriction, the measured SMSR was restricted at 25 dB [Talneau2004a]. A W5/W1 constriction is then preferred because it can provide a larger reflection efficiency (figure 5.6(b)); thus, it may leads to a larger SMSR value.

The multiple-constrictions can be considered as an additional periodicity built on the PhC matrix, which provides the contradirectionnal feedback for the fundamental mode at a certain order. The mechanism is known as high-order DFB effect. To estimate the proper cavity length operating at an in-phase modulation, we rely upon effective index estimation, as previously proposed in [Talneau2004a]. For example, we consider a PhC matrix (periodicity a) with a PBG range where the light emission wavelength at 1.55 μm lies. For the fundamental mode of W5 guide in refractive-like domain with effective index n_{eff}, the feedback can occur when the additional periodicity is

$$\Lambda = 1.55/2n_{eff}$$

Because the constriction is built on the grid of the PhC matrix with period a, the distance $P \times a$ between two constrictions would produce a DFB effect operating at order m when:

$$P \times a = m \times \Lambda \text{ } (P, \, m \text{ are integers})$$

This rough estimation mentioned above was a first attempt for the MCW de-

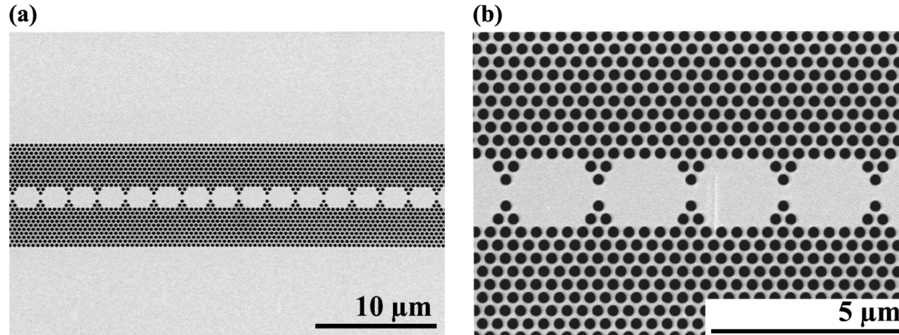

Figure 5.8: (a) SEM top view of etched PhC multiple W5/W1 constricted waveguide laser. (b) Magnification on the constrictions and coupled cavities.

sign. Numerical calculation that gives both the reflection amplitude and phase values at the constriction is expected to assist in conceiving a correct MCW design. But, up till now, we have not yet obtained all the required data.

In order to ensure the feedback effect on the fundamental mode, we intent to calculate the folded dispersion curve of the periodic structure and identify the fundamental mode through the field pattern. This systematic research is difficult because the dispersion diagram is very dense due to a large periodicity (4 or 6 periods) and also due to the wide guide (W5) which leads to a large number of guided modes. The dispersion curve of a W5/W1 MCW with a shorter periodicity ($3 \times a$) is calculated and presented in section 2.4.2.

5.5 PhC multiple-constricted-waveguides laser fabrication

The PhC multiple-constricted-waveguides laser is fabricated on the InGaAs/ InGaAsP multiple quantum wells structure emitting around 1.55 μm wavelength. The vertical stacking has been described in detail in section 3.2.1. The investigated PhC MCW lasers are W5 waveguides constricted to W1 along the ΓK direction with a constriction length of 4, 6, or 8 periods. The PhC building block is composed of a triangular periodicity of air holes ($a = 400$ nm and $f = 35\%$). Figure 5.8 shows the SEM top views of a fabricated W5/W1 MCW laser with a cavity length of $6 \times a$ and a single-row constriction.

To attain a good light confinement in the planar direction, the 2D PhC air holes should be etched through the active layer and reach an etch depth more than 4 μm. The optimized ICP Cl_2/Ar plasma reported in section 3.5.2 is then difficult to meet this demand. Therefore, the etching method by CAIBE with chlorine as the reactive gas [Berrier2007] is chosen and performed by A. Berrier and S. Anand

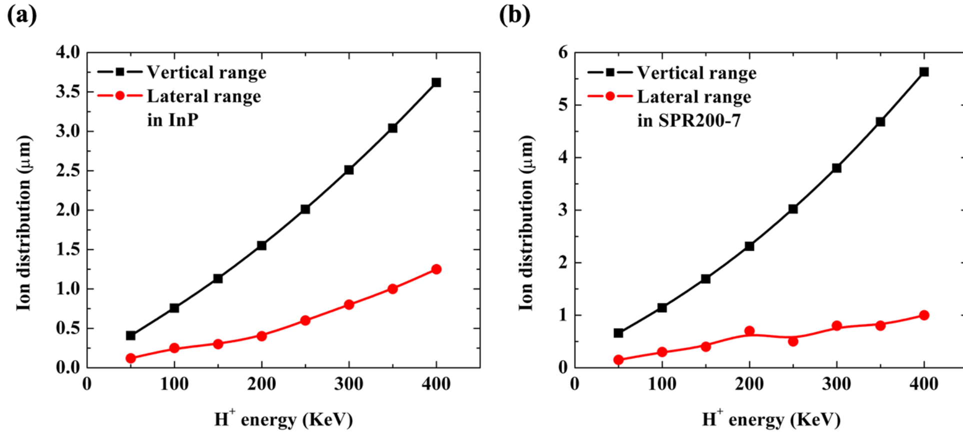

Figure 5.9: The simulation results of H^+ ion distributions in vertical and lateral directions in (a) InP and (b) photo-resist SPR 200-7 materials.

in KTH Sweden.

After etching the PhC holes and removing the dielectric mask, the metals including 150 nm-Au/30 nm-Ti/150 nm-Pt are deposited on the top of InGaAs layer, patterned by the electron beam lithography, and then etched by ion beam etching (IBE) to form the p-side electrode. To localize the electrical current path, the implantation of hydrogen ions (H^+) is often employed to isolate a major part of InGaAs and InGaAsP layers. The photo-resist, for the electrical pad etching, can also be used as the mask for H^+ ion implantation. Figure 5-9 presents the simulation results of ion distribution ranges (vertical and lateral) in InP and photo-resist with the function of H^+ energy. The simulation was performed using the SRIM software developed by J. F. Ziegler et al. [SRIM2003]. To reach a good injection current confinement, H^+ ions are expected to arrive closely to the active layer, about 200∼500 nm above the quantum wells. The H^+ distribution extends as well laterally and should be considered during patterns design. It is possible to control precisely the non-implanted area by adjusting the width photo-resist pattern.

Once the ion implantation is done, the sample is thinned to a thickness of 120∼140 μm and followed by the n-side electrode (150 nm-Au/30 nm-Ti) deposition. Finally, the sample is cleaved to form smooth crystalline mirror-like facets.

5.6 Discussion

It should be emphasized that, in a MCW system, the coupling between cavities are relatively strong. Therefore, the coupling through several neighbors should be considered, not only the nearest neighbor coupling. The simulations reported in section 5.4.1 and 5.4.2 can allow us a simplified depiction to conceive the proper

layouts of PhC MCW laser for wavelength selection purpose. To fully understand and control the mode selection, a more rigorous simulation study should be developed as well as the experimental results analysis. The fabrication and optical measurement of PhC MCW laser are in progress in LPN.

Chapter 6

Photonic crystals membrane waveguides

6.1 Introduction

The developments of 2D PhC defect waveguides with the vertical confinement provided by the heterostructure are somehow limited due to the large propagation losses, in which values in the range of 15$\sim$100 dB/cm have been reported for W3 waveguides. Those losses can origin from the properties of PhC geometries (intrinsic losses) and the out-of-plane scattering (extrinsic losses). However, in the heterostructure, this out-of-plane loss to the substrate is often inevitable due to the low index contrast. As a result, the PhC membrane characterized by high index contrast is being paid attention widely since several years. It has been reported that, for PhC membrane waveguides, the guided modes are without losses while situating below the light line; on the contrary, modes can exhibit losses due to the coupling to the continuum of the radiation modes [Johnson1999, Johnson2000].

Up to now, the PhC membrane waveguides are mostly realized on GaAs and Si materials since the fabrication technologies for silicon are mature and those for GaAs-based PhC have progressed remarkably. Therefore, the fabrication imperfections arising from etching process can be minimized. For the GaAs W1 PhC membrane waveguides, the minimum measured propagation losses value has been reported to be 5 dB/cm [Combrie2006]. For the Si materials, the propagation losses were found to be in the order of 2-10 dB/cm [Dulkeith2005, Kuramochi2005, Kuramochi2006]. In which, the bandwidth of low-loss propagation can be even increased to 125 nm [Kuramochi2005].

Except pursuing a low-loss propagation regime, the specific properties of small group velocity at the band edges and high quality factor are under investigation based on PhC membranes. The group velocity can be slowed down through the designs of hole sizes modification in PhC matrix, coupled resonators, and PhC coupled

waveguides. Experimentally, the group velocities have been reported to be in the range of $c/30 \sim c/60$ (c is the light velocity in vacuum) [Frandsen2006, Huang2007, Mori2007]. Further, an extreme high quality factor reaching 800,000 has been obtained by using a mode-gap confined PhC membrane nanocavity [Kuramochi2006].

The PhC membrane waveguides based on InP materials are also being developed [Letartre2001, Mulot2004b] because not only a theoretically lossless propagation can be sustained while operating below the light line, but the light emission can be also enhanced due to a reduced group velocity once the quantum-wells or quantum-dots structures are included. It is known already that the etching process of PhC hole structures for InP materials are not yet completely established compared to GaAs and Si. But, for the PhC suspended membrane devices, the deep etching issue can be avoided subtly since the membrane thickness does not exceed 300 nm while operating in a mono-mode regime. Therefore, the requirements of smooth and vertical sidewalls turn to be critical and play important roles in determining the propagation losses and the quality factors.

In the following sections, the selection wet etching would be characterized for InP membrane fabrication. Then, the PhC W1 suspended membrane waveguides are fabricated using an ICP BCl_3/N_2 plasma (section 3.6.3) in order to determine the propagation losses.

6.2 Selective wet etching calibration

The selective wet etching is used to realize InP suspended membranes. The principle is to chemically dissolve a sacrificial layer and the membrane is then suspended in air. In figure 6.1, the selective wet etching is shown schematically for a InP membrane with PhC holes structure. It is mandatory that the etch depth extends to the InGaAs sacrificial layer. Subsequently, the sample is dipped into the solu-

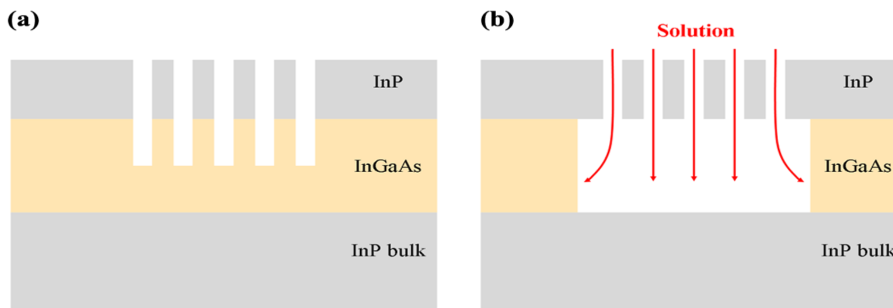

Figure 6.1: The schematic of selective wet etching process on a InP membrane with PhC holes structure. (a) PhC holes after dry etching and removal of mask. The etch depth is extended to the sacrificial layer. (b) The solution enters through the PhC holes and etches selectively the sacrificial InGaAs layer.

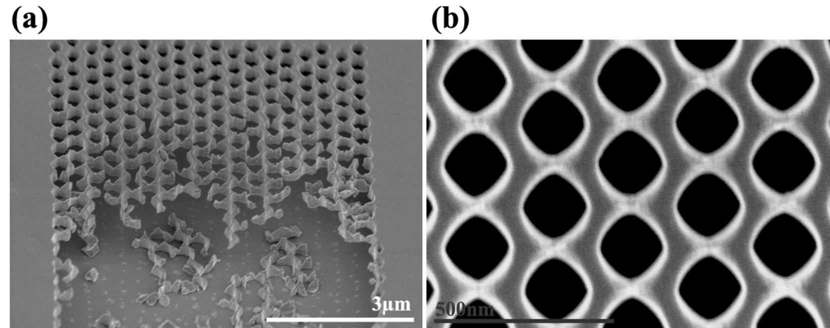

Figure 6.2: The SEM top views of (a) a InP suspended membrane with PhC holes structure. The selective wet etching of InGaAs layer was realized using a H_2SO_4:H_2O_2:H_2O = 1:1:10 solution (4 minutes). (b) Magnified view on PhC holes.

tion. Due to the holes opening, the solution is allowed to pass through and then etch selectively the sacrificial layer.

In the following, the calibrations of selective wet etching including H_2SO_4, H_3PO_4, and Fe-based different solutions were performed on a InP (340 nm)/ InGaAs (750 nm)/InP bulk sample with InGaAs as the sacrificial layer. The PhC holes structure was a triangular array of air holes (a = 400 nm, d = 250 nm) etched using an ICP-RIE BCl_3/N_2 plasma. The SiO_2 mask was subsequently removed in a diluted HF solution. After the step of selective wet etching, the sample was rinsed in D.I. water and dipped in Ethanol before being exposed to the atmosphere. The sample was then examined by SEM after cleaving through the PhC section.

In figure 6.2, the solution consisted of H_2SO_4:H_2O_2:H_2O = 1:1:10 [Naitoh2007] was used. The InGaAs sacrificial layer could be etched away in this solution composition, as can be seen in figure 6.2(a) for 4 minutes etch time; but, the InP membrane was not formed successfully. From figure 6.2(b), the SEM top view on

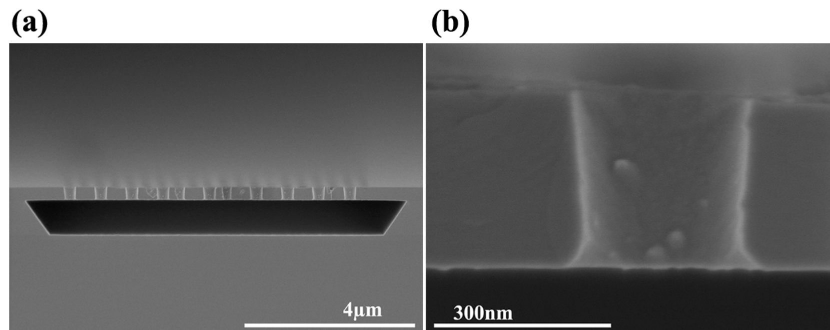

Figure 6.3: The SEM cross-section views of (a) a InP suspended membrane with PhC holes structure. The selective wet etching of InGaAs layer was realized using a H_3PO_4:H_2O_2:H_2O = 1:1:5 solution (3 minutes). (b) Magnified view on hole sidewalls.

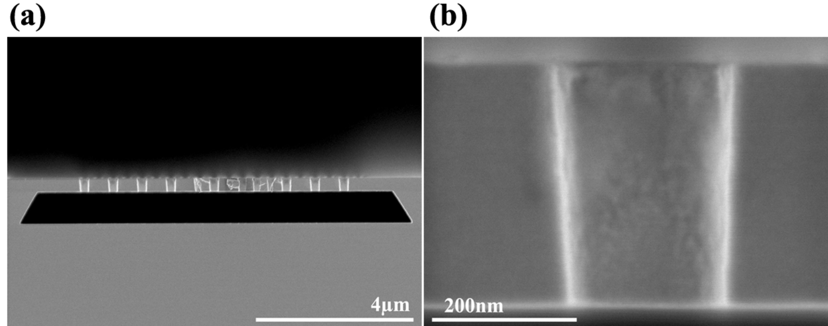

Figure 6.4: The SEM cross-section views of (a) a InP suspended membrane with PhC holes structure. The selective wet etching of InGaAs layer was realized using a solution based on Fe_3^+ ions (1.75 minutes). (b) Magnified view on hole sidewalls.

the PhC holes, it was found that the etching occurred as well along certain axes of InP materials. The PhC structure was more square-like and the interval distance was thus reduced; therefore the membrane was too fragile to be sustained.

We then tried another solution composed of H_3PO_4:H_2O_2:H_2O = 1:1:5 for InGaAs etching. After an etching duration of 3 minutes, a suspended InP membrane was obtained by this method, as shown in figure 6.4(a). But, from the magnification of hole sidewalls (figure 6.4(b)), this solution composition might deform slightly the InP layer. Another solution based on Fe_3^+ ions is then chosen for InP/InGaAs selective wet etching [Letartre2001] and shows a better performance. As presented in figure 6.4, not only the InP membrane is suspended in air successfully, but the hole profiles are also preserved by using this solution.

The selective wet etching with a solution based on Fe_3^+ ions is well demonstrated to etch the InGaAs sacrificial layer and to leave the InP membrane suspended in air.

6.3 PhC suspended membrane waveguide

6.3.1 Fabrication

The PhC membrane waveguide with one missing row along ΓK direction was fabricated on an InP (260 nm)/InGaAs (1500 nm)/ InP bulk heterostructure. The detailed vertical stack is described already in section 3.2.3. The PhC matrix was composed of a triangular array of air holes (a = 420 nm, $f \sim 30\%$). The PhC structure etching was realized using the ICP BCl3/N2 plasma with 24 and 99 sccm mass flow rates, respectively, and 5 mTorr total gas pressure, 1000W ICP power,

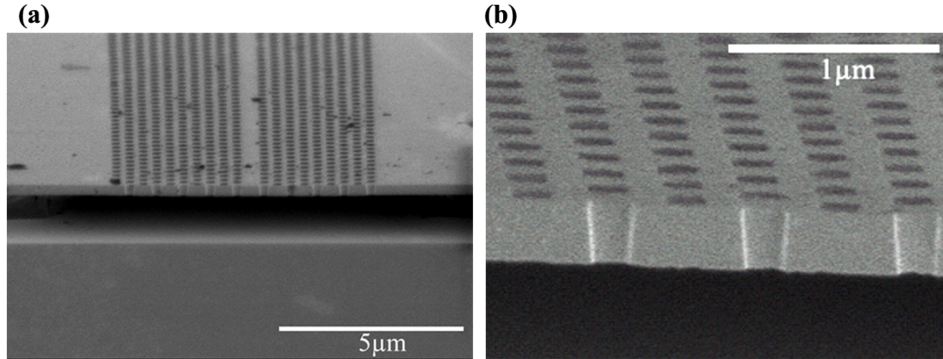

Figure 6.5: The SEM cross-section views of (a) a InP W1 PhC suspended membrane waveguide after InGaAs wet etching and supercritical drying in CO_2. (b) Magnification on the InP membrane with PhC holes. The PhC etching was performed using an ICP BCl_3/N_2 (24/99 sccm) plasma with 5 mTorr-gas pressure, 1000 W-ICP power, and -270 V-bias voltage.

-270V bias voltage. As the etch depth was only required to pass through the 260 nm-thick InP layer and to extend partly in the InGaAs layer, the etch time was limited to about 1.5 minutes in order to minimize the sidewall surface damages and the etched profile deformation due to the mask erosion. Figure 3.27(b) demonstrates the etching result in a InP substrate using these etching conditions. The slight surface roughness situating on the bottom of holes would not cause the influences on membrane waveguide performances, since it was removed away during the step of InGaAs selective wet etching.

After the ICP etching, the sample was thinned mechanically to a thickness of 120 μm and dipped in a diluted HF solution to remove the SiO_2 mask, followed by the cleavage for obtaining the input/output facets and several different waveguide lengths. Subsequently, the selective wet etching based on Fe_3^+ solution was applied and the supercritical drying in CO_2 was performed to release the strains in the structure. The SEM cross-section views on the fabricated InP W1 suspended membrane are presented in figure 6.5, in which the membrane is well suspended in air and the hole sidewall stays smooth after all the fabrication processes. It is noted that the cleavage should be performed before the wet etching; otherwise, the membrane was too fragile to be suspended.

6.3.2 Propagation losses measurement

To characterize the fabricated membrane waveguides, the transmitted powers were measured for waveguide lengths ranging from 300 μm to 1 mm by using the end-fire method injected with a fundamental even mode in TE polarization within the wavelength range of 1410-1525 nm. Figure 6.6(b) shows the spectrally resolved

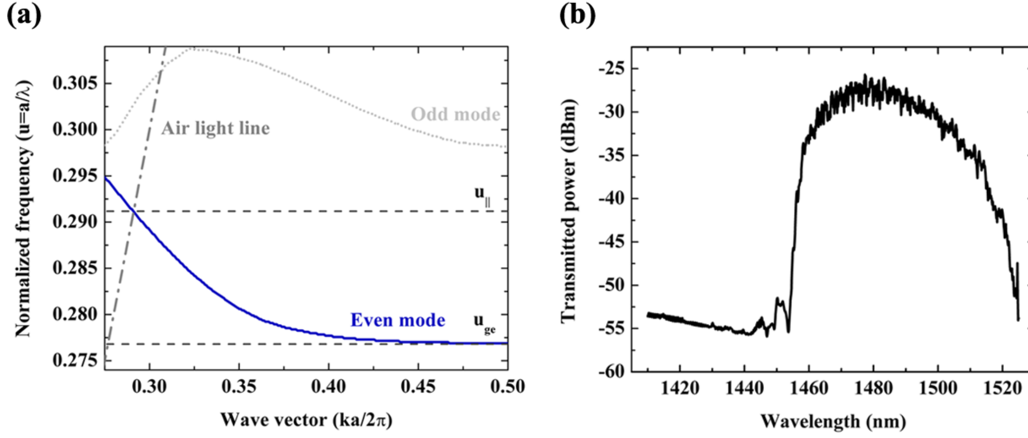

Figure 6.6: (a) Dispersion curve of InP W1 PhC suspended membrane waveguide for 280 nm-thick membrane (resized from figure 2.8(b)). (b) Spectrally resolved transmission spectrum of a fabricated 774 μm-long W1 guide.

transmission spectrum of a 774 μm-long InP W1 PhC suspended membrane waveguide. Above 1510 nm, the light transmission decays due to the mode-gap cutoff (u_{ge}), as indicated in the dispersion curve (figure 6.6(a)), at which the light propagation for the fundamental even mode is not allowed. Below 1453 nm, the light suffers pronounced losses. As marked as the light-line cutoff ($u_{||}$) in the dispersion curve, the mode above this cutoff would experience a large intrinsic radiation loss into the air.

The propagation loss value can be extracted by using the Fabry-Perot resonance method in a reduced frequency domain. In a PhC membrane waveguide, the guiding modes, with frequencies locating above the light line in the dispersion curve, may be coupled to radiation modes. Thus, it leads to a low intensity in the transmission spectrum. Hence, when we considered the frequency range situating below the air-light line, an overall propagation loss of 25 dB/cm [Talneau2008] was thus derived at 1480 nm wavelength.

Theoretically, the modes below the air light line and above the mode edge cutoff are lossless for ideal PhC membrane waveguides. Therefore, the measured propagation losses are extrinsic scattering losses due to fabrication imperfections including the surface roughness, the disorder on the hole shape [Gerace2004] and the hole position, and the hole verticality. It has been reported by numerical simulations that an additional propagation loss value of 5 dB/cm in PhC membrane waveguides is obtained arising from only 1^0 inclination [Tanaka2003]. In our suspended membrane waveguide, the propagation losses value might reduce to less than 15 dB/cm when the feature vertically will be further improved.

The InP W1 PhC suspended membrane waveguides etched using the ICP BCl_3/N_2 plasma are fabricated with smooth sidewall surfaces and nearly vertical feature profiles. A plateau of high transmission rate is found within 1453 nm and 1510 nm, corresponding to the range between the mode-gap cutoff and the light-line cutoff for the fundamental even mode. Theoretically, the modes are intrinsically lossless within this range. Hence, the measured overall propagation losses, 25 dB/cm at 1480 nm wavelength, are extrinsic and are mainly due to fabrication imperfections.

6.4 Discussion

With this dissertation, the developed ICP BCl_3/N_2 plasma was demonstrated successfully for the InP PhC suspended membrane waveguides fabrication. The etched sidewall surfaces are smooth using these conditions and the light scattering leading to losses is thus expected to be reduced. The measured propagation losses value for a W1 membrane guide is about 25 dB/cm and it can be diminished by further improving the fabrication processes. Even though this value is still relative large compared to the GaAs and Si materials, the study of small group velocity in InP membranes is still under investigation in LPN for the potential applications of delay lines and non-linear devices [Vecchi2007a, Vecchi2007b].

Chapter 7

Conclusion

Achievements

The scope of this thesis is to develop a fabrication method for InP-based photonic crystals structures that could be included in photonic integrated circuits. Passive as well as actives devices have been investigated from the design to the optical characterization. Among all the fabrication steps, efforts are focused mainly on the PhC dry etching by ICP-RIE.

Concerning the fabrication of PhC holes structure, the ICP Cl_2/Ar, $Cl_2/BCl_3/N_2$, and BCl_3/N_2 plasmas are investigated. The etching conditions under the Cl_2/Ar plasma have been optimized and applied for PhC tapers fabrication. An etch depth in the range of 1.9∼2.9 μm can be achieved for 110∼250 nm-diameter holes. The hole profile is vertical with surface roughness to some extent. With these etching conditions, the light propagation loss in a W3 InP/InGaAsP/InP PhCW is 80 dB/cm and the free-carrier lifetime for a InP/InGaAsP multiple quantum-wells with PhC holes structure is in the order of 100∼150 ps. The surface roughness has been shown to be greatly suppressed when N_2 is introduced into the plasma. The etched surfaces are smooth under TEM examination for BCl_3/N_2 and Cl_2/N_2 plasmas. In addition, the free-carrier lifetime increases to 1400 ps when the etching is performed using $Cl_2/BCl_3/N_2$ plasma. The BCl_3 is found to enhance the feature verticality. For a proper BCl_3/N_2 ratio, the etched surface can be smooth and the hole profile is nearly vertical and without undercut.

The PhC waveguide on InP membrane suspended in air has been realized with the reported etching process. A propagation loss of 25 dB/cm is obtained for the even mode of W1 PhC guide while propagating below the air light line.

As for the PhC taper waveguides, several geometries are studied to extend the optical field in the lateral plane in order to couple optical field from a W3 PhCW to a cleaved-facet single-mode fiber. The designed tapers are based on dominantly either the Bragg effect or the refractive index contrast. In the first

type, the linear defect width is augmented gradually from W3 to W23 with or without varied hole sizes at the intersections. The second type is inherited from the conventional index contrast taper waveguides. The PhC holes can provide index contrast as well as precise contour variation. With a PhC environment, the taper length can be as short as 40 μm, in contrast to several hundreds micrometers in a classical index contrast implementation. The modal behaviors while light traversing the PhC tapers are of interest especially. The far-field patterns are measured and compared to the simulation results. Within the investigated PhC tapers, the coupling efficiency is enhanced by a factor of 4 for a PhC taper with gaussian curve contour; in which, only 20% of mode conversion to higher modes is found after traversing the taper section. Moreover, the coupling loss between the output ridge waveguide and fiber is estimated to be 12.7 dB for the gaussian curve taper.

Regarding the PhC MCW laser, the mode selection can be obtained through the cavities coupling. Compared to the CROW design, the coupling is stronger for MCW because the cavities are not completely closed. It is then expected to lead to a higher external efficiency and a lower injection threshold current. The fundamental mode transmission and reflection intensities through a single constriction section are simulated with various narrowing section lengths for W5/W3 and W5/W1 constricted waveguides. Nevertheless, due to the simulation tool limitation, these results do not represent exactly the transmission/reflection rates of the constriction itself; hence, we were not able to produce the MCW design based on these calculation results.

Future work

The PhC holes etching by ICPR-RIE will be proceeded. On one hand, the achievable etch depth in PhC holes by ICP Cl_2/Ar plasma is still limited for the fabrication of InP-based heterostructure lasers. From the reported etching conditions and results, we consider that the etch depth is not saturated yet due to the insufficiency of chlorine radicals and/or the evacuation of etched products in small isolated features. Therefore, if one can prolong the etch time, a higher etch depth (> 4 μm) might be obtained. In this case, the developments to increase the mask thickness will be pursued. On the other hand, the influence of N_2 in Cl_2/N_2 and BCl_3/N_2 plasmas will be investigated. From the TEM-EDX analysis, under a N_2-containg plasma, the etched surface roughness suppression seems to be not directly related to the nitridation. Instead, it might be attributed to the dilution of chlorine radicals. But, in a BCl_3/N_2 mixture, the mechanism would be more complicated since it has been reported that the BCl_3 dissociation rate can be enhanced by N_2. As a result, a more thorough study to identify the species (ex: radicals, positive ions) in plasmas and the density of species by OES would be required with varied N_2 ratio. In addition, the mechanism of the P-enriched amorphous layer formation will be investigated through OES and TEM-EDX measurements.

The future of integrated optics will be based on silicon, which can be used as a platform where all the optics elements are soldered; especially, it can be served as the efficient guiding layer. By taking advantage of genuine optical functions resulting from the periodic environment, we can implement PhC structures into InP-based devices. Subsequently, the InP PhC devices can be integrated on SOI via wafer bonding. The fabrication technology of PhC holes on InP membrane with smooth etched surfaces developed within this thesis is an important step towards the integration scheme.

Bibliography

[Akahane2003] Y. Akahane, T. Asano, B. S. Song, and S. Noda. High-Q photonic nanocavity in a two-dimensional photonic crystal. *Nature*, 425:944, (2003).

[Almeida2003] V. R. Almeida, R. R. Panepucci, and M. Lipson. Nanotaper for compact mode conversion. *Opt. Lett.*, 28:1302, (2003).

[Baba1996] T. Baba, M. Hamasaki, N. Watanabe, P. Kaewplung, A. Matsutani, T. Mukaihara, F. Koyama, and K. Iga. A novel short-cavity laser with deep-grating distributed bragg reflectors. *Jpn. J. Appl. Phys.*, 35:1390, (1996).

[Baba1999] T. Baba, N. Fukaya, and J. Yonekura. Observation of light propagation in photonic crystal optical waveguides with bends. *Electron. Lett.*, 35:654, (1999).

[Bae2003] J. W. Bae, W. Zhao, J. H. Jang, I. Adesida, A. Lepore, M. Kwakernaak, and J. H. Abeles. Characterization of sidewall roughness of InP/InGaAsP etched using inductively coupled plasma for low loss optical waveguide applications. *J. Vac. Sci. Technol. B*, 21:2888, (2003).

[Bayindir2000] M. Bayindir, B. Temelkuran, and E. Ozbay. Tight-binding description of the coupled defect modes in three-dimensional photonic crystals. *Phys. Rev. Lett.*, 84:2140, (2000).

[Bendelli1991] G. Bendelli, K. Komori, S. Arai, and Y. Suematsu. A new structure for high-power TW-SLA. *IEEE Photon. Technol. Lett.*, 3:42, (1991).

[Berenger1994] J. P. Berenger. A perfectly matched layer for the absorption of electromagnetic waves. *J. Comput. Phys.*, 114:185, (1994).

[Berrier2007] A. Berrier, M. Mulot, S. Anand, A. Talneau, R. Ferrini, and R. Houdré. Characterization of the feature-size dependence in Ar/Cl_2 chemically assisted ion beam etching of InP-based photonic crystal devices. *J. Vac. Sci. Technol. B*, 25:1, (2007).

[Bienstman2003] P. Bienstman, S. Assefa, S. G. Johnson, J. D. Joannopoulos, G. S. Petrich, and L. A. Kolodziejski. Taper structures for coupling into photonic crystal slab waveguides. *J. Opt. Soc. Am. B*, 20:1817, (2003).

[Boscolo2002] S. Boscolo, M. Midrio, and T. F. Krauss. Y junctions in photonic crystal channel waveguides: high transmission and impedance matching. *Opt. Lett.*, 27:1001, (2002).

[Bouchoule2008] S. Bouchoule, G. Patriarche, S. Guilet, L. Gatilova, L. Largeau, and P. Chabert. Sidewall passivation assisted by a silicon coverplate during Cl_2/H_2 and HBr inductively coupled plasma etching of InP for photonic devices. *J. Vac. Sci. Technol. B*, 26:666, (2008).

[Braithwaite1996] N. St. J. Braithwaite, J. P. Booth, and G. Cunge. A novel electrostatic probe method for ion flux measurements. *Plasma Sources Sci. Technol.*, 5:677, (1996).

[Carlstrom1999] C. F. Carlström, S. Anand, and G. Landgren. Extremely smooth surfaxe morphologies in $N_2/H_2/CH_4$ based low energy chemically assisted ion beam etching of InP/GaInAsP. *Thin Solid Films*, 343-344:374, (1999).

[Carlstrom2005] C. F. Carlström, R. van der Heijden, A. A. M. Kok, R. W. van der Heijden, F. Karouta, J. J. G. M. van der Tol, R. Nötzel, P. J. van Veldhoven, and H. W. M. Salemink. Inductively coupled plasma etching of deep photonic crystal holes in InP using Cl_2. In *Proceedings of IPRM*, (2005).

[Carlstrom2006] C. F. Carlström, R. van der Heijden, F. Karouta, R. W. van der Heijden, H. W. M. Salemink, and E. van der Drift. Cl_2/O_2 inductively coupled plasma etching of deep hole-type photonic crystals in InP. *J. Vac. Sci. Technol. B*, 24:L6, (2006).

[Checoury2004] X. Checoury, P. Boucaud, J-M. Lourtioz, F. Pommereau, C. Cuisin, E. Derouin, O. Drisse, L. Legouezigou, F. Lelarge, F. Poigt, G-H. Duan, D. Mulin, S. Bonnefont, O. Gauthier-Lafaye, J. Valentin, F. Lozes, and A. Talneau. Distributed feedback regime of photonic crystal waveguide lasers at 1.5 μm. *Appl. Phys. Lett.*, 85:5502, (2004).

[Cheng1995] C. C. Cheng and A. Scherer. Fabrication of photonic band-gap crystals. *J. Vac. Sci. Technol. B*, 13:2696, (1995).

[Cheng1996] C. C. Cheng, V. Arbet-Engels, A. Scherer, and E. Yablonovitch. Nanofabricated three dimensional photonic crystals operating at optical wavelengths. *Phys. Scr.*, T68:17, (1996).

[Chinzei1998a] Y. Chinzei, M. Ogata, H. Shindo, T. Ichiki, and Y. Horiike. Flow rate rule for high aspect ratio SiO_2 hole etching. *J. Vac. Sci. Technol. A*, 16:1519, (1998).

[Chinzei1998b] Y. Chinzei, T. Ichiki, N. Ikegami, Y. Feurprier, H. Shindo, and Y. Horiike. Residence time effects on SiO_2/Si selective etching employing high density fluorocarbon plasma. *J. Vac. Sci. Technol. B*, 16:1043, (1998).

[Combrie2005] S. Combrié, S. Bansropun, M. Lecomte, O. Parillaud, S. Cassette, H. Benisty, and J. Nagle. Optimization of an inductively coupled plasma etching process of GaInP/GaAs based material for photonic band gap application. *J. Vac. Sci. Technol. B*, 23:1521, (2005).

[Combrie2006] S. Combrié, E. Weidner, A. DeRossi, S. Bansropun, S. Cassette, A. Talneau, and H. Benisty. Detailed analysis by Fabry-Perot method of slab photonic crystal line-defect waveguides and cavities in aluminum-free material system. *Opt. Exp.*, 14:7353, (2006).

[Constantine1995] C. Constantine, R. J. Shul, C. T. Sullivan, M. B. Snipes, G. B. McClellan, M. Hafich, C. T. Fuller, J. R. Mileham, and S. J. Pearton. Etching of GaAs/AlGaAs rib waveguide structures using $BCl_3/Cl_2/N_2/Ar$ electron cyclotron resonance. *J. Vac. Sci. Technol. B*, 13:2025, (1995).

[Cubukcu2003] E. Cubukcu, K. Aydin, E. Ozbay, S. Foteinopolou1, and C.M. Soukoulis. Subwavelength resolution in a two-dimensional photonic-crystal-based superlens. *Phys. Rev. Lett.*, 91:207401, (2003).

[Dinges1991] H. W. Dinges, B. Kempf, H. Burkhard, and R. Göbel. Determination of ion beam etching damage on InP by spectroscopic ellipsometry. *Appl. Surf. Sci.*, 50:359, (1991).

[Dossou2006] K. Dossou, L. C. Botten, C. M. de Sterke, R. C. McPhedran, A. A. Asatryan, S. Chen, and J. Brnovic. Efficient couplers for photonic crystal waveguides. *Opt. Commun.*, 265:207, (2006).

[Dulkeith2005] E. Dulkeith, S. J. McNab, and Y. A. Vlasov. Mapping the optical peoperties of slab-type two-dimensional photonic crystal waveguides. *Phys. Rev. B*, 72:115102, (2005).

[Etrillard1997] J. Etrillard, P. Ossart, G. Patriarche, M. Juhel, J. F. Bresse, and C. Daguet. Anisotropic etching of InP with low sidewall and surface induced damage in inductively coupled plasma etching using $SiCl_4$. *J. Vac. Sci. Technol. A*, 15:626, (1997).

[Fan1998] S. Fan, P. R. Villeneuve, J. D. Joannopoulos, and H. A. Haus. Channel drop tunneling through localized states. *Phys. Rev. Lett.*, 80:960, (1998).

[Ferrini2003] R. Ferrini, R. Houdré, H. Benisty, M. Qiu, and J. Moosburger. Radiation losses in planar photonic crystals: two-dimensional representation of hole depth and shape by an imaginary dielectric constant. *J. Opt. Soc. Am. B*, 20:469, (2003).

[Foteinopoulou2003] S. Foteinopoulou, E. N. Economou, and C. M. Soukoulis. Refraction in media with a negative refractive index. *Phys. Rev. Lett.*, 90:107402, (2003).

[Frandsen2006] L. H. Frandsen, A. V. Lavrinenko, J. Fage-Pedersen, and P. I. Borel. Photonic crystal waveguides with semi-slow light and tailed dispersion properties. *Opt. Exp.*, 14:9444, (2006).

[Franz1998] G. Franz. High-rate etching of GaAs using chlorine atmospheres doped with a Lewis acid. *J. Vac. Sci. Technol. A*, 16:1542, (1998).

[Franz2001] G. Franz, W. Hösler, and R. Treichler. Sidewall passivation of GaAs in BCl_3-containing atmospheres. *J. Vac. Sci. Technol. B*, 19:415, (2001).

[Frost1998] F. Frost, A. Schindler, and F. Bigl. Ion beam smoothing of indium-containing $III-V$ compound semiconductors. *Appl. Phys. A: Mater. Sci. Process.*, A66:663, (1998).

[Fujita2004] M. Fujita, A. Sugitatsu, T. Uesugi, and S. Noda. Fabrication of indium phosphide compound photonic crystal by hydrogen iodide/xenon inductively coupled plasma etching. *Jpn. J. Appl. Phys.*, 43:L1400, (2004).

[Gatilova2008] L. Gatilova, S. Bouchoule, S. Guilet, and P. Chabert. Investigation of InP etching mechanisms in a Cl_2/H_2 inductively coupled plasma by optical emission spectroscopy. *J. Vac. Sci. Technol. A*, submitted:April, (2008).

[Gerace2004] D. Gerace and L. C. Andreani. Disorder-induced losses in photonic crystal waveguides with line defects. *Opt. Lett.*, 15:1897, (2004).

[Gortz1995] W. Görtz, B. Kempf, and J. Kretz. Resolution enhanced scanning force microscopy measurements for characterizing dry etching methods applied to titanium masked InP. *J. Vac. Sci. Technol. B*, 13:34, (1995).

[Gottscho1992] R. A. Gottscho, C. W. Jurgensen, and D. J. Vitkavage. Microscopic uniformity in plasma etching. *J. Vac. Sci. Technol. B*, 10:2133, (1992).

[Happ2001a] T. D. Happ, A. Markard, M. Kamp, A. Forchel, S. Anand, J.-L. Gentner, and N. Bouadma. Nanofabrication of two-dimensional photonic crystal mirrors for 1.5 μm short cavity lasers. *J. Vac. Sci. Technol. B*, 19:2775, (2001).

[Happ2001b] T. D. Happ, A. Markard, M. Kamp, and A. Forchel. Single-mode operation of coupled-cavity lasers based on two-dimensional photonic crystals. *Appl. Phys. Lett.*, 79:4091, (2001).

[Happ2001c] T. D. Happ, M. Kamp, and A. Forchel. Photonic crystal tapers for ultracompact mode conversion. *Opt. Lett.*, 26:1102, (2001).

[Happ2003] T. D. Happ, M. Kamp, A. Forchel, J.-L. Gentner, and L. Goldstein. Two-dimensional photonic crystal coupled-defect laser diode. *Appl. Phys. Lett.*, 82:4, (2003).

[Heijden2003] R. van der Heijden, E. van der Drift, E. J. Geluk, R. W. van der Heijden, F. Karouta, P. A. M. Nouwens, Y. S. Oei, T. de Vries, and H. W. M. Salemink. Deep dry etching process development for InP-based photonic crystals. In *Proceedings of IEEE/LEOS*, (2003).

[Heijden2005] R. van der Heijden, C. F. Carlström, E. van der Drift, R. W. van der Heijden, R. Nötzel, R. van Veldhoven, F. Karouta, H. W. M. Salemink, and A. Talneau. Cl_2/O_2 and Cl_2/N_2-based inductively coupled plasma etching of photonic crystals in InP: sidewall passivation. In *Proceedings of IEEE/LEOS*, (2003).

[Ho1990] K. M. Ho, C. T. Chan, and C. M. Soukoulis. Existence of a photonic gap in periodic dielectric structures. *Phys. Rev. Lett.*, 65:3152, (1990).

[Holzman2005] J. F. Holzman, P. Strasser, R. Wüest, D. Erni F. Robin, and H. Jäckel. Ultrafast carrier dynamics in InP photonic crystals. *Nanotechnology*, 16:949, (2005).

[Huang2007] S. C. Huang, M. Kato, E. Kuramochi, C. P. Lee, and M. Notomi. Time-domain and spectral-domain investigation of inflection-point slow-light modes in photonic crystal coupled waveguides. *Opt. Exp.*, 15:3543, (2007).

[Iber1997] H. Iber, S. Mo, E. Peiner, G. Vollrath, A. Schlachetzki, and F. Fiedler. Characterization of surface damage in dry-etched InP. *Semicond. Sci. Technol.*, 12:755, (1997).

[Ide2006] T. Ide, J. Hashimoto, K. Nozaki, E. Mizuta, and T. Baba. InP etching by HI/Xe inductively coupled plasma for photonic-crystal device fabrication. *Jpn. J. Appl. Phys.*, 45:L1102, (2006).

[Joannopoulos1995] J. D. Joannopoulos, R. D. Meade, and J. N. Winn. *Photonic Crystals: Molding the Flow of Light.* Princeton University Press, Princeton, (1995).

[John1987] S. John. Strong localization of photons in certain disordered dielectric superlattices. *Phys. Rev. Lett.*, 58:2486, (1987).

[Johnson1998] S. G. Johnson, C. Manolatou, S. Fan, P. R. Villeneuve, J. D. Joannopoulos, and H. A. Haus. Elimination of cross talk in waveguide intersections. *Opt. Lett.*, 23:1855, (1998).

[Johnson1999] S. G. Johnson, S. Fan, P. R. Villeneuve, J. D. Joannopoulos, and L. A. Kolodziejski. Guided modes in photonic crystal slabs. *Phys. Rev. B*, 60:5751, (1999).

[Johnson2000] S. G. Johnson, P. R. Villeneuve, S. Fan, and J. D. Joannopoulos. Linear waveguides in photonic-crystal slabs. *Phys. Rev. B*, 62:8212, (2000).

[Johnson2001] S. G. Johnson and J. D. Joannopoulos. Block-iterative frequency-domain methods for Maxwell's equations in a planewave basis. *Opt. Exp.*, 8:173, (2001).

[Johnson2002] S. G. Johnson, P. Bienstman, M. A. Skorobogatiy, M. Ibanescu, E. Lidorikis, and J. D. Joannopoulos. Adiabatic theorem and continuous coupled-mode theory for efficient taper transitions in photonic crystals. *Phys. Rev. E*, 66:066608, (2002).

[Kamoun1997] M. Kamoun. *Etude et réalisation de structures de diodes laser à divergence ré duite.* PhD thesis, Paris-Sud University, 1997.

[Katzschner1986] W. Katzschner, U. Niggebrügge, R. Löffler, and H. Schröter-Janssen. Reactive ion beam etching of InP with N_2 and N_2/O_2 mixtures. *Appl. Phys. Lett.*, 48:230, (1986).

[Khoo2005] E. H. Khoo, A. Q. Liu, and J. H. Wu. Nonuniform photonic crystal taper for high-efficiency mode coupling. *Opt. Exp.*, 13:7748, (2005).

[Kim1999] H. S. Kim, G. Y. Yeom, J. W. Lee, and T. I. Kim. Characteristics of inductively coupled Cl_2/BCl_3 plasmas during GaN etching. *J. Vac. Sci. Technol. A*, 17:2214, (1999).

[Kim2005] G. H. Kim, A. M. Efremov, D. P. Kim, and C. I. Kim. Inductively coupled Cl_2/N_2 plasma: Experimental investigation and modelling. *Microelectronic Engineering*, 81:96, (2005).

[Kosaka1998] H. Kosaka, T. Kawashima, A. Tomita, M. Notomi, T. Tamamura, T. Sato, and S. Kawakami. Superprism phenomena in photonic crystals. *Phys. Rev. B*, 58:10096, (1998).

[Kosaka1999] H. Kosaka, T. Kawashima, A. Tomita, M. Notomi, T. Tamamura, T. Sato, and S. Kawakami. Superprism phenomena in photonic crystals: toward microscale lightwave circuits. *J. Lightwave Technol.*, 17:2032, (1999).

[Kotlyar2004a] M. V. Kotlyar, L. O'Faolain, R. Wilson, and T. F. Krauss. High-aspect-ratio chemically assisted ion-beam etching for photonic crystals using a high beam voltage-current ratio. *J. Vac. Sci. Technol. B*, 22:1788, (2004).

[Kotlyar2004b] M.V. Kotlyar, T. Karle, M.D. Settle, L. O'Faolain, and T. F. Krauss. Low-loss photonic crystal defect waveguides in InP. *Appl. Phys. Lett.*, 84:3588, (2004).

[Krauss1996] T. Krauss, R. de la Rue, and S. Brand. Two-dimensional photonic-bandgap structures operating at near infrared wavelengths. *Nature*, 383:699, (1996).

[Kuramochi2005] E. Kuramochi, M. Notomi, S. Hughes, A. Shinya, T. Watanabe, and L. Ramunno. Disorder-induced scattering loss of line-defect waveguides in photonic crystal slabs. *Phys. Rev. B*, 72:161318, (2005).

[Kuramochi2006] E. Kuramochi, M. Notomi, S. Mitsugi, A. Shinya, T. Tanabe, and T. Watanabe. Ultrahigh-Q photonic crystal nanocavities realized by the local width modulation of a line defect. *Appl. Phys. Lett.*, 88:041112, (2006).

[Lalanne2002] Ph. Lalanne and A. Talneau. Modal conversion with artificial materials for photonic-crystal waveguides. *Opt. Exp.*, 10:354, (2002).

[Lan2002] S. Lan and H. Ishikawa. Broadband waveguide intersections with low cross talk in photonic crystal circuits. *Opt. Lett.*, 27:1567, (2002).

[Lee1996a] J. W. Lee, J. Hong, and S. J. Pearton. Etching of InP at > 1 μm/min in Cl_2/Ar plasma chemistries. *Appl. Phys. Lett.*, 68:847, (1996).

[Lee1996b] J. W. Lee, J. Hong, C. R. Abernathy, E. S. Lambers, S. J. Pearton, W. S. Hobson, and F. Ren. Cl_2/Ar plasma etching of binary, ternary, and quaternary InP-based compound semiconductors. *J. Vac. Sci. Technol. B*, 14:2567, (1996).

[Lee2006] K. H. Lee, S. Guilet, I. Sagnes, and A. Talneau. Reduced features two-dimensional photonic crystals on InP-based materials etched using Cl_2/Ar inductively coupled plasma. In *Proceedings of IPRM*, (2006).

[Letartre2001] X. Letartre, C. Seassal, C. Grillet, P. Rojo-Romeo, P. Viktorovitch, M. Le Vassor d'Yerville, D. Cassagne, and C. Jouanin. Group velocity and propagation losses measurement in a single-line photonic crystal waveguide on InP membranes. *Appl. Phys. Lett.*, 79:2312, (2001).

[Lin2002] S. Y. Lin, E. Chow, J. Bur, S. G. Johnson, and J. D. Joannopoulos. Low-loss, wide-angle Y splitter at 1.6 μm wavelengths built with a two-dimensional photonic crystal. *Opt. Lett.*, 27:1400, (2002).

[Loncar2002] M. Lončar, T. Yoshie, A. Scherer, P. Gogna, and Y. Qiu. Low-threshold photonic crystal laser. *Appl. Phys. Lett.*, 81:2680, (2002).

[Loncar2004] M. Lončar, M. Hochberg, A. Scherer, and Y. Qiu. High quality factors and room-temperature lasing in a modified single-defect photonic crystal cavity. *Opt. Lett.*, 29:721, (2004).

[MacLaren1992] S. W. MacLaren, J. E. Baker, N. L. Finnegan, and C. M. Loxton. Surface roughness development during sputtering of GaAs and InP: Evidence for the role of surface diffusion in ripple formation and sputter cone development. *J. Vac. Sci. Technol. A*, 10:468, (1992).

[Matsutani2003] A. Matsutani, H. Ohtsuki, and F. Koyama. Low-temperature dry etching of InP by inductively coupled plasma using HI/Cl_2. *Jpn. J. Appl. Phys.*, 42:L1414, (2003).

[McCrary1991] V. R. McCrary, J. W. Lee, S. N. G. Chu, S. E. G. Slusky, M. A. Brelvi, G. Livescu, P. M. Thomas, L. J. P. Ketelsen, and J. L. Zilko. Growth of InGaAsP/InP single-quantum-well and multiple-quantum well structures by low-pressure metal-organic chemical vapor deposition. *J. Appl. Phys.*, 69:7267, (1991).

[McNevin1986] S. C. McNevin. Chemical etching of GaAs and InP by chlorine: The thermodynamically predicted dependence on Cl_2 pressure and temperature. *J. Vac. Sci. Technol. B*, 4:1216, (1986).

[Meade1991] R. D. Meade, K. D. Brommer, A. M. Rappe, and J. D. Joannopoulos. Photonic bound states in periodic dielectric materials. *Phys. Rev. B*, 44:13772, (1991).

[Mekis1996] A. Mekis, J. C. Chen, I. Kurland, S. Fan, P. R. Villeneuve, and J. D. Joannopoulos. High transmission through sharp bends in photonic crystal waveguides. *Phys. Rev. Lett.*, 77:3787, (1996).

[Mekis2001] A. Mekis and J. D. Joannopoulos. Tapered couplers for efficient interfacing between dielectric and photonic crystal waveguides. *IEEE J. Lightwave Technol.*, 19:861, (2001).

[Mitomi1994] O. Mitomi, K. Kasaya, and H. Miyazawa. Design of a single-mode tapered waveguide for low-loss chip-to-fiber coupling. *IEEE J. Quantum Electron.*, 30:1787, (1994).

[Miyakuni1995] S. Miyakuni, R. Hattori, K. Sato, H. Takano, and O. Ishihara. Low ion energy electron cyclotron resonance etching of InP using a Cl_2/N_2 mixture. *J. Appl. Phys.*, 78:5734, (1995).

[Mookherjea2004] S. Mookherjea. Semiconductor coupled-resonator optical waveguide laser. *Appl. Phys. Lett.*, 84:3265, (2004).

[Mori2007] D. Mori, S. Kubo, H. Sasaki, and T. Baba. Experimental demonstration of wideband dispersion-compensated slow light by a chirped photonic crystal directional coupler. *Opt. Exp.*, 15:5264, (2007).

[Mulot2003] M. Mulot, S. Anand, M. Swillo, M. Qiu, B. Jaskorzynska, and A. Talneau. Low-loss InP-based photonic-crystal waveguides etched with Ar/Cl_2 chemically assisted ion beam etching. *J. Vac. Sci. Technol. B*, 21:900, (2003).

[Mulot2004a] M. Mulot, S. Anand, R. Ferrini, B. Wild, R. Houdré, J. Moosburger, and A. Forchel. Fabrication of two-dimensional InP-based photonic crystals by chlorine based chemically assisted ion beam etching. *J. Vac. Sci. Technol. B*, 22:707, (2004).

[Mulot2004b] M. Mulot, M. Swillo, M. Qiu, M. Strassner, M. Hede, and S. Anand. Fabry-Pérot cavities based on two-dimensional photonic crystals fabricated in InP membranes. *J. Appl. Phys.*, 95:5928, (2004).

[Naitoh2007] H. Naitoh, S. Sakamoto, M. Ohtake, T. Okumura, T. Maruyama, N. Nishiyama, and S. Arai. 80^0C CW operation of GaInAsP/InP membrane BH-DFB laser with air-bridge structur. In *Proceedings of IPRM*, (2007).

[O'Brien1996] J. O'Brien, O. Painter, R. Lee, C. C. Cheng, A. Yariv, and A. Scherer. Lasers incorporating 2D photonic bandgap mirrors. *Electron. Lett.*, 32:2243, (1996).

[Ohki1987] S. Ohki, M. Oda, H. Akiya, and T. Shibata. Cavernous undercuts appearing in reactive ion etched submicron-wide deep trenches. *J. Vac. Sci. Technol. B*, 5:1611, (1987).

[Olivier2001] S. Olivier, C. Smith, M. Rattier, H. Benisty, C. Weisbuch, T. Krauss, R. Houdré, and U. Oesterlé. Miniband transmission in a photonic crystal coupled-resonator optical waveguide. *Opt. Lett.*, 26:1019, (2001).

[Olivier2002] S. Olivier, H. Benisty, C. J. M. Smith, M. Rattier, C. Weisbuch, and T. F. Krauss. Transmission properties of two-dimensional photonic crystal channel waveguides. *Optical and Quantum Electronics*, 34:171, (2002).

[Olivier2003a] S. Olivier, C. Weisbuch, and H. Benisty. Compact and fault-tolerant photonic crystal add-drop filter. *Opt. Lett.*, 28:2246, (2003).

[Olivier2003b] S. Olivier, H. Benisty, C. Weisbuch, C. J. M. Smith, T. F. Krauss, and R. Houdré. Coupled-mode theory and propagation losses in photonic crystal waveguides. *Opt. Exp.*, 11:1490, (2003).

[Painter1999] O. Painter, R. K. Lee, A. Scherer, A. Yariv, J. D. O'Brien, P. D. Dapkus, and I. Kim. Two-dimensional photonic band-gap defect mode laser. *Science*, 284:1819, (1999).

[Pan1996] J. S. Pan, A. T. S. Wee, C. H. A. Huan, H. S. Tan, and K. L. Tan. XPS studies on nitridation of InP(100) surface by N_2^+ ion beam bombardment. *J. Phys. D: Appl. Phys.*, 29:2997, (1996).

[Park2001] S. R. Park and B. H. O. Novel design concept of waveguide mode adapter for low-loss mode conversion. *IEEE Photon. Technol. Lett.*, 13:675, (2001).

[Park2004] H. G. Park, S. H. Kim, S. H. Kwon, Y. G. Ju, J. K. Yang, J. H. Baek, S. B. Kim, and Y. H. Lee. Electrically driven single-cell photonic crystal laser. *Science*, 305:1444, (2004).

[Pearton1990] S. J. Pearton, U. K. Chakrabarti, A. P. Perley, and K. S. Jones. Ion milling damage in InP and GaAs. *J. Appl. Phys.*, 68:2760, (1990).

[Pearton1994] S. J. Pearton. Reactive ion etching of III-V semiconductors. *Int. J. Mod. Phys. B*, 8:1781, (1994).

[PhotonDesign] Photon design software http://www.photond.com.

[Plihal1991] M. Plihal and A. A. Maradudin. Photonic band structure of two dimensional systems: the triangular lattice. *Phys. Rev. B*, 44:856571, (1991).

[Pommereau2004] F. Pommereau, L. Legouézigou, S. Hubert, S. Sainson, J.-P. Chandouineau, S. Fabre, G.-H. Duan, B. Lombardet, R. Ferrini, and R. Houdré. Fabrication of low loss two-dimensional InP photonic crystals by inductively coupled plasma etching. *J. Appl. Phys.*, 95:2242, (2004).

[Pottier2003] P. Pottier, I. Ntakis, and R. M. De la Rue. Photonic crystal continuous taper for low-loss direct coupling into photonic crystal channel waveguides and further device functionality. *Opt. Commun.*, 223:339, (2003).

[Qiu2002] M. Qiu. Effective index method for heterostructure-slab-waveguide-based two-dimensional photonic crystals. *Appl. Phys. Lett.*, 81:1163, (2002).

[Ren1995] F. Ren, W. S. Hobson, J. R. Lothian, J. Lopata, J. A. Caballero, S. J. Pearton, and M. W. Cole. High rate dry etching of InGaP in BCl_3 plasma chemistries. *Appl. Phys. Lett.*, 67:2497, (1995).

[Ren1996a] F. Ren, J. R. Lothian, J. M. Kuo, W. S. Hobson, J. Lopata, J. A. Caballero, S. J. Pearton, and M. W. Cole. BCl_3/N_2 dry etching of InP, InAlP, and InGaP. *J. Vac. Sci. Technol. B*, 14:1758, (1996).

[Ren1996b] F. Ren, W. S. Hobson, J. R. Lopata, S. J. Pearton, J. A. Caballero, and M. W. Cole. Extremely high etch rates of In-based $III-V$ semiconductors in BCl_3/N_2 based plasma. *J. Electrochem. Soc.*, 143:3394, (1996).

[Rommel2002] S. L. Rommel, J. H. Jang, W. Lu, G. Cueva, L. Zhou, I. Adesida, G. Pajer, R. Whaley, A. Lepore, Z. Schellanbarger, and J. H. Abeles. Effect of H2 on the etch profile of InP/InGaAsP alloys in $Cl_2/Ar/H_2$ inductively coupled plasma reactive ion etching chemistries for photonic device fabrication. *J. Vac. Sci. Technol. B*, 20:1327, (2002).

[Russell2006] P. St. J. Russell. Photonic-crystal fibers. *J. Lightwave. Technol.*, 24:4729, (2006).

[SRIM2003] J. F. Ziegler, J. P. Biersack, and M. D. Ziegler. SRIM: the stopping and range of ions in matter. In *SRIM software http://www.srim.org/*.

[Sauvan2005] C. Sauvan, G. Lecamp, P. Lalanne, and J. P. Hugonin. Modal-reflectivity enhancement by geometry tuning in photonic crystal microcavities. *Opt. Exp.*, 13:245, (2005).

[Seo2007] M. K. Seo, K. Y. Jeong, J. K. Yang, Y. H. Lee, H. G. Park, and S. B. Kim. Low threshold current single-cell hexapole mode photonic crystal laser. *Appl. Phys. Lett.*, 90:171122, (2007).

[Shul1997] R. J. Shul, G. B. McClellan, R. D. Briggs, D. J. Rieger, S. J. Pearton, C. R. Abernathy, J. W. Lee, C. Constantine, and C. Barratt. High-density plasma etching of compound semiconductors. *J. Vac. Sci. Technol. A*, 15:633, (1997).

[Smith1996] G. M. Smith, J. S. Hughes, R. M. Lammert, M. L. Osowski, G. C. Papen, J. T. Verdeyen, and J. J. Coleman. Very narrow linewidth asymmetric cladding InGaAs-GaAs ridge waveguide distributed bragg reflector lasers. *IEEE Photon. Technol. Lett.*, 8:476, (1996).

[Soukiassian1992] P. Soukiassian, H. I. Starnberg, and T. Kendelewicz. Rb- and K-promoted nitridation of cleaved GaAs and InP surfaces at room temperature. *Appl. Surf. Sci.*, 56-58:772, (1992).

[Strasser2004] P. Strasser, R. Wüest, F. Robin, D. Erni, and H. Jäckel. Process optimization for dry etching of InP/InGaAsP-based photonic crystals with a $Cl_2/CH_4/H_2$ mixture on an ICP-RIE. In *Proceedings of IPRM*, (2004).

[Strasser2005] P. Strasser, R. Wüest, F. Robin, K. Rauscher, B. Wild, D. Erni, and H. Jäckel. An ICP-RIE etching process for InP-based photonic crystals using $Cl_2/Ar/N_2$ chemistry. In *Proceedings of IPRM*, (2005).

[Strasser2007] P. Strasser, R. Wüest, F. Robin, D. Erni, and H. Jäckel. Detailed analysis of the influence of an inductively coupled plasma reactive ion etching process on the hole depth and shape of photonic crystals in InP/InGaAsP. *J. Vac. Sci. Technol. B*, 25:387, (2007).

[Sugimoto2002] Y. Sugimoto, N. Ikeda, N. Carlsson, K. Asakawa, N. Kawai, and K. Inoue. Light-propagation characteristics of Y-branch defect waveguides in AlGaAs-based air-bridge-type two-dimensional photonic crystal slabs. *Opt. Lett.*, 27:388, (2002).

[Sugitatsu2003] A. Sugitatsu and S. Noda. Room temperature operation of 2D photonic crystal slab defect-waveguide laser with optical pump. *Electron. Lett.*, 39:213, (2003).

[Suzuki2000] Y. Suzuki, H. Kumano, W. Tomota, N. Sanada, and Y. Fukuda. Nitridation of an InP(001) surface by nitrogen ion beams. *Appl. Surf. Sci.*, 162-163:172, (2000).

[Taflove1995] A. Taflove. *Computational Electrodynamics: The Finite-Difference Time-Domain Method*. Artech House INC, Norwood, (1995).

[Talneau2001] A. Talneau, L. Le Gouezigou, and N. Bouadma. Quantitative measurement of low propagation losses at 1.55 μm on planar photonic crystal waveguides. *Opt. Lett.*, 26:1259, (2001).

[Talneau2002] A. Talneau, L. Le Gouezigou, N. Bouadma, M. Kafesaki, C. M. Soukoulis, and M. Agio. Photonic-crystal ultrashort bends with improved transmission and low reflection at 1.55 μm. *Appl. Phys. Lett.*, 80:547, (2002).

[Talneau2004a] A. Talneau, L. LeGratiet, J. L. Gentner, A. Berrier, M. Mulot, S. Anand, and S. Olivier. High external efficiency in a monomode full-photonic-crystal laser under continuous wave electrical injection. *Appl. Phys. Lett.*, 85:1913, (2004).

[Talneau2004b] A. Talneau, M. Agio, C. M. Soukoulis, M. Mulot, S. Anand, and Ph. Lalanne. High-bandwidth transmission of an efficient photonic-crystal mode converter. *Opt. Lett.*, 29:1745, (2004).

[Talneau2008] A. Talneau, K. H. Lee, S. Guilet, and I. Sagnes. Efficient coupling to W1 photonic crystal waveguide on InP membrane through suspended access guides. *Appl. Phys. Lett.*, 92:061105, (2008).

[Tanaka2003] Y. Tanaka, T. Asano, Y. Akahane, B. S. Song, and S. Noda. Theoretical investigation of a two-dimensional photonic crystal slab with truncated cone air holes. *Appl. Phys. Lett.*, 82:1661, (2003).

[Thomas1995] S. Thomas III and S. W. Pang. Atomic force microscopy study of $III-V$ materials etched using an electron cyclotron resonance source. *J. Vac. Sci. Technol. B*, 13:2350, (1995).

[Vecchi2007a] G. Vecchi, F. Raineri, I. Sagnes, K-H. Lee, S. Guilet, L. Le Gratiet, A. Talneau, A. Levenson, R. Raj, F. Van Laere, G. Roelkens, D. Van Thourhout, and R. Baets. High contrast reflection modulation near 1.55 μm in InP 2D photonic crystals on silicon wafer. *Opt. Exp.*, 15:1254, (2007).

[Vecchi2007b] G. Vecchi, F. Raineri, I. Sagnes, A. Yacomotti, P. Monnier, T. J. Karle, K-H. Lee, R. Braive, L. Le Gratiet, S. Guilet, G. Beaudoin, A. Talneau, S. Bouchoule, A. Levenson, , and R. Raj. Continuous-wave operation of photonic bandedge laser near 1.55 μm on silicon wafer. *Opt. Exp.*, 15:7551, (2007).

[Vernon1992] M. Vernon, T. R. Hayes, and V. M. Donnelly. Intrinsic mechanism of smooth and rough morphology in etching of InP by Cl_2 determined by infrared laser interferometry. *J. Vac. Sci. Technol. A*, 10:3499, (1992).

[Villeneuve1998] P. R. Villeneuve, S. Fan, S. G. Johnson, and J. D. Joannopoulos. Three-dimensional photon confinement in photonic crystals of low-dimensional periodicity. *IEE Pro. Optoel.*, 145:384, (1998).

[Vuckovic2002] J. Vučković, M. Lončar, H. Mabuchi, and A. Scherer. Optimization of the Q factor in photonic crystal microcavities. *IEEE J Quantum Elect.*, 38:850, (2002).

[Wei1997] C. Wei, F. Groen, M. K. Smit, I. Moerman, P. Van Daele, and R. Baets. Integrated optical elliptic couplers: modeling, design, and applications. *IEEE J. Lightwave Technol.*, 15:906, (1997).

[Weissman1995] Z. Weissman and I. Hendel. Analysis of periodically segmented waveguide mode expanders. *IEEE J. Lightwave Technol.*, 13:2053, (1995).

[Woodworth1997] J. R. Woodworth, M. E. Riley, P. A. Miller, C. A. Nichols, and T. W. Hamilton. Ion distribution functions in inductively coupled radio frequency discharges in argon-chlorine mixtures. *J. Vac. Sci. Technol. A*, 15:3015, (1997).

[Yablonovitch1987] E. Yablonovitch. Inhibited spontaneous emission in solid-state physics and electronics. *Phys. Rev. Lett.*, 58:2059, (1987).

[Yablonovitch1991] E. Yablonovitch and T. J. Gmitter. Photonic band structure: the face-centered-cubic case employing nonspherical atoms. *Phys. Rev. Lett.*, 67:2295, (1991).

[Yablonovitch2007] E. Yablonovitch. Photonic crystals: what's in a name? *Optics & Photonics News*, 18:12, (2007).

[Yariv1999] A. Yariv, Y. Xu, R. K. Lee, and A. Scherer. Coupled-resonator optical waveguide: a proposal and analysis. *Opt. Lett.*, 24:711, (1999).

[Ying1997] F. Ying, W. H. Juan, and S.W. Pang. Etching of high aspect ratio microcavity structures in InP. *J. Vac. Sci. Technol. B*, 15:665, (1997).

[Zimmermann2004] J. Zimmermann, H. Scherer, M. Kamp, S. Deubert, J. P. Reithmaier, A. Forchel, R. März, and S. Anand. Photonic crystal waveguides with propagation losses in the 1 dB/mm range. *J. Vac. Sci. Technol. B*, 22:3356, (2004).

[deRossi2005] S. de Rossi, I. Sagnes, L. Le Gratiet, A. Talneau, A. Berrier, M. Mulot, S. Anand, and J. L. Gentner. Longitudinal mode selection in constricted photonic crystal guides and electrically injected lasers. *J. Lightwave Technol.*, 23:1363, (2005).

Résumé

Chapter 1
Introduction

1.1 Recherche sur le développement des cristaux photoniques

La photonique est désormais l'alternative au transport et au traitement de l'information dans les réseaux de communication, le mode électrique ayant atteint ses limites. Les signaux optiques sont transmis à grande vitesse et la réduction du cross-talk entre canaux est plus performante que pour les signaux électriques. La transmission des signaux optiques est assuré par les fibres optiques ainsi que par des composants optiques comme les guides d'ondes ou les résonateurs. En ce qui concerne le traitement des signaux optiques, les circuits intégrés photoniques (CIPs), dans lesquels les dispositifs photoniques sont compacts et intégrés monolithiquement sont préférables. Avec les développements de la nano-fabrication, les CIPs peuvent être réduits en dimension et fabriqués dans des matériaux semiconducteurs comme le silicium (Si), l'arséniure de gallium (GaAs) et le phosphure d'indium (InP). Par conséquent, non seulement les modes optiques peuvent être confinés et étroitement guidés en raison du fort contraste d'indice de réfraction dans le plan, mais des fonctions plus complexes associant des composants opto-électroniques sont aussi possibles.

Les cristaux photoniques (CP) représentent une alternative pour la miniaturisation et l'intégration de dispositifs photoniques. Ils ont été proposés pour la première fois en 1987 par E. Yablonovitch et simultanément par S. John pour l'inhibition de l'émission spontanée [Yablonovitch1987] et la localisation de photons [John1987]. Au sein d'un cristal photonique, la périodicité de la constante diélectrique génère une bande interdite photonique, domaine de fréquence dans lequel la propagation des modes optiques est interdite. L'introduction de défauts dans le CP permet à certains modes optiques localisés d'exister. De telles structures peuvent alors être utilisées comme brique élémentaire d'un circuit intégré photonique.

La caractéristique principale du CP est l'existence d'une bande interdite photonique (BIP). Cette BIP peut être vue pour les photons comme analogue à la

bande interdite électronique dans les cristaux semiconducteurs. Une bande photonique interdite complète, correspondant à une inhibition de la propagation pour toutes les directions ne peut exister que dans un système 3D. Mais la fabrication de telles structures est extrêmement difficile [Yablonovitch1991].

Dans une structure CP bidimensionnelle (2D), du type de celles que nous étudions, la variation de la constante diélectrique est périodique dans un plan et homogène dans la troisième direction. Le confinement des modes optiques se fait donc dans cette dernière direction de façon classique par contraste d'indice [Krauss1996]. Il peut être assuré soit par un guide d'onde planaire composé d'hétéro-structures sur substrat , dans ce cas le contraste d'indice est faible, soit par une membrane suspendue dans l'air, dans ce dernier cas le contraste d'indice est très élevé. Le choix substrat/membrane se fera selon les fonctions optiques et/ou les performances recherchées.

Nous nous plaçons maintenant dans le plan de la couche de fort indice, dans laquelle nous avons réalisé un cristal photonique. Ce sera un réseau de trous, de façon à conserver une surface connexe pour éventuellement déposer ultérieurement une électrode métallique, dans la cas de dispositifs rendus actifs par injection de courant ou par polarisation électrique. La géométrie d'un triangle équilatéral pour la maille du cristal est celle qui permet d'obtenir le gap le plus large pour les deux directions de haute symétrie dans le plan.

Des défauts au sein de ce cristal peuvent supporter des modes optiques localisés [Joannopoulos1995]. Les défauts que nous considérerons ici sont constitués par l'absence de trous. On retrouve alors localement le matériau semi-conducteur massif, qui a un indice plus élevé que toute zone contenant des trous En retirant des trous et en respectant la symétrie au sein de la maille triangulaire, on obtient des cavités hexagonales. En modifiant une suite continue de trous, et ce sur une ou plusieurs rangées, on crée un défaut dans le gap, ainsi on permet à des modes de Bloch de se propager sur ce défaut au sein du gap du cristal. Les guides étudiés ici sont tous définis dans la direction ΓK, celle qui correspond à des bords denses de période a.

Les CP présentent aussi, grâce à leur courbe de dispersion bien particulière hors du gap photonique, des propriétés spécifiques comme l'effet superprism ou la réfraction négative.

1.2 Objet de cette thèse

Les dispositifs à cristaux photoniques que nous étudions dans le cadre de cette thèse sont des dispositifs en CP 2D opérant dans le gap photonique, et réalisés dans les matériaux à base d'InP, de façon à démontrer un fonctionnement dans le domaine spectral autour de 1,55 μm, qui correspond au minimum d'absorption pour la propagation dans les fibres optiques. Les semi-conducteurs III-V comme

GaAs et InP sont connus pour leur gap électronique direct, qui permet de réaliser efficacement à la fois les fonctions d'émission et de propagation sur le même substrat. Les longueurs d'onde de la lumière émise couvrent une large gamme de 0,7 μm à 1,7 μm, au sein de laquelle les domaines 1,3 μm et 1,55 μm sont favorables pour les télécommunications en raison de la faible dispersion et atténuation au cours de la propagation dans les fibres.

Concernant la géométrie du cristal, nous considérons un cristal de maille triangulaire dans les matériaux à base d'InP. Le gap correspond alors à des fréquences normalisées autour de u=0,26, pour une longueur d'onde de 1,55 μm, la période du cristal a est de 400 nm. Le facteur de remplissage en air avec lequel on travaille est de l'ordre de $f = 30 - 40\%$, les trous ont alors un diamètre de 200 à 250 nm. Les structures actives sur InP ont une extension verticale d'au moins 3 μm (on compte une couche d'injection des porteurs relativement épaisse d'au moins 1,5 μm de façon à limiter le recouvrement du champ du mode optique avec le métal du contact électrique). Les trous doivent donc présenter un rapport d'aspect entre 10 et 20. Les dimensions inférieures au micromètre sont facilement accessibles par écriture directe par faisceau d'électrons. Cette méthode est très versatile et permet facilement de générer des structures très diversifiées, quand on souhaite étudier des mécanismes nouveaux. Les trous sont ensuite gravés par la méthode de gravure par plasma à couplage inductif (inductively coupled plasma reactive ion etching, ICP-RIE).

Un bref aperçu de la thèse est indiqué ci-dessous:

Le chapitre 2 examine d'abord la théorie électromagnétique dans une structure périodique en constante diélectrique et donne l'équation de propagation des champs. La courbe de dispersion du cristal sans défaut est présentée, dans les deux cas substrat et membrane, de façon à indiquer le domaine de fréquence dans lequel se situe la bande interdite photonique. Les courbes de dispersion sont calculées par la méthode de décomposition en ondes planes. On présente ensuite les courbes de dispersion des trois types de structures étudiées: guide d'onde avec le défaut linéaire large qu'est le taper, guide d'onde avec cavités couplés (constrictions) qui a été choisi comme géométrie pour le laser, ces deux structures sont sur substrat, et le guide d'onde en CP sur membrane suspendue. Ces courbes permettent d'identifier les modes optiques supportés. Dans le cas du taper, le calcul de la propagation par la méthode de différence finie dans le domaine temporel (FDTD) a permis de faire un étude résolue sur les modes, car la courbe de dispersion de ces guides qui sont larges donc très multimodes est difficile à exploiter.

Le chapitre 3 présente la technologie de fabrication des cristaux photoniques dans les matériaux à base d'InP. On donne les paramètres géométriques des dispositifs en CP étudiés, la préparation du masque par lithographie électronique, et les développements importants menés au cours de ce travail sur la gravure par la technique ICP-RIE. Le plasma Cl_2/Ar a été étudié en premier, avec comme objectif d'atteindre des profondeurs gravées importantes (> 2 μm). Puis, pour améliorer

la qualité des surfaces gravées, nous avons étudié un plasma contenant du chlore avec l'ajout d'azote. Le courant d'ions positifs dans le plasma a été mesuré grâce à une sonde ionique installée dans le bâti. Le courant ionique permet d'évaluer la pulvérisation ionique pendant la gravure. L'évaluation de la qualité de la gravure est faite dans un premier temps par observation par imagerie électronique. Mais nous allons au-delà, et mesurons les performances de certains dispositifs test: par exemple les pertes de propagation de guides CP, sur substrat et sur membrane, ainsi que la durée de vie de porteurs, par luminescence résolue en temps.

Le chapitre 4 s'intéresse aux adaptateurs de mode. Il contient la simulation, la fabrication, et les performances mesurées sur les dispositifs réalisés. Les adaptateurs de mode servent à coupler efficacement le mode optique issu d'une diode laser ou un guide d'onde planaire en CP à une fibre optique monomode clivée-droite. Un taper réalisé dans un environnement en CP sera directement intégrable au guide/laser, et sera beaucoup plus court qu'un taper classique basé sur le confinement par contraste d'indice, tout en assurant une transformation adiabatique. Seule la transformation du mode dans le plan est considérée ici. Nous considérons des adaptateurs de mode à base de l'effect de Bragg présent dans le CP et aussi à base du contraste d'indice qui est aussi présent. Les simulations de la transmission sont réalisées par FDTD pour un objet bidimensionnel. La transmission est résolue sur les modes supportés par le guide de sortie, de façon à considérer l'efficacité obtenue sur le mode fondamental. Les mesures du rendement de transmission et de la divergence du faisceau des adaptateurs de mode en CP fabriqués sont présentées.

Le chapitre 5 est consacré aux structures laser basées sur des guides larges, de type W5 avec des constrictions, sections où le guide voit sa largeur réduite. On a cherché à simuler les coefficients de transmission et de réflexion ainsi que le changement de phase à une constriction, à l'aide de la FDTD. Dans un laser classique à deux cavités couplées, la sélection en longueur d'onde est réalisée en ajustant les longueurs relatives des deux cavités de façon à fonctionner sur un effet vernier. Le taux de réjection dépend de la réflectivité et de la phase de la section réfléchissante entre les deux cavités. On a cherché à étendre ce concept, en multipliant le nombre de cavités. Il faut pour cela connaître les coefficients de transmission et de réflexion ainsi que le changement de phase à une constriction. Ce calcul n'a pu être que partiellement mené à bien. De plus, la fabrication des lasers a pris du retard, car la maîtrise de la gravure des membranes nous a fait nous intéresser à ces dispositifs, ce qui n'était pas envisagé au départ.

Le chapitre 6 présente les résultats obtenus sur les membranes en InP suspendues dans l'air. L'étude des membranes est entrée dans le cadre de la thèse en considérant les performances très intéressantes que l'on peut obtenir en travaillant sur le mode fondamental d'un guide W1 sur membrane, sous la ligne de lumière et proche de la coupure, dans un domaine où la vitesse de groupe se ralentit. On a alors choisi d'étudier la fabrication de ces guides. On présente ici la calibration de

la gravure humide sélective qui permet d'éliminer la couche sous-jacente au guide et de rendre ainsi la membrane suspendue. On présente alors les résultats des mesures des pertes de propagation dans les guides W1.

1.3 Principales contributions de cette thèse

Une contribution majeure de cette thèse est le développement de procédés de gravure selon la technique ICP-RIE pour les cristaux photoniques dans les matériaux à base d'InP. En particulier, le procédé à base du plasma BCl_3/N_2 permet de graver des trous lisses et à peu près verticaux, sur une profondeur suffisante pour réaliser des membranes performantes.

Les procédés de gravure par plasma pour les matériaux à base d'InP sont moins bien maîtrisés que ceux utilisés pour les matériaux Si et GaAs. Avec le plasma BCl_3/N_2, les surfaces gravées sont rendues très lisses par l'introduction de N_2 alors que la gravure chimique et la verticalité du profil sont assurées par BCl_3. Même si la profondeur gravée est inférieure à 1 μm pour les trous ayant un diamètre de 250 nm, cette profondeur est largement suffisante pour fabriquer les membranes. Les surfaces gravées sont examinées par TEM-EDX (transmission electron microscopy equipped with energy dispersive X-ray analysis) afin de comprendre la nature de la couche de passivation.

Ce procédé a été utilisé pour réaliser des guides W1 sur membrane InP, pour lesquels on a mesuré des pertes de propagation raisonnablement faibles, de 25 dB/cm (chapitre 6). Maîtriser la fabrication de ces membranes était une étape nécessaire qui permet maintenant de réaliser des guides spécifiques supportant des modes lents.

Par ailleurs, ce procédé est aussi utilisé par les groupes du laboratoire travaillant sur les guides en CP pour l'optique non linéaire, ou sur des cavités à haut coefficient de surtension.

Dans la littérature, plusieurs géométries d'adaptateurs de mode en CP permettant d'élargir la taille du mode de 1$\sim$2 μm dans le guide en matériau semi-conducteur vers une valeur de 8$\sim$10 μm dans le plan correspondant à la taille du mode dans une fibre monomode ont déjà été calculées numériquement. Toutefois, les performances expérimentales de tels adaptateurs de mode en CP n'avaient pas à notre connaissance été publiées. Nous proposons ici une étude complète de la transmission résolue sur les modes du guide de sortie pour différentes géométries d'adaptateur de mode. (chapitre 4). La transmission et le champ lointain des adaptateurs de mode fabriqués sont caracterisés et comparés avec les résultats de la simulation. L'efficacité de couplage peut être améliorée par un facteur 4 quand l'adaptateur de mode en CP est ajouté et seulement 20% de la puissance optique transmise est couplée sur des modes d'ordre supérieur.

Chapter 2
Propriétés des cristaux photoniques 2D

2.1 Les équations de Maxwell

Dans tous les milieux macroscopiques, y compris les structures comme les cristaux photoniques, la propagation de la lumière est régie par les équations de Maxwell. Les milieux étudiés ici sont limités à des matériaux diélectriques homogènes sans charge ni courant. En outre, il est supposé que le champ de déplacement est lié au champ électrique dans un régime linéaire et le matériau est isotrope et sans pertes. Avec toutes ces hypothèses, les équations de Maxwell sont simplifiées et l'équation aux valeurs propres est exprimée comme l'équation (2.13).

Une propriété importante des équations électromagnétiques est que l'équation aux valeurs propres est indépendante de la longueur d'échelle. Pour deux cristaux photoniques ayant des dimensions physiques différentes seulement par un facteur donné, les modes optiques dans l'un peuvent être déduits de ceux dans l'autre simplement en re-échelonnant les longueurs d'onde ou les fréquences.

2.2 Méthodes de modélisation

Plusieurs méthodes sont utilisées pour simuler les structures périodiques que sont les cristaux photoniques. La décomposition en ondes planes (plane wave expansion, PWE) [Ho1990] permet de calculer les modes propres supportés par la structure. La méthode de différence finie dans le domaine temporel (finite-difference-time-domain, FDTD) [Taflove1995] permet de calculer numériquement la propagation des ondes électromagnétiques dans les cristaux photoniques. Cette méthode très générale s'applique à n'importe quelle structure, périodique ou non.

La méthode de décomposition en ondes planes est utilisée pour calculer la courbe de dispersion et la distribution du champ pour les structures infinies péri-

odiques, 2D ou 3D dans le cas où le théorème de Bloch est applicable. Les modes supportés par des défauts dans la structure périodique tels que cavités ou guides d'onde peuvent être trouvés en simulant une cellule qui inclut ce défaut, et en périodisant la structure. On utilise alors une super-cellule, et on doit alors faire attention à limiter le couplage entre les cellules. Dans ce travail de thèse, les diagrammes de dispersion des guides d'ondes en CP, des guides d'ondes à constriction en CP, ainsi que des guides d'ondes sur membrane suspendue sont tous calculés en utilisant la méthode PWE. Les calculs PWE en 2D sont réalisés à l'aide du soft commercial Photon Design et le programm de MIT-bandes est utilisé pour les calculs 3D des membranes.

La méthode FDTD est largement utilisée pour les calculs électromagnétiques, car elle peut être appliquée quelque soit la géométrie de la structure. Mais la durée des calculs peut devenir prohibitive si l'on souhaite calculer des structures propagatives en 3D, comme c'est notre cas. Dans cette thèse, nous avons utilisé cette méthode pour simuler la propagation dans les guides lasers contenant des constrictions, et pour les adaptateurs de mode en CP, mais toujours dans un cas 2D en représentant l'empilement vertical par un indice effectif. Cette approximation est tout à fait acceptable car les lasers comme les adaptateurs de mode seront ensuite réalisés sur substrat, c'est-à-dire dans un environnement vertical où le contraste d'indice est faible, et où donc cette approximation est valide.

2.3 Courbes de dispersion

Les structures CP considérées dans cette thèse sont formées à partir d'une maille triangulaire de colonnes d'air dans un matériau semi-conducteur. Une structure CP peut être caractérisée par la périodicité de la maille (a) et le facteur de remplissage en air (f). Le facteur de remplissage représente le rapport entre le volume d'air au volume total du CP. Pour un cristal photonique triangulaire de colonnes d'air, de période a = 400 nm, et de facteur de remplissage en air f = 35% dans une géométrie représentée par un indice effectif n_{eff} = 3,25, la BIP pour la polarisation TE est obtenue à la fréquence normalisée ($u = a/\lambda$) allant de 0,223 à 0,297, ce qui correspond à l'intervalle de longueur d'onde à 1346∼1793 nm. Pour ces valeurs de f, il n'y a pas de BIP pour la polarisation TM.

La fréquence normalisé à mi-bande et la largeur de la bande interdite varient en fonction du facteur de remplissage. La bande interdite pour la polarisation TE apparaît pour une valeur de $f > 12\%$ et celle dans les polarisations TE et TM est obtenue lorsque $f > 64\%$. Néanmoins, un facteur f élevé n'est pas favorable du point de vue de la fabrication parce que les grands trous d'air sont difficiles à réaliser dans une périodicité dense. Pour les applications optiques à 1,55 μm, notre intérêt est donc limité à la polarisation TE avec un facteur de remplissage modéré entre 30%∼ 45%. La maille triangulaire de 2D CP ayant les paramètres (a = 400 nm, d = 250 nm) est alors un bloc essentiel à la base des dispositifs en CP étudiés

dans cette thèse, et toutes les mesures en transmission exigeront de contrôler la polarisation de la lumière injectée. Dans le cas de l'émission, la polarisation TE est déjà favorisée par l'utilisation de couches actives à base de puits quantiques en compression.

2.4 Dessins des structures

Lorsque qu'un défaut est inclus dans un CP, l'invariance par translation est rompue, et un ou plusieurs modes sont supportés au sein de la BIP. Ce phénomène permet de pièger, localiser ou bien guider la lumière. Le guide d'onde en CP (PhC channel defect waveguides, PhCW) est obtenu par l'introduction de défauts linéaires, dans lequel une ou plusieurs rangées de colonnes d'air sont retirées d'une maille du CP. Pour un guide W3 le long de la direction ΓK, la courbe de dispersion montre plusieurs modes guidés dans la BIP. Expérimentalement, le creux observé dans le spectre de transmission correspond à la diminution de la transmission dans le domaine spectral de la mini-stop band, MSB [Olivier2002]. A ces fréquences, le mode fondamental incident peut se coupler via la périodicité du CP au 5éme mode et la lumière est alors rétro-diffusée.

Dans le diagramme de dispersion du guide d'onde comportant des constrictions (W5 rétréci localement à W1), plusieurs domaines de fréquence interdits apparaissent. Pour les fréquences au bord de ces bandes interdites, la vitesse de groupe est très réduite, favorisant l'oscillation laser. Dans une structure de CP à fort contraste fort d'indice comme celui rencontré dans une membrane de InP suspendue dans l'air, la calcul 2D+n_{eff} n'est plus valable que dans un domaine restreint de fréquence. La calcul 3D doit ici être utilisé, même s'il prend beaucoup de temps. Théoriquement, la propagation est sans pertes dans la direction hors du plan quand le guidage est assuré par le mode fondamental fonctionnant au-dessous de la ligne de lumière [Johnson1999, Johnson2000]. Pour W1 PhCW le long de la direction ΓK en membrane suspendue (280 nm-épaisseur d'InP, $a = 400$ nm, $d = 250$ nm), la courbe de dispersion est plate quand $\mathbf{k}_x$ est entre $0.4 \sim 0.5[\times 2\pi/a]$. La vitesse de groupe estimée pour le mode fondamental est réduite à $c/40$ quand $\mathbf{k}_x = 0.4[\times 2\pi/a]$ et peut même être aussi lente que $c/400$ à $\mathbf{k}_x = 0.48[\times 2\pi/a]$. Elle tend vers zéro en $\mathbf{k}_x = 0.5[\times 2\pi/a]$. La vitesse de groupe étant un vecteur, la réduction en vitesse de groupe présentée ici ne concerne que la direction ΓK.

Chapter 3
Fabrication des cristaux photoniques

3.1 Introduction, état de l'art

Les dispositifs en cristaux photoniques présentés dans cette thèse sont réalisés dans les matériaux InP/InGaAsP réalisés par épitaxie par MOVPE (metal-organic vapor phase epitaxy) sur substrat d'InP. Le procédé de fabrication retenu ici est celui d'un masque réalisé en deux étapes: une première lithographie électronique (EBL) définit les motifs dans une couche de résine PMMA, ces motifs sont alors transférés dans un masque diélectrique de SiO_2 par CCP-RIE (capacitively coupled plasma reactive ion etching) avec un plasma à base de CHF_3. C'est ce masque diélectrique plus dur que la résine PMMA qui permettra de graver le matériau semi-conducteur InP par ICP-RIE (inductively coupled plasma reactive ion etching) à l'aide d'un plasma contenant du chlore.

Les difficultés de la gravure des matériaux à base d'InP viennent principalement de la pulvérisation préférentielle du phosphore (P), atome tout petit par rapport à l'Indium (In) [Pearton1990]. Au cours de la gravure, la surface se retrouve enrichie en In et des îlots d'indium peuvent se former [MacLaren1992], ce qui apparaît comme une rugosité des faces gravées. Dans le cadre d'un plasma contenant du di-chlore, la gravure se produit en formant les produits $InCl_x$ et PCl_x. Mais $InCl_x$ est faiblement volatil à la température ambiante par rapport à PCl_x. Pour régler cet inconvénient, le chauffage du substrat (>150^0C) [McNevin1986] et/ou le bombardement d'ions sont nécessaires pour promouvoir la désorption des produits $InCl_x$.

La gravure par plasma des trous du CP dans InP/InGaAsP par la méthode ECR (electron cyclotron resonance) a été étudiée en utilisant un plasma Cl_2/Ar [Happ2001a]. Une profondeur gravée de 3,1 μm pour des trous de 250 nm-diamètre a été obtenue. La méthode ICP-RIE utilisée avec un plasma de $SiCl_4$ a présenté avec succès une profondeur gravée de 4,5 μm pour les trous de 270 nm-diamètre

[Pommereau2004]. Une autre méthode de gravure, qui associe une contribution chimique à de l'IBE, la CAIBE (chemically assisted ion beam etching) avec le chlore comme gaz réactif [Mulot2004a, Kotlyar2004a] présente une très bonne sélectivité et permet aussi d'obtenir une profondeur gravée de plus de 5 μm pour des trous de 250 nm-diamètre.

Même si la gravure par CAIBE montre un très bon résultat au niveau de la profondeur pour les trous d'un CP dans InP/GaInAsP, il semble que l'homogénéité de la gravure sur de grandes surfaces ne soit pas complètement maîtrisée. Au contraire, dans un système ICP-RIE, la gravure est généralement peu dépendante de l'endroit du porte-échantillon où se trouve fixé l'échantillon. Cette méthode est donc plus appropriée pour la fabrication de dispositifs photoniques intégrés de grande surface. Un plasma ICP composé de $Cl_2/CH_4/H_2$ a été proposé pour graver les trous d'un CP dans InP [Heijden2003, Strasser2004], mais il a présenté un rapport d'aspect faible, limité à 3:1. Un plasma de Cl_2 pur a été étudié ultérieurement mais il a présenté une gravure fortement isotrope et beaucoup d'undercut [Carlstrom2005]. Les recherches se sont alors orientées vers l'introduction d'autres gaz (ex: Ar, H_2, N_2, O_2) dans le plasma de Cl_2 pour diminuer la gravure latérale par la passivation des flancs ou bien par la pulvérisation ionique. Un plasma de Cl_2/O_2 a démontré une réduction de l'undercut [Heijden2005, Carlstrom2006]. Le plasma $Cl_2/Ar/N_2$ a été aussi étudié, et a permis d'obtenir une profondeur gravée de 3,5 μm pour des trous de 250 nm-diamètre avec un profil vertical [Strasser2007].

3.2 Géométries des couches utilisées

Les structures étudiées dans le cadre de cette thèse sont réalisées sur substrat InP. Pour les lasers, l'empilement est celui typique d'une SCH (separate-confinement heterostructure) avec des puits quantiques multiples (multiple quantum-wells, MQW) de InGaAs/InGaAsP comme région active, et un buffer de 2 μm d'InP dopé n et p de part et d'autre pour l'injection des porteurs. L'empilement vertical de l'adapteur de mode se compose d'une seule couche massive de InGaAsP (n = 3,38) d'épaisseur 500 nm pour le guidage, et d'une fine couche d'InP (n = 3.17) d'épaisseur de 200 nm par dessus. Quant à l'empilement des structures membrane, il est composé d'une couche sacrificielle d'InGaAs d'épaisseur 1,5 μm déposée sur le substrat d'InP suivie par une couche d'InP de 260 nm d'épaisseur qui sera la membrane. La couche d'InGaAs sera retirée par une gravure humide sélective, la membrane d'InP sera alors suspendue dans l'air.

3.3 Lithographie électronique

Les motifs en CP étudiés dans cette thèse ont été fabriqués par lithographie électronique au LPN. Une stratégie de masque double a été adoptée. Ce masque

comporte une couche de SiO_2 de 250 nm-épaisseur déposée sur le matériau semiconducteur et une couche de resine PMMA de 300 nm. Les motifs de CP ont été définis dans la couche de PMMA en utilisant l'EBL (machine Leica 5000+) fonctionnant à une énergie de 100 keV pour les électrons. Pour certaines géométries de structures en CP, les trous peuvent être déplacés hors de la maille du CP ou bien certaines tailles de trous peuvent être ajustées. A cause des effets de proximité particulièrement importants quand on travaille sur les matériaux à base d'InP, toutes ces variations locales de la géométrie du CP conduisent à des modifications indésirables des géométries souhaitées. Ces effets doivent donc être corrigés pour conduire aux géométries les plus proches possible de celles calculées. La correction se fait via la modification de la dose électronique, et ce après plusieurs étapes de calibration.

3.4 Gravure ionique réactive

La gravure ionique réactive (reactive ion etching, RIE) est une méthode de gravure sèche bien connue. Elle associe une contribution chimique, via les neutres présents dans le plasma, à une contribution physique venant des ions. On peut ainsi obtenir des gravures très isotropes, ce qui n'est pas accessible en gravure humide.

Le transfert des motifs CP définis dans le PMMA vers la couche de SiO_2 est réalisé par CCP-RIE en utilisant un plasma à base de CHF_3. Les flancs des trous gravés dans le SiO_2 sont lisses et presque parfaitement verticaux, avec un petit angle d'inclinaison résiduel de 3^0. La déformation des motifs gravés dans le semiconducteur ayant pour origine la géométrie du masque SiO_2 est ainsi minimisée.

La gravure du CP dans les matériaux à base d'InP a été réalisée par ICP-RIE. Le réacteur Sentech est équipé de deux générateurs radio-fréquence, ce qui permet de contrôler séparément la densité du plasma (via la puissance appliquée sur l'antenne) et l'énergie des ions (via la tension appliquée à la cathode). Dans notre système Sentech, le couplage antenne-plasma est efficace et on obtient une forte densité du plasma dès lors que la puissance RF injectée dans l'antenne est supérieure à 150 W.

3.5 La gravure profonde des trous du CP par plasma Cl_2/Ar

En nous basant sur les résultats publiés obtenus en CAIBE et en ICP-RIE, le plasma Cl_2/Ar est choisi au laboratoire pour rechercher des conditions permettant d'obtenir une gravure profonde des trous dans InP. Nous rappelons ici qu'il faut obtenir une profondeur d'au moins 4 μm dans le cas des structures laser. Afin d'optimiser les conditions de gravure, l'impact sur la gravure des paramètres suiv-

ants a été étudié: la température de l'électrode, la puissance RF injectée dans le plasma, la tension de bias, la pression totale des gaz et le flux des gaz. La microscopie électronique à balayage (MEB) a été utilisée pour examiner les profils et les profondeurs gravés après clivage dans les motifs. Parce que la ligne de clivage ne passe pas nécessairement au centre de trous, les profondeurs mesurées sont données avec une incertitude de ± 10%, car le trou n'est pas parfaitement cylindrique.

Pour obtenir des trous verticaux à l'aide d'un plasma Cl_2/Ar, le ratio de Cl_2 ne doit pas dépasser 25%. Une proportion de Cl_2 inférieure à 15% n'est pas favorable car la vitesse de la gravure et la sélectivité (InP:masque) sont fortement réduites. Une pression de gaz extrêmement basse est essentielle pour les motifs petits et denses. Une puissance ICP modérée allant à 100∼150 W est préférable pour minimiser l'undercut et la rugosité des flancs. Il est également apparu que la vitesse de gravure augmente avec la température dans le domaine de température que nous avons considéré 180∼195^{0}C. Nous sommes limités à 195^{0}C par construction de la machine.

Dans les conditions optimisées de la gravure par un plasma ICP Cl_2/Ar, une profondeur gravée maximum de 2,9 μm pour les trous de 240 nm-diamètre a pu être obtenue avec un masque de SiO_2 de 250 nm d'épaisseur. Pour les trous de plus petits diamètres, une profondeur de 1,9 μm est obtenue pour les trous de 110 nm de diamètre. Ces valeurs correspondent à une sélectivité de 18 pour 1 (d = 240 nm) , qu'il serait difficile d'améliorer car la densité de courant d'ions positifs reste relativement élevée dans un plasma ICP. Si l'on choisit d'augmenter l'épaisseur du masque, on aura alors accès à des profondeurs gravées plus importantes. Mais ceci demande de réaliser la lithographie dans une couche de résine plus épaisse, ce qui limite le contrôle que l'on aura des dimensions des motifs dans le cas de géométries de CP où l'on déplace les trous sur la maille triangulaire. Nous n'avons pas retenu cette voie.

Nous avons caractérisé les performance de ce procédé de gravure par deux types de mesure. La durée de vie des porteurs pour une structure en InP/InGaAsP comportant un puits quantique comportant des trous gravés a été mesurée, et vaut de l'ordre de 100∼150 ps, à comparer à la valeur de 3∼6 ns pour les régions sans CP gravés. Nous pensons que cette valeur assez faible est due aux rugosités et états de surface créés lors de la gravure. Nous avons aussi mesuré les performances d'un dispositif représentatif. Les pertes de propagation de la lumière dans un guide W3 (3 rangées manquantes) sont de 80 dB/cm. Cette valeur assez élevée doit pouvoir être réduite si on supprime la rugosité des surfaces gravées.

3.6 Gravure des trous conduisant à des surfaces lisses par plasmas $Cl_2/BCl_3/N_2$ et BCl_3/N_2

Le procédé de gravure à base du plasma Cl_2/Ar présente une bonne sélectivité entre InP et le masque de SiO_2 mais nous n'avons pas su trouver de conditions permettant de supprimer totalement la rugosité résiduelle des flancs. Il est connu que non seulement la profondeur finie des trous quand elle est trop faible, mais aussi la rugosité des surfaces gravées contribuent à la détérioration des performances des dispositifs, en particulier à l'augmentation des pertes de propagation dans des guides PhCW. Par conséquent, il était nécessaire de trouver un procédé nous permettant de supprimer la rugosité des surfaces gravées.

L'ajout de gaz N_2 peut améliorer la gravure anisotrope et supprimer la rugosité sur les flancs [Miyakuni1995, Carlstrom1999, Frost1998]. Le gaz BCl_3 est une alternative au gaz Cl_2 comme source de gaz qui peut fournir des radicaux chlorés. Le plasma Cl_2/BCl_3 a été utilisé pour graver des structures de type ridge dans les matériaux III-V, et l'anisotropie de la gravure a été largement améliorée [Franz1998, Franz2001]. Suivant ces résultats, nous avons choisi d'étudier les plasmas $Cl_2/BCl_3/N_2$ et BCl_3/N_2 dans cette thèse pour la gravure des trous du CP dans les matériaux InP/InGaAsP en espérant ainsi supprimer la rugosité des surfaces et améliorer la verticalité.

Dans le cas de la gravure des trous du CP dans InP par un plasma $Cl_2/BCl_3/N_2$, nous montrons que le gaz N_2 inhibe largement la gravure latérale et conduit à des surfaces lisses lorsque le ratio de N_2 est supérieur à 65%. Nous montrons aussi que le gaz BCl_3 permet d'améliorer la verticalité des profils et d'augmenter la vitesse de la gravure. Quand le ratio de BCl_3 varie de 0% à 15%, l'angle d'inclinaison du flanc gravé diminue de 6^0 à 1^0 et la vitesse de la gravure augmente de 38%. Au delà, un ratio de BCl_3 plus élevé produit des dommages sur les surfaces gravées.

En connaissant le flux d'ions positifs dans le plasma, nous sommes capable d'estimer la pulvérisation ionique pendant la gravure. Nous avons donc mesuré le flux d'ions positifs dans le plasma $Cl_2/BCl_3/N_2$ lorsque l'on fait varier plusieurs paramètres (pression, flux..), et ce à l'aide d'une sonde planaire électrostatique fournie par P. Chabert du LPTP (Laboratoire de Physique et Technologie des Plasmas). Dans le plasma $Cl_2/BCl_3/N_2$, la densité de courant d'ions positifs augmente linéairement avec la puissance ICP et diminue avec la pression totale des gaz. En ce qui concerne la composition du plasma, la densité de courant d'ions positifs augmente avec la proportion de Cl_2 et de BCl_3, puis une saturation est observée lorsque la proportion de BCl_3 est de l'ordre de 35%. La densité de courant maximum est obtenue lorsque la proportion de gaz N_2 est de 20%.

On peut observer dans certains cas de gravure une rugosité des surfaces gravées juste au dessous du masque. On parle d'undercut. Cet undercut est très préjudiciable aux performances des structures sur membrane, car il est présent sur une bonne partie de la profondeur gravée. Cet undercut a été observé assez systéma-

tiquement quand les gravures sont réalisées avec le plasma $Cl_2/BCl_3/N_2$. Nous montrons ici qu'il peut être éliminé en remplaçant complètement le Cl_2 par le BCl_3 et en augmentant l'énergie des ions. La présence de BCl_3 fournit principalement les radicaux chlore et les ions positifs lourds (ex: BCl_2^+ et BCl_3^+), qui peuvent renforcer la verticalité des profils. La proportion des gaz BCl_3/N_2 doit être choisie de façon subtile: en effet, augmenter la proportion de BCl_3 conduit à induire des dommages sur les surfaces à cause de la forte masse (donc énergie cinétique) des ions, alors que réduire la proportion de BCl_3 conduit à diminuer la vitesse de gravure et rendre les flancs moins verticaux.

Afin de clarifier l'existence de la couche de passivation au cours de la gravure et identifier sa composition, les surfaces des trous gravés par les plasmas contenant N_2 ((BCl_3/N_2 et Cl_2/N_2) ont été analysées par microscopie électronique par transmission. Le TEM est aussi équipé d'une analyse de l'énergie des rayons X (TEM-EDX). Les gravures mesurées par TEM ont été réalisées dans l'empilement utilisé pour les membranes, à savoir une couche de GaInAs sur substrat InP, et en surface une couche d'InP qui est la membrane. Dans le cas d'une gravure réalisée par le plasma BCl_3/N_2, une couche amorphe très mince (<2 nm) composée de silicium et d'oxygène a été observée. Le dépôt de silicium peut venir du masque diélectrique en SiO_2 ou bien du transporteur sur lequel l'échantillon est collé, qui est une plaque de Silicium. La présence d'oxygène peut être due à l'oxydation de la surface une fois que l'échantillon gravé est sorti du réacteur et se trouve donc exposé dans l'atmosphère. Cette couche amorphe étant très mince et situé tout près des couches d'InP et de l'InGaAs, il n'a pas été possible d'y identifier la présence de In, P, Ga, ou As. Dans le cas d'une gravure réalisée par le plasma Cl_2/N_2, une couche amorphe a été observée le long des surfaces du masque de SiO_2, ainsi que sur les flancs d'InP et de InGaAs. Etonnamment, cette couche amorphe existe aussi à l'interface masque SiO_2/InP, interface non exposé à la gravure. Son épaisseur est de l'ordre de 25 nm le long de la section d'InP qui correspond au sommet de la gravure et diminue à 3 nm dans l'InGaAs qui est le fond de la gravure. Cette couche est composée de 74%-P, 19%-O, 4%-In, et 3%-Cl.

On retient des mesures obtenues par analyse TEM-EDX que la passivation par nitridation ne se produit pas au cours de la gravure BCl_3/N_2. La suppression de la rugosité dans les trous du CP dans ce cas peut être due à la dilution des radicaux chlorés.

De même ici, nous avons caractérisé les performance de ce procédé de gravure en mesurant la durée de vie des porteurs pour une structure en InP/InGaAsP comportant un puits quantique et comportant des trous gravés à l'aide du procédé $Cl_2/BCl_3/N_2$. Cette durée de vie est maintenant de l'ordre de 1400~1415 ps, que l'on compare à la valeur de 3~6 ns pour les régions sans CP. Cette valeur élevée indique que peu de défauts sont formés sur les surfaces gravées, contrairement au cas de la gravure par plasma Cl_2/Ar.

3.7 Conclusion

Dans cette thèse, les procédés de gravure par plasmas ICP Cl_2/Ar, $Cl_2/BCl_3/ N_2$, et BCl_3/N_2 ont été étudiés et présentés. Dans un plasma de Cl_2/Ar, une profondeur gravée de $\sim$3 μm est obtenue; ce procédé peut donc être utilisé pour la fabrication de guide d'onde planaire en CP sur substrat InP. Si l'on souhaite réaliser des lasers en CP qui demandent des profondeurs gravées plus importantes, de l'ordre de 4 μm, il faudra alors utiliser un masque plus épais.

La rugosité des flancs gravés dans un plasma contenant du chlore peut être produite par deux mécanismes, soit la pulvérisation par les ions positifs énergiques soit l'inégalité des vitesses de la gravure chimique entre In et P. Dans un plasma Cl_2/N_2, l'azote est rajouté afin de limiter l'isotropie de la gravure et de réduire la rugosité des surfaces. Nous avons montré qu'il est possible d'obtenir une gravure fortement anisotrope lorsque le ratio du gaz N_2 est important, à hauteur de $\sim$67% dans le plasma. Mais, la vitesse de gravure reste faible, le profil gravé est conique et de l'undercut est présent. Pour améliorer la gravure, nous avons remplacé Cl_2 par BCl_3 et nous avons ainsi obtenu une bonne verticalité des profils et une plus grande vitesse de gravure. Les trous ont un profil vertical et lisse lorsque le ratio de BCl_3 est d'environ 19% (81%-N_2). Même si la profondeur gravée avec ce plasma BCl_3/N_2 est limitée à environ 800 nm, elle convient parfaitement à la fabrication des dispositifs CP sur membrane d'InP, l'épaisseur de la membrane étant de 250-300 nm.

Il n'est pas simple de proposer des mécanismes expliquant une réduction de la gravure latérale ainsi qu'une très faible rugosité des surfaces gravées suite à l'introduction de N_2. On pense plutôt à une dilution des radicaux de chlore, car la nitridation des surfaces n'est pas visible quand on étudie les surfaces gravées par TEM. Pour comprendre les mécanismes de la gravure en présence de N_2, des études plus rigoureuses conduisant à connaître la composition du plasma sont nécessaires. On peut mettre en oeuvre la spectroscopie d'émission optique (optical emission spectroscopy, OES) ou la mesure par spectrométrie de masse quadripolaire (quadrupole mass spectrometer, QMS). Ces études permettraient d'identifier les espèces (ions, neutres) présentes dans le plasma ainsi que les produits gravés.

Chapter 4
Adaptateurs de mode en cristaux photoniques

4.1 Introduction

Dans les circuits intégrés photoniques (CIP), la lumière est confinée dans des guides d'onde optiques, et se propage sur les modes supportés par ces guides. Ces modes ont en général un profil elliptique, car la couche guidante est d'épaisseur submicronique de façon à ce que le guide soit monomode verticalement, alors que le confinement latéral est assuré par un guide de largeur supérieure au micron. Il y a toutefois des moments où la lumière doit se propager soit dans l'espace libre, soit dans des fibres optiques. Le profil du mode émis par une diode laser est petit, le faisceau émergeant est donc fortement divergent. Dans ce cas, l'alignement entre une diode laser et une fibre optique est rendu difficile et l'efficacité de couplage est donc réduite. Pour améliorer le couplage, une région intermédiaire est insérée entre le CIP et la fibre optique. Cette section de guide doit faire évoluer le profil et la taille du mode, tout en préservant la répartition de la puissance lumineuse sur le mode fondamental. Un dispositif présentant cette fonction optique spécifique est désigné comme un adaptateur de mode. Le terme taper est souvent employé car sa géometrie implique une variation des dimensions structurelles.

Dans cette these, nous avons étudié des géométries d'adaptateur de mode permettant de coupler le mode issu d'un guide en CP à une fibre monomode (single-mode fiber, SMF) clivée-droite. Les géométries de taper sont définies dans l'environnement périodique du cristal photonique de façon à être intégrées avec le guide CP. On souhaite ainsi démontrer que cet environnement permet de produire des tapers beaucoup plus compacts que les tapers classiques fonctionnant par confinement par contraste d'indice.

Dans le PhCW, le mode optique est souvent elliptique, le grand axe de l'ellipse étant dans le plan, et valant 1$\sim$2 μm. En revanche, le mode de la SMF est circulaire de diamètre 8$\sim$10 μm. Pour coupler actuellement la lumière dans les PhCW,

nous utilisons une fibre micro-lentillée, ce qui n'est pas bénéfique pour l'intégration optique car ce type de fibre a une très faible tolérance d'alignement. Si l'on est capable d'élargir la taille du mode à la sortie de PhCW, alors le couplage direct à une SMF clivée-droite sera plus efficace.

Les géométries de taper considérées ici transforment la taille du mode dans le plan de propagation, la taille du mode dans la direction verticale n'est pas modifiée, car nous ne modifions pas l'empilement vertical. Nous ne considérons donc pas ici les géométries de taper qui se terminent avec un guide très étroit de façon à transférer la totalité du mode dans une couche guidante sous-jacente. L'étude s'est portée sur l'analyse modale de la transmission, de façon à assurer le maximum de puissance couplée sur le mode fondamental du guide de sortie. Les adaptateurs de mode ont été conçus de façon à minimiser la conversion modale aux modes d'ordre supérieur ou aux modes radiés, ainsi que la réflexion.

4.2 Théorie du couplage

L'efficacité du couplage entre un laser ou un guide d'onde et une fibre optique peut être améliorée, ainsi que les tolérances d'alignement, en insérant en sortie du laser/guide d'onde un adaptateur de mode.

4.3 Géométries retenues pour les adaptateurs de mode en CP

Pour les guides d'ondes en CP opérant sur des modes localisés dans la bande interdite photonique, le confinement de la lumière dans le plan par le contraste d'indice se rajoute au confinement assuré par l'effet Bragg du CP. En effet, le cIJur du guide où les rangées de trous ont été omises a un indice supérieur aux bords du guide où les trous ont été réalisés.

Des guides d'onde en CP dans lesquels on fait varier progressivement la largeur du défaut (nombre de rangées de trous manquantes) peuvent conduire à une transformation de la taille du mode. Nous avons étudié des géométries correspondant à une forme en marches d'escalier abruptes et aussi en marche d'escalier avec une transition plus douce pour la marche. La largeur du défaut linéaire évolue en partant d'un W3 (1$\sim$2 μm) pour terminer à un W23 (8 μm) avec une longueur fixe de 8-périodes pour chaque section (longueur totale $\sim$34,4 μm). Pour la géométrie en marches d'escalier graduelles, les diamètres des 4 derniers trous de chaque section sont réduits afin de diminuer la réflexion ainsi que la projection sur les modes d'ordre supérieur qui se produisent au niveau de la marche.

Les zones de matériau où le cristal photonique a été gravé représentent un matériau ayant un indice effectif plus petit que le matériau non gravé, celui qui

forme le centre du guide. On peut alors considérer que le confinement de la lumière est réalisé par le contraste d'indice. Ceci peut être acceptable car le taper est constitué par des guides qui sont rapidement larges, et donc pour lesquels l'effet de la périodicité affecte peu les modes supportés. Dans ce cas, on peut envisager des géométries de tapers "classiques" [Bendelli1991, Wei1997, Mitomi1994, Park2001], l'environnent du CP permettant de dessiner sur mesure la variation d'indice souhaitée. Nous avons étudié des adaptateurs de mode en CP avec un contour gaussien, en forme de parabole, ou d'ellipse. Les positions et diamètres de certains trous sont alors modifiés pour s'adapter très exactement à la géométrie souhaitée pour les limites du taper.

L'objectif principal de l'étude des tapers est de comprendre comment la puissance optique se répartie sur les différents modes supportés par le guide ruban de sortie qui est un guide large, donc fortement multimode. Ce guide a été choisi de largeur physique comparable à un PhCW de largeur W23. Le mode fondamental de ce guide ne sera pas exactement celui d'une fibre car nous utilisons du matériau de fort indice contrairement à la fibre en silice. Nous pensons néanmoins que l'étude modale reste pertinente.

4.4 Simulation des adaptateurs de mode en CP

Les simulations des adaptateurs de mode en CP ont été réalisées en utilisant la méthode FDTD (le soft utilisé est celui de Photon Design). Le calcul est un calcul 2D car le taper est long, un calcul 3D serait prohibitif en durée. De plus, nos géométries étant sur substrat, l'utilisation d'un indice effectif pour représenter l'empilement vertical est une approximation tout à fait acceptable. Tous les adaptateurs de mode ont été insérés entre deux sections de guide ridge classique pour les accès , les ridges ayant une largeur de 1,38 μm à l'entrée, cette largeur correspond à la largeur physique d'un guide W3, et une largeur de 8,3 μm à la sortie, cette largeur correspondant à la largeur physique d'un guide W23. L'insertion des ridges d'accès est nécessaire, car le logiciel Photon Design ne calcule la répartition de la puissance sur les modes que dans le cas des modes d'un guide à contraste d'indice. De cette façon, on injecte via le ridge d'accès sur le mode fondamental TE pair de W3, et on collecte les modes du CP projetés sur les modes du guide de sortie. Tous les calculs sont faits sans inclure de pertes de propagation.

Une efficacité moyenne de transmission intégrée sur tous les modes de $\sim$95% est obtenue pour toutes les géométries, sauf à la longueur d'onde de 1,52 μm. Le creux de transmission visible autour de 1,52 μm dans le spectre est due à la mini-stop bande (MSB) du guide W3 qui a été adopté comme le début de nos adaptateurs de mode en CP.

Quant à la distribution modale de la puissance transmise, tous les adaptateurs de mode, à l'exception de la géométrie en ellipse, montrent un état dominant pour

le mode fondamental pair. Le ratio moyen du mode fondamental hors de la MSB est d'environ 73% pour le taper de géométrie gaussienne. Dans le cas du taper à géométrie en ellipse, 70% du mode fondamental injecté se retrouve en sortie couplé au 2ème mode pair.

Concernant les adaptateurs de mode basés sur une variation de la largeur du guide par marches graduelles, le contrôle de la position et des diamètres de trous est d'autant plus critique que l'on souhaite réaliser une taper de petite longueur. Ces géométries sont potentiellement les plus compactes, mais deviennent très sensibles aux erreurs de fabrication.

4.5 Fabrication des adaptateurs de mode en CP

Les adaptateurs de mode ont été fabriqués à l'aide d'un empilement vertical comportant une couche guidante InGaAsP sur substrat InP. Les motifs sont réalisés en utilisant la lithographie électronique en incluant des modifications locales des doses électroniques afin de compenser l'impact des effets de proximité. Ils sont gravés en utilisant le plasma Cl_2/Ar, avec lequel une profondeur gravée de 2,8 μm est obtenue pour des trous de 250 nm-diamètre.

4.6 Caractérisation optique: transmission et divergence du mode optique

Pour démontrer les performances des adaptateurs de mode fabriqués, nous avons mesuré le spectre de transmission en collectant la puissance optique à l'aide d'une fibre clivée-droite , ainsi que la divergence du mode optique en sortie, à l'aide d'une photodiode.

On voit dans les spectres de transmission la réduction de la puissance transmise autour de la longueur d'onde de 1,54 μm, ce qui est la signature de la mini-stop bande du guide W3 qui est notre guide initial. Dans les adaptateurs de mode, cette diminution de la transmission est faible car la longueur de la section W3 est très réduite.

La meilleure performance en transmission est obtenue pour le taper ayant une forme gaussienne. Elle correspond à une amélioration de la puissance transmise par un facteur 4 dans le domaine spectral 1.61-1.62 μm, quand on compare à la transmission sur un guide W3.

Pour la mesure des champs lointains, une tendance similaire aux résultats de la simulation est constatée pour tous les adaptateurs de mode en CP. Les angles de divergence du mode de sortie sont d'environ 19^0 et 23^0 correspondant à des tailles de mode de 6,1 μm et 5,1 μm dans le plan latéral, ce pour les tapers de géométrie respectivement en marche d'escalier et en forme gaussienne. Le ratio d'intensité

du 2ème mode pair est faible, de l'ordre de 0,2 par rapport au mode fondamental, pour ces deux géométries.

4.7 Conclusion

Les géométries proposées pour les adaptateurs de mode réalisés dans un environnement en cristal photonique conduisent à des tapers compacts, et opérant majoritairement sur le mode fondamental. Le domaine spectral d'utilisation sera toujours limité par la (les) mini-stop band(s) des guides PhCW de départ. On choisira alors la périodicité de façon à exclure les MSB du domaine d'utilisation recherchée.

Chapter 5
Laser à cristaux photoniques

5.1 Introduction

On peut tirer avantage de l'environnement périodique qui existe dans un cristal photonique pour obtenir l'émission monomode d'un laser, sans avoir besoin d'insérer un réseau ou une cavité additionnels. Plusieurs approches ont été proposées, comme le laser à cavités couplées, qui ne comporte que deux cavités, le cristal photonique jouant le rôle du réflecteur intra-cavité, ou bien un grand nombre de cavités couplées, le laser est alors une section à gain d'un guide de type CROW (coupled-resonator optical waveguide) [Yariv1999], guide formé d'une succession de résonateurs périodiques faiblement couplés. Un laser de type CROW pompé électriquement a été fabriqué et a montré une très bonne réjection de 40 dB (side mode suppression ration, SMSR) [Happ2003]. Mais, dans cette première réalisation, le courant de seuil reste relativement élevé et le rendement externe plutôt faible. Ces deux performances doivent pouvoir être améliorées si on réalise des cavités plus fortement couplées.

Nous avons étudié dans cette thèse des géométries de laser en cristaux photoniques basées sur des guides relativement larges présentant des constrictions régulièrement espacées: cette géométrie peut être décrite comme un guide CROW dans lequel les cavités sont fortement couplées. Il n'y a alors plus de trous gravés le long de l'axe de la cavité, ce qui doit conduire à une efficacité externe plus grande. Dans un dispositif fonctionnant en pompage électrique, nous recherchons le design conduisant au meilleur compromis entre une bonne sélection spectrale (SMSR $>$30 dB), un courant de seuil faible et un rendement externe élevé.

5.2 Cavités Lasers basées sur des cavités couplées

Dans les géométries classiques de lasers à cavités couplées, les deux paramètres jouant sur la sélection du mode qui lase sont d'une part le coefficient de réflexion du réflecteur interne et d'autre part le rapport des longueurs des deux cavités. De

la même façon ici, nous pourrons définir la géométrie de notre guide à constriction après avoir calculé le coefficient de réflexion d'une constriction.

5.3 Dessins de cavités lasers en CP basées sur des guides d'onde à constrictions multiples

Un guide d'onde avec des constrictions multiples (multiple-constricted-waveguides, MCW) régulièrement positionnées peut être traité comme une variété de CROW, dans lequel le couplage entre cavités est plus fort que dans un CROW classique dans lequel les cavités sont complètement fermées. Un MCW peut être caractérisé par la longueur d'une cavité qui est la distance entre deux constrictions et par le couplage entre les cavités. Ces deux paramètres sont liés, de façon à ce que toutes les constrictions assurent des contre-réactions en phase. Nous avons tenté de calculer l'amplitude et la phase de la réflexion à une constriction par un calcul FDTD 2D. Ayant choisi une géométrie pour la constriction et connaissant les deux paramètres décrivant le passage de la constriction, on peut alors avec un calcul de type miroir de Bragg multi-couches définir la distance entre deux constrictions conduisant à l'oscillation dans la cavité.

5.4 Simulation des guides d'ondes avec constrictions

Pour calculer l'amplitude et la phase de la réflexion à une constriction, nous avons considéré un guide d'onde composé de une section de guide W5 le long de la direction ΓK se trouvant réduit à un guide plus étroit de largeur W3 ou W1 , et ce pour différentes longueurs de la section de guide de largeur réduite, la constriction n'étant pas nécessairement limitée à une rangée de trous. De la même façon que au chapitre précédent, nous avons inséré des guides d'accès de 1,8 μm de largeur qui assurent un couplage efficace à W5, pour pouvoir calculer la répartition modale de la réflexion.

Pour la constriction W5/W3, l'efficacité de la réflexion sur le mode fondamental est inférieure à 1%, ce qui suggère un régime de couplage fort entre deux cavités. L'efficacité en transmission sur le mode fondamental est comprise entre 0,6 et 0,9 selon les longueurs d'onde et selon la longueur de la section de guide de largeur réduite.

Pour la constriction W5/W1, la transmission est plus faible et la réflexion plus élevée que pour la constriction W5/W3. L'efficacité de la transmission sur le mode fondamental varie dans une gamme de 0,15 et 0,45 selon la longueur de la section réduite et selon les longueurs d'onde. Quant à l'efficacité de la réflexion sur le mode

fondamental, elle varie entre 0,05∼0,2. Si cette constriction plus étroite est plus efficace sur le mode fondamental, elle a l'inconvénient de projeter une partie de la lumière (réfléchie et transmise) sur les modes d'ordre supérieurs, ce qui est perdu pour le seuil et le rendement externe.

Nous avons rencontré des difficultés pour calculer le comportant des constrictions. Concernant la distribution modale, nous n'avons accès qu'à la distribution modale calculée sur les guide de type ruban qui sont placés en entrée et en sortie du guide CP. Or, si le guide ruban de largeur 1.8 μm est correctement matché au guide W5 lorsque que celui-ci opère sur le mode fondamental, il ne l'est plus quand les modes d'ordre supérieur de W5 sont excités. Donc, la proportion de puissance transmise que l'on donne pour le mode fondamental est celle qui est recouplée dans le mode fondamental du guide ruban, et donc pas véritablement celle du mode fondamental du guide W5. D'autre part, il ne nous a pas été possible de correctement calculer la phase de réflexion à la constriction, pour la même raison d'avoir à associer l'interface guide ruban/guide CP.

Le choix des géométries pour les MCW s'est donc réduit à un calcul élémentaire de mise en phase de cavités ouvertes.

5.5 Fabrication des lasers à base de guides à constrictions multiples en CP

Les lasers MCW en CP sont fabriqués dans un empilement de couches permettant l'injection électrique, et comportant une couche active à base de multi-puits quantiques InGaAs/InGaAsP émettant autour la longueur d'onde de 1,55 μm. Cet empilement est réalisé au LPN par MOVPE. Les géométries retenues sont de type guide W5 le long de la direction ΓK réduit à W1 avec une distance entre constriction de 4, 6 ou 8 périodes. Pour atteindre un bon confinement du mode dans le plan, les trous d'air doivent être gravés à une profondeur de plus de 4 μm, de façon à intercepter la totalité du mode optique. Dans la mesure où nous n'avons pas trouvé de procédé ICP permettant d'atteindre de telles profondeurs gravées, la gravure des cristaux photoniques a été réalisée pour ces dispositifs par CAIBE, en utilisant le chlore comme gaz réactif, par A. Berrier et S. Anand au laboratoire de KTH (Kista, Suède). La localisation de l'injection électrique par implantation de protons est l'autre étape critique de la fabrication des lasers CP.

Nous avons laissé la réalisation des lasers prendre du retard, et avons choisi de consacrer plus de temps à la fabrication de structures en CP sur membrane InP. Ceci est l'objet du chapitre suivant.

5.6 Discussion

Nous avons considéré les guides à constrictions multiples comme de bons candidats pour définir une cavité performante (seuil, SMSR, rendement). Le couplage entre cavités successives y est plus important que dans les géométries de type CROW proposées dans la littérature. Le calcul de l'amplitude et de la phase de la réflexion à la constriction est nécessaire pour correctement définir la géométrie du MCW.

Chapter 6
Guide d'ondes à cristaux photoniques sur membrane suspendue

6.1 Introduction

Les applications des guides d'ondes à CP 2D dans lesquels le confinement vertical est assuré par une hétérostructure sont limitées en raison des pertes de propagation élevées: des valeurs de 15 à 100 dB/cm ont été reportées pour le guide W3. Ces pertes proviennent essentiellement du couplage des modes guidés à des modes radiés hors du plan, puisque dans l'hétero-structure à faible contraste d'indice le gap photonique se situe toujours au dessus de la ligne de lumière du substrat (cf chapitre 2).

Pour des guides d'onde à CP sur membrane suspendue dans l'air, une partie du gap photonique se situe au dessous de la ligne de lumière de l'air, et donc, pour certaines fréquences les modes guidés peuvent se propager théoriquement sans pertes. Jusqu'à maintenant, la plus faible valeur rapportée pour les pertes de propagation pour un guide W1 est de 5 dB/cm pour une membrane de GaAs [Combrie2006], et de 2-10 dB/cm pour une membrane Si [Dulkeith2005, Kuramochi2005, Kuramochi2006].

L'intérêt des guides sur membrane suspendue est de pouvoir supporter des modes qui ont à la fois de faibles pertes de propagation et une vitesse de groupe lente, par exemple le mode fondamental du guide W1 en bord de bande. Contrôler la vitesse de groupe de la lumière permet de définir des lignes à retard optique, ce qui ouvrirait enfin la voie au traitement tout optique de l'information. La maîtrise de la technologie des membranes permet aussi de réaliser des cavités à très fort coefficient de surtension. Expérimentalement, des vitesses de groupe de l'ordre de c/30∼c/60 (c est la vitesse de la lumière dans le vide) ont été rapportées. Aussi, un facteur de qualité extrême haut atteignant 800,000 a été obtenu dans une nano-

cavité CP sur membrane Si. Enfin, si les membranes contiennent des couches émettrices de lumière, de type puits ou boites quantiques, le ralentissement du mode permet d'augmenter l'interaction lumière-matière.

6.2 Fabrication, gravure sélective de la couche sacrificielle

Concernant la gravure des trous du cristal photonique pour les dispositifs sur membrane suspendue, nous ne rencontrons pas la difficulté de la gravure profonde car l'épaisseur de la membrane ne dépasse jamais 300 nm de façon à assurer un fonctionnement dans un régime mono-mode. Par contre, l'exigence se porte maintenant sur la qualité des flancs gravés, qui doivent être lisses, pour limiter les pertes par diffusion, et verticaux pour ne pas engendrer de couplage entre les deux polarisations.

La membrane se retrouve suspendue dans l'air par le retrait d'une couche sous-jacente. Ce retrait est réalisé par gravure humide sélective. Le principe est d'attaquer chimiquement le matériau de la couche sacrificielle en GaInAs située sous la membrane, alors la membrane d'InP se retrouve suspendue dans l'air. La solution chimique atteint la couche sacrificielle sous-jacente en pénétrant par les trous. Différentes chimies ont été étudiées pour cette attaque sélective.

6.3 Guide d'ondes à CP sur membrane suspendue

Des guides d'onde W1 sur membrane InP ayant une épaisseur de 260 nm ont été fabriqués en utilisant le procédé à base du plasma ICP BCl_3/N_2 pour la gravure des trous et la gravure humide sélective pour le retrait de la couche sacrificielle. Le séchage super critique permet d'assurer une bonne tenue mécanique de la membrane, les guides faisant jusqu'à 1mm de long.

Selon le spectre de transmission mesuré en polarisation TE, un plateau d'efficacité haute en transmission est observé entre 1453 nm et 1510 nm, correspondant au domaine spectral commençant au passage de la ligne de lumière de l'air, et se terminant à la coupure du mode en bord de bande. Les modes étant théoriquement sans pertes dans cette gamme de fréquence, les pertes de propagation mesurées de 25 dB/cm à la longueur d'onde de 1480 nm sont principalement attribuables aux imperfections de la fabrication.

6.4 Discussion

Le procédé de gravure des cristaux photoniques à l'aide du plasma ICP contenant les gaz BCl_3/N_2 que nous avons développé dans le cadre de cette thèse a permis de réaliser avec succès la fabrication de guide d'ondes à CP sur membrane InP suspendue. Les pertes de propagation peuvent être réduites en améliorant le procédé de fabrication, en particulier en augmentant la verticalité des flancs gravés. Même si cette valeur de pertes est actuellement relativement grande par rapport aux valeurs obtenus sur des guides sur membrane GaAs ou Si, elle ne limite pas l'étude au LPN de structures supportant des modes lents, pour des applications potentielles telles que lignes à retard optiques ou dispositifs non-linéaires.

Chapter 7
Conclusion

Réalisations

Dans ce travail de thèse, nous avons étudié plusieurs dispositifs en cristaux photoniques bi-dimensionnels, dispositifs réalisant des fonctions optiques qui peuvent, par le biais des CP, être miniaturisés et intégrés dans les circuits intégrés photoniques. Les dispositifs étudiés couvrent du transformateur modal visant à étendre le mode pour optimiser le couplage à une fibre monomode clivée droite, aux lasers monofréquences basés sur des guides à constriction pour les structures sur substrat, jusqu'aux guides sur membrane InP suspendue. Parmi toutes les étapes de fabrication, les efforts ont été importants pour développer un procédé de gravure performant pour les CP sur membrane par ICP-RIE . Outre l'intérêt des guides en CP sur membrane pour accéder à des modes de faible vitesse de groupe, ce développement technologique a été utilisé par d'autres équipes du laboratoire pour la réalisation de cavité à fort coefficient de surtension.

Concernant la gravure des trous du cristal photonique, nous avons étudié la gravure par RIE ICP avec des plasmas comportant les gaz Cl_2/Ar, Cl_2/BCl_3 /N_2, et BCl_3/N_2. Les conditions de gravure dans un plasma Cl_2/Ar ont été optimisées et utilisées pour la fabrication des adaptateurs de mode à CP. Une profondeur gravée de l'ordre de 1,9∼2,9 μm peut être obtenue pour des trous de 110∼250 nm de diamètre. Le profil du trou est correctement vertical mais les flancs gravés sont rugueux. Pour un guide W3 fabriqué dans une hétéro-structure InP/InGaAsP/InP avec ces conditions de gravure, les pertes de propagation du mode fondamental restent élevées et valent 80 dB/cm. La rugosité des surfaces gravées a été supprimée largement par l'introduction du gaz N_2 dans le plasma. L'ajout de BCl_3 permet en outre d'améliorer la verticalité du trou. Pour une proportion appropriée des gaz BCl_3/N_2, les surfaces gravées sont lisses et le profil du trou est presque vertical et sans undercut. Pour un guide d'onde W1 sur membrane InP suspendue dans l'air réalisé avec le processus de gravure par le plasma du BCl_3/N_2, les pertes de propagation sont de 25 dB/cm pour le mode pair, lorsqu'il opère au-dessous de la ligne de lumière de l'air.

Concernant les adaptateurs de mode à CP, plusieurs géométries sont étudiées pour étendre le mode optique dans le plan afin de coupler efficacement la puissance optique transportée dans un guide W3 vers une fibre optique mono-mode clivée-droite. Les géométries des adaptateurs de mode sont basées soit principalement sur l'effet d'interférences multiples ou sur le contraste d'indice réfractif. Dans le premier type, la largeur du défaut linéaire est augmenté progressivement de W3 à W23 en faisant varier ou non la taille des trous entre deux sections de guide de largeur différente. Le deuxième type est hérité des adaptateurs de mode conventionnels en utilisant le contraste d'indice réfractif. La géométrie des trous du CP peut alors fournir une variation finement ajustée du contraste d'indice. La longueur de l'adaptateur de mode peut dans l'environnement du CP être réduite à 40 μm, contrairement à celle d'un adaptateur de mode classique qui a une longueur de plusieurs centaines de micromètres. Nous nous sommes surtout intéressés au comportement modal de l'adaptateur. Sur les adaptateurs fabriqués, les champs lointains sont mesurés et comparés avec les résultats de simulation. Parmi les adaptateurs de mode étudiés, l'efficacité du couplage est renforcée par un facteur 4 pour le taper de géométrie gaussienne ; et seulement 20% de la puissance optique se trouve projetée sur les modes d'ordres plus élevés. Dans ce cas, les pertes de couplage entre le ridge d'accès coté sortie et la fibre optique sont estimées à 12,7 dB.

Pour obtenir l'émission laser monofréquence dans l'environnement périodique du CP, nous avons choisi d'étudier des guides à constriction (MCW, multiple-constricted-waveguides). Par rapport à un guide CROW, le couplage entre cavités est plus fort dans le MCW parce que les cavités ne sont pas complètement fermées. Il devrait conduire à une efficacité externe plus importante, le mode étant moins localisé sur chaque cavité. Afin de définir la géométrie des constrictions, nous avons cherché à simuler la transmission et la réflexion du mode fondamental au passage d'une constriction, selon la longueur de la constriction et sa dimension, les géométries les plus favorables étant un guide W5 réduit à W3 et un guide W5 réduit à W1. Le calcul du comportement modal de la constriction elle-même s'est avéré difficile à isoler de la contribution de l'interface guide ruban d'accès/guide CP, celle-ci devant être nécessairement incluse car le calcul résolu sur les modes du guide ne peut se faire que sur les modes d'un guide ruban. Nous avons donc dessiné les MCW en omettant la contribution de la phase de la réflexion à la constriction. La réalisation des lasers a pris du retard car nous avons dirigé nos efforts sur les structures sur membrane.

Perspectives

Une partie importante de la thèse a été consacrée au développement de procédés de gravure des CP, car c'est l'étape la plus critique de la fabrication des structures. Les procédés RIE ICP à base de plasmas Cl_2/N_2 et BCl_3/N_2 peuvent être encore améliorés, en particulier pour conduire à des flancs parfaitement verticaux. En

effet, tout écart à la verticalité permet du couplage entre les deux polarisations, ce qui est très préjudiciable pour les performances, tant en propagation que pour les dispositifs résonants. L'amélioration des procédés passe par une étude approfondie de la composition du plasma, pour déterminer les espèces (radicaux, ions positifs) présentes , en particulier en fonction du ratio de N_2. L'anisotropie de la gravure vient de la présence d'une couche de passivation. C'est en maîtrisant la formation et la composition de cette couche que l'on atteindra la verticalité des flancs gravés.

Les dispositifs étudiés ici sont des dispositifs passifs ou actifs (émetteurs de lumière à 1.55 μm) sur substrat InP, ou des guides sur membrane InP. Mais l'avenir de l'optique intégrée est maintenant basé sur l'intégration de toutes les fonctions optiques sur Silicium. Pour inclure les fonctions actives (émission, accordabilité rapide), il faut pouvoir intégrer de façon hybride les émetteurs à base de matériau III-V sur le Si, par la technique de collage moléculaire. On conserve la liberté du design CP dans le matériau III-V dans le plan, le confinement vertical étant assuré par le matériau III-V et le guide en Si. La technologie de fabrication des trous d'air du cristal photonique que l'on a développée pour les membranes InP est une étape importante vers la réalisation de tels dispositifs intégrés.